Master's Thesis in Chemistry

THE SYNTHESIS, AND STRUCTURAL STUDIES OF ADVANCED FUNCTIONAL MATERIALS

Yanshun Liang

February 2021

School of Physical Sciences

University of Kent

Acknowledgement

My gratitude goes first to my supervisor Professor Mark Green. Thank you so much for giving me the opportunity to be your master's student this year. I feel privileged and grateful to have had the chance to visit the European synchrotron radiation facility and have my samples scanned at the Institut Laue-Langevin. This was personally a very proud moment for me to have such an honour. It is difficult to express myself through words and more importantly, without you, I would not be the person I am today so I would like to thank you for everything.

In addition, I would like to show my appreciation to the following members of the chemistry department:

- Special thanks to my PhD colleague Jake Minns for his continuous support in guiding me through XRD analysis and Fullprof refinement as well as helping me to complete my Panalytical XRD training.
- Dr Paul Saines for being so patient and pedagogic with my single crystal training and $MAPbI_3$ project.
- Dr Donna Arnold for providing the training on the SQUID equipment.

I would like also to thank my family, especially my parents and my brother Jing for their continuous support.

List of abbreviations and symbols

$MAPbI_3$	Methylammonium lead tri-iodide
HI	Hydroiodic acid
H_3PO_2	Hypophosphorous acid
PbO	Lead (ii) oxide
PbI_2	Lead (ii) iodide
MAI	Methylammonium iodide CH_3NH_3I
SQUID	Superconducting quantum interference device
D2B	High-resolution two-axis diffractometer at ILL
XRD	X-ray diffraction
RbF	Rubidium fluoride
FeF_2	Iron (ii) fluoride
FeF_3	Iron (iii) fluoride
$CrF_3.3H_2O$	Chromium (iii) fluoride trihydrate
ZnF_2	Zinc fluoride
CuF_2	Copper (ii) fluoride
$FeF_3.3H_2O$	Iron (iii) fluoride trihydrate
CsF	Caesium fluoride
$Cs_{0.05}MA_{0.95}PbI_3$	$Cs_{0.05}(CH_3NH_2)_{0.95}PbI_3$
$Cs_{0.10}MA_{0.90}PbI_3$	$Cs_{0.10}(CH_3NH_2)_{0.90}PbI_3$
Mixed metal fluorides	
	$RbFe_2F_6$
	$RbFeCsF_6$
	$RbFeZnF_6$
	$CsFeZnF_6$
	$CsFeCrF_6$

Page of Contents

List of Tables

List of Figures

Abstract

This research project is divided into two sections. The first section is an investigation into the stability of photovoltaic hybrid perovskites under various annealing conditions. Synthesis of $MAPbI_3$ and related systems has been performed using a solution precipitation method. The compounds have then been divided in many smaller batches and thermally treated at different temperatures under air, vacuum and in the presence of the gettering agent, Zn. The temperatures and conditions were chosen to coincide with those typically implemented in the manufacture of photovoltaic devices, with the aim of understanding how these annealing conditions affect the structure. Firstly, we show that annealing in air increases both the tetragonal a and c lattice parameters, but reduces the c/a ratio, as a result in improved packing and establishing more hydrogen bonding. Secondly, annealing in a vacuum at 90 ºC for up to 73 hours showed an increase in both the tetragonal a and c lattice parameters up to 5 hours but then there is a reduction to form a plateau around 40 hours, demonstrating that the annealing period is critical to tuning the MA packing and disorder in the structure. Finally, we show that annealing in a vacuum in the presence of Zn metal significantly reduces the lattice parameters, in contrast to the air and vacuum only environment, demonstrating that Zn can be used as a gettering agent to tune the composition during annealing. This work sheds some light on the wide variation in photovoltaic properties of $MAPbI_3$ that are reported in the literature, and the importance in determining the correlation of photovoltaic properties with annealing procedures on these very flexible hybrid perovskites. The second section is on the synthesis and characterisation of magnetically frustrated mixed metal fluoride pyrochlores. $RbFe_2F_6$ is a charged ordered defect pyrochlore, that is better described by the formula, $RbFe^{2+}Fe^{3+}F_6$. We have demonstrated that the average antiferromagnetic structure remains the same down to 1.5 K, despite recent inelastic neutron scattering studies showing a change in the dynamics. We have synthesised a number of related systems with the general formula $AFeMF_6$, where M = Cr, Zn and A = Rb and Cs. We have isolated a previously unreported phase, $RbFe_{1.3}Cr_{0.7}F_6$, that possesses the same charge ordered orthorhombic structure as $RbFe_2F_6$ with the space group *Pnma*. SQUID magnetometry shows $RbFe_{1.3}Cr_{0.7}F_6$ has a magnetic transition at ~10 K with divergence between zero field cooled and field cooled magnetic susceptibility. Neutron scattering confirms the system is a spin glass, and no long ranged magnetic order is observed. The magnetically dilute pyrochlore, $RbFeZnF_6$ was synthesised and showed Curie-Weiss behaviour down to 2 K.

Keywords: $MAPbI_3$, pyrochlores, mixed metal fluorides, powder X-ray diffraction, single crystal X-ray diffraction, Rietveld refinement, neutron diffraction

Aims of research for MAPbI$_3$:

We are at a critical point in the development of renewable energy resources. Global warming on an unprecedented scale has made is essential we replace carbon emitting fossil fuels before we cause irreversible damage to our planet. Solar energy, which provides many times the world's energy demands, is a viable option if it can be harnessed cheaply and effectively. Recently a functional material; organic-inorganic hybrid perovskite methyl ammonium lead iodide (MAPbI$_3$) has been studied extensively due to its easy and low production cost and its ever increasing photovoltaic performance of the devices. One of the main issues before commercialisation is viable is the poor chemical and thermal stability of the hybrid perovskites. In the manufacture of solar devices published in the literature, the perovskite is always annealed. This is done under various temperatures and environments and leads to different photovoltaic performance such as energy conversion, but it is not clear what effect this is having on the structure. This project aims to investigate structural variations of the photovoltaic perovskites, MAPbI$_3$ and related systems, synthesised through a solution-based method and then annealed under different treatments. The structural changes will be investigated with X-ray characterisation techniques. It is intended that the research findings are beneficial to the development of photovoltaic devices and explaining the wide range of photovoltaic performances reported in the literature.

Summary of Research Objectives:

1. To review the literature concerning the development of the photovoltaic performance of devices formed from MAPbI$_3$, and related systems.

2. To investigate the stability of MAPbI$_3$ through a solution-based synthesis and to examine their structural variation under a series of different thermal annealing treatments by the X-ray powder diffraction technique and Rietveld refinement.

3. To compare, analyse and evaluate the results of the Rietveld refinement of the X-ray powder diffraction data of MAPbI$_3$ with literature.

Aims of research for mixed metal fluorides:

Mixed-metal fluorides; a series of innovative functional material with a pyrochlore structure is research-worthy due to their varied functional properties such as multiferroic behaviour and magnetic frustration. This project is intended to use the recently published hydrothermal synthesis method of RbFe$_2$F$_6$ to form new mixed metal fluoride materials, and investigate their structure and magnetism using X-ray and neutron powder diffraction and SQUID magnetometry. It is intended the research findings will contribute to the development of mixed metal fluoride compounds with a pyrochlore structure and extend the range of known frustrated magnets.

Summary of Research objectives:

1. To review the literature on the structure and magnetism of mixed metal fluoride materials with the pyrochlore structure.
2. To synthesis hydrothermally a range of mixed metal fluorides and characterised them through X-ray and, neutron diffraction and SQUID magnetometry.
3. To compare, analyse and evaluate the results of the Rietveld refinement of the X-ray powder diffraction data, neutron scattering diffraction data with literature.

Chapter 1. Introduction

1.1.0 Background information on photovoltaics

1.1.1 The use of photovoltaics and why alternative energy solutions are needed

There is an increase in the global energy demand by 2.1 % as well as the rise of emission of energy related carbon dioxide reported in 2017 [1] with fossil fuels including oil, natural gas and coal which account for the 81 % of the energy supply. These energy sources are non-renewable and pose long term damaging effects to the environment such as contributing to global warming, pollution and land degradation induced by extraction and mining of fossil fuels [2]. The demand in energy sources has also caused the increase in energy price hence there is more of a need for cheaper and sustainable energy solutions such as solar energy.

Photovoltaics is a technology that converts sunlight to electricity directly using semiconducting materials such as methylammonium lead iodide. The first photovoltaic cell was built by scientists at Bell laboratories where they discovered the exposure of silicon material to sunlight triggered the generation of an electric charge [3]. Subsequently, silicon - based solar cell production dominates the photovoltaic industry due to its high efficiency. The second generation of photovoltaic cells adopted the effectiveness of silicon as they are made of thin films of amorphous silicon and non-silicon materials such as cadmium telluride [4]. The third generation solar cells are made from new materials besides silicon. One of the main focuses of this thesis is to analyse the development of innovative solar cells based on metal halide perovskites materials which has become a major area in the functional materials research field over the past decades.

The benefits behind the ever-increasing interest are:

- Products of various compositions can be synthesised using cheap, and readily available starting materials at a low temperature.
- They can be employed as an excellent light absorber in highly efficient photovoltaic devices. They have now been reported to have reached unprecedented power conversion efficiency exceeding 23 % using a newly fabricated device with multi-layered absorbers each consisting of different bandgaps [5].

The general chemical formula for the metal halide perovskite compounds is ABX_3 (A can be organic or inorganic components such as $CH_3NH_3^+$ or Cs^+; B= Pb^{2+} and its fellow d-block elements and with X is anions from the halogen group i.e. Cl^-, Br^- and I^- [6]. The most studied of the hybrid perovskite is the three dimensional structure methylammonium lead iodide (MAPbI$_3$, $CH_3NH_3PbI_3$). It belongs to the I4/m space group and has a tetragonal structure with lattice parameters a, b = 8.795(1) Å and c= 12.610(3) Å and is illustrated in Figure 1.1 [7].
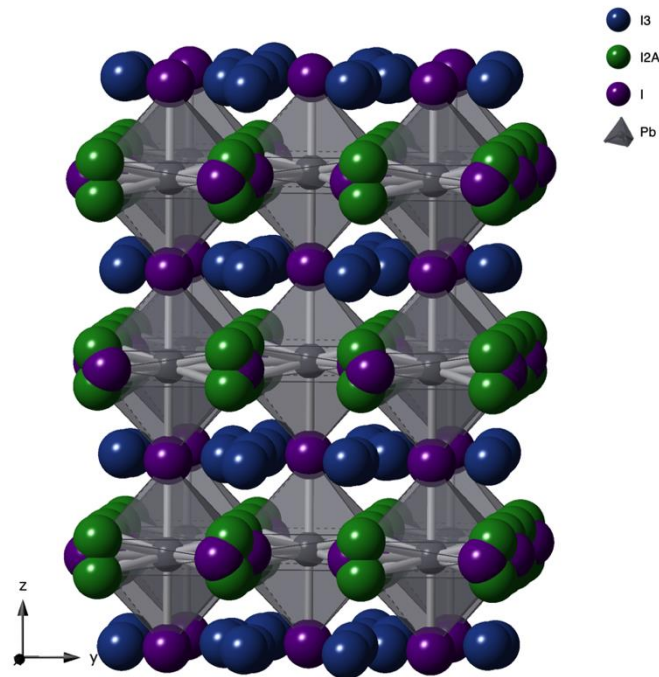
Figure 1.1 A published crystal structure of MAPbI$_3$ with *I4/m* space group [7].

1.1.2 Potential risks and development prospects of perovskite materials

Despite having a power conversion efficiency exceeding 20 %, the underlying principles of the optoelectronic characteristics that facilitate such an excellent photo harvesting property is yet to be fully understood. In addition, maintaining the long-term operational stability of the devices remains a barrier for commercialisation. The other apparent disadvantage of this material is the presence of lead which is toxic, although it can be replaced with less toxic counterparts such as tin or bismuth metals, but their photovoltaic performance is yet to be optimised [8]. Environmental factors such as the level of humidity, oxygen concentration and UV radiation can contribute to the degradation of the MAPbI$_3$ that releases the toxic lead and iodide components. Improvement in fabrication of stable, non–toxic device is crucial before commercialisation.

1.1.3 The device architecture of existing perovskite solar cells

A typical perovskite solar cell device has a thin perovskite layer being employed between a hole selective contact (HSC) and an electron selective contact (ESC) layers, making it a heterojunction cell with each layer having a different band gap energy. There are two types of common device architectures of perovskite solar cells and a simple schematic diagram is shown in Figure 1.2 [9]. A sensitized cell with a charge conducting mesoporous scaffold, which can either be a conducting material like TiO$_2$ or an insulator like Al$_2$O$_3$ layer coated with a layer of active perovskite materials. 2. Planar perovskite solar cells which can be sub-divided into two categories: dual interface architecture with a perovskite layers sandwiched between the HSC and ESC layer, or a single interface architecture composed of the active perovskite material and either of the HSC or ESC layer [10,11].

Electrode		Electrode
HSC		HSC
Perovskite layer		**Perovskite layer**
TiO₂ layer		
ESC		ESC
FTO or ITO		FTO or ITO

a) Mesoporous structure   b) Planar structure
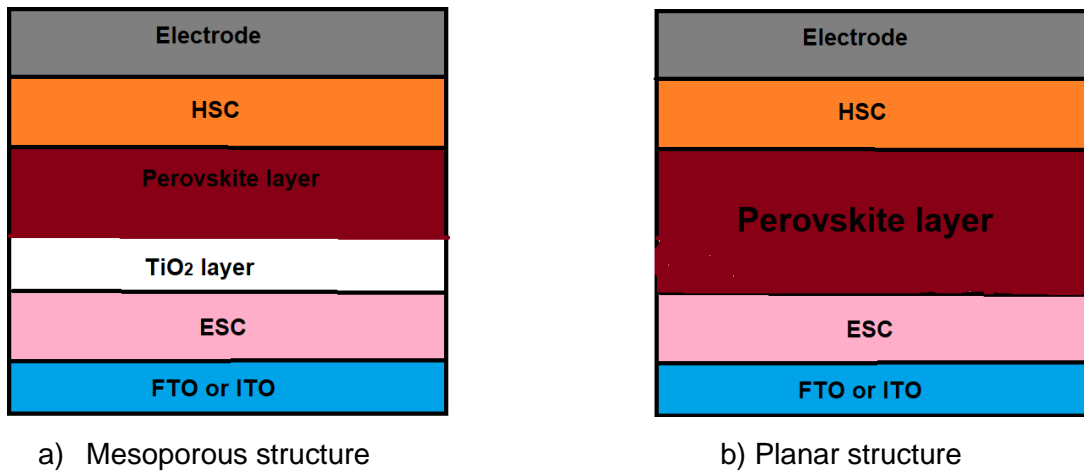
Figure 2.2 A simple schematic diagram showing the difference between a) mesoporous scaffold perovskite solar cell and b) planer structure perovskite solar cell.

1.1.4 The band-gap theory and how it relates to the working mechanism of perovskite solar cells

The basic working mechanism of a photovoltaic solar cell can be described as follows. The power conversion efficiency of a typical perovskite solar cell can be explained by the band-gap theory [12]. This theory states that electronic energies are separated into discrete energy bands, and the size of the gap between the conduction band and the valence band determines the amount of energy that is needed for electron promotion. The valence band is in the highest occupied molecular orbital also known as the outermost electron orbital of an atom that can promote an electron into the conduction band if enough thermal energy is applied. The mechanism of this electron promotion can be summarised by the electron-hole pair process which is essential in understanding the working principle of solar cells, since the movement of an electron from the valence band will leave a vacancy or a hole behind in the valence band. Therefore, the valence band is classified as the positive charge carrier whereas the conduction band is where negative charge carriers are found.

The schematic diagram in Figure 1.3 (a) shows the band gap of an insulator, a semi-conductor and a conductor, and the importance of the Fermi level (the highest occupied energy level at absolute zero temperature), and the difference in energy level in designing perovskite solar cells. In an insulator, the band gap is large which hinders the free movement of electrons between two energy bands. Whereas in a semi-conductor, the band gap is lower and little thermal or electromagnetic energy can promote an electron. Conductivity is achievable in a conductor since there is no barrier between the two energy bands. Therefore, this overlap of the conduction band and valence band allows electrons to move freely between them. In designing the solar cell, the Fermi level [13], is crucial as it sets out the limit in which only the electrons closest to it can participate in the electron-hole pair, also known as an exciton [14] (the production of the combination of an excited electron and a positive hole in the valence band held by electrostatic Coulomb force) generation at absolute zero. In the conventional silicon solar cells, this Fermi level can be tailored by doping silicon with trivalent elements like group 3 elements, making the valence band electron - deficient and hence holes are formed. (P-type semi-conductor) [15]. On the other hand, an n – type [16] semi-conductor can be made by doping the silicon with pentavalent atoms in the group 5 elements, this makes the electron pairs in the conduction band more favourable, and this semi-conductor is more conductive than pure silicon conductors [17].

A perovskite solar cell works in an analogous way to the conventional solar cells, when a photon of light is absorbed into the light absorber, an exciton is created in the active perovskite layer. This exciton can be made uncharged by the dissociation from the electronic attraction from electrons in the electron transport layer and the pulling force from the holes in the hole transport layer. The dissociated charges will be collected by both the cathode and anode, resembling an electrical circuit and hence generates electricity which is illustrated in Figure 1.3 (b) [18].
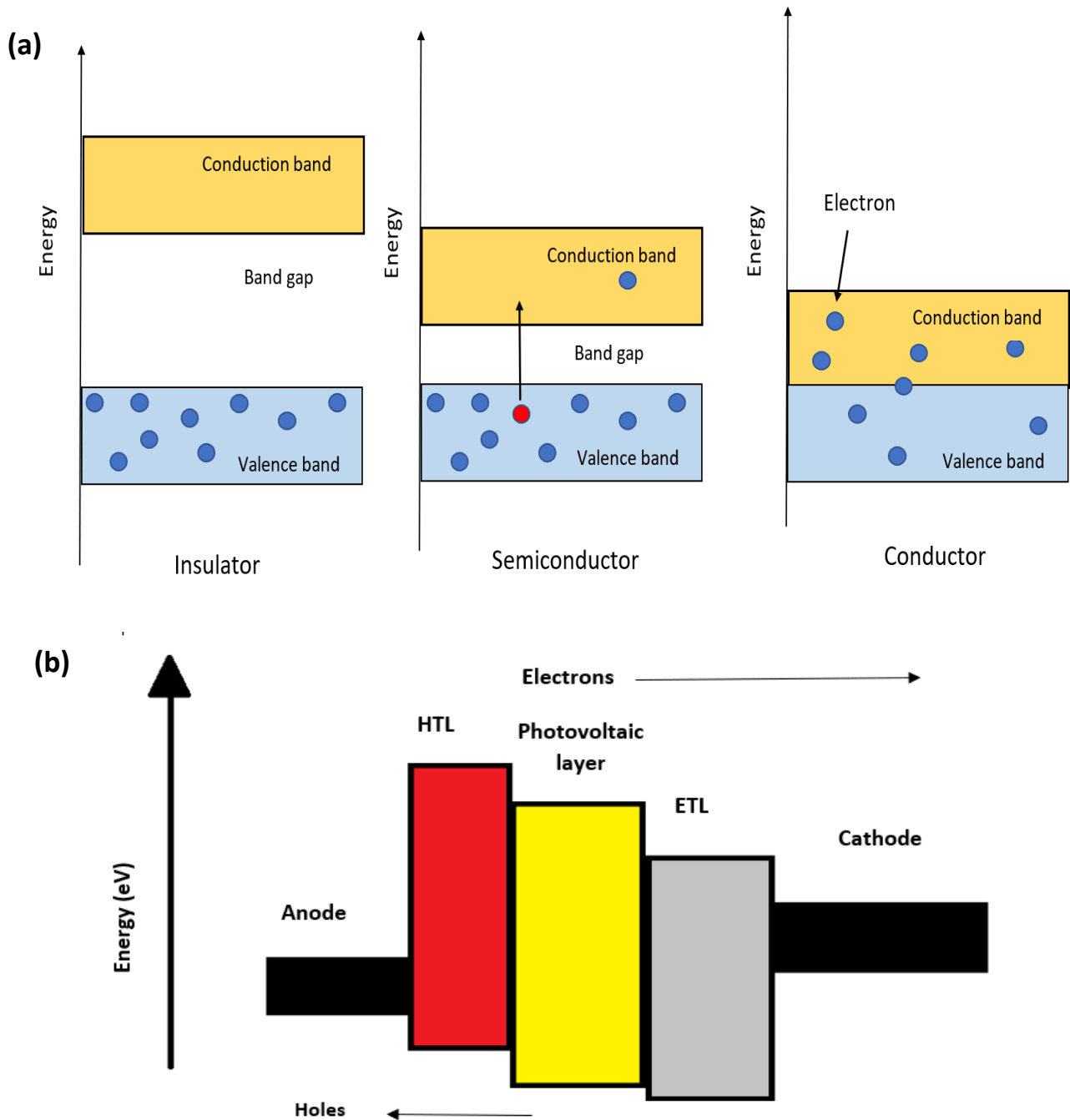
Figure 1.3 (a) A schematic diagram showing the difference in the band gap energy in an insulator, a semiconductor and a conductor. (b) A schematic diagram showing the electron and hole movement in between an anode and cathode.

1.1.5 Types of charge carrier separation in relation to the operation of a solar cell

There are two types of charge carrier separation that facilitates the operation of a solar cell. The Fick's law of diffusion states that the rate of diffusion of particles is proportional to the concentration gradient. Therefore, electrons will tend to diffuse from the conductor which is electron-rich to the conductor which is electron-deficient. The other mechanism is drifting of the charge carriers. The distribution of electrons to holes which builds up charges that drift to the corresponding electrodes, this will generate an electric field leading to a flow of electric current between the two electrodes [19].

1.1.6 Factors that lower the power conversion efficiency - The induction of charge trapping with interstitial iodine migration

Several studies have provided evidence for ion mobility in $MAPbI_3$. Any ions present in the perovskite may be subject to migration, and their mobility is characterised by the activation energy (E_A) and the migration rate (r_m) which can be expressed with the formula:

$$r_m \propto \exp\left(\frac{E_A}{k_{BT}}\right)$$

K_B being the Boltzmann constant and T being temperature. Factors such as crystal structure, ionic radius and charge of ions will affect how fast the ions migrate. Iodide ions are most likely to migrate due to the short interstitial distance between neighbouring iodine in the corner sharing PbI_6^{4-} octahedra which is about 4.46 Å rather than MA^+ and Pb^{2+} ions which is about 6.28 Å. A computational model simulated by Azpiroz [20] showed that the activation energy is 0.08, 0.80 and 0.46 eV for I^-, Pb^{2+} and MA^+ ions respectively for interstitial defect migration. The migration speed for iodide ions is measured to be within 1 µs, which is not sufficient to explain low power conversion efficiency.

A further insight into the structure of $MAPbI_3$ is crucial before we can explain the migration of iodide/iodine counterparts in the framework. A new structure of $MAPbI_3$ with *I4/m* space group and lattice parameters of *a* and *b* = 8.8756(1) Å; *c* = 12.6517(3) Å was found. This structure is different to $MAPbI_3$ with a *Pm$\bar{3}$m* space group that is commonly found in the cubic perovskite structure at high temperature. This study showed that three different iodine positions (identified as I1, I2(A) and I3 in Figure 1.4) are observed using a combination of powder neutron diffraction and single crystal X-ray diffraction [21]. The point defect formation in $MAPbI_3$ perovskites is intrinsic [22] as it occurs naturally due to the thermally driven interstitial iodine migration. The changes in the composition of in the I1 and I2 positions are when the temperature is raised to about 335 K and cooled to 320 K. This change is also analogous to the phase transition from tetragonal to cubic. When the temperature is raised to above 289 K, the iodide ions will migrate interstitially from I2 to I2A and the I3 positions which is represented by the drop in composition in I2 position and an increased occupancy in both the I2A and I3 sites. The above observation proves that interstitial iodine migration is temperature - dependent. Iodide ions can also adopt different I-I bond lengths and intermolecular I_2 distances in terms of the bonding and charges on the iodine [23]. As quoted from literature: '*Structure of solid I_2 is an orthorhombic zig-zag structure with intramolecular I – I bond lengths of 2.68 Å, and intermolecular I2 distances of 3.56 Å.*' [24].The experimental results showed that the bond lengths in two different position of I3 to I2A in the *I4/m* $MAPbI_3$ are 2.7(1) Å and 2.6(1) Å respectively. The similarity observed in bond lengths found in the I3 to I2A found in $MAPbI_3$ compares to the bond length of Iodide ions in solid I_2 provides evidence for the formation of covalent bonding of I_2 and hence the production of neutral diatomic I_2 molecule in the perovskite framework and is shown in Figure 1.5 [25]. This is a redox reaction between iodide ion (I-) and iodine atom being triggered, resembling an

electron – hole pair system that is fundamental in perovskite solar cells [26]. The interstitial iodide migration from I1 to I2 towards I3 is suggested to be achieved via a gate opening mechanism (reorientation of methylammonium ions that alters the perovskite structure to allow interstitial ion movements) within the MAPbI$_3$ perovskite framework. It was proven that there are two orientations for the methylamine (CH$_3$NH$_3$) molecules in the (220) and (2$\bar{2}$0) planes respectively. However, these orientations and the centre of mass of these two molecules are pointing at the same iodide positions, I2, in the z = 0.25 plane [21]. As stated in literature [27], methylammonium ions can undergo several reorientation within a PbI$_3$ cage in cubic MAPbI$_3$. They are summarised as the following: (i) Free orientation of methylammonium ions in the inorganic framework and with the methylammonium ions pointing at non-specific positions. (ii) '*π-flips*' – rotation of the methylammonium ion from one end to an opposite end. (iii) '*Corner-to-corner hops*', where the methylammonium ion reorientates from one diagonal to an adjacent diagonal. (iv) '*Edge-to-edge hops*' where the methylammonium ion reorientates from one edge to point at a different edge. (v) '*Face-to-face hops*', in which the methylammonium ions reorientates from one face to an adjacent face. In conclusion, it was suggested that when the methylammoniums are orientated in perpendicular to the PbI$_6$ octahedra, it would be facilitating the migration of iodides ions from I1, I2 to I3 position.

The stable structural formula of perovskite MAPbI$_3$ is (CH$_3$NH$_3$) PbI$_{3-2x}$(I$_2$)$_x$ with x ~ 0.007 [25]. In addition, this iodine migration leaves a vacancy in the original interstitial position. This vacant space, along with the grain boundaries formed during crystallisation both serve as charge trapping reservoirs. Charges will be trapped in these vacant spaces and leads to the current voltage hysteresis [20]. These effects combined will lead to a lower power conversion efficiency.
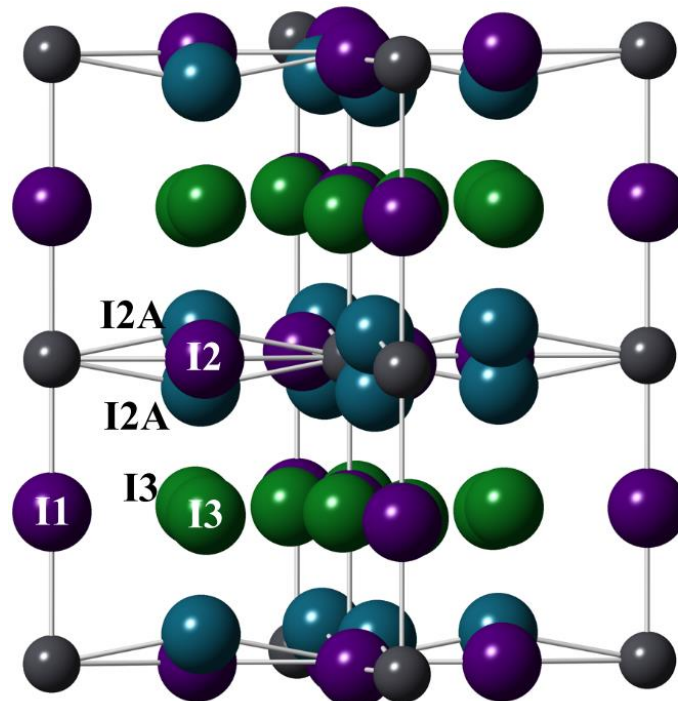
Figure 1.4 A structure of MAPbI$_3$ at room temperature with *I4/m* space group, showing different iodide positions (I1 and I2 (purple), I2A (blue sphere) and I3 (grey sphere)) [25].
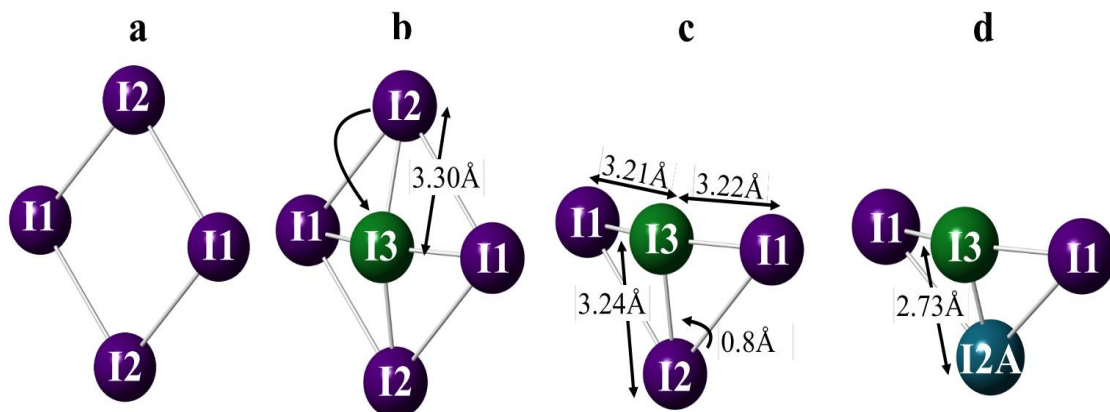
Figure 1.5 a. schematic diagram showing the formation of neutral charge I2 atom in MAPbI$_3$ quoted from literature. a. two different iodide positions (I1 and I2) in the perovskite framework. b. the iodide migration from I2 to interstitial I3 position leaving a vacant space in I2. c. I3 surrounded by three roughly equidistant iodine ions from I1 and I2 position. d. bond formation to produce I2 molecules [25].

1.2.1 Structural and phase transitions of MAPbI$_3$ at different temperatures

With increasing temperature from 100 to 352 K on heating, positional disorder occurs in both the organic and inorganic components within the MAPbI$_3$ perovskite framework. It was shown to undergo a transformation of three different structural phases on heating. As stated in literature, at temperature above 330 K, the MAPbI$_3$ exhibits a cubic $Pm\bar{3}m$ phase, and a tetragonal $I4/m$ structure from 160 to 330 K, and an orthorhombic $Pnma$ phase below 160 K [28]. In the MAPbI$_3$ framework, the methylammonium (MA) cation is surrounded by PbI$_6$ octahedra, the iodine ions are not fixed and can undergo interstitial migration with a very low activation and this action is vacancy assisted, the MA cations are oriented towards the dimensions of the cage formed by the linked PbI$_6$ octahedra. At low temperature such as in the orthorhombic phase, the orientation of the MA cation is fully ordered and shows hydrogen bonding between the NH$_3$ groups and the iodine atoms in the octahedra. Increasing the temperature weakens the bonding between the NH$_3$ groups and iodine atoms interaction, which will then lead to a partial distortion of MA cations in the tetragonal phase at 160 to 330 K, and eventually a full distortion of MA cations in the cubic phase when temperature exceeded 330 K on heating [29]. The volatility of phase transitions and the complex dynamics of the ionic migration make the structural studies of this material complicated. Therefore, the effect of temperature annealing was prioritised in this study, promising results were obtained and will be discussed in the results section.

1.2.2 The effects of different thermal annealing treatment on the structural changes of MAPbI$_3$.

Thermal annealing
In a previous thermal annealing study by Lung-Chien Chen [30] in which thermal annealing were performed from 80 to 140 °C for 5 minutes, the structure of MAPbI$_3$ decomposes upon heating to around 120 °C, and the CH$_3$NH$_3$I component deteriorates and breaks from the perovskite film to form PbI$_2$ on decomposition. This can be proved by the X–ray diffraction where the existence of an extra peak at 12.7 ° 2θ (Figure 1.6) [30]. In general, the strongest diffraction peak at around 14 ° 2θ is characteristic of MAPbI$_3$ samples regardless of different annealing condition and indexed on the (110) reflection.

The exciton lifetime is an indication to the degree of recombination in the $CH_3NH_3PbI_3$ and it is proportional to the appearance of PbI_2. The exciton lifetime of the $MAPbI_3$ annealed at 140 °C appeared to be lower than the ones annealed at a lower temperature (80, 100 and 120 °C) [30]. Despite the lowering of exciton lifetime at elevated temperature when heating, the growth of $MAPbI_3$ crystal grain size is positively correlated with temperature, and this may lead to the increase of carrier mobility due to larger grain size within the perovskite films and reduces the recombination from PbI_2 to perovskite by the associated intercalation of CH_3NH_3I. Having larger crystals enhances photovoltaic efficiency as it can increase the photon absorbance of $MAPbI_3$. Therefore, more sunlight can be absorbed and is able to generate more photocurrent in device performance. Another similar study conducted [31] using $MAPbI_3$ and $(FAPbI_3)_{0.85}(MAPbBr_3)_{0.15}$ annealed at higher temperatures (160, 180, 200, 220 and 240 °C respectively) but a shorter heating time (15 seconds) also supported the fact that crystallisation of $MAPbI_3$ is greater at higher temperature annealing. Other advantages include an enhancement in grain orientation of the perovskite film and the collection of charge carriers becomes more efficient, narrower grain boundaries and greater intrinsic stability of the film structure [30].
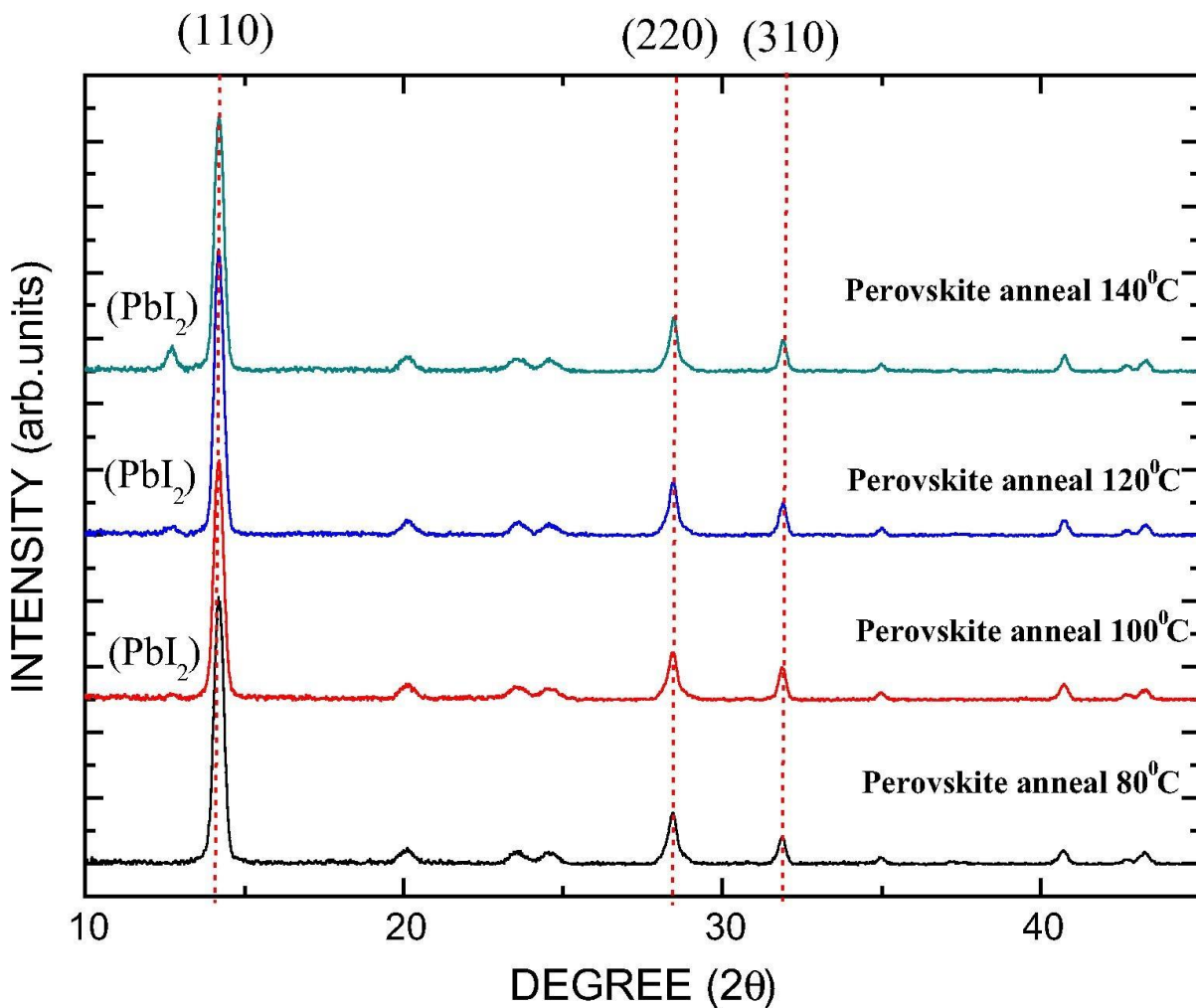
Figure 1.6 The presence of PbI_2 from decomposition of $MAPbI_3$ is showed in 12.7 ° at (110) reflection in the 2θ degree at different temperature annealing quoted from literature [30].

1.2.3 The effect of Caesium doping on the power conversion efficiency of perovskite solar cells

Apart from thermal annealing, the power conversion efficiency of the perovskites can be improved through doping with the other materials. The efficiency of a solar cell is determined as the fraction of the input power, which is converted to electricity, and is defined as [32]:

$$\eta = \frac{V_{OC} \, I_{SC} \, FF}{p_{in}}$$

V_{OC}: the open-circuit voltage;
I_{SC}: the short-circuit current;
FF is the fill factor and
η is the efficiency.

MAPbI$_3$ has a well – established light absorber properties with a low energy band gap of 1.5 eV and high extinction coefficient. The crystal framework of the perovskites is influenced by the A site cation, and its properties contribute to the size of the band gap and electronic characteristics. The band gap of MAPbI$_3$ is easily tuneable with materials of similar size to the methylamine cation, i.e. caesium in this case.
Experiment of different ratio of caesium doped MAPbI$_3$ were performed in a previous study [33]. This study found out the ideal ratio of caesium for doping is at 10 %, Cs$_{0.10}$MA$_{0.90}$PbI$_3$ itself has the optimal power conversion efficiency of 7.68 % compared to the poor performance of pure MAPbI$_3$ (5.51 %) and CsPbI$_3$ (0.09 %). This is due to a 18 % increase in the band gap or also known as the open-circuit energy (Voc) from 0.89 to 1.05 V. Furthermore, a 14 % increase in the short-circuit current density (Jsc) from 8.89 to 10.10 mA cm^{-2}. These features will also enable a better light absorption in the UV and visible wavelength regions and hence greater photovoltaic performance [34, 35].

1.2.4 The effect of zinc metal annealing on the stability of perovskite solar cells

Apart from changing the composition of the A-site cations. Similarly, it has been reported that partially replacing the composition of the B-site cations (Pb^{2+}) with divalent metal species such as zinc improves photovoltaic performance and optical properties of MAPbI$_3$ perovskite [36]. Zn^{2+} ions are smaller in atomic radius compared to Pb^{2+} ions and doping of zinc metals '*causes a unit cell contraction of the (hh0) plane and this results in enhanced nucleation and crystallization during fabrication, resulting in bigger grains and fewer pinholes.*' as reported in literature [37]. The fewer number of grain boundaries presented in crystallisation means it there will be less non-radiative losses (an unwanted process that involves the transformation of electronic excitation energy into heat other than light, creates lattice defects and photochemical changes of the electronically excited materials) [38], hence increases stabilisation of the resulting film as most degradation starts at grain boundaries and at pinholes. Furthermore, zinc metal is a better option compared to lead as it is non-toxic, its intact nature means that it is not likely to be oxidised or reduced and its abundance on Earth.

1.3.0 Magnetism

1.3.1 Brief introduction of magnetisation

Some forces can affect an object from a distance, such as magnets can attract objects made of iron and some other metals (nickel and cobalt), but magnets can also repel other magnetic materials. This non-contact force is an invisible area of magnetism created by a magnetic material and it is called magnetic field.

Magnetisation [39] is a spontaneous phenomenon that happens in a magnetic material such as a bar of iron or magnet. It is a form of combined electromagnetic force (a magnetic dipole moment) caused by the motion of electrons that is exerted by a magnetic field to attract or repel an object. When working at an atomic level, the correlation between magnetic dipole moment with an input of electric current from an electron I over an area A, is μ = IA, which can be further quantised to Bohr magneton [40] which is the basic unit of dipole moment, where e is the charge, ℏ is the Planck's constant and m is the mass of an electron.

$$\mu B = \frac{e\hbar}{2m_e}$$

Furthermore, the macro concept of magnetism is composed of two angular momentums of electrons. In terms of describing a single ion moment, orbital angular momentum [40] is the circulation of the electrons around the nucleus under the influence of the coulomb potential, these electrons have an intrinsic angular momentum which is quantised with quantum number of $m_s = 1/2$ or $-1/2$. When these two momentums combine, a total angular momentum, J, that accounts for an individual magnetic moment can be used to calculate magnetisation per unit mass or volume [41].

1.3.2 Curie-Weiss law and magnetic susceptibility

People used to think that all materials are either magnetic or non-magnetic. However, even materials that we considered to be non-magnetic can also be affected by magnetism to some extent. The extent to which a material can be magnetized is called magnetic susceptibility. When a magnetic field is being introduced to a system, its response can be a negative (paramagnetic) or positive (diamagnetic) alignment corresponding to the applied magnetic field. Lenz's law [42] states that when a magnet is bought near a conductor, the induced current will produce a magnetic field opposing the direction of applied magnetic field. On the other hand, the non-interacting unpaired electrons will induce Curie – law paramagnetism and the internal magnetic field will go along the direction of the applied magnetic field [39].

This spontaneous magnetisation is temperature dependent and magnetisation is reversible below the Curie temperature, with materials losing their magnetisation above the Curie temperature T_c and leads to paramagnetisation. The magnetic susceptibility χ is defined as $\chi = M/H$ but can be expressed as the Curie's law:

$$\chi = C/T$$

χ = magnetic susceptibility

C = Curie constant, related to the material's effective magnetic moment

T = temperature

The Weiss constant θ (which is an adjustable constant) is later introduced to modify the Curie law to express the interaction between magnetic moments, and therefore the Curie – Weiss law [41].

$$\chi = \frac{C}{T - \theta}$$

1.3.3 Difference between paramagnetisation and ferromagnetisation in remanence

All materials exhibit magnetic interactions to some extent. The partially filled d or f shells of transition metals of the pyrochlore material generate magnetic ordering such as paramagnetism, ferromagnetism, anti-ferromagnetism, and ferrimagnetism [43].

As illustrated in Figure 1.7, paramagnetisation occurs when the spins (unpaired electrons) are aligned in a random order that align in the direction of an applied magnetic field. Ferromagnetisation arises when the Weiss constant is positive, and all the spins will order in a parallel fashion below the Curie temperature. The susceptibility increases as the spin alignment give rises to effective dipole moments. On the other hand, in antiferromagnets the Weiss constant is negative, and ordering occurs below the critical temperature, Néel temperature T_N. The spins will arrange in an anti-parallel direction and the susceptibility decreases as the spins cancel each other out [44].

Furthermore, there is a mixture of anti-ferromagnetism and ferromagnetism called ferri-magnetisation where the dipole moments will align in an anti-parallel direction of the applied field, but the moments are different and do not completely cancel, leaving an effective moment in one direction [45].

Paramagnetism   **Ferromagnetism**   **Anti - ferromagnetism**   **Ferrimagnetism**
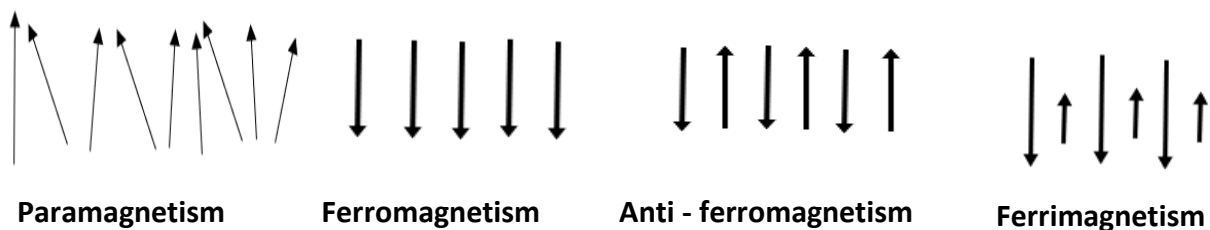
Figure 1.7 Types of magnetic behaviour with the direction of spins: Paramagnetism, ferromagnetism, anti-ferromagnetism and ferrimagnetism.

1.3.4 Methods of measuring magnetism under field-cooled and zero-field cooled condition

Magnetic susceptibility can be measured with SQUID magnetometer as this equipment is able to detect very small magnetic fields as the tunnelling process between superconducting materials separated by a thin insulating barrier (across the Josephson junction) [46].

The magnetisation of a material is different depending on whether it has been in the process of zero-field cooling or field cooling since the magnetic anisotropy allows spins to align in their preferred orientation. In the process of zero-field cooling, the sample is cooled in zero applied magnetic field, all the spins are randomly ordered with respect to each other, when a field is applied, the magnetic susceptibly is measure on heating from below the Curie

temperature, and the resultant magnetisation is dependent on the magnetic anisotropy of the material. On the other hand, a field cooling measurement is taken when a field is applied at high temperature, then the sample is cooled, and the magnetic susceptibility is measured on heating. Therefore, the spin moments (magnetisation) are orientated in a particular direction of the applied magnetic field [47].

1.3.5 Magnetic frustration and Spin-glass system

Magnetic frustration occurs naturally in crystal lattices such as in the Kagome and the pyrochlores. It occurs in triangular and tetrahedral lattices where there is a competing interaction between different magnetic spins, results in the dissatisfaction in one or several competing manners within the lattice. Magnetic frustration is a common phenomenon when all the atoms within the lattice framework tend to arrange in a non-trivial position [48].

The difference between a conventional and a frustrated system is in the conventional system, the magnetic moments within the system are created by the unpaired electrons on the outer shells of transition metal cations of the compound. Exchange interaction between these magnetic moments tend to arrange in an anti-ferromagnetic ordering. However, in a frustrated system, these magnetic moments are in a competition to become an ordered system, but the nearest-neighbour interactions cannot be satisfied by any exchange interaction of the magnetic moments (a comparison of a unfrustrated and frustrated lattice is showed in Figure 1.8). Furthermore, this geometrical frustration can lead to short ranged ordering at a low temperature and the formation of spin liquid, spin glass or spin ice system [49]. In addition, the hallmark of frustration is the increase in the degeneracy of the ground states. This magnetic frustration can be illustrated by two mathematical models: the Ising model and the Heisenberg model [50].

Figure 1.8 A comparison of a square lattice showing anti-ferromagnetic arrangement in a lattice (Left, not frustrated). A triangular lattice showing the magnetic spins are unable to form anti-ferromagnetic arrangement due to unsatisfied interaction between the nearest neighbours. (right, frustrated)

A spin glass state as shown in Figure 1.9 is the freezing of spins in random direction below a characteristic temperature showing short ranged order as opposed to a long-ranged ordered system at low temperature, and magnetic frustration is present in the spin glass system [51]. The spin liquid has the similar property as the spin glass system, it is in a disordered state in comparison to long-ranged order (ferromagnetic) state and will not order even at low temperature. Furthermore, the quantum fluctuations and geometrical frustration combined to prevent the spins from freezing [52, 53].
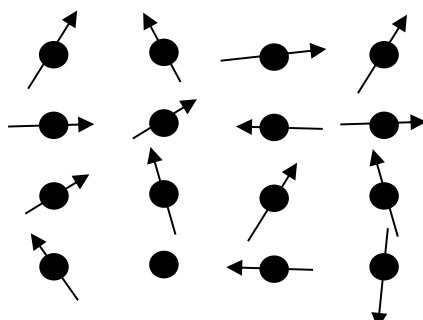
Figure 1.9 A spin glass state showing the randomness of spins in a system

1.3.6 A new-charge-ordered magnetically frustrated pyrochlore-related mixed metal fluoride

Pyrochlores are a group of potential multifunctional materials that has caught our attention due to their explicit properties in the development of the next generation technologies. These mixed-metal fluorides with a pyrochlore-related structure can be synthesised with different metals which fulfils a range of functional properties. These include multiferroic behaviour, magnetic frustration, ferroelectricity and non-linear optical behaviour [54]. Pyrochlores belong to the $Fd\bar{3}m$ space group with four molecules per unit cell [55] (z = 4, a face centred unit cell with eight atoms on each of the corners that contributes to 1/8 of the unit cell and six atoms that sit on each of the faces each contributing 1/2, and hence gives a total number of (8 x 1/8) + (6 x 1/2) = 4; four atoms per unit cell) regardless of them being in the normal (ordered) or defect arrangement. The normal pyrochlore structure is a three-dimensional framework consisting of corner–sharing metal tetrahedra (a visual diagram of a normal pyrochlore lattice quoted from literature is showed in Figure 1.10) [56] with a general formula of $A_2B_2O_7$ where A is a trivalent rare earth ion like Gadolinium, Gd^{3+} and monovalent or divalent elements like the group 1 and 2 elements, B is usually the d-block transition metals but with an appropriate oxidation state to fulfil the $A_2B_2O_7$ structure [57].

The flexibility in the stoichiometry of the cation and anion lattice of pyrochlores $A_2B_2O_7$ makes disorder in the system a common phenomenon. This mean that they will undergo an order-disorder transition from an ordered pyrochlore to a long-range, disordered defect-fluorite structure as a function of composition; which is related to the ratio of the ionic radii of cations in the A-site and B-site [58], temperature, pressure and radiation damage. [59] The other type relates to the short–range ordering with a degenerate configuration being observed in the $Y_2Mo_2O_7$ pyrochlores [60] which will lead to a non-trivial magnetic state which is known as geometrical frustration.

This project focused on the synthesis and characterisation of a series of mixed metal fluorides to investigate the frustrated magnetisation of this defect pyrochlore-related structure [61]. The defect pyrochlores have a slightly different structure to the normal pyrochlores, these compounds have a general formula of AM_2F_6 with A being the alkali metals and this project focuses mainly on the synthesis and characterisation of Rb and Cs derivates. M is usually the transition metal with M^{2+} and M^{3+} charges. In addition to the difference in structural composition, the magnetisation is observed along the A site ions [62] on normal pyrochlores whereas it is observed along the M site cations along the [111] Kagome lattice [63] in defect pyrochlores. Charge ordering [63] is also found predominantly in the M site cations in the defect pyrochlores due to the disproportionation resulting from the charges present on the two transition metal ions [64].This unique defected structure leads to

spin-glass behaviour [65] being observed in $CsMnFeF_6$ [65] resulting from the frustrated magnetisation where the magnetic ions have the tendency to stick to a positional disorder arrangement. Apart from the occurrence of magnetic frustration, other functional properties such as multiferroic behaviour, ferroelectricity also have great contribution towards the development of modern technology [66].
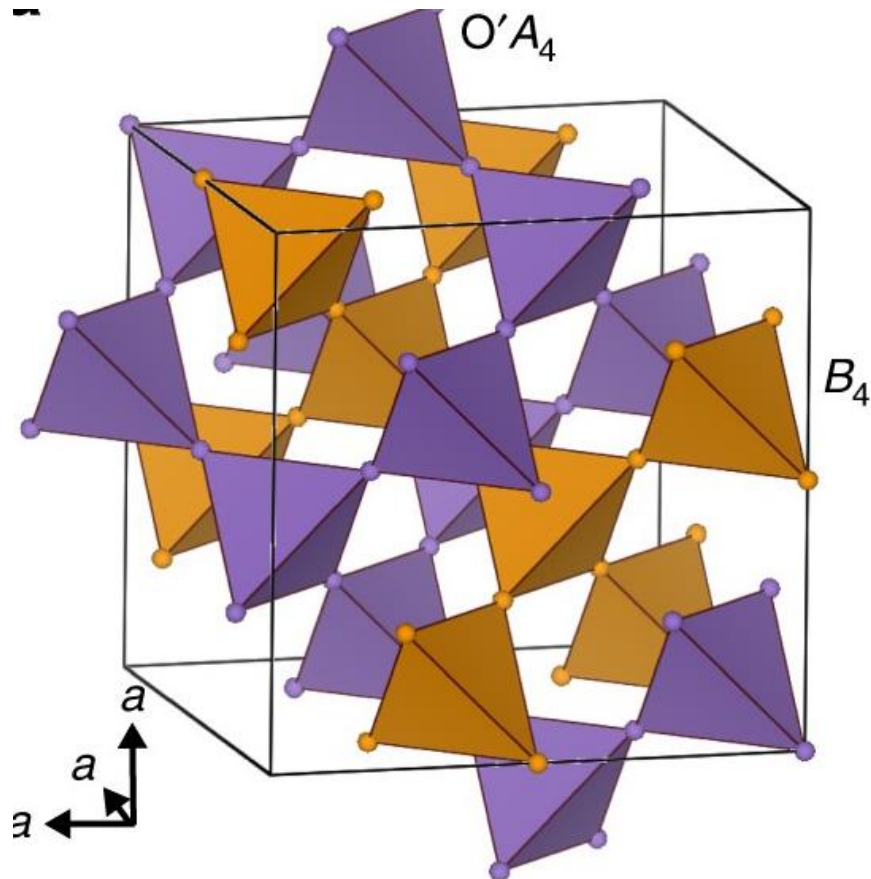
Figure 1.10 A normal $A_2B_2O_7$ pyrochlore lattice showing the connection of corner – sharing oxide-A site and B4 site tetrahedra quoted from literature [56].

1.3.7 Kagome lattice vs defect pyrochlore lattice

$RbFe_2F_6$ is a very good example to explain the correlation between the defect pyrochlore lattice to a Kagome lattice. It has a *Pnma* (orthorhombic) space group with lattice parameters of $a = 7.02134(7)$ Å, $b = 7.45093(7)$ Å and $c = 10.1795(1)$ Å which is distorted from the $Fd\bar{3}m$ symmetry that is presented in the normal pyrochlores. The structure of $RbFe_2F_6$ is a three dimensional lattice connected by corner – sharing FeF_6 octahedra that are separated by Rb^+ cations. The distorted arrangement of these octahedra is in analogue to the symmetry of Kagome lattice as a result of the geometrical frustration caused by the presence of transition metals. A comparison of a pyrochlore spin configuration on to a typical Kagome plane and a Kagome lattice observed in the $RbFe_2F_6$ pyrochlore lattice are showed in Figure 1.11 and Figure 1.12 both are quoted from literature [54].
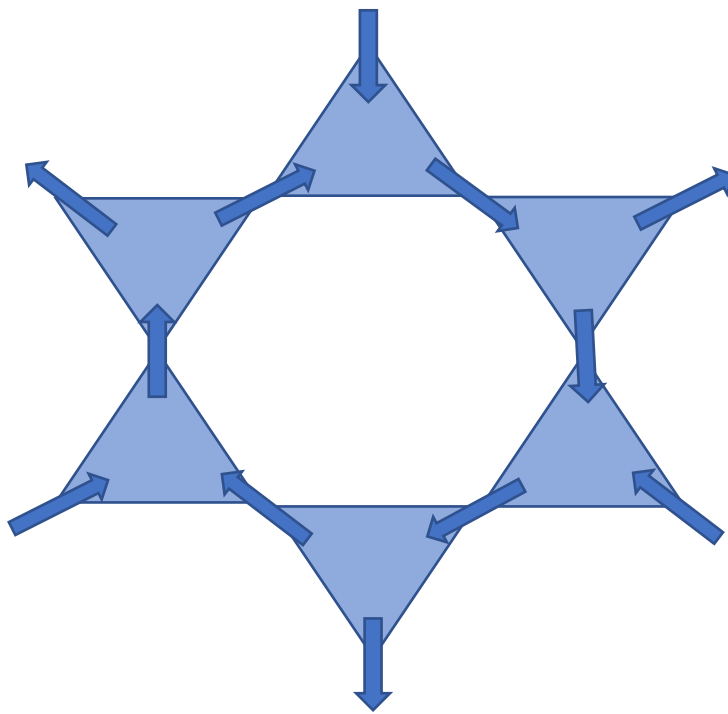
Figure 1.11 Two-dimensional projection of the pyrochlore spin configuration on to a Kagome plane.
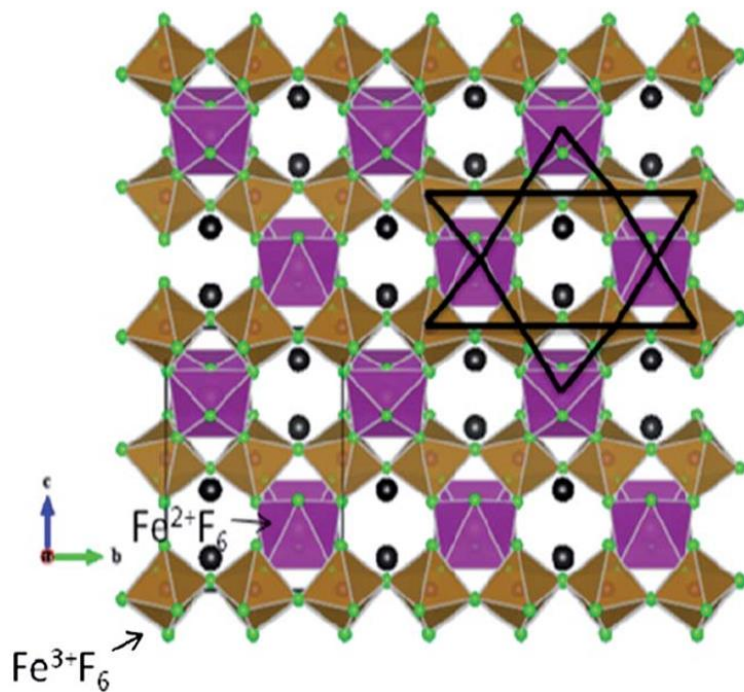
Figure 1.12 A Kagome lattice (black line) is observed in the RbFe$_2$F$_6$ pyrochlore lattice [54].

Chapter 2. Experimental section

2.1.1 X–ray crystallography (powder and single crystal X-ray diffraction)

$MAPbI_3$, the material that is being studied has a crystalline structure and each crystalline solid has its own 'fingerprint' which outlines its characteristic X-ray diffraction pattern. Therefore, powder X–ray diffraction technique was used throughout the project for identification and structural characterisation for all the samples synthesised.

2.1.2 X-ray generation

X–rays are electromagnetic radiation with a wavelength of about 1 Å (10^{-10} m) [67]. They are generated when a beam of high-energy charged particles (such as electrons), collide with a metal target; in this case Cu. During the collision, two types of X-rays are emitted in this process. One type of these X-rays is a continuous energy spectrum of electromagnetic radiation; the white radiation (braking radiation or Bremsstrahlung) that is produced by the deceleration of this beam of high-energy charged electrons after it was deflected by the Cu target inside the X-ray chamber. The other type of X-rays produced is the characteristic peaks in the emission spectrum which is used for structural determination. This radiation is made by the electronic transitions from the ionisation of electrons from atoms of the target material in particular from the K – shell orbital (with a principal quantum number n = 1). A strong radiation will be produced when an excited electron falls back from a higher level (the L - shell orbital with a principal quantum number n = 2) to a vacant space in the lower level which is the K - shell orbital. A x–ray photon with a distinctive wavelength is emitted [68], and this wavelength is equivalent to energy difference between the two shells, and the radiation produced is called Kα radiation (Figure 2.1) [64].
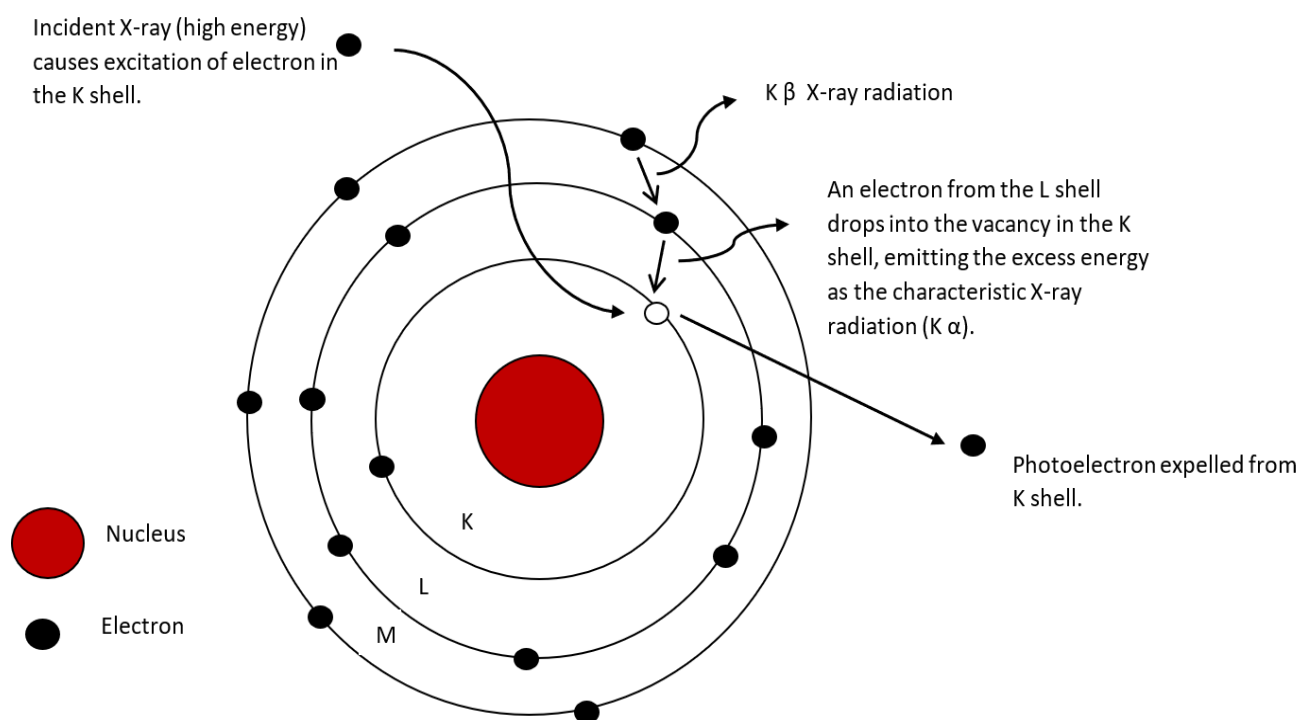
Figure 2.1 The production of characteristic X–ray radiation, showing the fall of electron from the L shell to K shell produces Kα X–ray radiation.

2.1.3 X-ray diffraction in relation to Bragg's law

As discussed previously in 2.1.2, X-rays are high energy electromagnetic radiation with a distinctive wavelength of about 1 Å, since the wavelength of the X-rays is similar to the spacing atoms in a crystal, an interference effect called 'diffraction' occurs when the X-rays interact with a crystal, in which it will be deflected, and the incident beam scatters into random directions. When the X-rays interact with each other in planes they will produce constructive interference which is an amplified signal in that direction. If the waves are out of planes, the signal is destroyed, and this is destructive interference.

To satisfy the Bragg's law (shown in Figure 2.2) [69], in a crystal, repeating arrangement of atoms form distinct lattice planes separated by a well-defined spacing (d). These layers of lattice planes each acting as a semi-transparent mirror, when they are exposed to the incident X-rays, the X-rays are scattered by the regularly spaced atoms. Some of the X-rays are reflected by a given plane at a very specific angle θ whilst the rest are transmitted to be reflected by a subsequent plane. The Bragg equation[69] produces the conclusion for the occurrence of an X-ray diffraction in a crystal, as it states that the θ angle can be calculated easily in terms of the difference in the path between an incident radiation after it hits and reflected by the next plane in the lattice [70].

Different crystal lattice plane (hkl) have their own set of characteristic d–spacing which indicates the distance between two neighbouring lattice planes. And the letter n being the order of diffraction, λ is the wavelength of the incident and reflected radiations.

$$2d\, Sin\theta = n\lambda$$

During a powder X-ray diffraction scanning, the different angles and intensities of these diffraction lines produced will be collected, and a three-dimensional image with the density of electrons within the examined crystal is visualised. This enables the identification of the positions and size of atoms, the length and types chemical bonds and distortions within the crystal [71][72].
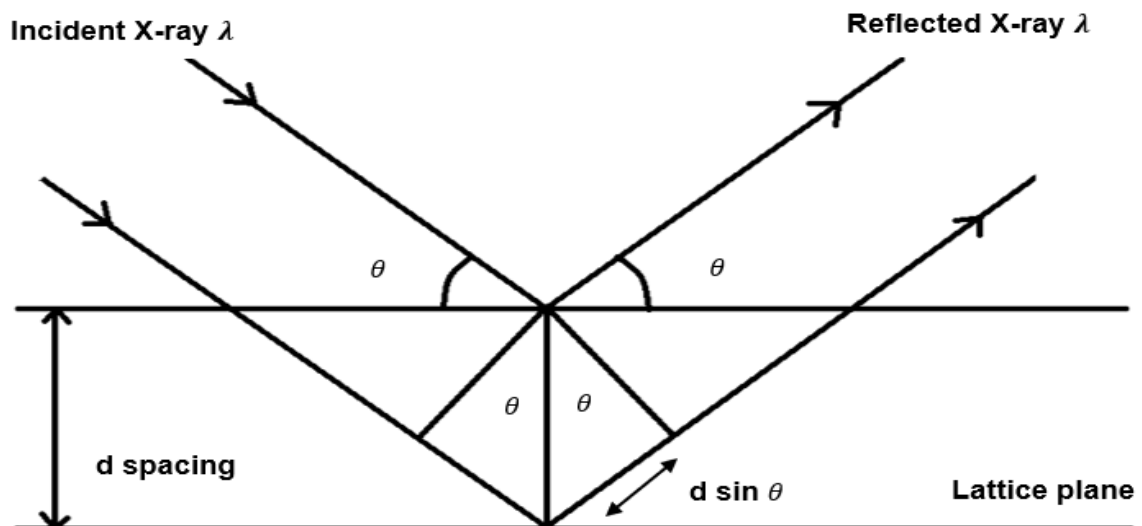
Figure 2.2 Bragg's law reflection with the directions of incident X-rays and diffracted X-rays [69].

2.1.4 Single crystal X-ray diffraction measurement

In a single-crystal X-ray diffraction measurement, a single crystal with dimensions less than 0.5mm such as the $MAPbI_3$ crystals is selected, and mounted on a goniometer, and molybdenum radiation was used throughout the project for $MAPbI_3$ and the mixed metal fluoride samples due to their heavier molecular mass. When a focused finely focused monochromatic beam of X-rays strikes through the single crystal, a diffraction diagram with regularly scattering spots is produced and the 2D images generated will be converted to a 3D model of the density of electrons within the crystal.

If the single crystal is being too small or impure, it will lead to poor resolution and unexpected results. And the other limitations of X-ray diffraction technique are; it is unable to distinguish the near isoelectronic atoms such as carbon and nitrogen. And the X-ray beams do not interact very well with light atoms such as hydrogen in the presence of the heavy atoms such as lead or iodine [41].

2.1.5 Neutron scattering

Neutron scattering technique is chosen for the investigation of the magnetic structures of mixed metal fluorides as its non-invasive which means it do not alter the properties of the investigated samples, and the diffracted intensity are affected by the isotopic mass of an atom rather than the actual atomic mass. The beneficial sides of this technique are the neutron wavelength spectrum is equivalent to their interatomic distances in a material, this high sensitivity in scattering lengths gives an advantage in application of isotopic labelling besides structural determination, and it means light atoms such as hydrogen can be investigated in the presence of heavy elements. It provides complementary information to X-ray diffraction techniques, since X-rays interact with samples through electrostatic interaction with electrons mainly. Neutrons carrying characteristic magnetic dipole moments will interact directly through nuclear magnetic moments, the intensity with which neutrons are scattered will not be influenced by the number of electrons and neighbouring elements in the periodic table that might scatter neutrons with distinctly different intensities [73]. The magnetic moments arising from the electron clouds will scatter allowing for magnetic structure determination. Since neutrons are uncharged sub-atomic particles, this means they are less likely to interact with the samples being scanning, and thus allows a deeper penetration into the target nuclei and aids the interpretation of scattering data. Having a weak interaction with matters means that each analysis will require a large quantity of samples, and using a large quantity of samples lowers the chance of developing systematic errors that are common in X-ray diffraction analysis [74]. Crystal growth for certain samples such as large single crystals remains a certain degree of difficulty. Investigation using neutron diffractometer is time-consuming because they are characterised by low fluxes compared to X-ray sources, which means there is fewer number of neutrons emitted from the neutron source in all directions per unit energy per second at neutron kinetic energy E [75].

There are two types of neutron generation, one is from a reactor source where neutrons are generated in a nuclear reactor by nuclear fission. The advantages of reactor neutron sources are it uses a high continuous flux that makes it good for measuring large objects and low dynamics. The disadvantage of the reactor source are the build-up and maintenance costs are very expensive since it requires a nuclear reactor, i.e. The Institut Laue–Langevin in Grenoble, France. Another one is generated in a process of spallation which is when a beam of high energy protons bombards a tungsten target, this bombardment excites the nuclei and give off an extremely intense neutron pulse [76]. The advantages of spallation source are the diffraction patterns produced are of excellent resolution by high discontinuous flux, and this method is safer than nuclear fission and environmentally friendly.

There are four main types of neutron scattering, ranging from 1) the simplest type involving transmission measurement to measure the atomic ratios of elements in a crude sample. 2) elastic neutron scattering that measures the scattered intensity for sample structure investigation using different scattering angles. 3) Quasielastic/inelastic neutron scattering that analyse the transfer of neutron energies during diffraction. 4) The Spin-echo method, another type of quasielastic method that employs polarised neutrons that are made for spin precession in the pre and post sample flight path. The number of spin precession before and after the sample being analysed is proportional to the neutron velocity change during scattering and hence the energy transfer can be found [74, 77].

2.2.0 Instrumentation

2.2.1 Rigaku miniflex 600

The Rigaku Miniflex 600 X-ray diffractometer was used to collect data of $MAPbI_3$ samples, and the caesium doped samples ($Cs_{0.10}MA_{0.90}PbI_3$ and $Cs_{0.05}MA_{0.95}PbI_3$). The crystal samples were ground into fined powders and placed onto the silicon or aluminium sample holders. A step degree of 0.02 at a speed of 0.2 degree/minute, from 5 to 80 ^{o} in the 2θ degree, total scanning time was 3 hours per sample. The phase identification and purity of the samples were then compared with the self-built-in Crystallography Open Database (COD) with the use of the plotting software Highscore.

2.2.2 Panalytical X'pert³ powder diffraction

Original and annealed $MAPbI_3$ samples (vacuum, zinc and air annealing), and the mixed metal fluorides were analysed by the Panalytical X'pert³ powder diffractometer. Sample preparation was done by grinding. All samples were scanned with an absolute continuous scan from 3 to 80 ^{o} in the 2θ degree, with 100.9 seconds per step and a step degree of 0.0167 and at a speed of 0.0210 degree per second, total scanning time is 1 hour per sample.

2.2.3 Rigaku Oxford Supernova diffractometer

Copper radiation has greater wavelength radiation (K_α= 1.54184 Å and K_β = 1.39222 Å) compared to molybdenum (K_α= 0.71073 Å and K_β = 0.63229 Å). Molybdenum radiation was chosen for the analysis for all rubidium mixed metal fluoride samples as iron containing compounds will fluoresce and produce noisy background and weak scattering under X-ray radiation produced by copper anodes. The setting for the scanning $RbFeCrF_6$ samples were as followed: in the pre-experiment, a cubic cell (90.16(6) Å , 90.00(6) Å and 90.07(6) Å) with diffraction limit of beyond 9.80 A were acquired. A target resolution of 0.800 Ang, target I/sig of 15.00 and an experiment type of Laue symmetry were used, and the samples were scanned for 2 hours.

2.2.4 Quantum design MPMS 7 SQUID magnetometer

Two samples of the mixed metal fluorides, $RbFe2CrF_6$ (15.46 mg) and $RbFeZnF_6$ (14.75 mg) were selected and measured for magnetisation. $RbFeCrF_6$ was measured at 1000 Oe from 2 to 80 K both at ZFC/FC condition, and at 100 Oe from 2 to 300 K both under ZFC/FC condition. $RbFeZnF_6$ was measured at 1000 Oe from 2 to 80 K under ZFC/FC condition.

Chapter 3. Methylammonium lead iodide MAPbI$_3$

3.1.0 Experimental

3.1.1 Preparation of Methylammonium iodide for MAPbI$_3$ synthesis

The synthetic method was modified from Stamplecoskie's experimental method [78]. In a 250 mL round-bottomed flask in an ice bath (at 0 °C), methylamine (27.80 mL) was reacted with hydroiodic acid 57 % w/w (30 mL) for 2 hours and stirred with magnetic stirrer. The white-yellow precipitate was recovered by evaporation at 65 °C in a bead bath for 2 days. The product was then washed with distilled water and dried overnight in an oven at 50 °C before collection for future uses.

3.1.2 Synthesis of Methylammonium lead iodide MAPbI$_3$ with a solution based method

The synthetic method was modified from the synthetic method for MAPbI$_3$ used by Stoumpos' [6]**.** PbO powder (2.2320 g, 10 mmol) was dissolved in a mixture of 57 % w/w HI solution (10 mL) and 50 % w/w aqueous H$_3$PO$_2$ (1.7 mL) and heated to boiling (87 °C) under magnetic stirring for 5 minutes until a bright yellow solution formed. Subsequent addition of the solid MAI (1.1196 g, 10 mmol) to the hot yellow solution, and a black precipitate will have formed. The heating was continued for 1 hour at 87 °C and left to cool to room temperature for the crystallisation of MAPbI$_3$. The product MAPbI$_3$ was collected by suction filtration and dried overnight in a heating oven.

The balanced equations for solution – based synthesis of MAPbI$_3$ samples are given below:

PbO (s) + 4 HI (aq) $\rightarrow$ PbI$_2$ (s) + H$_2$O (aq) + I$_2$ (aq)

PbI$_2$ (s) + CH$_3$NH$_3$I (s) $\rightarrow$ CH$_3$NH$_3$PbI$_3$ (s)
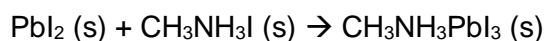
The two MAPbI$_3$ samples used in this study were synthesised by the same solution based method and dried in an oven at 50 °C. However, the quantity of PbO and solid MAI varies but the precision of each measurement was maintained at +/- 0.0005 g. They are assigned to compound 1, compound 2 (both were treated with air-annealed), compound 1 vacuum annealed and compound 2 zinc annealed.

3.1.3 Caesium doped MAPbI$_3$ (5 and 10% caesium) - Synthesis of Caesium doped MAPbI$_3$ with a solution-based method

The synthesis of the 5 % and 10 % caesium doped MAPbI$_3$ was modified from the synthesis of MAPbI$_3$ used in Stoumpos' paper [6] and the doping stage was modified from Choi's paper [33].

3.1.4 Synthesis of 5% caesium doped sample: Cs$_{0.05}$MA$_{0.95}$PbI$_3$

The balanced equations for the direct synthesis of Cs$_{0.05}$MA$_{0.95}$PbI$_3$ are given below:
PbO (s) + 4 HI (aq) $\rightarrow$ PbI$_2$ (s) + H$_2$O (aq) + I$_2$ (aq)

PbI$_2$ (s) + 0.95 CH$_3$NH$_3$I (s) + 0.05 CsI (s) $\rightarrow$ Cs$_{(0.05)}$CH$_3$NH$_{3(0.95)}$PbI$_3$
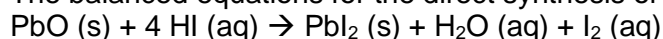
PbO powder (2.2398g, 10 mmol) was dissolved in a mixture of 57 % w/w HI solution (10 mL) and 50 % w/w aqueous H$_3$PO$_2$ (1.7 mL) and heated to boiling (87 °C) under magnetic stirring for 5 minutes until a bright yellow solution formed.

In the doping stage, the precursors: MAI (1.0640 g, 9.5 mmol), and CsI (0.1323 g, 0.5 mmol) were added directly into the hot yellow solution, the mixture was heated for 2 hours at 87 $^{\circ}$C and left to cool to room temperature. The product was collected by suction filtration and dried inside an oven.

3.1.5 Synthesis of 10 % caesium doped sample: $Cs_{0.1}MA_{0.90}PbI_3$

The balanced equations for the direct synthesis of $Cs_{0.10}MA_{0.90}PbI_3$ are given below:
PbO (s) + 4 HI (aq) $\rightarrow$ PbI_2 (s) + H_2O (aq) + I_2 (aq)

PbI_2 (s) + 0.90 CH_3NH_3I (s) + 0.10 CsI (s) $\rightarrow$ $Cs_{(0.10)}CH_3NH_{3(0.90)}PbI_3$

PbO powder (2.2335 g, 10 mmol) was dissolved in a mixture of 57 % w/w HI solution (10 mL) and 50 % w/w aqueous H_3PO_2 (1.7 mL) and heated to boiling (87 $^{\circ}$C) under magnetic stirring for 5 minutes until a bright yellow solution formed.

In the doping stage, the precursors: MAI (1.0083 g, 9.0 mmol), and CsI (0.2623 g, 1.0 mmol) were added directly into the hot yellow solution, the mixture was heated for 2 hours at 87 $^{\circ}$C and left to cool to room temperature. The product was collected by suction filtration and dried overnight in an oven.

3.1.6 Annealing treatment for $MAPbI_3$

3.1.7 Air annealing treatment

A $MAPbI_3$ sample was annealed at different temperatures and different lengths of time to investigate the effect of temperature to the crystal structures.

$MAPbI_3$ compound 1 and compound 2 were annealed both at 50, 70, 90 and 110 $^{\circ}$C for 1 and 3 hours.

3.1.8 Vacuum annealing treatment

$MAPbI_3$ compound 1 was used for vacuum treatment. The vacuum oven was set to 90 $^{\circ}$C and 1000 kPa pressure, a spatula full of the sample was placed into a sample boat. Small fractions of sample was taken out during the annealing process in the time interval of from 1 to 5 hour, and after 24, 48 and 72 hours of heating.

3.1.9 Annealing treatment with zinc metal under vacuum condition

Compound 2 was used for zinc annealing at vacuum condition at 275 and 300 $^{\circ}$C.

The samples were divided and placed at three different positions inside a sample boat, this sample boat was placed into a sealed tube with zinc metal located at the end of the tube. At 300 $^{\circ}$C, the samples were heated for 20 hours and the sample at position 1 (closest to the centre of the furnace) was burned and disintegrated. And the sample treatment was re-attempted at 300 $^{\circ}$C for 12 hours.

The furnace was programmed to heat for 12 hours at 275 $^{\circ}$C. More zinc annealing experiments were performed at 250, 200, 150 and 100 $^{\circ}$C with and without the exposure to zinc metal to investigate the correlation between temperature to extent of structural changes in the $MAPbI_3$ samples. The temperature at different position (a total of three different temperatures per treatment) of the sealed tube was measured using a metal probe attached to an infrared thermometer. The hottest temperature was detected nearest to the centre of the furnace and gets colder nearer to the far end.

3.2.0 Results and discussion

3.2.1 Synthesis of methylammonium lead iodide MAPbI₃ a solution based method

All the MAPbI$_3$ samples were made by dissolving the orange lead (ii) oxide powder into a mixture of HI and H$_3$PO$_2$ and a bright yellow solution was formed upon boiling at 87 °C. Subsequent addition of the lab synthetic methylammonium iodide powder to the hot yellow solution produced a black precipitate. This black precipitate is the black shiny crystal of MAPbI$_3$ product after collection. This proves the modified synthetic method has successfully produced the expected black, shiny MAPbI$_3$ crystals as shown in Figure 3.1.

Figure 3.1 the synthetic product of MAPbI$_3$, black; shiny crystals.

3.2.2 Powder X-ray analysis of methylammonium lead iodide MAPbI₃

All the MAPbI$_3$ samples were characterised by Panalytical X-ray diffractometer and their structural patterns and other related information were characterised by Rietveld refinement. Table 1 shows the refined atomic positions of MAPbI$_3$ (*I4/m* space group) under ambient conditions obtained from Rietveld refinement of powder X-ray diffraction data will be used for comparison and reference to all the refinement data in this study. Figure 3.2 shows the calculated pattern for MAPbI$_3$ with *I4/m* space group extracted from ICSD. This cif file will be used as the starter for Rietveld refinement of all the samples synthesised and annealed in this study.

The calculated X-ray patterns (Figure 3.2) of MAPbI$_3$ shows sharp characteristic peaks at 14.1 ° (110), 19.9 ° (112), 28.1 ° (004), 28.4 ° (220), 31.7 ° (114), 40.5 ° (224), 43.1 ° (1$\bar{3}$4) and 50.2 ° (044). This cif file provides the fundamental crystallographic information for comparison of structural changes in samples treated with different condition and used as the starting point for Reitveld refinement for all MAPbI$_3$ related samples synthesised in this project.

The refinement for all MAPbI$_3$ as well as the annealed samples were done using the software Fullprof in the space group *I4/m* (*a*= 8.8756 Å, *b*= 8.8756 Å, *c*= 12.6517 Å), tetragonal phase. Figure 3.3 shows the result of the Rietveld refinement of MAPbI$_3$ compound 1 including the measured and calculated XRD patterns and their differences. In the process of refinement, the atomic positions, site occupancies, lattice parameters were refined under isotropic thermal factor. The isotropic displacement parameter (B) were 23.55957(-), 4.82246(-), 4.82246(-), 1.03126(-) and 1.03126(-) Å^2 for C1, I1, I2, Pb1 and Pb2 respectively, and methylammonium molecules were not refined due to instability (table can be viewed in Appendix 1).

Satisfactory agreement results was obtained between measured and calculated patterns as the Bragg R-factor = 10.1, Rf-factor = 6.40 and χ^2 = 8.57. Table 1 summarises the refined crystal structure parameters for carbon, iodine and lead in their x, y and z positions.

The same refinement parameters were used in the profile matching for compound 2. The characteristic peaks are observed at 14.0 ° (110), 19.9 ° (112), 28.1 ° (004), 28.4 ° (220), 31.7 ° (114), 40.5 ° (224), 43.1 ° ($1\bar{3}4$) and 50.2 ° (044). The observed, calculated and difference in diffraction are shown in Figure 3.4. When the two XRD pattern of compound 1 and 2 are compared, compound 1 appears to be more crystalline than compound 2. These can be seen in the increase in intensities in the lower region at 14.0 ° (110), 28.4 ° (220) and 31.7 ° (114) and 43.1 ° ($1\bar{3}4$). However, the diffraction in 40.5 ° (224) is particularly higher in compound 2. This high intensity peak could be a result of impurity in the sample or on the sample holder for the X-ray diffractometer. Since MAPbI$_3$ is a polycrystalline material which means there could be multiple single crystals that varied in size and orientated in their preferred orientation, hence it will cause X-ray radiation to produce scattering peaks. The two samples synthesised are confirmed to be MAPbI$_3$ and crystallised in their preferred orientation and this can be seen in the atomic positions shown in table 1 for compound 1 with the lattice parameters were determined to a= 8.8624(2) Å, b= 8.8624(2) Å , c= 12.6639(3) Å. The lattice parameters for compound 2 are determined to be a= 8.86863 Å, b= 8.86863 Å , c= 12.67281 Å. Compound 1 and 2 have the same c/a ratio 1.4289 but different pattern at 40 °, and hence both are suitable for future annealing treatment.
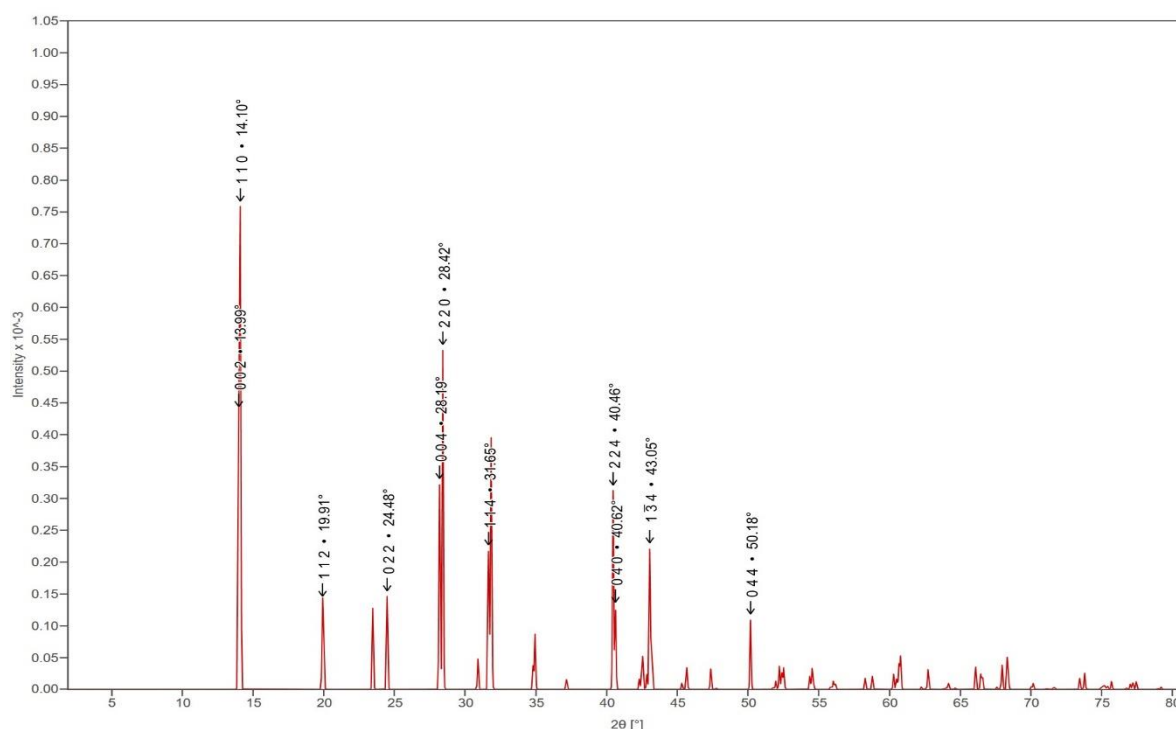
Figure 3.2 The calculated X-ray pattern of MAPbI$_3$ (*I4/m* space group at 300 K) with all the characteristic peaks being labelled [21].
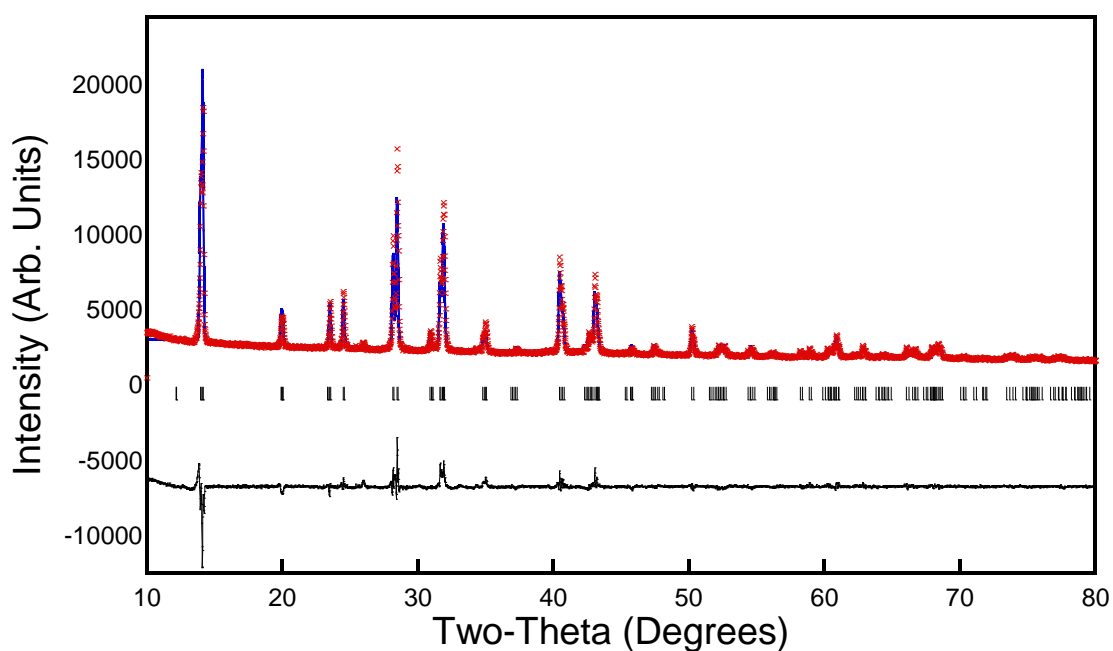
Figure 3.3 Observed (blue), calculated (red) and difference (black) data obtained from Rietveld refinement of powder X-ray diffraction data of MAPbI$_3$ compound 1.

	Atomic positions		
Atom	x	y	z
C1*	-0.03500(-)	0.43800(-)	0.22100(-)
I1	0.00000(-)	0.00000(-)	0.24972(13)
I2	-0.21272(17)	-0.28589(17)	0.50000(-)
Pb1	0.00000(-)	0.00000(-)	0.00000(-)
Pb2	0.00000(-)	0.00000(-)	0.50000(-)

Table 1. The atomic positions of MAPbI$_3$ compound 1 under ambient conditions obtained from Rietveld refinement of powder X-ray diffraction data. The lattice parameters were determined to be a= 8.8624(2) Å, b= 8.8624(2) Å , c= 12.6639(3) Å. * methylammonium molecules were not refined due to instability.
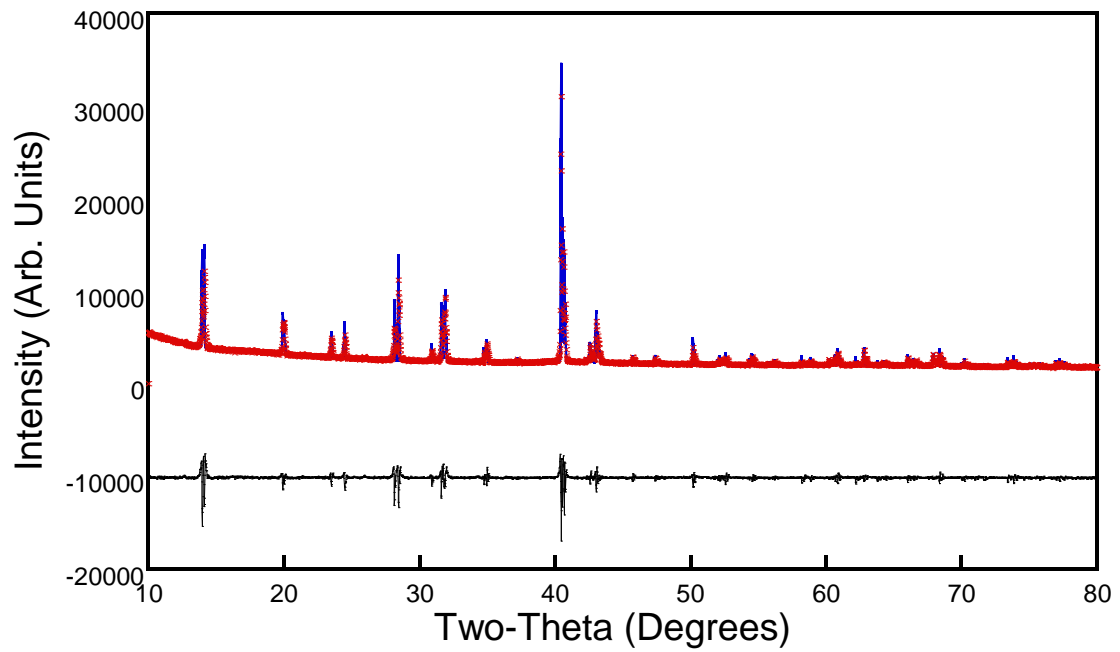
Figure 3.4 Observed (blue), calculated (red) and difference (black) data obtained from profile matching of powder X-ray diffraction data of MAPbI$_3$ compound 2 due to preferred orientation.

3.2.3 Caesium doped MAPbI$_3$ (5 and 10 % caesium) - Synthesis of caesium doped MAPbI$_3$ with a solution-based method

The Cs doped MAPbI$_3$ are black, shiny crystals. The approach for identification and for structural change studies was done by comparing the experimental X-ray patterns of Cs$_{0.05}$MA$_{0.95}$PbI$_3$, Cs$_{0.10}$MA$_{0.90}$PbI$_3$ with MAPbI$_3$ compound 1 and the calculated x-ray patterns of CsPbI$_3$ (from ICSD) and the crystal structure of CsPbI$_3$ in orthorhombic phase is shown in Figure 3.5.

The calculated X-ray pattern of CsPbI$_3$ with *Pnma* space group and orthorhombic crystal system, and lattice parameters (*a*= 10.4342 Å, *b*= 4.7905 Å and *c*= 17.7610 Å) was plotted and labelled in Figure 3.5.The characteristic peaks for a pure CsPbI$_3$ are presented at 9.9° (002), 13.1 ° (102) , 22.1 ° (111) 25.7 ° (211) and 26.5 ° (105) respectively, indicating the presence of an orthorhombic phase [33].

MAPbI$_3$ with *I4/m* shows sharp characteristic peaks at 13.9 ° (002), 14.1 ° (110), 19.9 ° (112), 28.1 ° (004), 28.4 ° (220), 31.7 ° (114), 40.5 ° (224), 43.1 ° (1$\bar{3}$4) and 50.2 ° (044) shown in Figure 3.2 was used for comparison. A comparison plot of the X-ray pattern of Cs$_{0.05}$MA$_{0.95}$PbI$_3$ (red), Cs$_{0.10}$MA$_{0.90}$PbI$_3$,(blue) MAPbI$_3$ (black) and CsPbI$_3$ (green) is shown in Figure 3.6. There were negligible differences in diffraction peaks between CsPbI$_3$ and Cs$_{0.10}$MA$_{0.90}$PbI$_3$ (blue) whereas the characteristic peaks for MAPbI$_3$ are clearly seen: peaks at 14.1 ° (110), 19.9 ° (112), 40.5 ° (224) and 43.1 ° (1$\bar{3}$4). There are a gradually increase in intensities for the peaks responsible for the CsPbI$_3$ composition which can be seen in the region around 25.7 ° (211) and 26.5 ° (105) respectively. This indicates that the doping experiment for 5 % caesium was successful incorporated into the A-site and co-exists with MA cations.

The same conclusion can be applied to the 10 % caesium doped MAPbI$_3$. The synthesis was successful, and it is proven by the experimental data for Cs$_{0.10}$MA$_{0.90}$PbI$_3$ showed in Figure 3.6. There is similarity in the intensities of X-ray patterns observed with an increase in intensities in the region around 25.7 ° (211) and 26.5 ° (105). Therefore, the wet-lab synthesis of by varying the ratio of MA and Cs allows incorporation of Cs in to the MAPbI$_3$ structure.
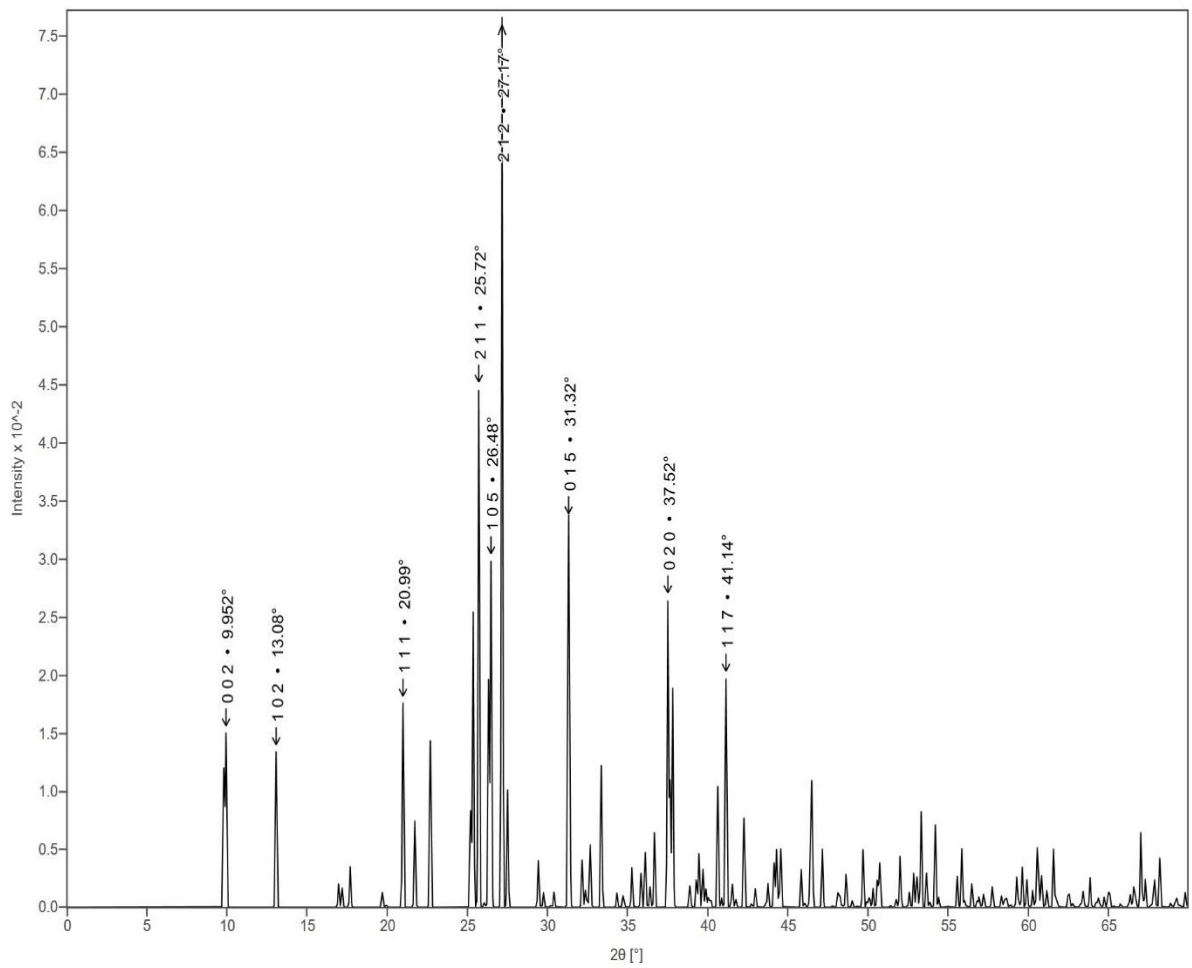
Figure 3.5 The calculated X-ray pattern of CsPbI$_3$ with characteristic peaks labelled.
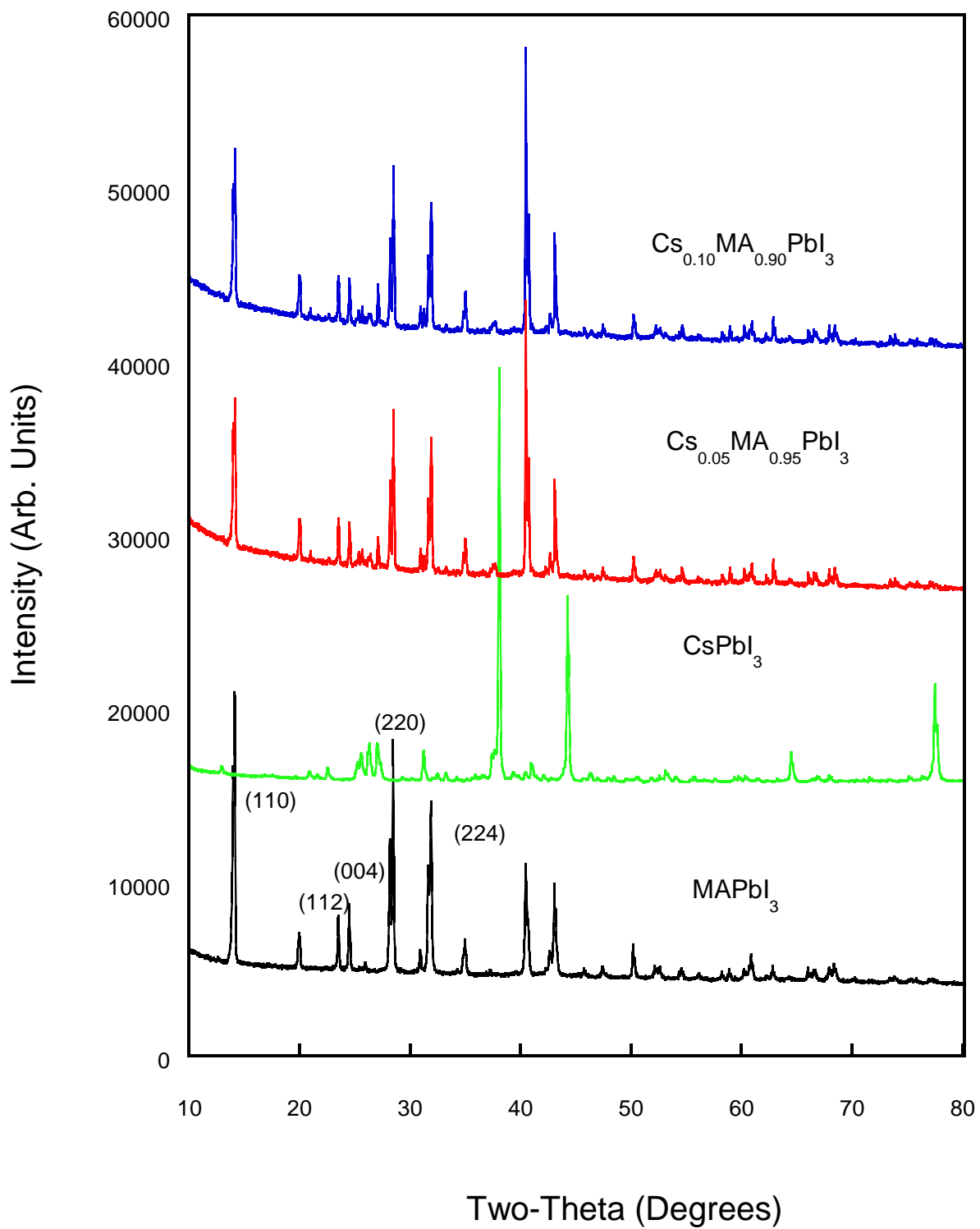
Figure 3.6 Comparison of the experimental X-ray patterns of MAPbI₃ (black), Cs$_{0.10}$MA$_{0.90}$PbI$_3$ (blue), Cs$_{0.05}$MA$_{0.95}$PbI$_3$ (red) and CsPbI₃ (green).

3.2.4 One and three hours of air annealed treatment of MAPbI$_3$ compound 1 and 2 results discussion

MAPbI$_3$ compound 1 and compound 2 were annealed both at 50, 70, 90 and 110 ^{o}C for 1 and 3 hours. A total of 16 treatments were done and XRD analysis were performed and shown in Appendix 1. However, Rietveld refinement were unsuccessful for the annealed samples as crystallinity changes and it does not fit perfectly with the *I4/m* MAPbI$_3$ cif. Profile matching with constant scale factor were used for the structure characterisation. The calculated, observed and difference in X-ray patterns for all annealed samples are attached in Appendix 1, and discussion is made upon the changes in the lattice parameters and on comparison of X-ray diffraction patterns. The refinement on compound 1 annealed at 70 ^{o}C for 3 hours were not presentable, and the raw data of their X-ray patterns will be presented, and their lattice parameters will be discussed.

A plot that compares the X-ray diffraction patterns of compound 1 at 50, 70, 90 and 110 ^{o}C is shown in Figure 3.7. A decrease in the intensities in diffraction peaks is observed at 14.0 ^{o} (110), 20.0 ^{o} (112), 28.2 ^{o} (220), 32.0 ^{o} (114), 40.6 ^{o} (114) and 43.1 ^{o} (1$\bar{3}$4) respectively. The reduce in the intensities is positively correlated to an increase in temperature which is observed at 70, 90 and 110 ^{o}C respectively. This result is exceptional to literature where an increase in temperature should result in greatly crystallinity as high temperature leads to a greater surface mobility for deposited atoms, so they can orientate in their lowest thermodynamically favoured lattice positions [79], hence strengthens these peaks as MAPbI$_3$ annealed at a higher temperature would produce crystals with greater grain size; smaller grain boundaries [80].

Therefore, compound 1 was also annealed for 3 hours to look at the relationship between temperature and structural changes. The same result was obtained but started at 50 ^{o}C, a decrease in intensities is observed in the 14.0 ^{o} (110), 20.0 ^{o} (112), 28.2 ^{o} (220), 32.0 ^{o} (114), 40.6 ^{o} (114) and 43.1 ^{o} (1$\bar{3}$4) respectively when annealed at 50, 70, 90 and 100 ^{o}C and a comparison of samples is shown in Figure 3.8.

The lattice parameter *a*, *c* and *c/a* ratio (can be found in Appendix 1) for compound 1 annealed for 1 hour and 3 hours at 50, 70, 90 and 100 ^{o}C are plotted with error bars and presented in Figure 3.9, 3.10 and 3.11 respectively. When annealed for 1 hour, the lattice parameter *a* increases with temperature from 8.867860 Å (at 50 ^{o}C) to 8.867900 Å (at 70 ^{o}C) and followed by a significant drop to 8.855080 Å at (90 ^{o}C) and then shifts back up to 8.872890 Å (at 110 ^{o}C). However, the c/a ratio decreases with temperature from 1.429095 at 50 ^{o}C to 1.427984 at 110 ^{o}C.

A similar change in lattice parameters is observed for compound 1 that was annealed for 3 hours, the lattice parameter *a* generally increases with temperature from 8.868440 Å (at 50 ^{o}C) to 8.870410 Å (70 ^{o}C), and then a smooth drop is observed from 70 ^{o}C to 8.870110 Å at 90 ^{o}C and 8.866570 Å eventually at 110 ^{o}C. The same fluctuation is also observed in lattice parameter *c* and *c/a* ratio which indicates that there is no significant changes in MAPbI$_3$ structure regardless of temperature. The volume of compound 1 annealed at different temperatures was also calculated and found to be 996.59, 996.02, 991.19 and 997.51 Å^3 respectively (Figure 3.12), this indicates that annealing at 90 ^{o}C reduces the lattice parameters and hence leading to a smaller volume size.

In conclusion, the poor peak height observed in diffraction patterns for compound 1 annealed as a function of temperature can be explained by the following points. Thermal annealing could lead to structural degradation of perovskite by inducing lattice strains in the sample during thermal expansion and contraction during annealing and when cooling from

100 °C [81]. However, all these samples were annealed below 100 °C and further studies are needed to confirm lattice straining. Another study [82] suggests that external stimuli such as moisture and oxygen can also alter perovskite structure. The organic constituent methylamine has a high water-solubility which makes the perovskite prone to moisture-related degradation, the formation of hydrated species will lead to the decomposition of MAPbI$_3$ into aqueous HI, solid PbI$_2$ and CH$_3$NH$_2$ [83]. No sign of decomposition is observed (a PbI$_2$ peak will appear at 12.7 ° at (110) when decomposed) except a decrease in intensity. The time and temperature play a crucial role in structure changes of MAPbI$_3$. The combination of the two suggestions; degradation and lattice straining combined with experimental data showed that increasing temperature causes changes in lattice parameters and hence a decrease in crystallinity of MAPbI$_3$. This could be that the stoichiometry of the material is changing as a function of temperature, as this can be seen in the c/a ratio for all annealing experiments is greater than $\sqrt{2}$, a distortion of the body centered cubic lattice [84], and the resulting composition suggests the lowering in the X-ray peak height. Heating at 90 °C for 1 hour leads to a greatest change in lattice parameter *a* and *c* (shown in Figure 3.9 and 3.10). Further studies such as thermogravimetric analysis (TGA) might be helpful to investigate this anomalous [85].

A plot that compares the X-ray diffraction patterns for compound 2 annealed for 1 and 3 hours at 50, 70, 90 and 110 °C is summarised in Figure 3.13 and 3.14 respectively. The lattice parameter *a*, *c* and *c/a* ratio are plotted in Figure 3.15, 3.16 and 3.17. In the one hour annealing treatment, the X-ray diffraction patterns show a greater reduction in crystallinity in 14.0 ° (110) and 40.6 ° (114) at temperature between 70 and 90 °C, this corresponds to the changes in lattice parameter *a* (a significant decrease from 8.87035 Å to 8.866620 Å) and lattice parameter *c* (a decrease from 12.67780 Å to 12.66988 Å) as shown in Figure 3.15 and 3.16. Generally, the lattice parameters *a* increases when annealed between 50 °C and 70 °C, followed by a sharp decrease as a function of temperature from 70 to 90 °C, then a smooth decrease from 90 to 110 °C. The changes in lattice parameter *c* is inconsistent with temperature, as it follows a steady decrease as a function of temperature; a significant decrease is observed between 70 °C and 90 °C (from 12.67780 Å to 12.66988 Å and followed by an increase between 90 °C to 110 °C.

When compound 2 (Figure 3.14) was annealed for 3 hours at 50, 70, 80 and 110 °C, crystallinity of MAPbI$_3$ seems fairly consistent with temperature from 50 to 90 °C until a decrease in crystallinity is seem at 110 °C. As shown in Figure 3.15, the changes in lattice parameter *a* is inconsistent with temperature but the greatest change is observed between 50 and 70 °C (a change from 8.868830 Å to 8.870510 Å). The fluctuation in lattice parameter c is fairly consistent as a function of temperature (Figure 3.16). However, the c/a ratio (Figure 3.17) for compound 1 annealed for 3 hours also showed that the c/a ratio is greater than $\sqrt{2}$, a distortion of the body centered cubic lattice. Figure 3.18 summarises the volume size of compound 2, they were 997.24, 997.53, 996.07 and 996.11 Å^3 respectively, temperature has no significant effect on the volume size of compound 2.

In conclusion, thermal annealing treatment for MAPbI$_3$ at 90 °C for 1 hour causes the greatest change in lattice *a* and *c*, which means a greater change in MAPbI$_3$ structure. The changes in lattice parameter, and the decrease in crystallinity in compound 2 could be a result of smaller grain size; since thermal annealing treatment tend to induce fewer grain boundaries in the powder sample. In addition, the structure is likely to be compressed when heated at a higher temperature, this leads to a short bond lengths between atoms, and hence a decrease in lattice parameters occur [86].
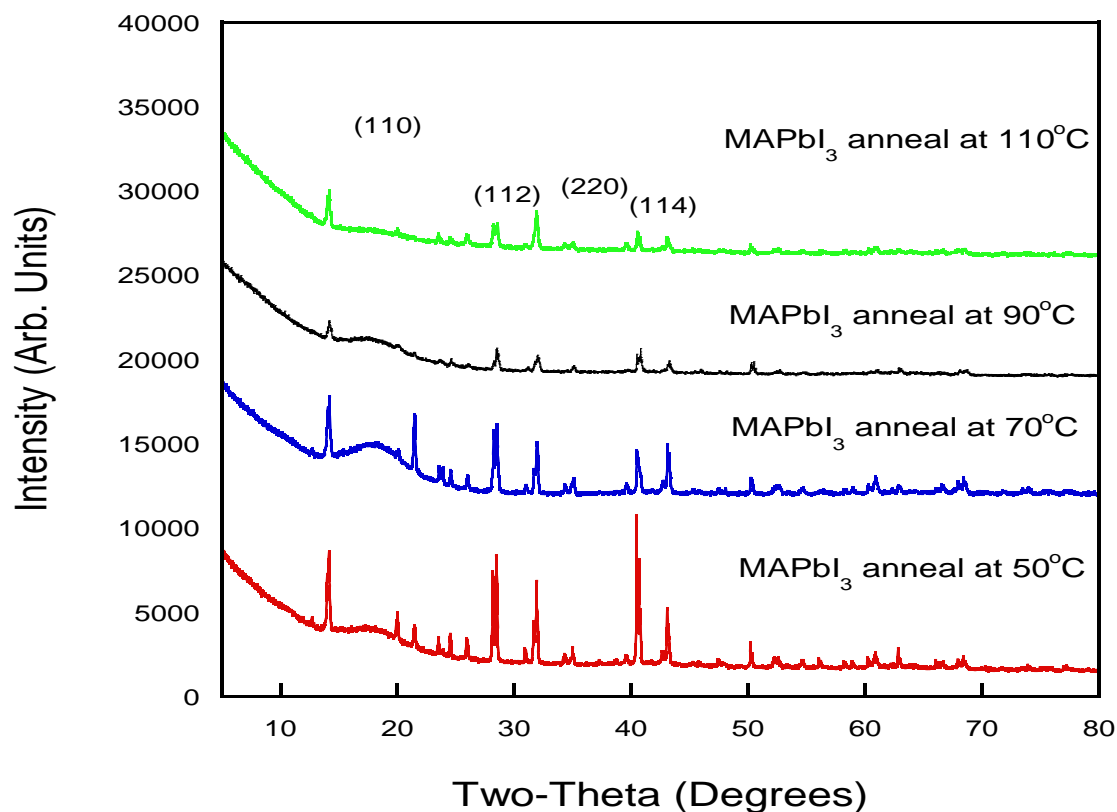
Figure 3.7 The experimental X-ray patterns of MAPbI₃ compound 1 air annealed for 1 hour at 50 (red), 70 (blue), 90 (black) and 110 °C (green).
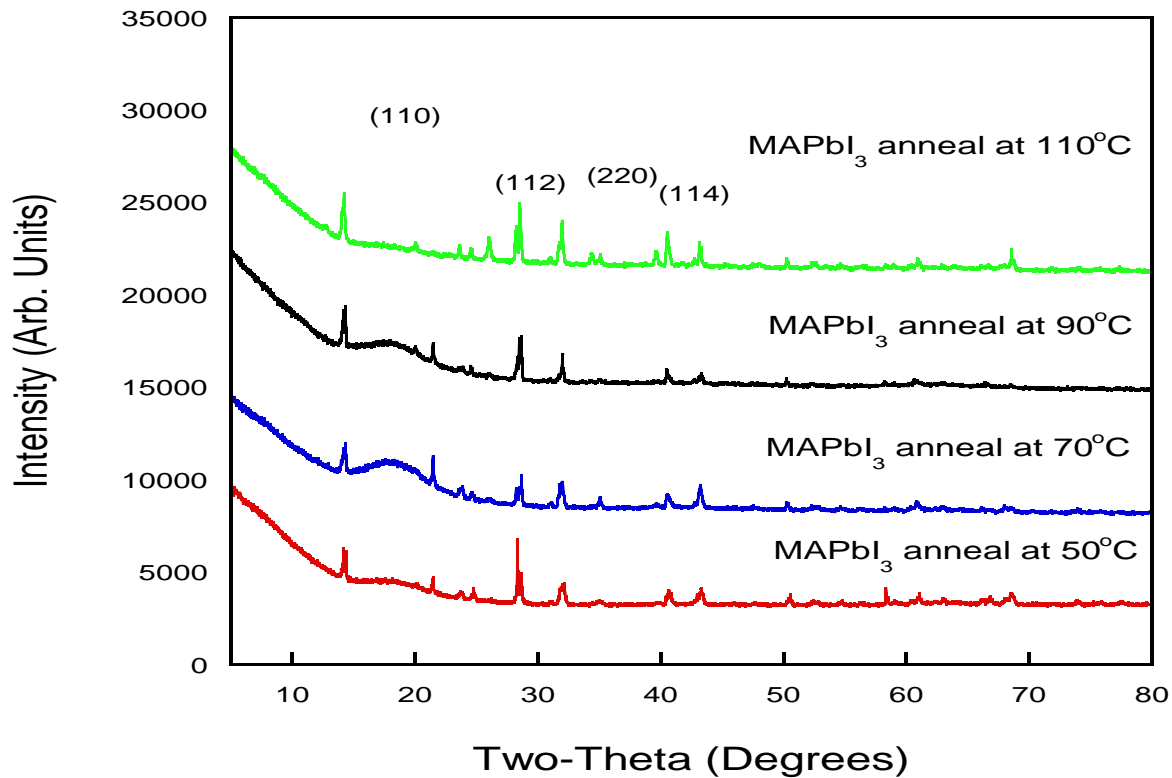
Figure 3.8 The experimental X-ray patterns of MAPbI₃ compound 1 air annealed for 3 hours at 50 (red), 70 (blue), 90 (black) and 110 °C (green).
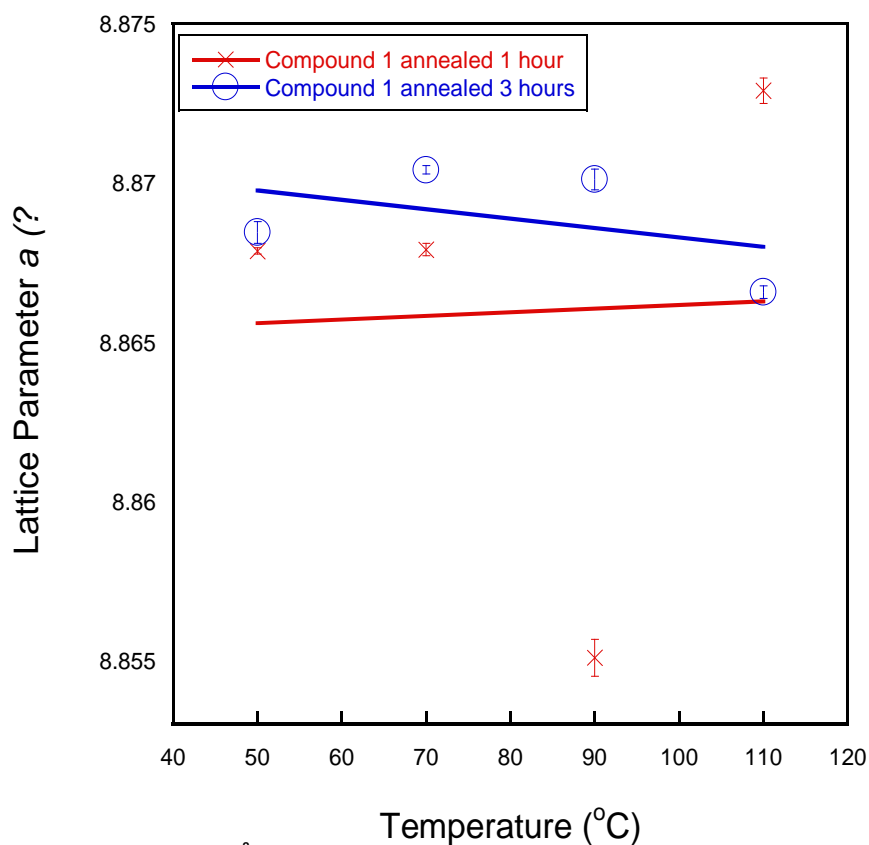
Figure 3.9 Lattice parameter *a* (Å) (with error bars) of MAPbI$_3$ compound 1 annealed for 1 hour (red) and 3 hours (blue) vs temperature (^{o}C)
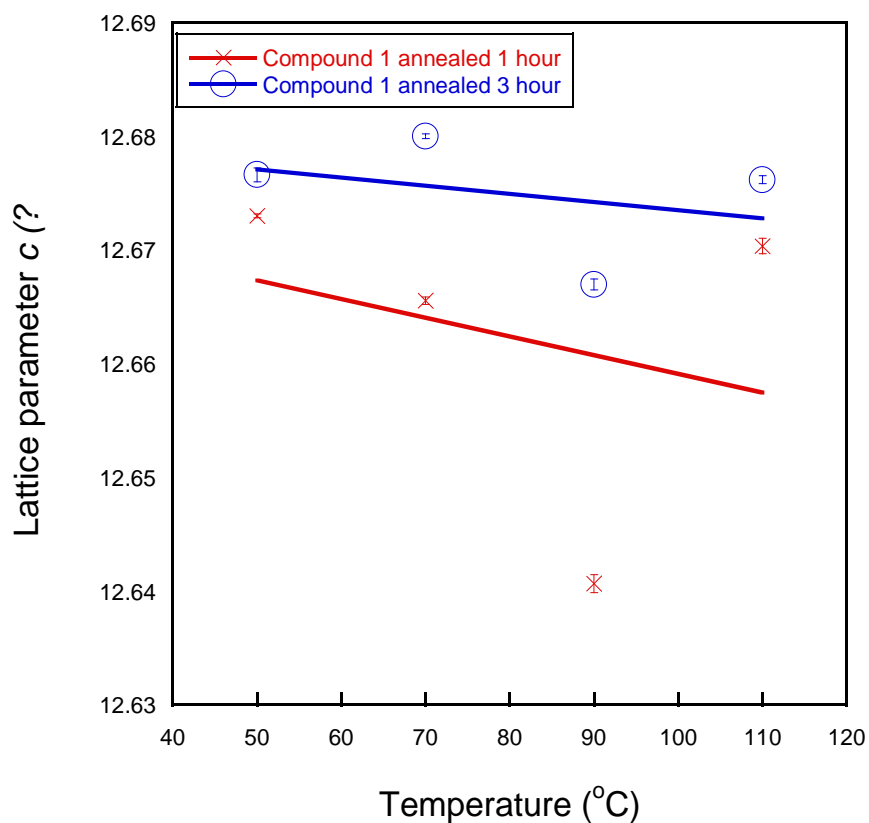
Figure 3. 10 lattice parameter *c* (Å) (with error bars) of MAPbI$_3$ compound 1 annealed for 1 hour (red) and 3 hours (blue) vs temperature (^{o}C)
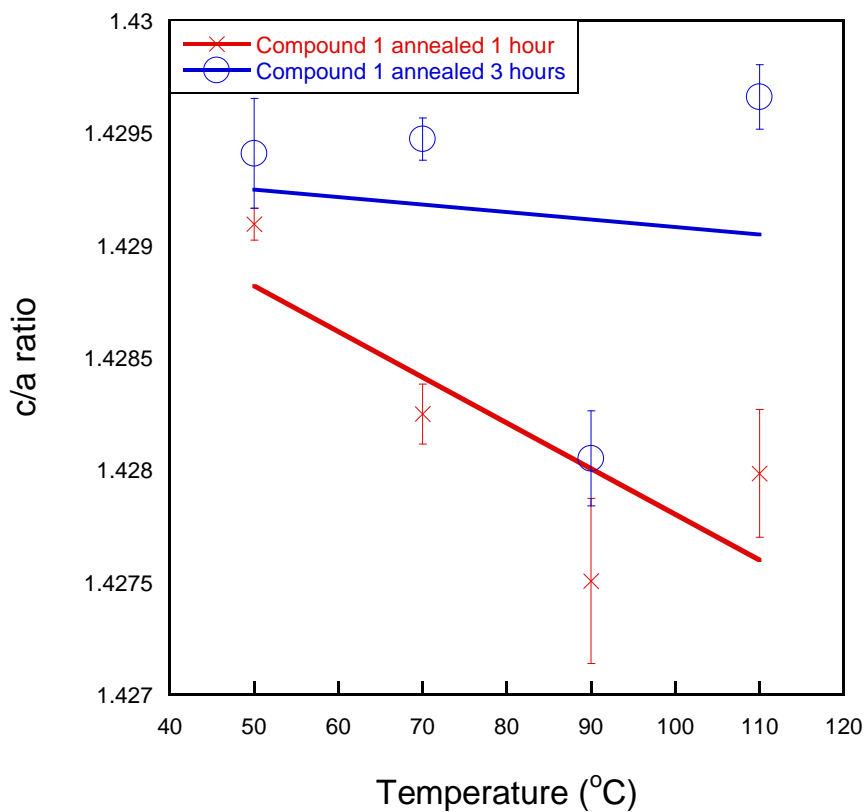
Figure 3. 11 *c/a* ratio (with error bars) of MAPbI$_3$ compound 1 annealed for 1 hour (red) and 3 hours (blue) vs temperature (^{o}C)
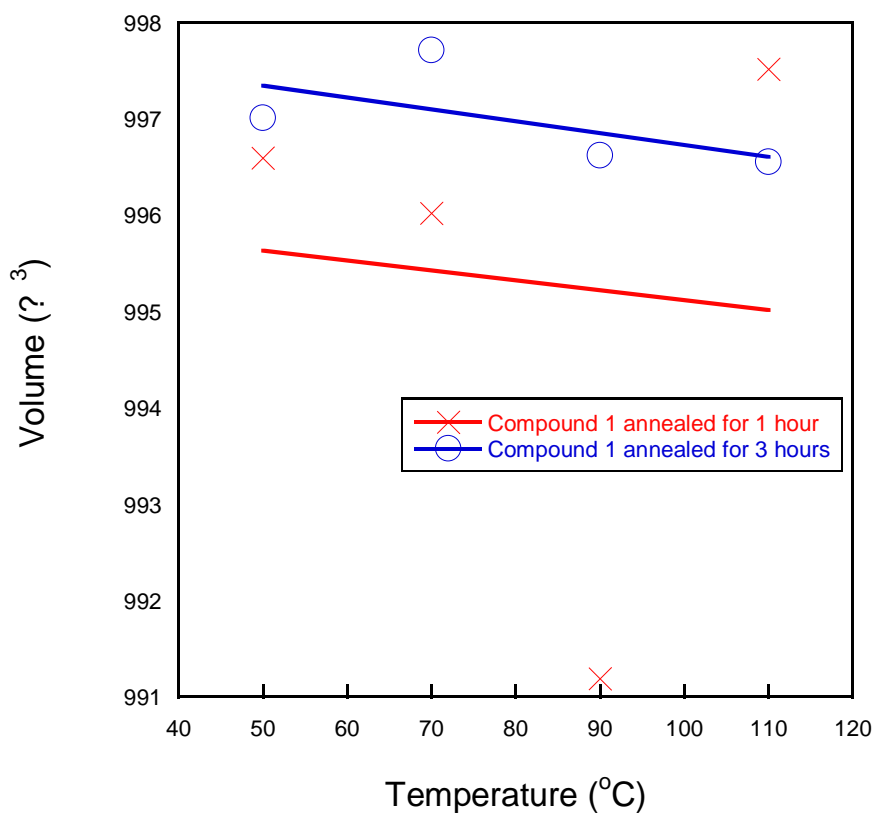
Figure 3.12 Volume (Å^3) of MAPbI$_3$ compound 1 at annealed for 1 hour and 3 hours vs temperature (^{o}C)
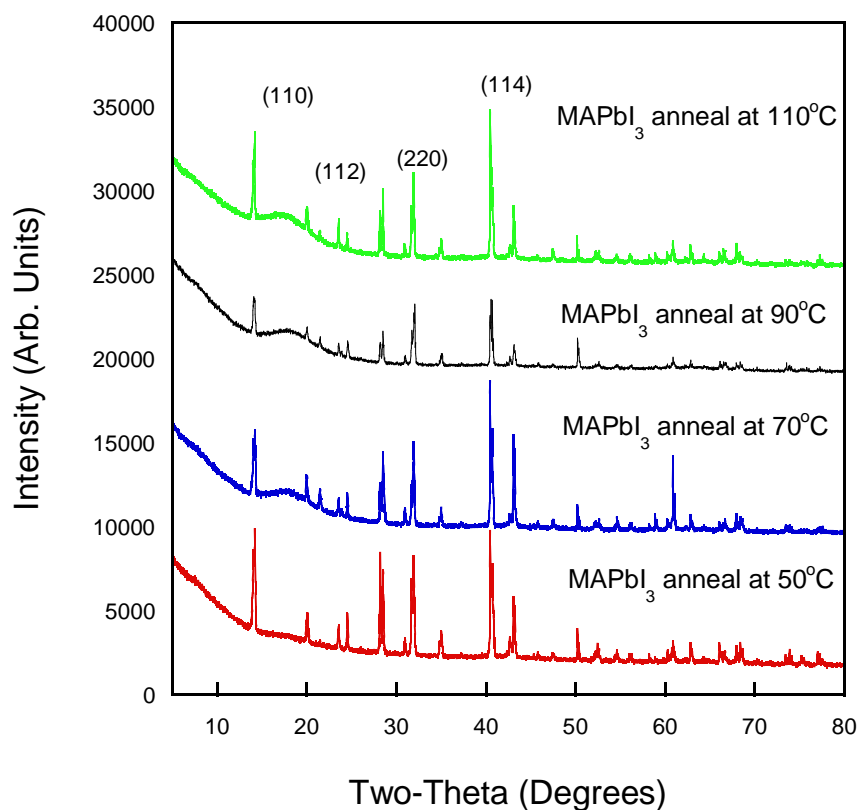
Figure 3.13 The experimental X-ray patterns of MAPbI₃ compound 2 air annealed for 1 hour at 50 (red), 70 (blue), 90 (black) and 110 °C (green).
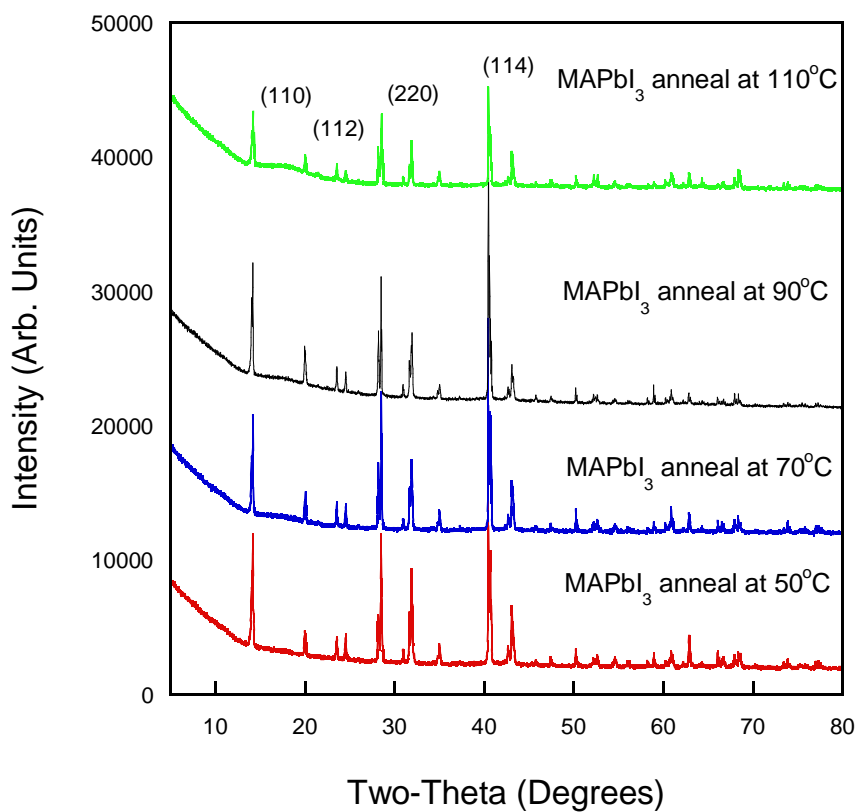
Figure 3.14 The experimental X-ray patterns of MAPbI₃ compound 2 air annealed for 3 hours at 50 (red), 70 (blue), 90 (black) and 110 °C (green).
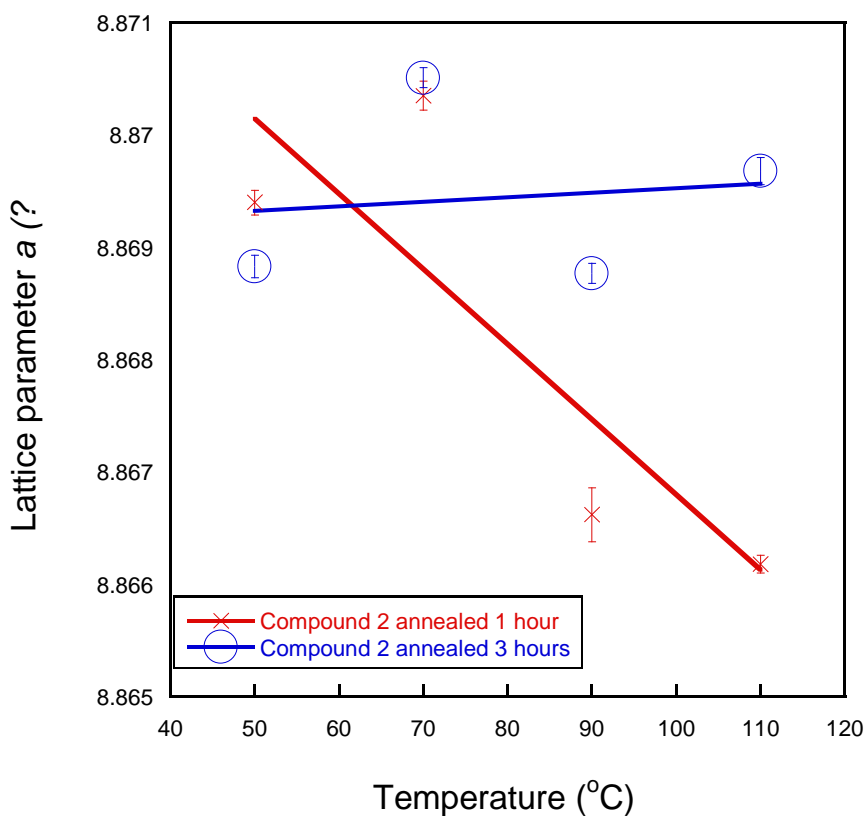
Figure 3.15 Lattice parameter *a* (Å) with error bars of MAPbI$_3$ compound 2 annealed for 1 hour (red) and 3 hours (blue) vs temperature (^{o}C)
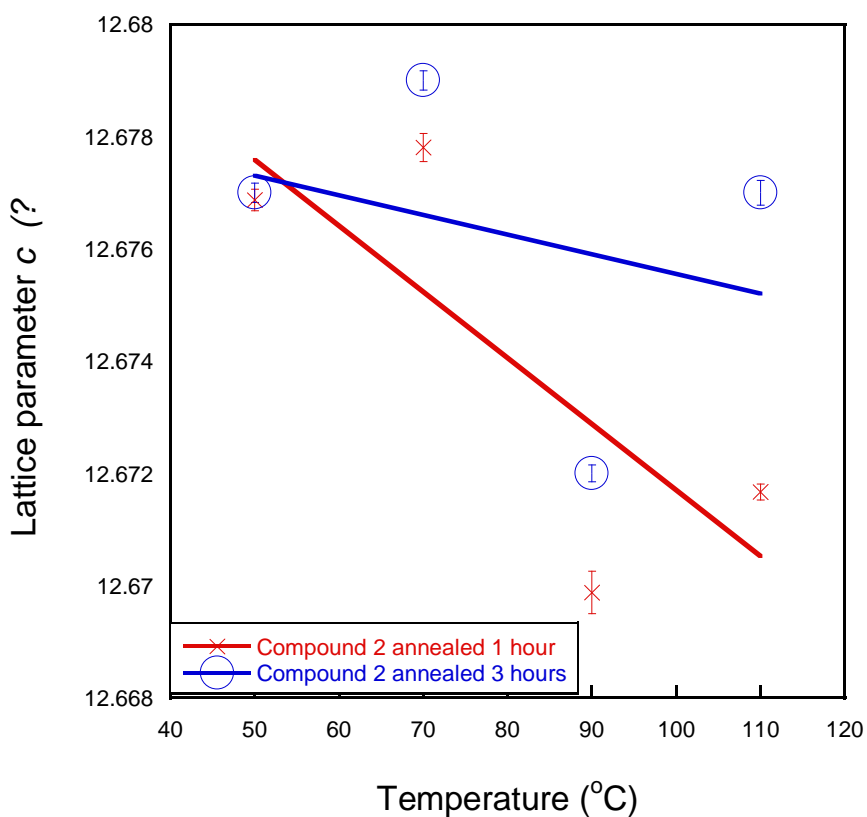
Figure 3. 16 Lattice parameter *c* (Å) (with error bars) of MAPbI$_3$ compound 2 annealed for 1 hour (red) and 3 hours (blue) vs temperature (^{o}C)
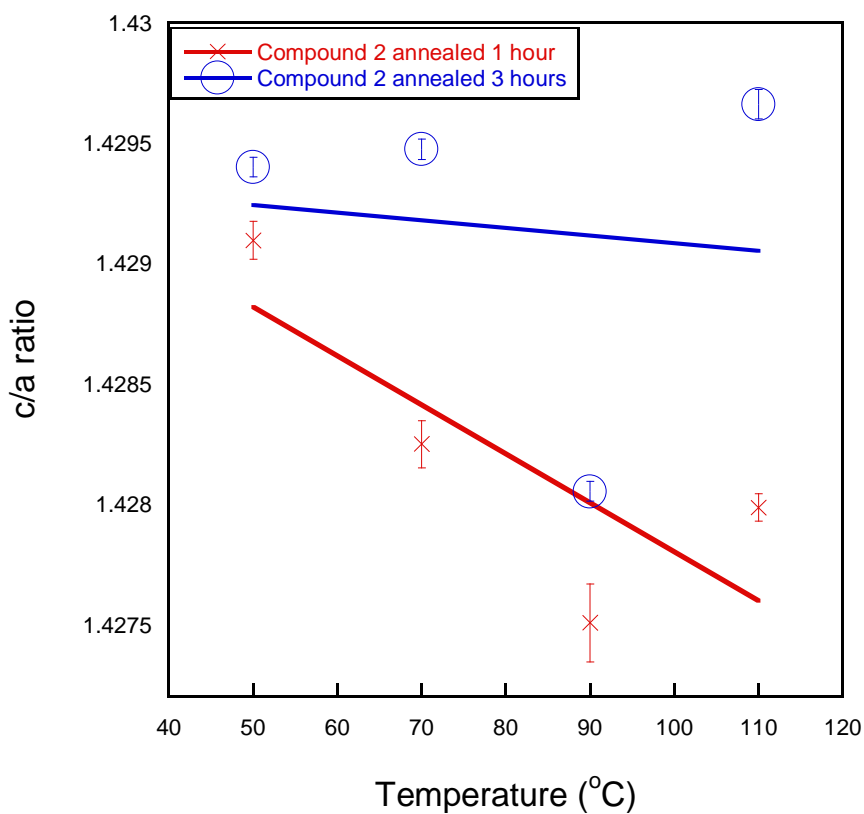
Figure 3.17 *c/a* ratio with (with error bars) of MAPbI$_3$ compound 2 annealed for 1 hour (red) and 3 hours (blue) vs temperature (°C)
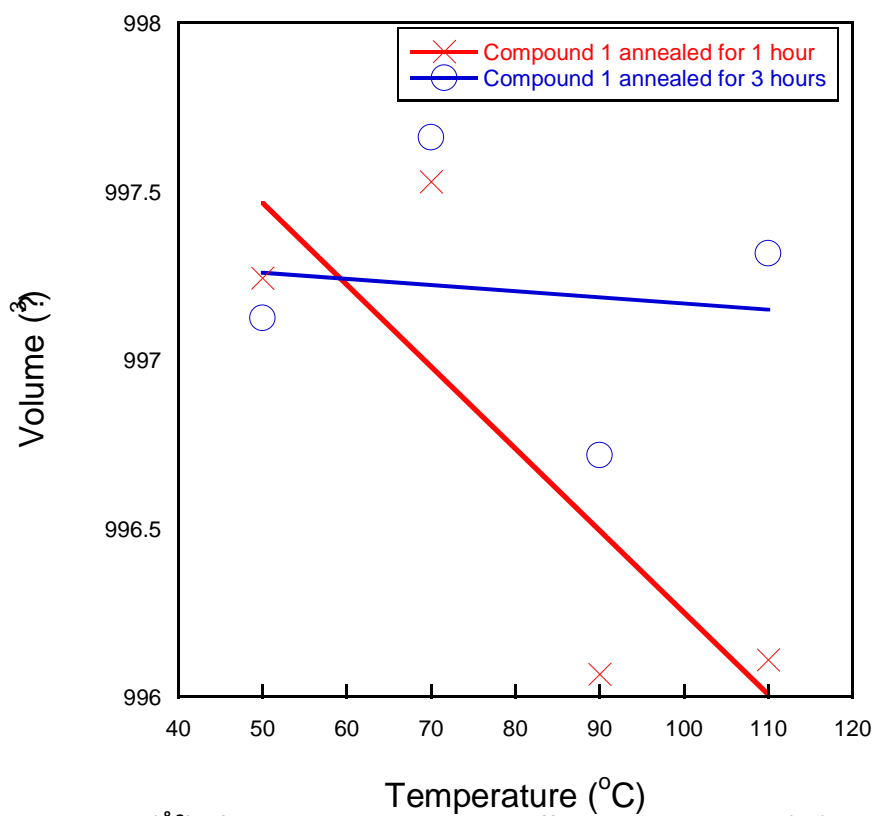
Figure 3.18 Volume (Å³) of MAPbI$_3$ compound 2 at different temperature (°C)

3.2.5 Discussion of the vacuum annealing treatment at 90 ºC

As reported in literature, a vacuum-assisted thermal annealing method has proven effectivenes in controling the crystallisation of perovskites at 60 ºC in vacuum [87]. Compound 1 was chosen for vacuum annealing treatment at 90 ºC for 1, 2, 3, 4, 5, 24, 48 and 72 hours respectively. The colour of the $MAPbI_3$ powder sample stays as black throughout the whole experiment. Rietveld refinement were unsuccessful for some patterns, hence profile matching with constant scale factor was used for structure characterisation with the *I4/m* $MAPbI_3$ cif. Tables of atomic positions, lattice parameters and the observed, calculated and differences in X-ray diffraction are attached in Appendix 1. Discussion will be made upon the changes in lattice parameters and in X-ray diffraction patterns.

A plot that compares the vacuum annealing between 1 to 72 hours is shown in Figure 3.19. It is verfied that crystallinity of $MAPbI_3$ has improved after vacuum annealing as a function of time at 90 ºC. An unusual increase in the peak intensity is observed at 40.5 º (224) for $MAPbI_3$ annealed in the range of 1 to 72 hours (the difference between 1 and 72-hour annealed is shown in Appendix A) which is believed to be impurities on the sample holder for the X-ray diffractometer, but there is an general increase in 14.1 º (110), 28.4 º (220), 31.7 º (113) respectively. The lattice paramater *a* (Figure 3.20) increases as a function of temperature from 1 hour annealed up 5 hours (from 8.868250 Å to 8.869500 Å) and a drop is observsed between 5 to 48 hours and eventually a significant increase from 48 to 72 hours (from 8.867960 Å to 8.870570 Å). The same trend is also observed in lattice parameter *c* (Figure 3.21), the increase is observed at the 5-hour annealed (from 12.67105 Å at 1 hour to 12.67873 Å), this is also proven in the *c/a* ratio of the 5-hour annealed which is 1.4295 (in Figure 3.22); which proves compond 1 annealed with this method showed that it is a distortion of the body centered cubic structure. The volume of compound 1 annealed at different lengths of time was also calculated (Figure 3.23), the changes in volume size is inconsistent with the length of annealing time. However, heating for 4, 5 or 72 hours lead to the greatest change in volume size, which are 997.43, 997.41 and 997.43 Å^3 respectively.

The increase in peak intensity is fairly consistent and it is attributed by lattice straining as a function of time [80], no shifts in peak position are observed but only the changes in diffraction intensity. No sign of decompostion is observed across all annealed treatment. In conclusion, vacuum annealed at 90 ºC for 5 hours is the most effective in terms of structural change in $MAPbI_3$ compound 1 [88]. This demonstrates that the vacuum annealing has little effect on compound 1 compared to air annealed in 3.2.4. However, repeat experiments are needed to test the effectiveness of vacuum annealed, further investigation such as SEM (scanning electron microscopy) will be helpful in comparing the changes in grain boundaries before and after annealing to consolidate the effectiveness of the vacuum treatment.
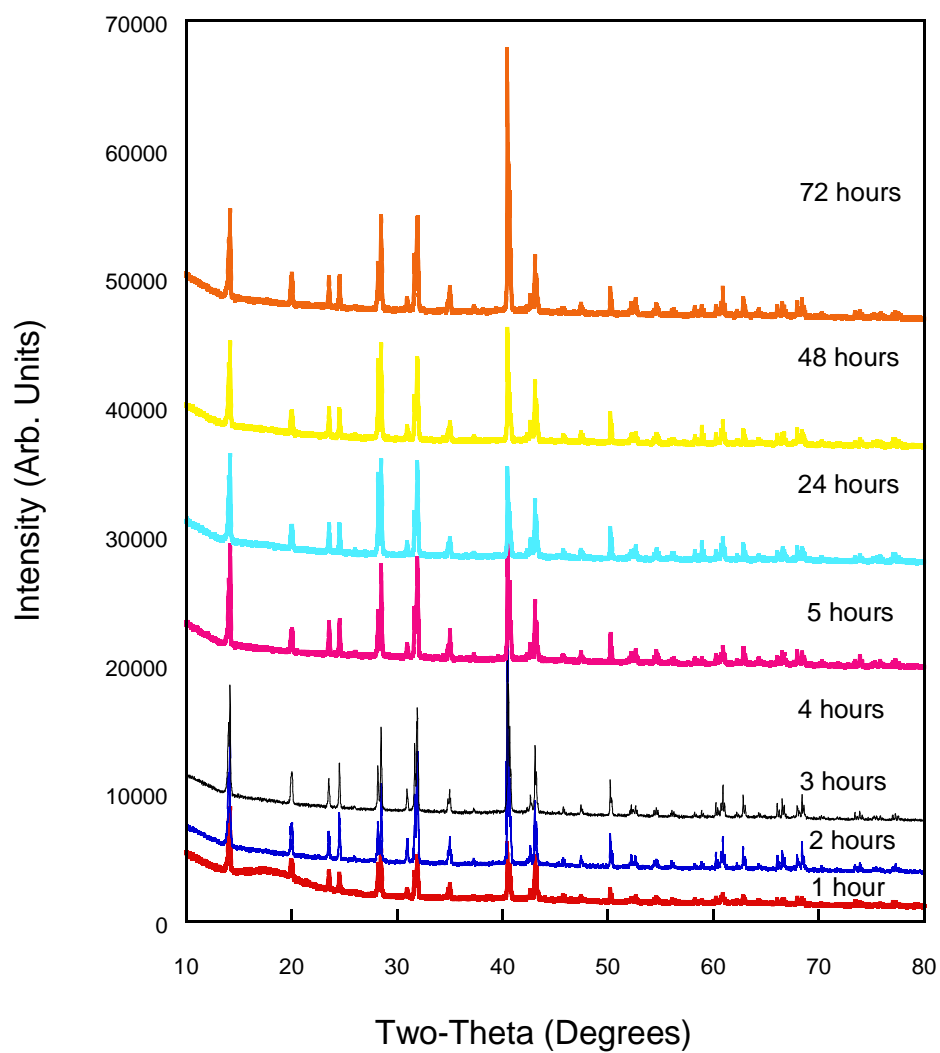
Figure 3.19 The comparison of the experimental X-ray patterns of the vacuum annealed MAPbI3 samples at 90 °C for 1 (red), 2 (blue), 3 (black), 4 (green), 5 (purple), 24 (cyan), 48 (yellow) and 72 (orange) hours.
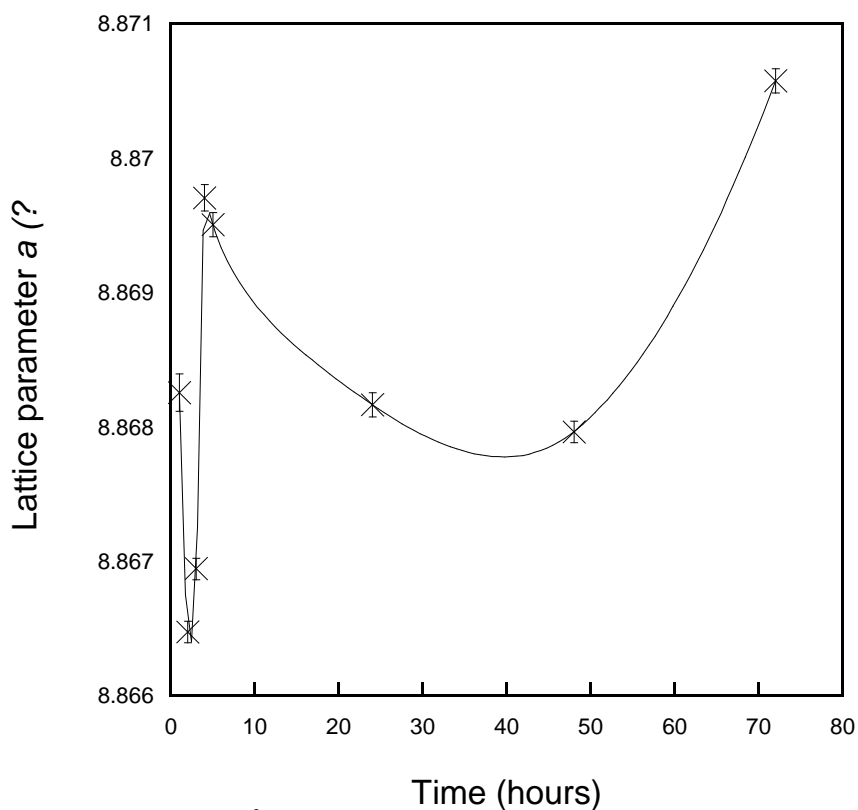
Figure 3.20 Lattice parameter *a* (Å) of MAPbI$_3$ compound 1 (with error bars) annealed under vacuum condition from 0 to 72 hours at 90 °C.
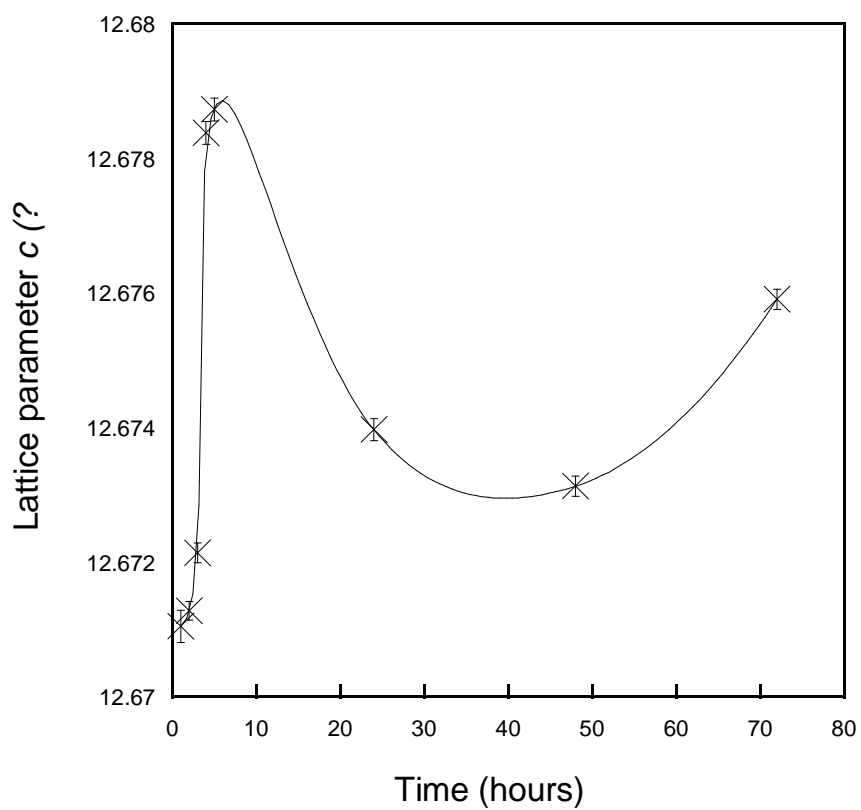
Figure 3.21 lattice parameter *c* (Å) of MAPbI$_3$ compound 1 (with error bars) annealed under vacuum condition from 0 to 72 hours at 90 °C.
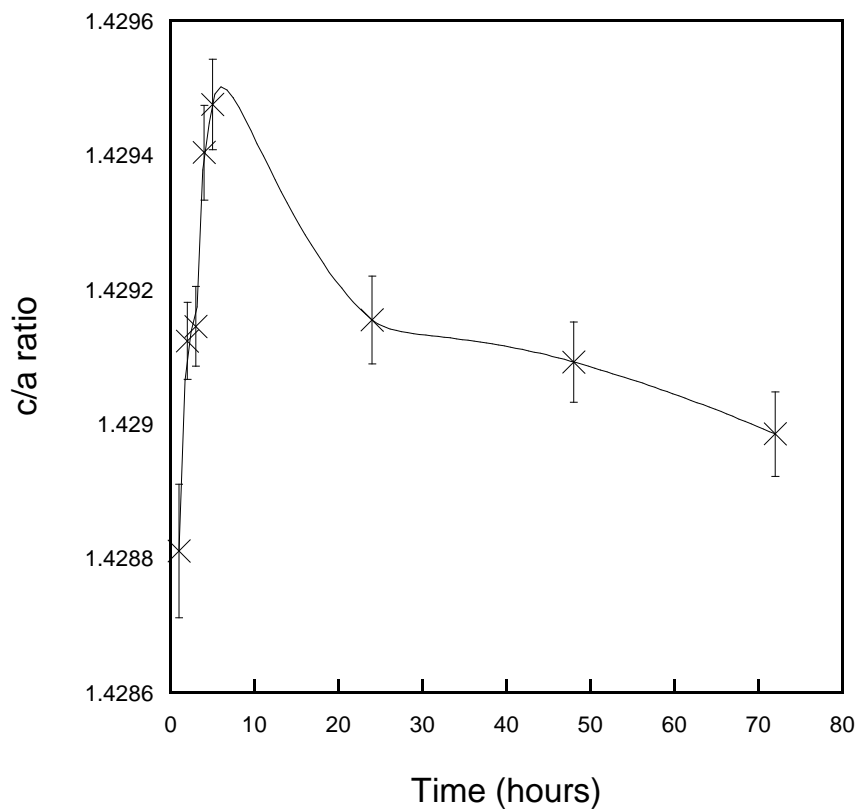
Figure 3.22 The *c/a* ratio of MAPbI$_3$ compound 1 (with error bars) annealed under vacuum condition from 0 to 72 hours at 90 $^{\circ}$C.
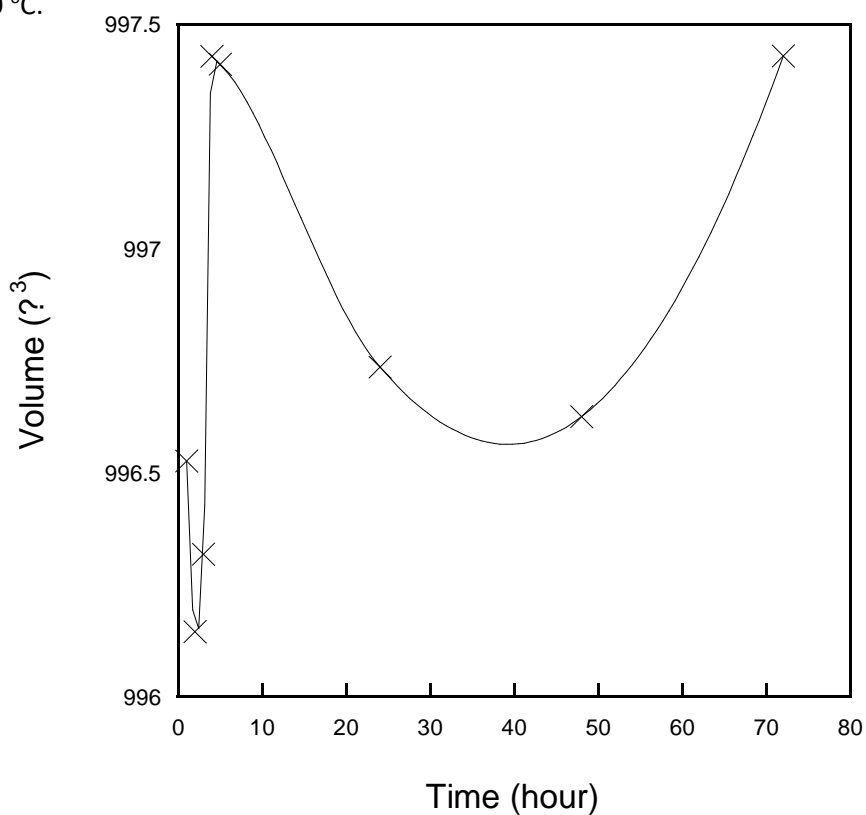
Figure 3.23 Volume (Å^3) of MAPbI$_3$ compound 1 vacuum annealing treatment at 90 $^{\circ}$C for 1, 2, 3, 4, 5, 24, 48 and 72 hours.

3.2.6 Annealing with zinc metal at temperatures 300 °C, 275 °C and 250 °C under vacuum condition

Zinc annealing treatment has been studied extensively and used in cell fabrication as a substitute to the conventional TiO_2 electron transport layers [89] or a Zinc oxide/methylammonium lead iodide field effect transistor. It showed promising results in solar cell performance in terms of material structure alteration. The benefits of incorporating zinc into $MAPbI_3$ perovskite are it can greatly reduce the current hysteresis effect of the solar cell, and it can reduce the ion migration within the lattice framework [90]. A further approach with zinc annealed method was taken in this study.

$MAPbI_3$ samples that had been exposed to zinc metal under vacuum condition had a physical and colour change from black, shiny crystals to brown/orange powders. The initial idea for this annealing treatment was to investigate the stability of $MAPbI_3$ structure in the exposure to zinc metal under a vacuum condition. The sample was first annealed at 300 °C for 12 hours, but the experimental outcome turned out to be a mismatch to the initial assumption. According to literature, Zn^{2+} would be incorporated into the Pb^{2+} position due to its smaller atomic radius, the successful incorporation of Zn^{2+} can be proven by a shift towards a higher degree in the 14.1 ° (110) plane [37].

However, the experimental X-ray patterns (Figure 3.24) showed that $MAPbI_3$ samples undergoes decomposition to form its constituent PbI_2 at 12.6 ° (110) after heated to 250 °C, 275 °C and 300 °C. The $MAPbI_3$ samples annealed at 271 °C, 289 °C and 300 °C all showed signs of decomposition. The same repeating pattern occurred to the samples annealed at 256 °C, 265 °C and 275 °C Samples heated at 238 °C, 244 °C and 250 °C showed different states of decomposition. A representative XRD pattern of a decomposed $MAPbI_3$ sample annealed at 300 °C is showed in Figure 3.24, samples annealed at 275 °C and 250 °C all have similar crystal structure with scattering peaks in the plot region between 20° and 35°.

In conclusion, $MAPbI_3$ samples decompose when annealed at temperature at above 250 °C, and all the relevant data were discarded, and further studies were conducted but at a lower temperature range.
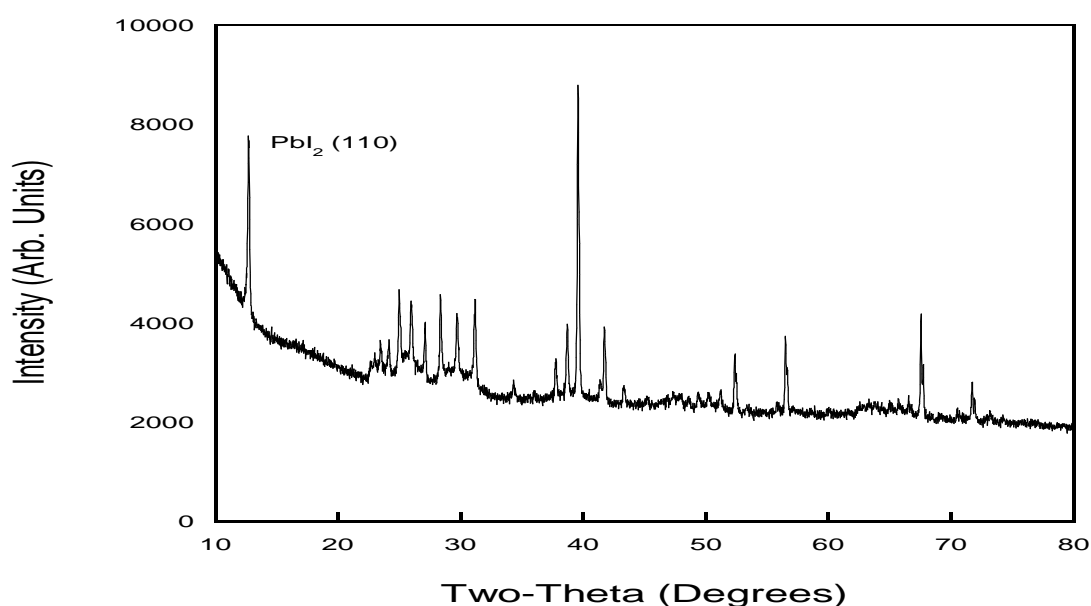
Figure 3.24 X-ray diffraction pattern of $MAPbI_3$ annealed with zinc metal under vacuum at 300 °C.

3.2.7 Annealing with zinc metal at 100 °C, 150 °C and 200 °C under vacuum condition

The same annealing procedure was carried out at a lower temperature range between 100 °C, 150 °C and 200 °C for 12 hours to further the investigation into the correlation between temperature and MAPbI$_3$ structure variation induced by the incorporation of Zn^{2+} in the Pb^{2+} positions.

Structural characterisation of MAPbI$_3$ compound 2 annealed with zinc metal under vacuum condition was done by profile matching with constant scale factor with the *I4/m* MAPbI$_3$ cif. Tables of lattice parameters and the observed, calculated and differences in X-ray diffraction are attached in Appendix 1. Discussion will be made upon the changes in lattice parameters and in X-ray diffraction patterns. Representative plots (Figure 3.26) showing the observed, calculated and difference in X-ray diffraction patterns of MAPbI$_3$ annealed with and without zinc at 100 °C are shown in Figure 3.25 and 3.26 respectively. The X-ray diffraction pattern of MAPbI$_3$ annealed at 100 °C shows characteristic peaks at 14.1 ° (110), 19.9 ° (112), 28.1 ° (004), 28.4 ° (220), 31.7 ° (114), 40.5 ° (224), 43.1 ° (1$\bar{3}$4) and 50.2 ° (044) respectively.

There is no sign of zinc incorporation into the Pb^{2+} positions (B-site) for all samples as the peak at 14.1 ° (110) remains at its preferred orientation, successful zinc incorporation will be shown by a slight shift to a higher degree in the (110) plane [37]. Samples annealed at 95 °C and 100 °C under vacuum condition showed little variation in lattice parameter *a*, *c* and *c/a* ratio as a function of temperature. However, there is a significant difference in lattice parameter *a* (8.875660 Å with zinc and 8.864130 Å without zinc), in lattice parameter *c* (12.68056 Å with zinc and 12.66370 Å without zinc) when annealed at 90 °C as shown in Figure 3.27 and 3.28 respectively. This suggests that the presence of zinc causes lattice expansion in MAPbI$_3$ at 90 °C, but no significant changes are shown in c/a ratio as they are all close to 1.249 (Figure 3.29). The volume of each sample was calculated and summarised in Figure 3.30. A significant variation is observed at 90 °C between the zinc anneal and untreated sample (with zinc: 998.94 Å³, without zinc: 995.02 Å³). In addition, the changes in volume size is consistent with temperature for each treatment; the volume size increases with temperature in the zinc anneal treatment, but it decrease with temperature in the untreated sample.

MAPbI$_3$ samples annealed with zinc at 150 °C shown an increase in peak intensity in the presence of zinc (shown in Appendix 1), since there is no sign of zinc corporation, this indicates that higher temperature annealing leads to strengthening of X-ray diffraction pattern in the characteristic regions such as in the (110), (220) and (114) planes in MAPbI$_3$ as described in the air annealed section 3.1.7.

The variation in the lattice parameter *a* and *c* is inconsistent with temperature between 140 °C, 145 °C and 150 °C (shown in Figure 3.31 and 3.32) There is no significant changes observed at 140 °C and 145 °C but the presence of zinc causes a greater lattice expansion which are shown in lattice parameter *a* (8.885910 Å with zinc and 8.867750 Å without zinc) and lattice parameter *c* (12.69102 Å with zinc and 12.67191 Å without zinc) when annealed at 150 °C as shown in Figure 3.27 and 3.28 respectively. However, there is no variation shown in the c/a ratio as they are all close to 1.429 (shown in Figure 3.33). The volume size of samples treated at different condition and temperature is summarised in Figure 3.34, the changes in sample size are consistent with temperature increase for the untreated sample. However, a significant change is observed at 150 °C for the zinc annealed sample, it is 1002.1 Å³ compared to 995.17 Å³ for the zinc anneal sample at 145 °C, and 996.48 Å³ for the untreated sample at 150 °C.

MAPbI$_3$ samples decomposed when annealed with zinc metal under vacuum condition at 200 °C, no accurate lattice parameters can be obtained from Rietveld refinement or profile matching, this data set was excluded from the study.

In conclusion, temperature plays an important role in determining the structural changes when samples are treating under vacuum condition. The X-ray analysis shows even though there is no incorporation of zinc into the B-site position, and yet zinc still has little effect in increasing crystallinity of MAPbI$_3$ at 150 °C. This can be proved by the increase in peak intensity along the (110), (220) and (114) planes. The method used in this study that anneals zinc metal and MAPbI$_3$ powder at low temperature did not allow the substitution of zn^{2+} with Pb^{2+}, as zinc has a melting point of 419.5 °C, a solution-based synthesis that uses ZnI$_2$ is more suitable for making Zn-doped MAPbI$_3$ compounds [91]. However, zinc is a good gettering reagent in controlling the composition of MAPbI$_3$.
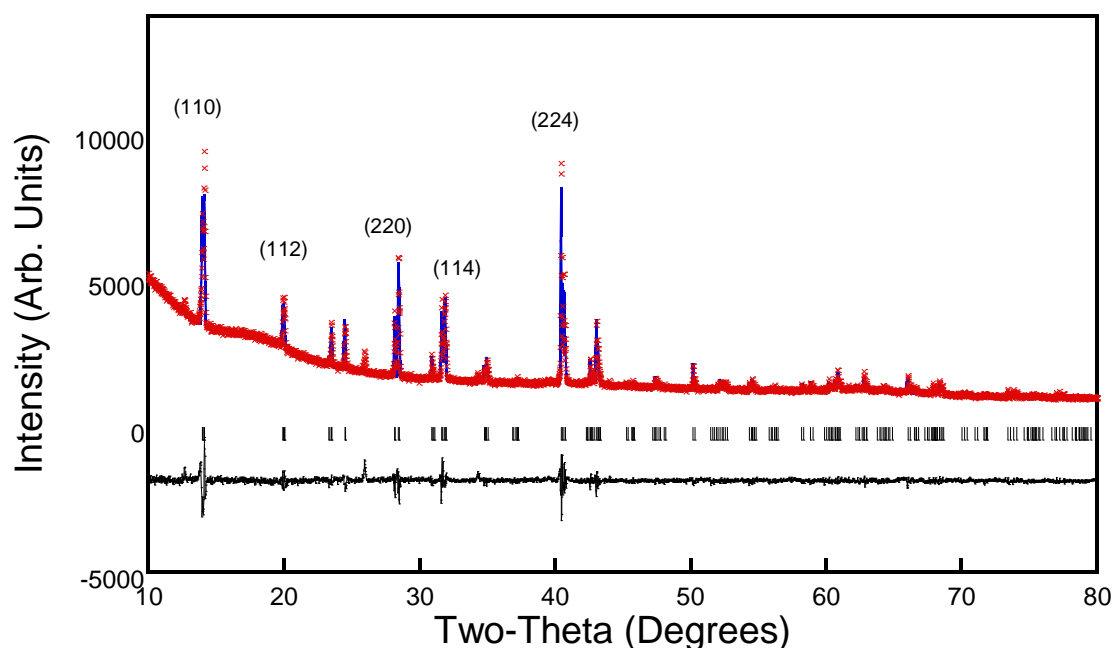
Figure 3.25 Observed (blue), calculated (red) and difference (black) data obtained from profile matching with constant scale factor of powder X-ray diffraction data of MAPbI$_3$ annealed with zinc metal under vacuum condition at 100 °C.
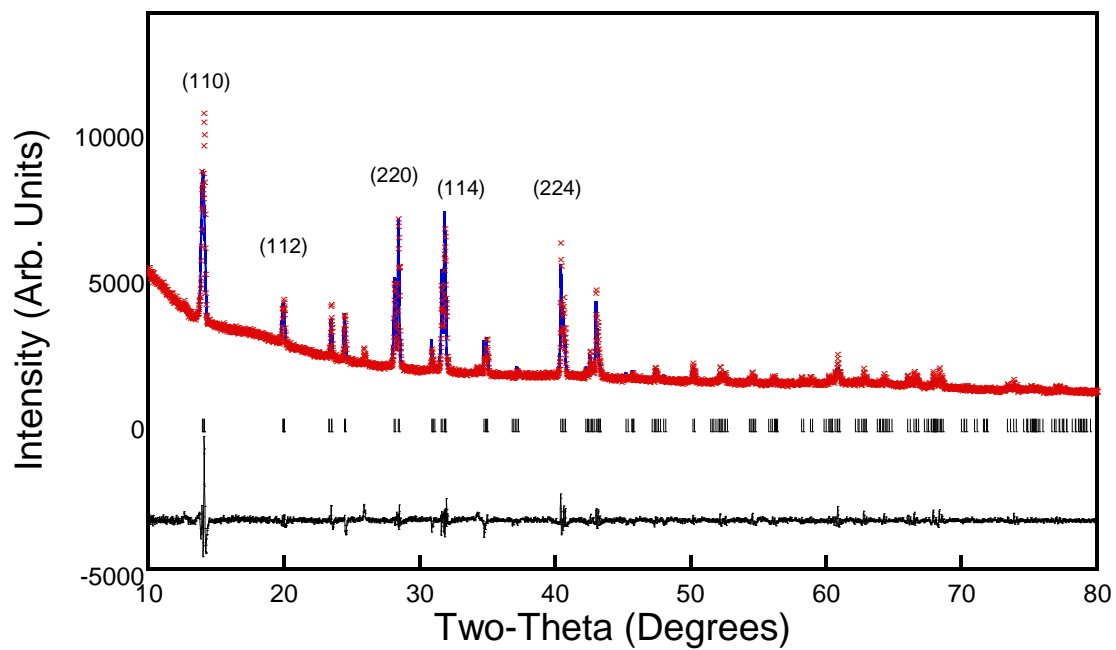
Figure 3.26 Observed (blue), calculated (red) and difference (black) data obtained from profile matching with constant scale factor of powder X-Ray diffraction data of MAPbI$_3$ annealed without zinc metal under vacuum condition at 100 °C.
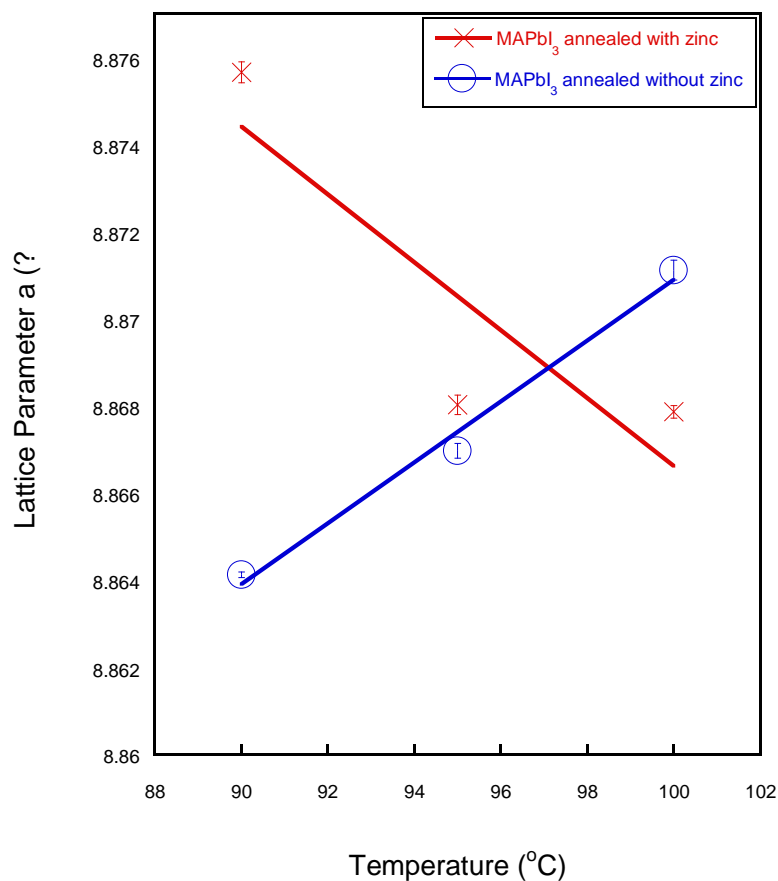
Figure 3.27 Lattice parameter *a* (Å) vs temperature of MAPbI₃ (with error bars) annealed with and without zinc metal under vacuum condition at 90, 95 and 100 °C
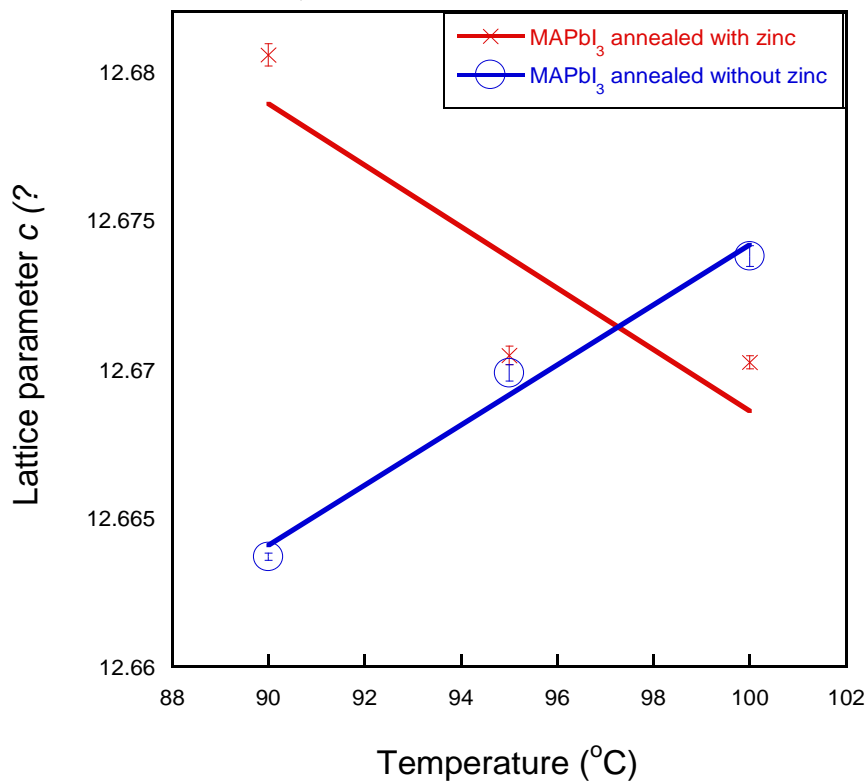
Figure 3.28 Lattice parameter *c* (Å) vs temperature of MAPbI₃ (with error bars) annealed with and without zinc metal under vacuum condition at 100 °C.
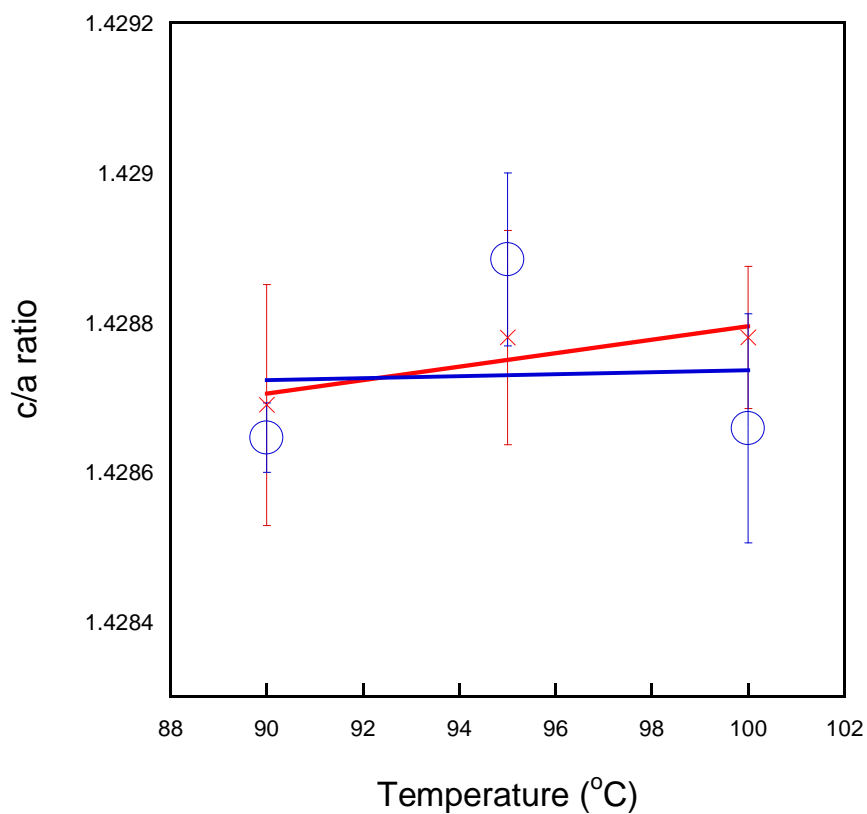
Figure 3.29 *c/a* ratio vs temperature of MAPbI$_3$ (with error bars) annealed with and without zinc metal under vacuum condition at 90, 95 and 100 ^{o}C

Figure 3.30 Volume (Å^3) of MAPbI$_3$ annealed with and without zinc metal under vacuum condition at 90, 95 and 100 ^{o}C
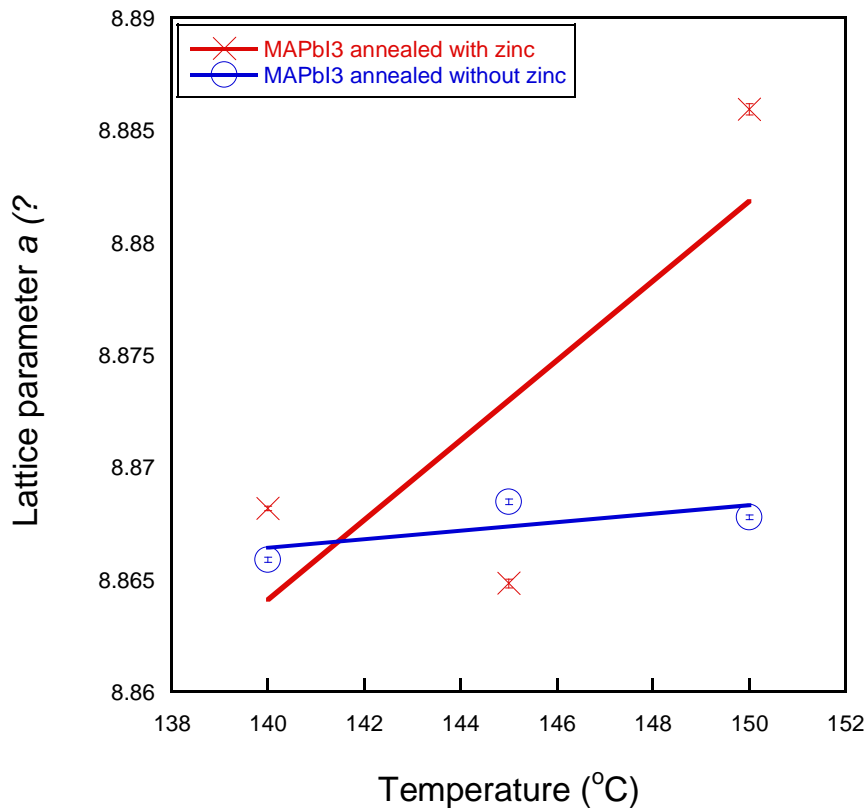
Figure 3.31 Lattice parameter *a* (Å) vs temperature of MAPbI₃ (with error bars) annealed with and without zinc metal under vacuum condition at 140, 145 and 150 ºC
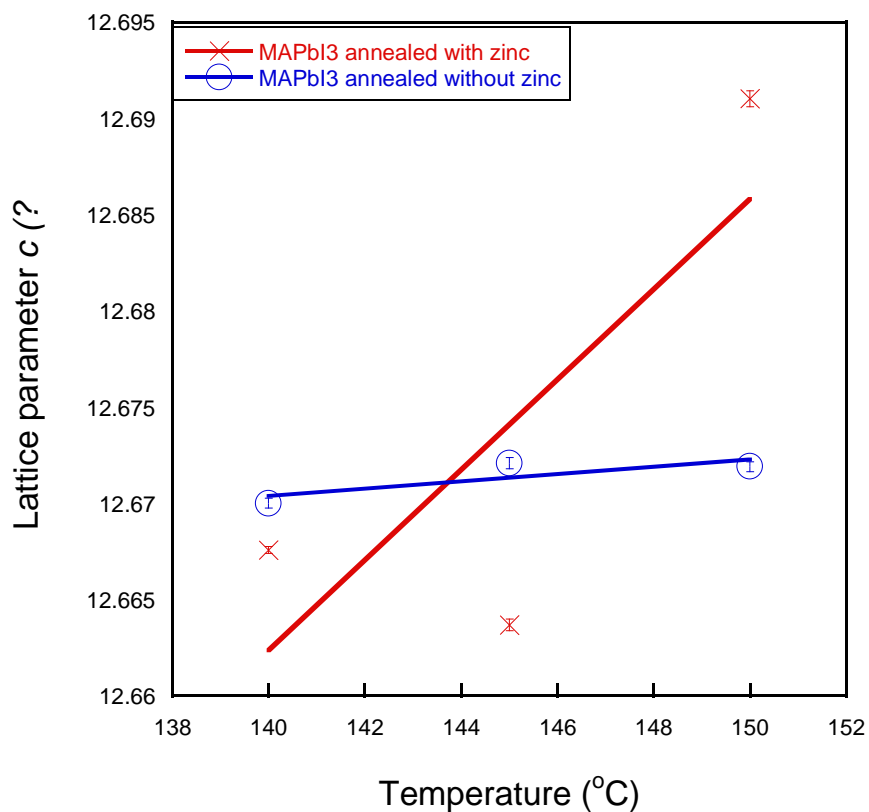
Figure 3.32 Lattice parameter *c* (Å) vs temperature of MAPbI₃ (with error bars) annealed with and without zinc metal under vacuum condition at 140, 145 and 150 ºC
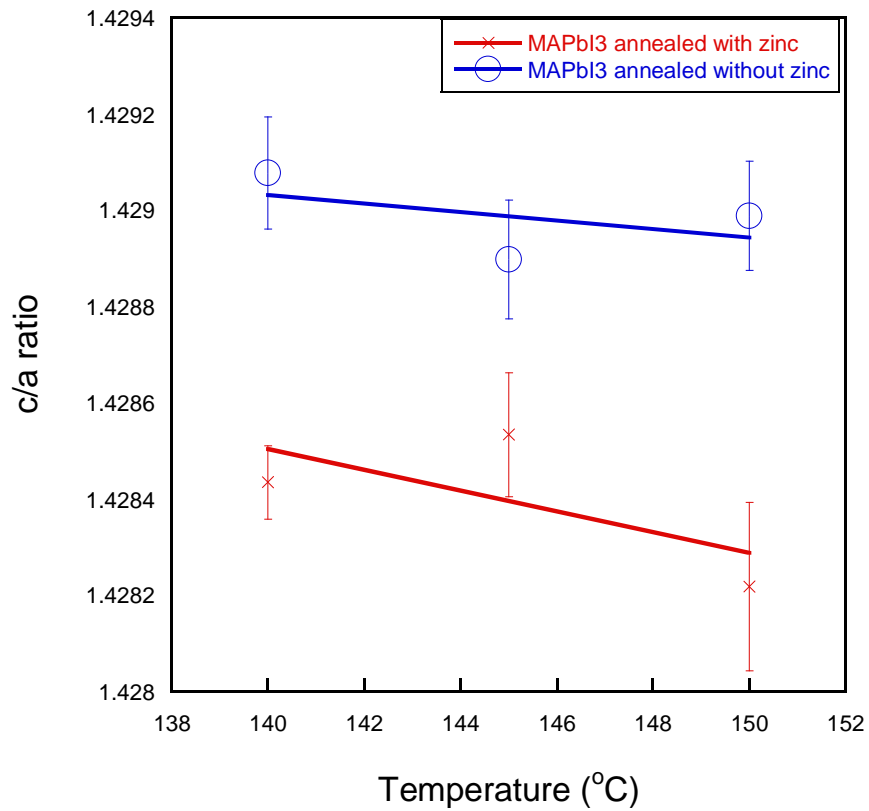
Figure 3.33 *c/a* ratio vs temperature of MAPbI$_3$ (with error bars) annealed with and without zinc metal under vacuum condition at 140, 145 and 150 °C
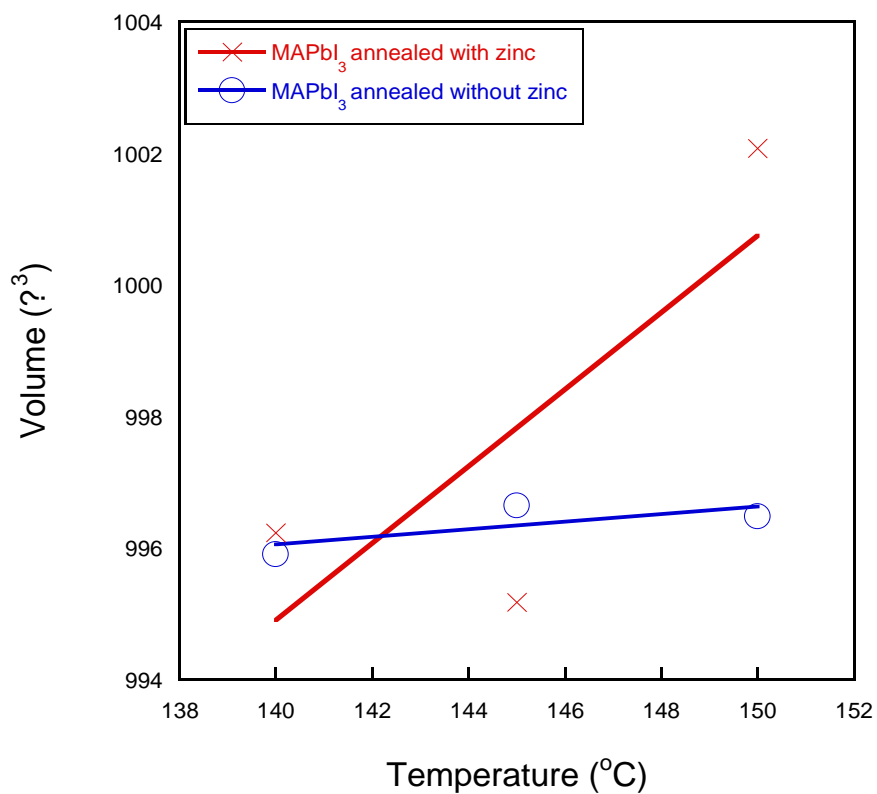
Figure 3.34 Volume (Å³) of MAPbI$_3$ annealed with and without zinc metal under vacuum condition at 140, 145 and 150 °C

3.3.0 Overall conclusion

In this project, MAPbI$_3$, the caesium doped MAPbI$_3$ (5 % and 10 %) were synthesised successfully with a solution-based method. The characterisation was performed with a combination of Rietveld refinement and profile matching method to obtain atomic positions and lattice parameters. Samples crystallised in their preferred orientation adds to the difficulties in refinement, characterisation was done by a comparison to XRD patterns of the published data.

Air annealing:

MPbI$_3$ are sensitive to temperature and moisture and this can be seen in the air annealed treatment. For compound 1, lattice parameter *a*, *c* of the crystals increases on annealing for 1 hour. The 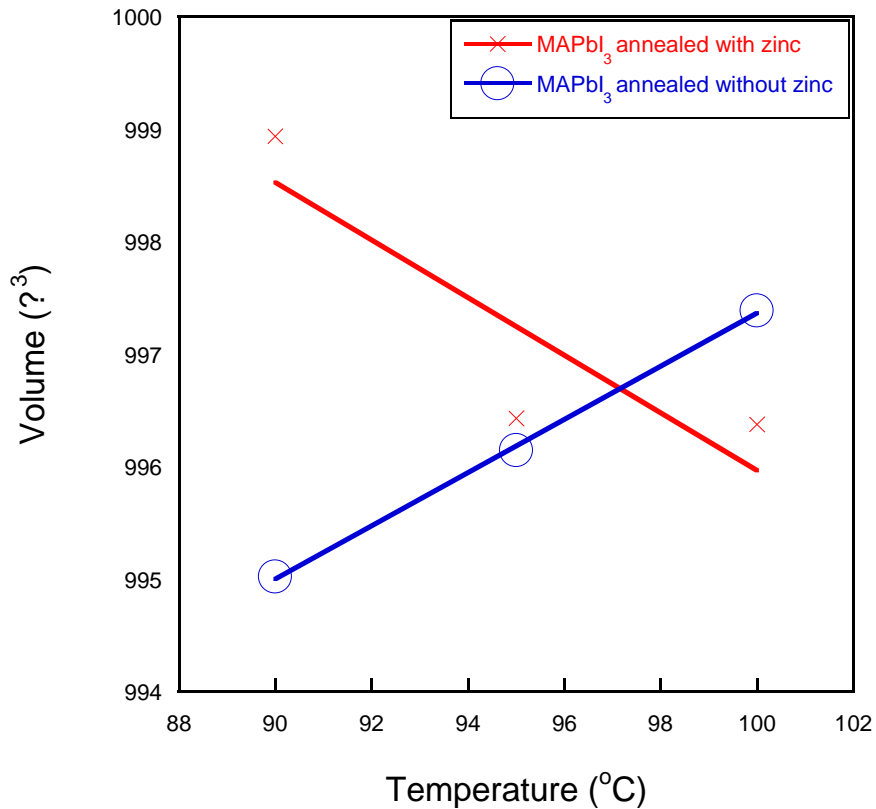same finding is also observed in the 3 hours annealing and is more significant, but little variation over different temperatures investigated. The changes in lattice *a* and *c* is lesser at higher temperatures. Overall, this gives a c/a ratio of the 1 hour annealing that is similar to 3 hour annealing, but much reduced for 1 hour particularly those annealed at higher temperatures.

In conclusion, annealing at 1 hour increases the lattice parameters and reduces the *c/a* ratio suggesting this treatment improves the packing within the hybrid perovskite framework and reduces disorder, which is enhanced on increasing temperature from 50 °C up to 110 °C. The increases in lattice parameters and the little variation in *c/a* ratio in the 3 hour annealing suggesting that the packing is changed but the sample retains certain degree of disorder.

Vacuum annealing:

Compound 1 was annealed at 90 °C for up to 73 hours. The changes in lattice parameters are positively correlated to temperature up to a certain point. Lattice parameter *a* increases up to around 5 hours in annealing, but subsequent heating reduces the lattice parameters down to a plateau around 40 hours after which it increases again. The same pattern is observed in Lattice parameter *c*, it increases up to around 5 hours, but subsequent heating reduces the lattice parameters down to a plateau around 40 hours after which it increases again. Overall, the c/a ratio and the volume also increase up to and before reaching the 5 hour scale, and slowly declines at around 40 hours leading to a smallest volume being recorded in this treatment.

In conclusion, heating at 90 °C up to around 5 hours under vacuum condition increases lattice parameters and hence their c/a ratio and volume, but subsequent heating possesses a negative effect in the lattice parameters up to 40 hours and the effect is reverted. This suggest that heating improves the packing within the hybrid perovskite, but it is inconsistent with temperature in this treatment.

Zinc annealing:

There is a sharp contrast in the lattice parameters in the MAPbI$_3$ samples annealed with and without zinc metal. For both lattice parameters *a* and *c*, an increase is observed in MAPbI$_3$ samples annealed without zinc which is consistent with the results from the air annealing and vacuum annealing experiment. However, the presence of Zn greatly reduces lattice parameter *a* across the temperature range investigated. This demonstrates the ability of zinc metal to act as a gettering reagent under this vacuum condition and control the perovskite's

composition. Interestingly, the results show that there is change in the *c/a* ratio of both treatments at all temperature. Overall, the volume is significantly reduced for the Zn annealing, as compared to being just in a vacuum. This demonstrated that annealing the perovskite in a gettering environment could be used to control the perovskite composition and thus the photovoltaic properties. Annealing at a higher temperature in vacuum leads to an increase in lattice parameters *a* and *c* respectively at both the zinc and without zinc treatments, with the c/a ratio remains subtle to no variation. These results indicate a signature of increased disorder as a result of thermal degradation of these samples.

In summary, these types of hybrid perovskites have enormous amount of flexibility in their structure and significant structural changes can be induced by simple annealing conditions that are likely to lead to different physical properties, such as photovoltaic efficiencies.

Chapter 4. Synthesis, structural characterisation of a new mixed valence iron (Fe^{2+}/Fe^{3+}) metal fluoride pyrochlores

4.1.0 Preparation of $RbFe_2F_6$:

A hydrothermal method was used to synthesise the mixed metal fluorides and characterised by powder and single crystal X-ray diffraction, neutron diffraction and magnetometry measurement.

In the synthesis, the molar quantity of each reagents was doubled compared to literature (1.14×10^{-3} moles of RbF, FeF_2 and FeF_3 respectively) [92] and the volume and molar quantity for solvents remained unchanged and the same experimental procedure was applied in all mixed metal fluoride synthesis.

RbF (0.238 g, 2.28×10^{-3} moles), FeF_2 (0.214 g, 2.28×10^{-3} moles) and FeF_3 (0.258 g, 2.28×10^{-3} moles) were put into an autoclave. In a fume cupboard, deionised water (5 mL) and trifluoro-acetic acid (3 mL) were slowly added to the powders. The autoclave was sealed and heated in an oven for 24 hours at 230 ^{o}C. The oven was turned off after 24 hours and slowly cooled to room temperature. The product was collected by washing with deionised water and dried overnight in a vacuum oven at 50 ^{o}C.

The balanced equations for the direct synthesis of $RbFe_2F_6$ is given below:

$$RbF + FeF_2 + FeF_3 \rightarrow RbFe_2F_6$$

4.1.1 Results and discussion

The products were analysed by powder X-ray diffraction and their patterns compared and matched with the Crystallography Open Database (COD) followed by plotting them with the Highscore software. All X-ray patterns presented in this work were first had their X-ray or neutron diffraction patterns refined by Rietveld refinement or profile matching to obtain the lattice parameters using Fullprof, only data with the least chi-squared number and in agreement with the published data retrieved from ICSD were used for further studies.

A total of eight $RbFe_2F_6$ samples were synthesised in two different batches with an average weight of 0.25 grams as a large quantity of sample was needed for neutron diffraction analysis.

4.1.2 Structural characterisation

Profile matching with constant scale factor was performed to all the $RbFe_2F_6$ samples to extract lattice parameters because of preferred orientation, no other data can be extracted, hence the neutron data will be used for structural parameters. $RbFe_2F_6$ has a characteristic double peak at 14.8^o (011) and 15.5^o (101), a triple peak of low intensity at 27.0^o (201), 28.6^o (121), and scattered peaks showing the diffraction from 35° onward to 150° along the 2θ Bragg's angle.

Figure 4.1 shows the powder neutron diffraction patterns obtained from the profile matching method for $RbFe_2F_6$ sample at 1.5 K. The observed characteristic peaks are at the lower angle 14.8 $^\circ$ (001), 17.5 $^\circ$ (002) and the triple peaks are at 25.6 $^\circ$ (200), 28.5 $^\circ$ (121) and 31.2 $^\circ$ (202), the observed patterns showed little difference to the calculated pattern. The lattice parameters *a, b* and *c* are 6.96557 Å, 7.43460 Å and 10.11603 Å respectively. This indicates that the crystals have grown into their preferred orientation and the synthesis is successful.
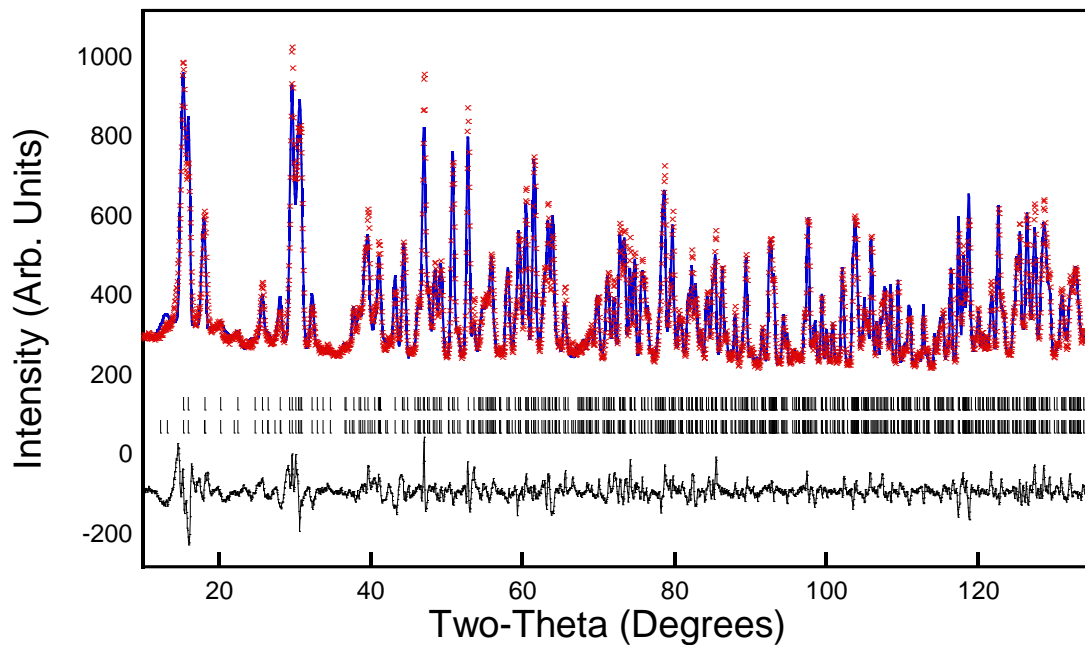

Figure 4.1 Observed (blue), calculated (red) and difference (black) data obtained from profile matching of neutron diffraction data of a representative $RbFe_2F_6$ sample at 1.5 K due to preferred orientation.

4.1.4 Single crystal diffraction analysis for structural characterisation

Since the hydrothermal synthesis is a good method to synthesise single crystals. Samples of $RbFe_2F_6$, $RbFeCrF_6$ and $RbFeCuF_6$ were selected for single crystal analysis. The crystal structures were solved and refined by the software AutoChem along with CrysAlis^{Pro}. However, purple and good quality $RbFeCuF_6$ single crystals were made and scanned, the result showed that the this was not a pyrochlore but pure CuF_2 crystals.

The $RbFe_2F_6$ product was brown coloured rod-shaped crystal and a fine grain of crystal was selected to perform a single crystal diffraction analysis. The identification of the $RbFe_2F_6$ was first confirmed by the visual observation with a microscope and the profile matching with constant scale factor. The crystallographic data retrieved using powder X-ray diffractometer and single crystal diffractometer showed that; the representative single crystal structure of synthetic $RbFe_2F_6$ sample has a *Pnma* space group, an orthorhombic crystal system and lattice parameters a = 7.0183 Å, b = 7.4447 Å and c = 10.1678 Å which show little variation to the crystallographic data published by ICSD and it is illustrated in table 2. The crystal structure of the synthetic $RbFe_2F_6$ is shown in Figure 4.2 [93]. The iron octahedra are positioned along the x and z-axis direction. Figure 4.3 shows the published crystal structure of the $RbFe_2F_6$ structure. In contrast, the synthetic sample shows variation in the positions of atoms within the framework, this could be a result of errors in the original cif file and revision is needed in future works.

Parameter	$RbFe_2F_6$ (synthetic)	$RbFe_2F_6$ (database)
Formula weight (g)	311.15	311.15
Chemical formula	Fe_8 $Rb_{4.03}$ F_{24}	Fe_2 Rb F_6
Display formula	Fe_{16} $Rb_{4.03}$ F_{24}	Fe_{19} Rb_4 F_{24}
Space group	*P n m a*	*P n m a*
Crystal system	Orthorhombic	Orthorhombic
Lattice parameter *a*	7.0183 Å	6.9663 Å
Lattice parameter *b*	7.4447 Å	7.4390 Å
Lattice parameter *c*	10.1678 Å	10.1216 Å
Asymmetric unit	7 sites	7 sites
Site density	0.0678 sites/Å³	0.0686 sites/Å³
Visible atoms	44	47
Cell volume	531.259 Å³	524.529 Å³
Density	3.8991 g/cm³	3.9404 g/cm³

Table 2. Crystallographic data of synthetic $RbFe_2CrF_6$ and published data of $RbFe_2CrF_6$ from ICSD.
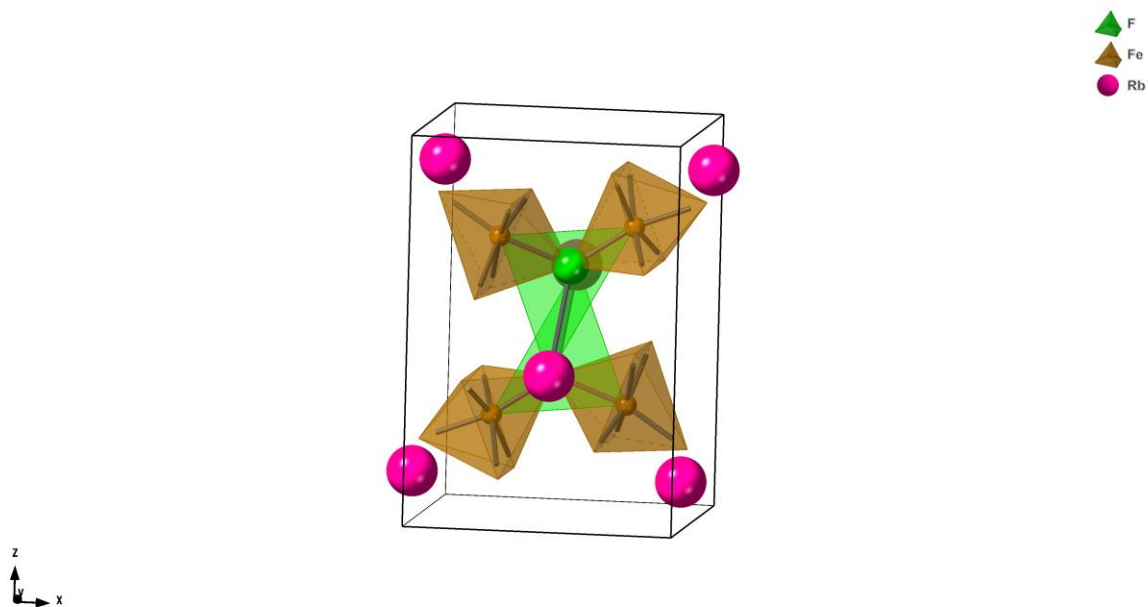
Figure 4.2 Ball-and-stick and polyhedral representations of the synthetic $RbFe_2F_6$ in the xz-plane obtained from AutoChem along with CrysAlisPro.
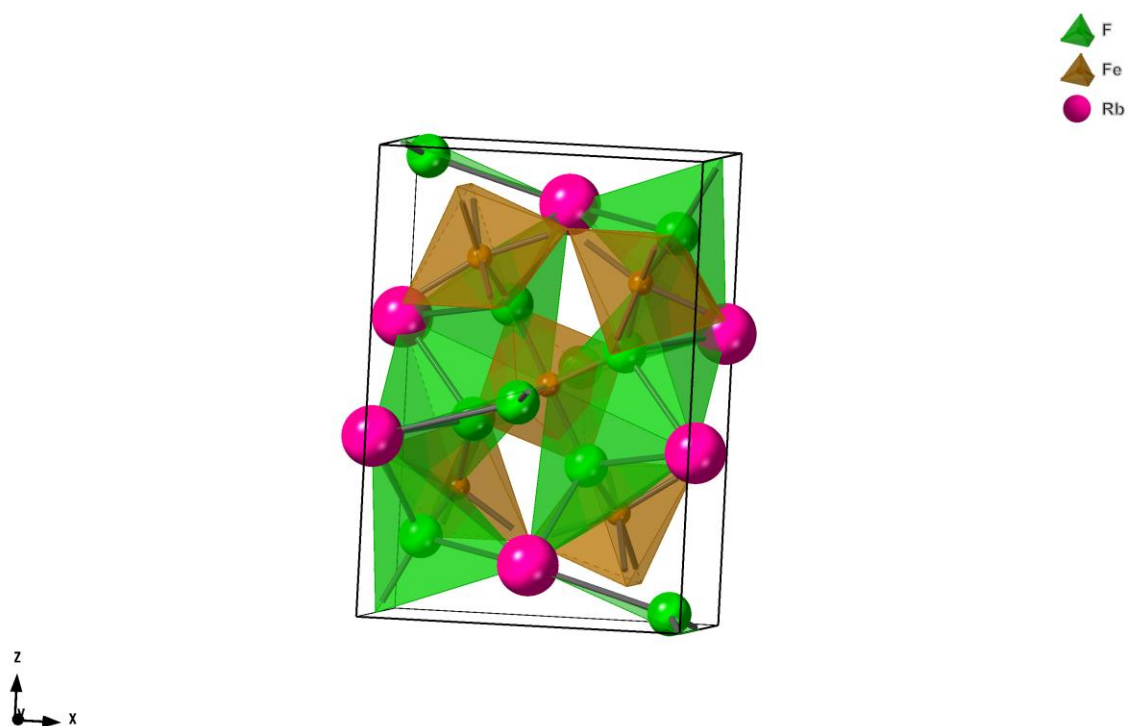

Figure 4.3 Ball-and-stick and polyhedral representations of the published $RbFe_2F_6$ in the xz-plane obtained from ICSD [94].

4.1.5 Neutron diffraction analysis by D2B - High-resolution two-axis diffractometer

Powder neutron diffraction was performed on the D2B High-resolution two-axis diffractometer at ILL (Institut Laue–Langevin) for magnetic structure determination. The scan was performed using a Germanium (335) monochromator at λ = 1.594 Å. Measurements were done in a cryostat from 1.5 K to 100 K, and at room temperature (298 K) on $RbFe_2F_6$ [75].

The $RbFe_2F_6$ sample was first scanned at room temperature to investigate the nuclear structure. $RbFe_2F_6$ carries iron cations of two different charges Fe^{2+} and Fe^{3+}. The partially filled d shells of these cations generates magnetic ordering through interactions with the magnetic dipole moment they produced. The experiment was carried out by scanning the sample at a very low temperature from 1.5 K to 100 K to detect diffraction peaks from low to very high Braggs angle (0° to 160°).

When scanned at room temperature (298 K) (Figure 4.5), the characteristic neutron scattering peaks for $RbFe_2F_6$ are outstanding at the low Bragg angle 15.1° (011) and 29.7° (121). The peaks remain as consistently sharp and low intensity up to 160° (484) along the Bragg angle. Magnetic ordering diffraction is observed below T_N = 16 K and this is shown as the characteristic double peak at 15° (011) and 18.7° (011) for $RbFe_2F_6$ [94]. When scanned at temperatures below 16 K, this characteristic double peak appears at 15° (011) and 18.7° (011) and a sharp, high intensity peaks appeared at 151° (440) along with diffused scatterings. The occurrence of new peaks with high intensity is an indication of magnetic ordering and these peaks are referred to as the magnetic Bragg peaks.

The magnetic ordering diffractions are being observed at lower temperatures starting from 1.5 K to 100 K and showed similar neutron diffraction pattern to $RbFe_2F_6$ scanned at 1.5 K, therefore only a representative Rietveld refinement pattern is showed (Figure 4.4). The two sets of tick marks correspond to the nuclear and magnetic structure.

In addition, a steady consistency in diffraction patterns are found in all the scanned samples (neutron patterns for all temperature range investigated in Appendix 2) i.e. double peak at 15° (011) and 18.7° (011) and the high intensity peak at around 150° (440). However, when the temperature was increase to 17.5 K (Appendix 2). The double peak disappeared at and left alone the single peak at 15.1° (011) which resembles the pattern of $RbFe_2F_6$ scanned at room temperature, and the peak at higher Bragg angle remains constant with increasing temperature [92].

Analysis of the magnetic structure at 1.5 K, shown in Figure 4.4 confirmed the previously published structure. The previous structure was determined at above 10 K, and from recent inelastic neutron scattering subtle changes in the magnetic dynamics was observed below 10 K. However, this work has demonstrated that the average magnetic structure remains the unchanged down to 1.5 K [95].

Figure 4.4 Observed (blue), calculated (red) and difference (black) data obtained from Rietveld refinements of neutron diffraction data of a RbFe$_2$F$_6$ sample scanned at 1.5 K. The two sets of tick marks correspond to the nuclear and magnetic structures.
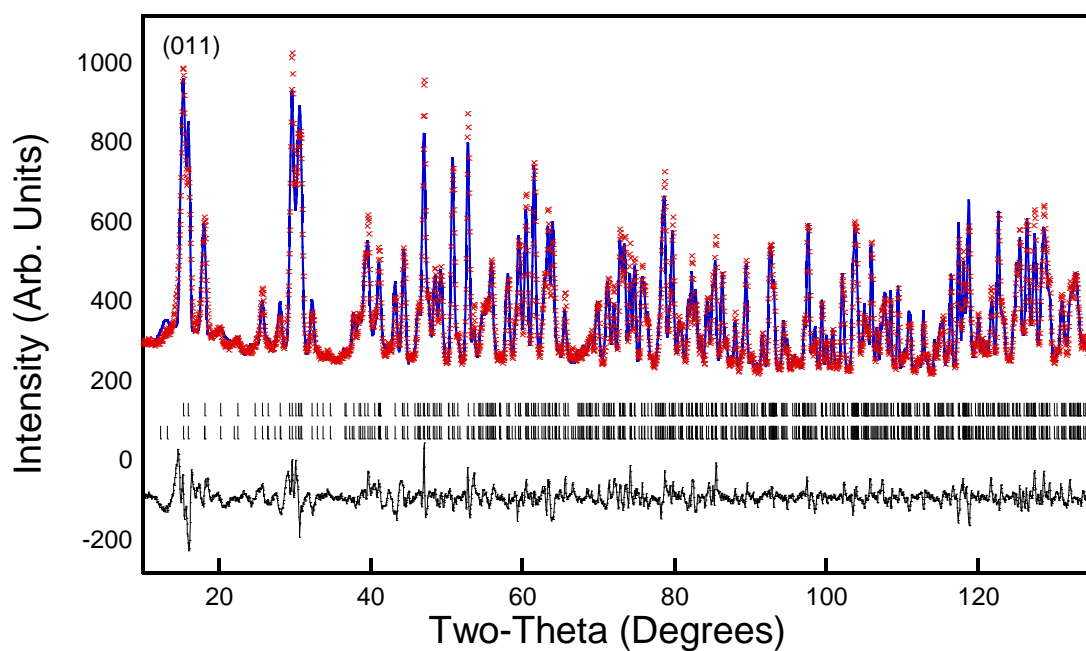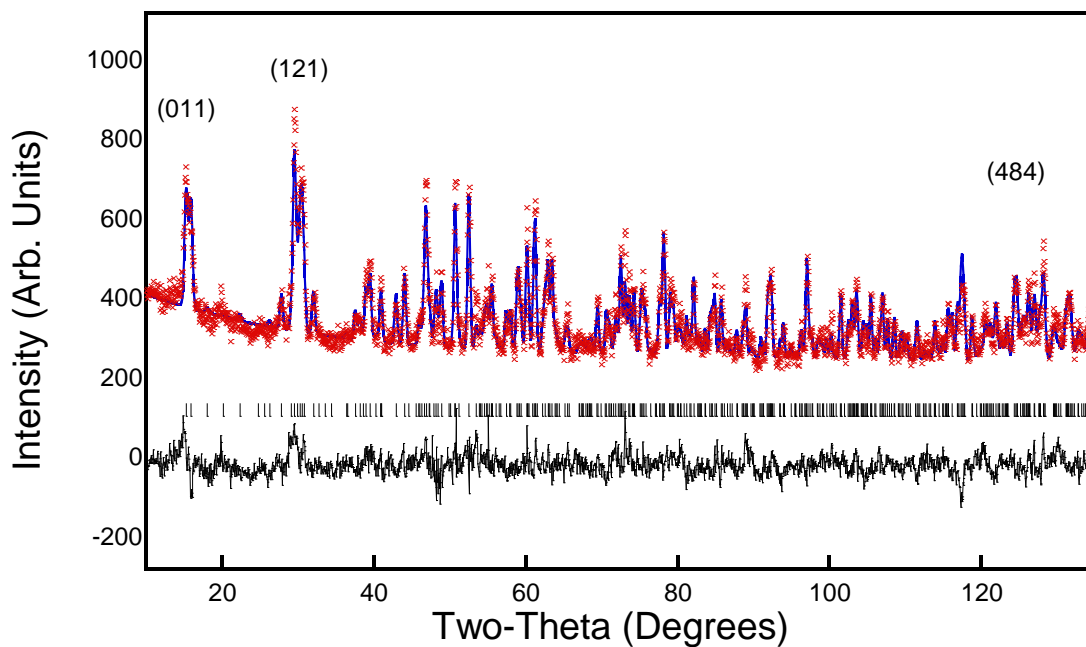

Figure 4.5 Observed (blue), calculated(red) and difference(black) data obtained from Reitveld refinement of neutron diffraction data of a RbFe$_2$F$_6$ sample scanned at room temperature (298 K)

4.2.0 RbFeCrF$_6$

The synthesis of RbFeCrF$_6$ was done with a hydrothermal method using dilute trifluoro-acetic acid and the expected chemical equation is as below:

$$RbF + FeF_2 + CrF_3.3H_2O \rightarrow RbFeCrF_6 + 3H_2O$$
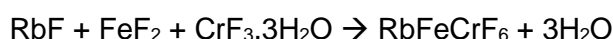
4.2.1 Experimental procedure

RbF (0.238 g, 2.28x10^{-3} mol), CrF$_3$.3H$_2$O (0.3032 g, 2.28 x 10^{-3} mol) and FeF$_2$ (0.214 g, 2.28 x 10^{-3} mol) were put into an autoclave. In a fume cupboard, deionised water (5 mL) and trifluoro-acetic acid (3 mL) were slowly added to the powders. The autoclave was sealed and heated in an oven for 24 hours at 230 ^{o}C [92].

The oven was turned off after 24 hours and slowly cool to room temperature. The product was collected by washing with deionised water.

4.2.2 Single crystal diffraction analysis for structural characterisation

A sample of RbFeCrF$_6$ was chosen to perform a single crystal diffraction analysis for structural identification using Rigaku Oxford Supernova diffractometer, and refinement were done using the self-built-in software AutoChem along with CrysAlisPro. As no published data of RbFeCrF$_6$ can be found on the ICSD database, two assumptions for the crystal structure characterisation were made and RbFeCrF$_6$ can be either having the same crystallographic information as CsFeCrF$_6$ which is cubic with lattice parameters a, b and c = 10.4000 Å with *Fd̄3m* space group. Alternatively, it might have an orthorhombic structure (similar to RbFe$_2$F$_6$) with lattice parameters a = 6.9663 Å, b = 7.4390 Å and c = 10.1216 Å.

When scanned at low temperature (100 K and 300 K), the crystal structure of RbFeCrF$_6$ is showed in Figure 4.6 (at 300 K) indicate that the synthetic sample has an corner-shared Fe ion separated by Cr in the centre of the orthorhombic structure. The experimental crystallographic data of RbFeCrF$_6$ at 100 K and 300 K can be seen in Table 3. The figure of the crystal structure of RbFeCrF$_6$ scanned at 100 K is omitted due to errors presented in the original cif file and difficulties in refinement.

However, the project was aimed to synthesise RbFeCrF$_6$, according to the RbFeCrF$_6$ (100 K) single crystal diffraction data, a new composition RbFe$_{1.3}$Cr$_{0.7}$F$_6$ is formed and crystallographic data is showed in Table 4, where the site occupancies showed that Cr: 0.7 and Fe: 0.3 in the Cr position, the lattice parameters obtained are a = 6.9970(4) Å, b = 7.3397(5) Å and c = 10.1081(7) Å (Full structure data can be viewed in Appendix 2).

The crystallographic data of RbFeCrF6 at 300 K are showed in Table 5, the sample has displayed an orthorhombic structure and with lattice parameters a = 7.0474(6) Å, b = 7.3482(7) Å and c = 10.1591(9) Å. (Full structure data can be viewed in Appendix 2).

Based on the single crystal data obtained from AutoChem/CrysAlisPro, a conclusion can be drawn that a new composition of RbFe$_{1.3}$Cr$_{0.7}$F$_6$ is formed and appeared at 100 K; it crystallised in the orthorhombic structure with *Pnma* space group, the lattice parameters are a = 6.9970(4) Å, b = 7.3397(5) Å and c = 10.1081(7) Å. These data suggests that this mixed metal fluoride compound RbFeCrF$_6$ would show magnetic moments and have magnetic frustration arise from the interactions of iron and chromium ions when scanned at low temperature as opposed to RbFe$_2$F$_6$ that have been extensively studied and proved to contain magnetic ordering. However, there are still doubts over the structure and composition of this synthetic sample as the position of chromium and iron cations seem to

be occupying different sites along the octahedral framework and more work is needed for structural characterisation.

Name of compound	$RbFe_{1.3}Cr_{0.7}F_6$ at 100 k	$RbFe_{1.3}Cr_{0.7}F_6$ at 300 k
Formula weight (g)	307.30	307.30
Chemical formula	$Cr_{2.8}Fe_{5.2}Rb_4F_{24}$	$Cr\,Fe\,Rb\,F_6$
Display formula	$Cr_{8.4}Fe_{7.6}Rb_4F_{24}$	$Cr_{15}Fe_4Rb_4F_{24}$
Space group	*Pnma*	*Pnma*
Crystal system	Orthorhombic	Orthorhombic
a	6.9970 Å	7.0474 Å
b	7.3397 Å	7.3482 Å
C	10.1081 Å	10.1591 Å
Asymmetric unit	7 sites	7 sites
Unit cell	36 sites per unit cell	36 sites per unit cell
Site density	0.0693 sites/Å³	0.0684 sites/Å³
Visible atoms	44	47
Cell volume	519.110 Å³	526.096 Å³
Density	3.9471 g/cm³	3.8801 g/cm³

Table 3. Crystallographic data of the synthetic $RbFe_{1.3}Cr_{0.7}F_6$ samples at 100 K and 300 K retrieved from Crystal Diffract software

Atom	Site	Occupancy	Atomic positions		
			x	*y*	*z*
F	F004	F: 1.0	0.2632(3)	0.5626(3)	0.0815(2)
F	F005	F: 1.0	0.6268(3)	0.5110(3)	0.0815(2)
F	F006	F: 1.0	0.4369(4)	0.7500(0)	0.1659(2)
F	F007	F: 1.0	0.4346(4)	0.2500(0)	0.3397(3)
Fe	Fe02	Fe: 1.0	0.2049(1)	0.7500(0)	0.0370(3)
Cr	Fe03	Cr: 0.7 Fe: 0.3	0.5000(0)	0.5000(0)	0.2318(1)
Rb	Rb01	Rb: 1.0	0.5094(1)	0.7500(0)	0.0000(0)

Table 4. The fractional coordinates (atomic positions and site occupancies) of $RbFeCrF_6$ sample at 100 K obtained from AutoChem along with CrysAlisPro of single crystal diffraction data. The lattice parameters were determined to be 6.9970 Å, 7.3397 Å and 10.1081 Å.

			Atomic positions		
Atom	Site	Occupancy	x	y	z
Cr	Cr03	Cr: 1.0	0.5000(0)	0.5000(0)	0.5000(0)
F	F004	F: 1.0	0.2676(4)	0.5617(3)	0.5849(3)
F	F005	F: 1.0	0.5595(6)	0.7500(0)	0.4622(4)
F	F006	F: 1.0	0.4402(6)	0.7500(0)	0.8379(4)
F	F007	F: 1.0	0.3691(4)	0.4871(4)	0.3366(3)
Fe	Fe02	Fe: 1.0	0.2078(1)	0.7500(0)	0.7330(1)
Rb	Rb01	Rb: 1.0	0.5105(1)	0.7500(0)	1.1234(1)

Table 5. The fractional coordinates (atomic positions and site occupancies) of RbFeCrF$_6$ sample at 300 K obtained from AutoChem along with CrysAlisPro of single crystal diffraction data. The lattice parameters were determined to be 7.0474 Å, 7.3482 Å and 10.1591 Å.
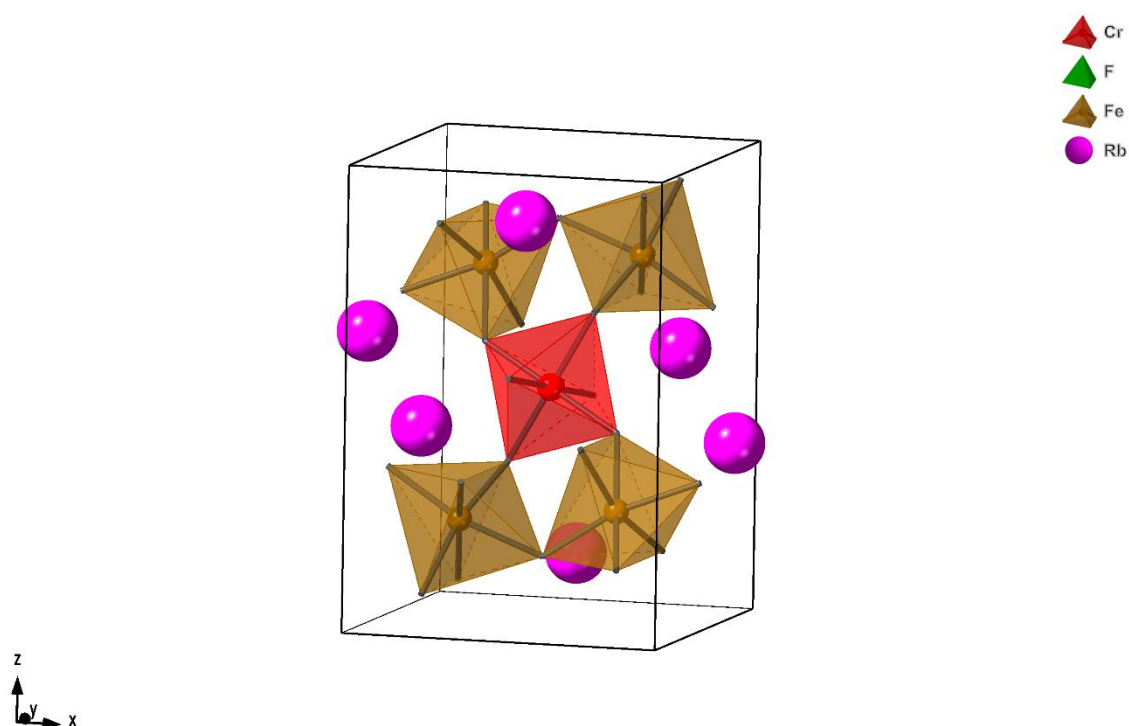

Figure 4.6 The crystal structure of RbFe$_{1.3}$Cr$_{0.7}$F$_6$ treated at 300 K with and data was retrieved from AutoChem along with CrysAlisPro.

4.2.3 Powder X-ray diffraction analysis for structural characterisation

Due to the lack of official published data and difficulties in Rietveld refinement caused by the synthetic structures, all the conclusion and evaluation for the structural determination are based on comparison plots and neutron diffraction data.

More samples of $RbFeCrF_6$ compounds were synthesised and all were scanned by powder X-ray analysis. The samples showed variable structures and impurities are also created during synthesis. As previous discussed, a single crystal sample of $RbFeCrF_6$ was proved by an orthorhombic structure with *Pnma* space group similar to $RbFe_2F_6$. The structural identification is being backed up by the comparison of powder X-ray diffraction patterns. However, the possibility of $RbFeCrF_6$ samples to grow into the expected structure is completely random. Figure 4.7 shows a comparison plot of two representative $RbFeCrF_6$ samples with $CsFeCrF_6$ (cubic) and RbFe2F6 (orthorhombic). One sample of $RbFeCrF_6$ (red) has grown into the orthorhombic structure and this can be proved by the occurrence of the emerge of a peak at 14.8 ° (011) and a micro peak at 15.5 ° (101). The occurrence of the characteristic peaks to confirm the orthorhombic identity are found in 28.7° (121), 29.9 ° (211) and 45.6 ° (033). Therefore, this sample has crystallised in an orthorhombic structure with *Pnma* space group but in its preferred orientation. In contrast, when it is compared to the X-ray pattern of $CsFeCrF_6$, the peak at 45.0 ° (333) suggests the occupancy of chromium ions in this sample. Another representative $RbFeCrF_6$ sample (green) is also compared, the occurrence of the tiny single peak at 14.8 ° (011) suggests the cubic structural features, and two peaks observed at 45.0 ° (330) and at 70.0 ° (137). The sample seems to be impure since the diffraction intensity is low throughout

In conclusion, since these X-ray diffraction patterns were compared with the published data of $RbFe_2F_6$ with an orthorhombic structure as well as $CsFeCrF_6$ with cubic structure. Both visual observations showed significant similarity in diffraction patterns. Therefore, there are two possibility of the structural formation. Firstly, a successful synthesis will produce a $RbFeCrF_6$ compound with both the chromium and iron cations co-occupying the same site in the octahedral framework. The single crystal diffraction results has partially proved this hypothesis, and occupation of iron and chromium is detected in the single crystal diffraction data (Table 3 and 4) as the lattice parameters a, b and c are slightly different from the $RbFe_2F_6$ samples, and a cubic phase is observed in the bulk powder sample. Secondly, the synthetic sample is a pure $RbFe_2F_6$ crystal without the occupancy of chromium. However, repeated experiments and a more detail refinement are needed to make the desirable $RbFeCrF_6$ crystal and for an accurate structural characterisation.
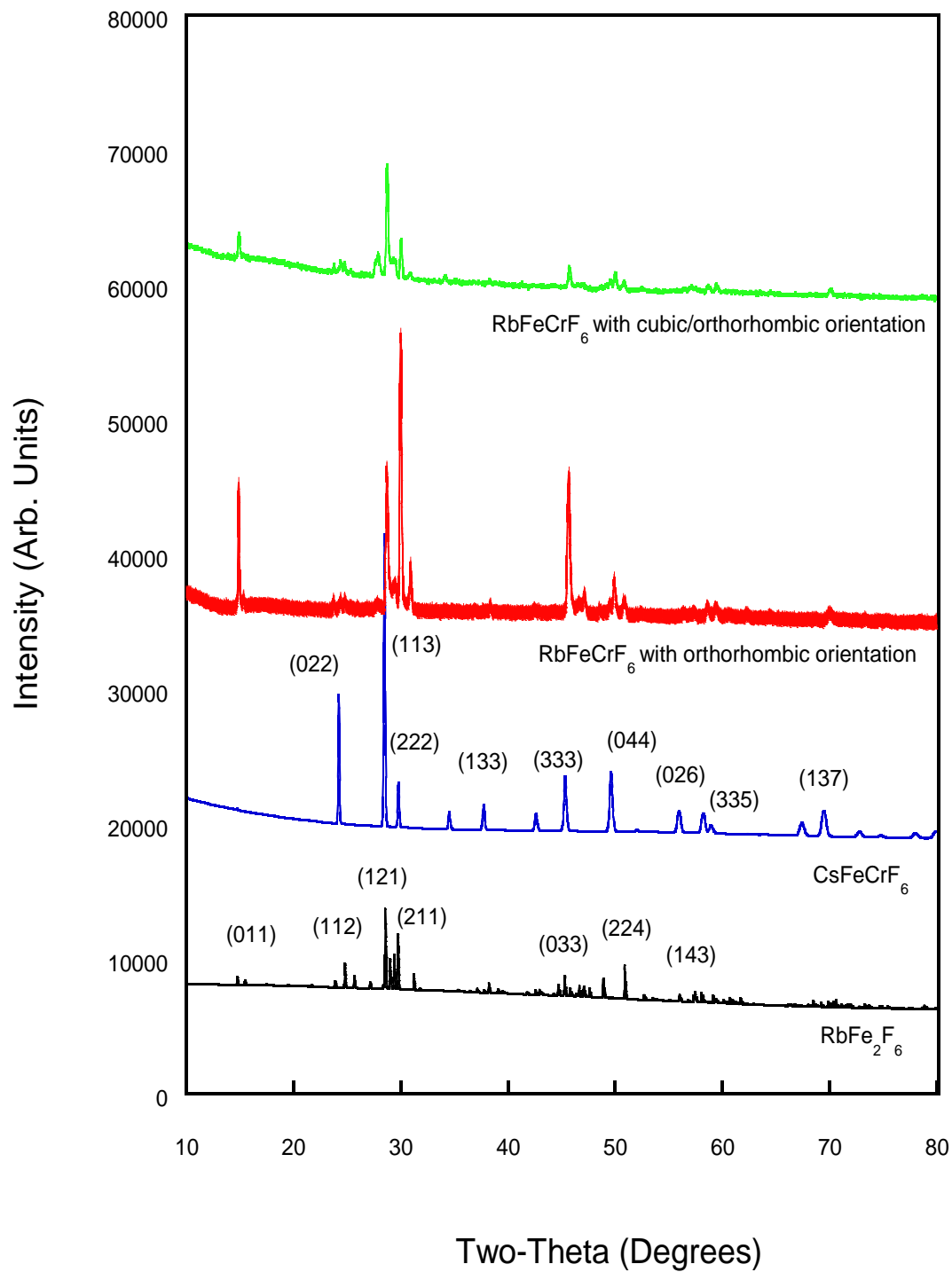
Figure 4.7 A comparison plot of the powder x-ray diffraction pattern of $RbFe_2F_6$, $CsFeCrF_6$, $RbFeCrF_6$ with orthorhombic orientation and $RbFeCrF_6$ with orthorhombic/cubic orientation.

4.2.4 Neutron diffraction analysis for magnetic ordering

Two sets of samples were used to perform a neutron diffraction analysis. RbFeCrF$_6$ compound with orthorhombic structure was scanned at both 1.5 K and at room temperature (298 K). The compound with cubic/orthorhombic structure was scanned at room temperature (298 K) only.

A comparison plot of the neutron diffraction pattern of RbFeCrF$_6$ sample with orthorhombic structure and with cubic/orthorhombic structure is showed in Figure 4.8. When scanned at 1.5 K, RbFeCrF$_6$ showed no magnetic ordering (double peak at 15 ° (011) and 18.7 ° (011)) as the diffraction patterns remain unchanged and overlapping with the characteristic peaks to its corresponding X-ray diffraction pattern (Figure 4.7). The RbFeCrF$_6$ sample with cubic/orthorhombic structure stays in its preferred orientation and showed similar diffraction patterns to the orthorhombic sample at 15.3 ° (011), 29.9° (211) and diffused scattering patterns are found at higher (above 80 °) 2θ Bragg angles, showing short-ranged ordering. In conclusion, no magnetic ordering is found in the two RbFeCrF$_6$ compounds being scanned over the temperature range investigated.
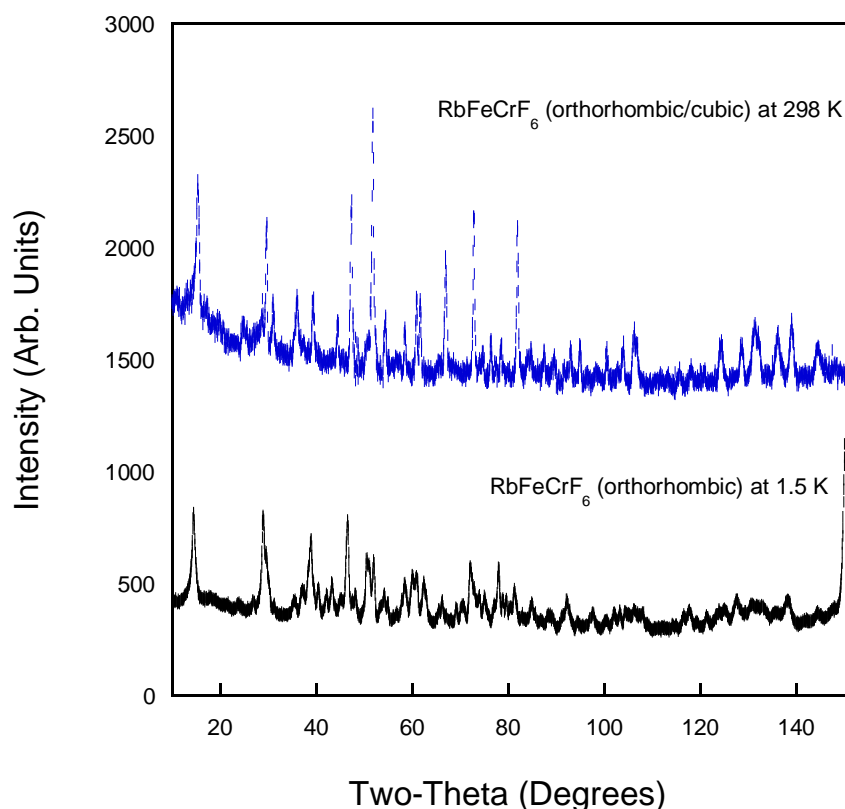

Figure 4.8 A comparison plot of experimental neutron patterns of a RbFeCrF$_6$ sample with orthorhombic orientation scanned at 1.5 K and a RbFeCrF$_6$ sample with orthorhombic/cubic orientation scanned at room temperature (298 K).

4.1.6 SQUID magnetometry

SQUID measurements were taken at two different temperature ranges to check for signs of magnetisation for the $RbFe_{1.3}Cr_{0.7}F_6$ sample. When it was measured at 1000 Oe from 2 to 80 K under ZFC/FC, difference is observed below 15 K, with 0.73 χ/H at FC and 0.54 χ/H at 0 K (shown in Figure 4.9). When it was measured at 100 Oe from 2 to 300 K under ZFC/FC. Diversion is observed below 50 K, that it has a magnetic transition at 20 K, with the greatest divergence observed in magnetic moments between zero field cooled and field cooled magnetic susceptibility; 0.03 χ/H in ZFC and 0.12 χ/H in FC which is shown in Figure 4.10.
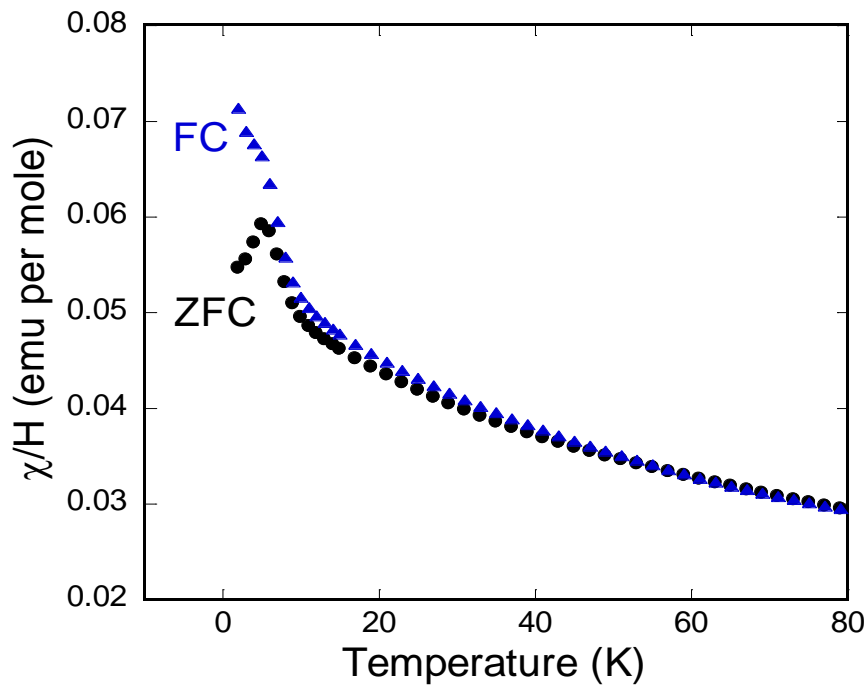

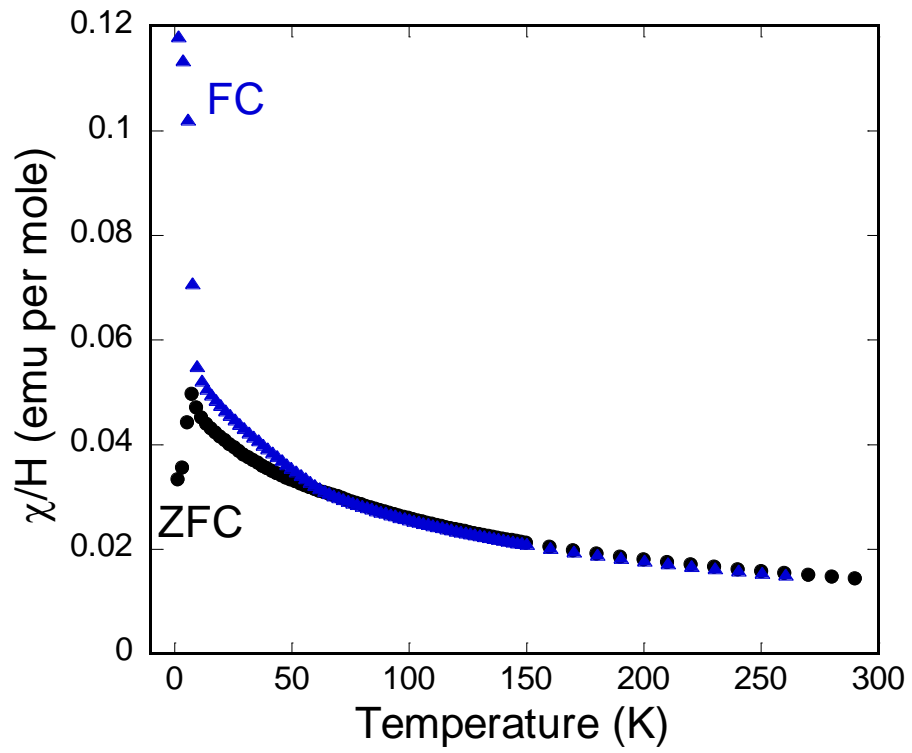Figure 4.9 FC (blue), ZFC (black) of SQUID moment plots of $RbFeCrF_6$ measured at 1000 Oe from 2 to 80 K under ZFC/FC.

Figure 4.10 FC (blue), ZFC (black) of SQUID moment plots of RbFeCrF$_6$ measured at 100 Oe from 2 to 300 K under ZFC/FC.

4.3.0 RbFeZnF$_6$

Synthesis of four pyrochlore samples RbFeZnF$_6$ with a hydrothermal method using dilute trifluoro-acetic acid, the expected chemical equation is as below:

$$RbF + ZnF_2 + FeF_3 \rightarrow RbFeZnF_6$$
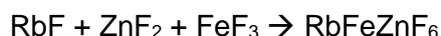
4.3.1 Experimental procedure

RbF (0.238 g, 2.28 x 10^{-3} mol), ZnF$_2$ (0.2360 g, 2.28 x 10^{-3} mol) and FeF$_3$ (0.258 g, 2.28 x 10^{-3} mol) were put into an autoclave. In a fume cupboard, deionised water (5 mL) and trifluoro-acetic acid (3 mL) were slowly added to the powders. The autoclave was sealed and heated in an oven for 24 hours at 230 °C [92].

The oven was turned off after 24 hours and slowly cool to room temperature. The product was collected by washing with deionised water.

4.3.2 X-ray diffraction analysis for structural characterisation

Due to difficulties in Rietveld refinement, The structural characterisation was done by comparison (Figure 4.11) with a published RbFe$_2$F$_6$ data with orthorhombic structure (*Pnma* space group) and a published data of CsFeZnF$_6$ with cubic (*Fd$\bar{3}$m* space group). This RbFeZnF$_6$ sample shows the characteristic double peak at 14.5 ° and 15.2 ° (011), and diffractions are observed at (112), (121), (033), (224) and (143) which are similar to the diffraction pattern of RbFe$_2$F$_6$. When compared to the CsFeZnF$_6$ X-ray pattern, sharp peaks are observed at 24.1 ° (022), 28.4 ° (113), 29.7 ° (222), 45.2 ° (333) and 49.4 (044). The assumptions made from this comparison plots are, this synthetic sample exhibits certain cubic/orthorhombic features, and zinc is incorporated into this mixed metal composition. However, the sample appears to contain impurities which is denoted by the reduction in peak intensity at (333) and (044). However, a more detailed refinement is needed to obtain crystallographic data such as atomic positions and lattice parameters to confirm the successfulness of the synthesis.
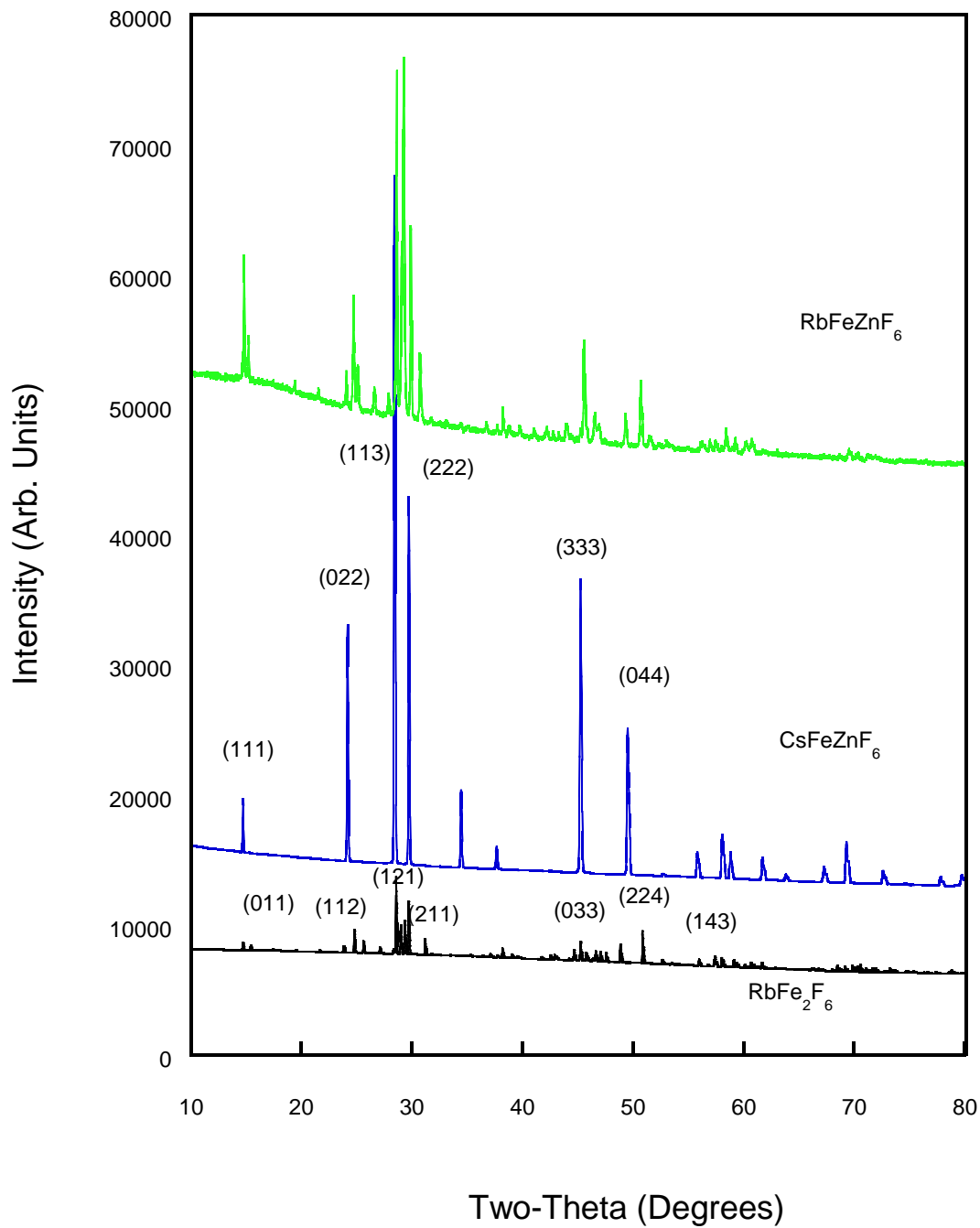
Figure 4.11 A comparison plot of the powder X-ray diffraction pattern of CsFeZnF$_6$, CsFeZnF$_6$ and RbFeZnF$_6$.

4.3.3 Neutron diffraction analysis for magnetic ordering

Due to the limited quantity and difficulties in Rietveld refinement for structural characterisation, only a room temperature scan was performed for the $RbFeZnF_6$ sample powders for 70 minutes to get an initial framework of the neutron diffraction patterns. Magnetic ordering is generally observed at a low temperature below $T_N = 16$ K, but this sample only shows two characteristic peaks at 15.3 $^{\circ}$ (011), 29.9° (211). No data for magnetic moments can be drawn from this neutron scan and the neutron data is shown in Figure 4.12.
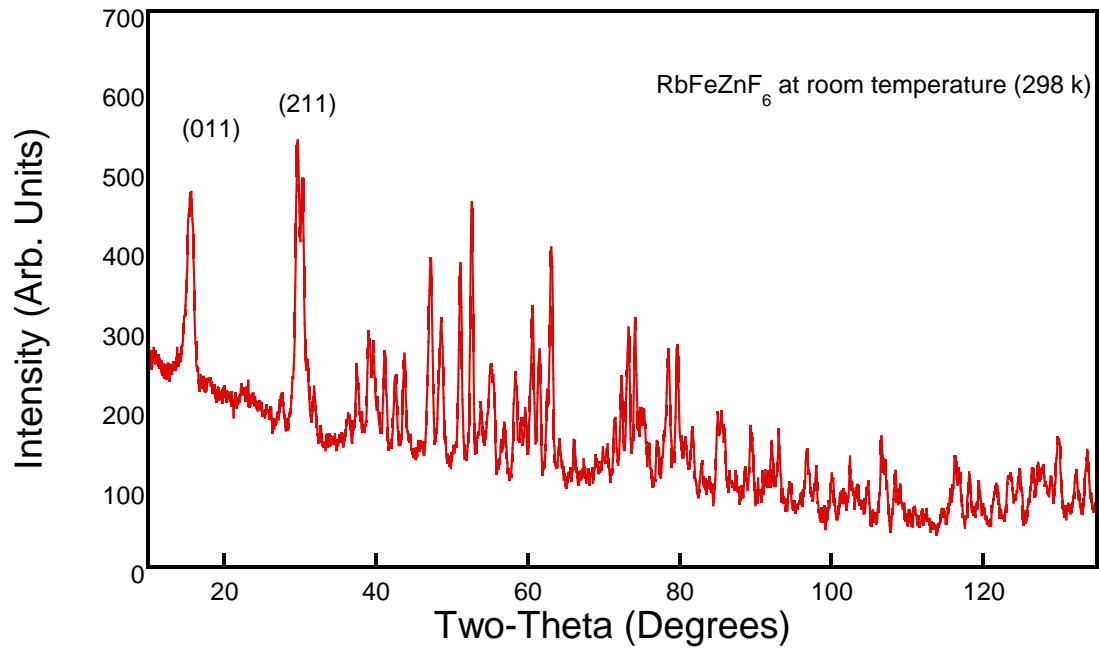
Figure 4.12 Neutron diffraction pattern of $RbFeZnF_6$ at room temperature (298 K).

4.3.4 SQUID magnetometry

SQUID measurements were taken to measure magnetic moments in $RbFeZnF_6$ at 1000 Oe from 2 to 80 K under ZFC/FC (shown in Figure 4.13). No diversion is observed at the temperature range investigated. However, Curie-Weiss behaviour is observed down to 2 K.

This indicates there is weak magnetic moment in this $RbFeZnF_6$ sample upon cooling, which is a sign of the liquid spins are trying to be more ordered at lower temperatures, leading to a glass state.
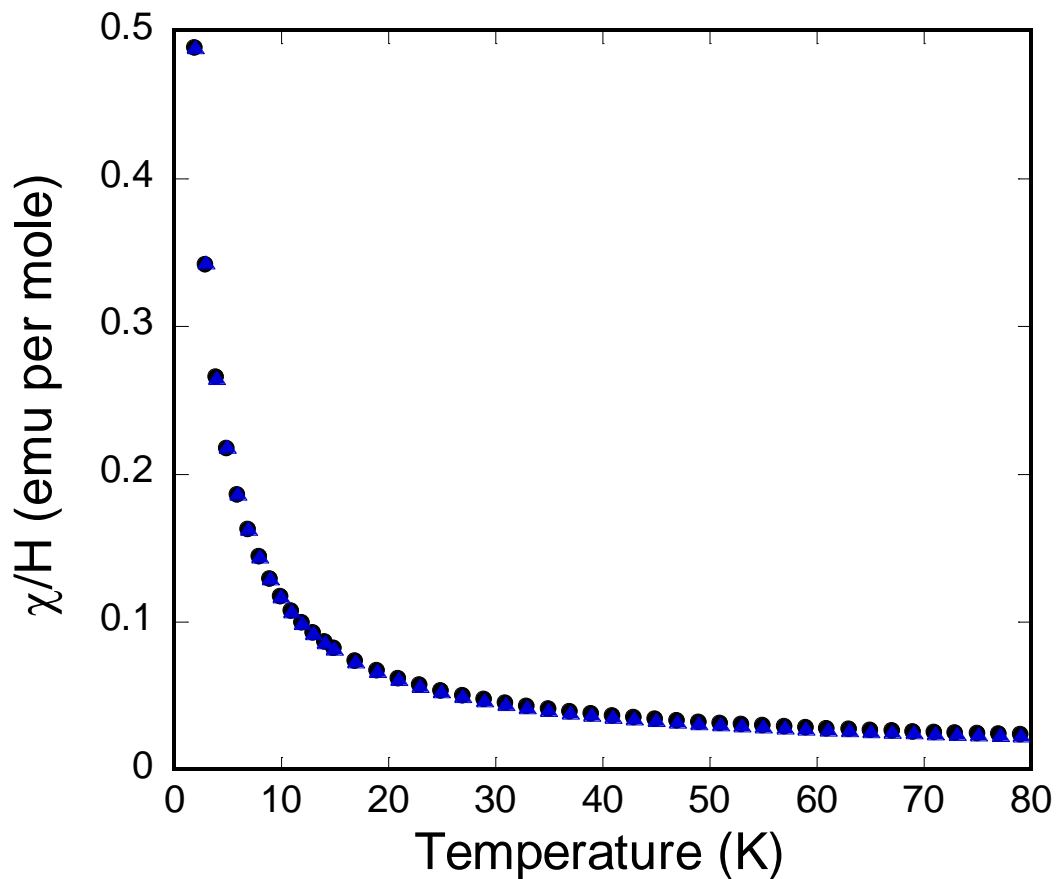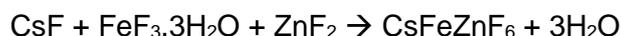
Figure 4.13 FC (blue), ZFC (black) of SQUID moment plots of $RbFeZnF_6$ measured at 1000 Oe from 2 to 80 K under ZFC/FC.

4.4.0 CsFeZnF$_6$

Synthesis of CsFeZnF$_6$ with a hydrothermal method using dilute trifluoro-acetic acid, the expected chemical equation is given as below:

$$CsF + FeF_3.3H_2O + ZnF_2 \rightarrow CsFeZnF_6 + 3H_2O$$

4.4.1 Experimental procedure[92][92]

CsF (0.4253 g, 2.28 x 10^{-3} mol), FeF$_3$.3H$_2$O (0.3805 g, 2.28 x 10^{-3} mol) and ZnF$_2$ (0.2360 g, 2.28 x 10^{-3} mol) were put into an autoclave. In a fume cupboard, deionised water (5 mL) and trifluoro-acetic acid (3 mL) were slowly added to the powders. The autoclave was sealed and heated in an oven for 24 hours at 230 °C.

The oven was turned off after 24 hours and slowly cool to room temperature. The product was collected by washing with deionised water.

4.4.2 X-ray diffraction analysis for structural characterisation

The structural characterisation was done by profile matching with constant scale factor to obtain the lattice parameters for CsFeZnF$_6$ sample (shown in Figure 4.14). The lattice parameter a, b and c obtained are 10.40375 Å, 10.40375 Å and 10.40375 Å respectively. The characteristic peaks appeared at 14.7 ° (111), 24.2 ° (022), 28.4 ° (113), 29.7 ° (222), 45.3 ° (333), 49.5 ° (044), 57.9 ° (335) and 69.2 ° (137). However, the observed X-ray diffraction pattern showed variation in terms of intensity of diffraction. The lowering in intensity of diffraction peaks at (113) and (222) could be the presence of impurity in the sample. Therefore, this CsFeZnF$_6$ sample is confirmed to crystallised in a cubic structure with $Fd\bar{3}m$ space group.
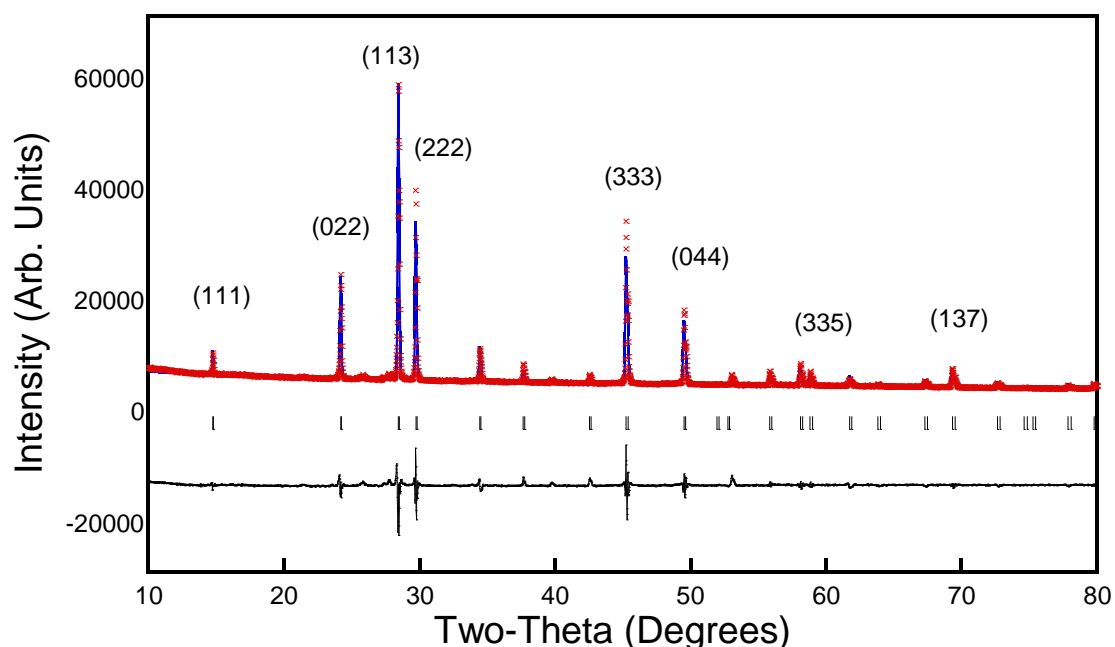

Figure 4.14 Observed (blue), calculated(red) and difference(black) data obtained from profile matching of powder X-ray diffraction data of CsFeZnF$_6$.

4.4.3 Neutron diffraction analysis for magnetic ordering

The CsFeZnF$_6$ sample was scanned at room temperature (298 K) to obtain an initial framework of the neutron diffraction pattern (Figure 4.15). The major diffraction peaks occur at 14.7 ° (111), 29.4 ° (113), 29.7 ° (222), and 51.2 ° (044), similar to the neutron diffraction patterns observed in the caesium doped mixed metal fluoride derivatives CsFeCrF$_6$. Since the magnetic ordering pattern can only be observed at a temperature below T$_N$ = 16 K. From the data obtained at 298 K, two assumptions can be made in regard to the occurrence of magnetic ordering, CsFeZnF$_6$ would exhibit spin glass behaviour and develop short-ranged ordering as the result of magnetic frustration from the competing interactions between the mixed metal components (iron and zinc). Alternatively, this sample would display long-ranged order characteristic similar to CsFeCrF$_6$. However, neutron scan at temperatures below 16 K, and SQUID magnetometry are needed to further study the magnetisation features in CsFeZnF6.

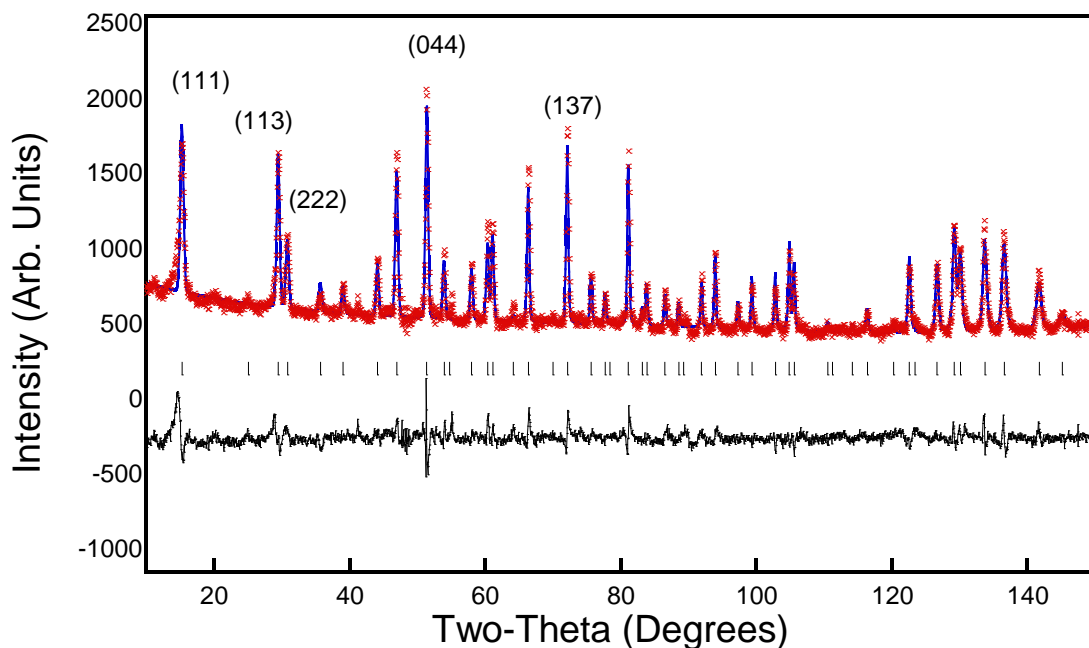

Figure 4.15 Observed (blue), calculated(red) and difference(black) data obtained from Rietveld refinement of neutron diffraction data of a CsFeZnF$_6$ sample scanned at room temperature (298 K)

4.5.0 CsFeCrF$_6$

Synthesis of CsFeCrF$_6$ with a hydrothermal method using dilute trifluoro-acetic acid and the chemical equation is as below:

$$CsF + CrF_3.3H_2O + FeF_2 \rightarrow CsFeCrF_6 + 3H_2O$$

4.5.1 Experimental procedure

CsF (0.4253 g, 2.28 x 10^{-3} mol), FeF$_2$ (0.2140 g, 2.28 x 10^{-3} mol) and CrF$_3$.H$_2$O (0.3032 g, 2.28 x 10^{-3} mol) were put into an autoclave. In a fume cupboard, deionised water (5 mL) and trifluoro-acetic acid (3 mL) were slowly added to the powders. The autoclave was sealed and heated in an oven for 24 hours at 230 °C.

The oven was turned off after 24 hours and slowly cool to room temperature. The product was collected by washing with deionised water.

4.5.2 X-ray diffraction analysis for structural characterisation

The structural characterisation was done by profile matching with constant scale factor to obtain the lattice parameters with the powder X-ray diffraction pattern of CsFeCrF$_6$ sample (Figure 4.16). The lattice parameter a, b and c are 10.39313 Å, 10.39313 Å and 10.39313 Å respectively. Figure 4.16 shows the X-ray pattern obtained from profile matching of a CsFeCrF$_6$ sample, the characteristic diffraction peaks are observed at 24.2 ° (022), 28.4 ° (113), 29.7 ° (222), 45.3 ° (333) and 49.5 ° (044). These data confirms that this synthetic CsFeCrF$_6$ sample crystallised in a cubic structure with a $Fd\bar{3}m$ space group. The small peak observed at 14.7 ° could be impurities in the sample. However, Reitveld refinement is needed to obtain crystallographic information such as atomic positions to confirm the occupancy and composition of chromium and iron in the sample.
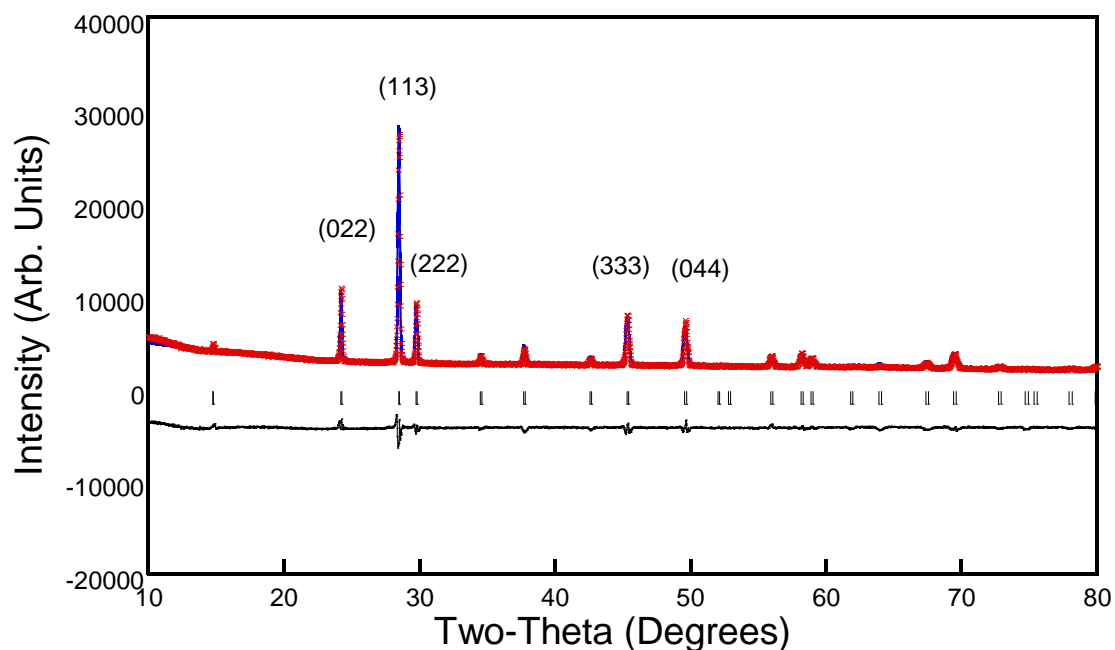

Figure 4.16 Observed (blue), calculated (red) and difference (black) data obtained from profile matching of powder X-ray diffraction data of CsFeCrF$_6$.

4.5.3 Neutron diffraction analysis for magnetic ordering

$CsFeCrF_6$ was scanned at both room temperature (298 K) and in the cryostat (1.5 K – 35 K). When scanned at 1.5 K, the characteristic peaks are observed at 14.7 ° (111), 28.4 ° (113), 42.6 ° (224), 45.3° (333), 49.5 ° (004) and 77.9 ° (228). No magnetic diffraction peaks (the double peak at (111)) are observed (shown in Figure 4.17). An identical diffraction pattern is observed when scanned at room temperature (298 K), and no magnetic ordering diffraction is detected (shown in Figure 4.18). (Refinement of neutron diffraction pattern of $CsFeCrF_6$ in the cryostat can be viewed in Appendix 2).

In conclusion, the sample retains its long-ranged order characteristic and no magnetic frustration is detected at low temperature [96]. If the compound $CsFeCrF_6$ has antiferromagnetic ordering, then additional magnetic reflections would be seen at new values of two-theta as seen for $RbFe_2F_6$.
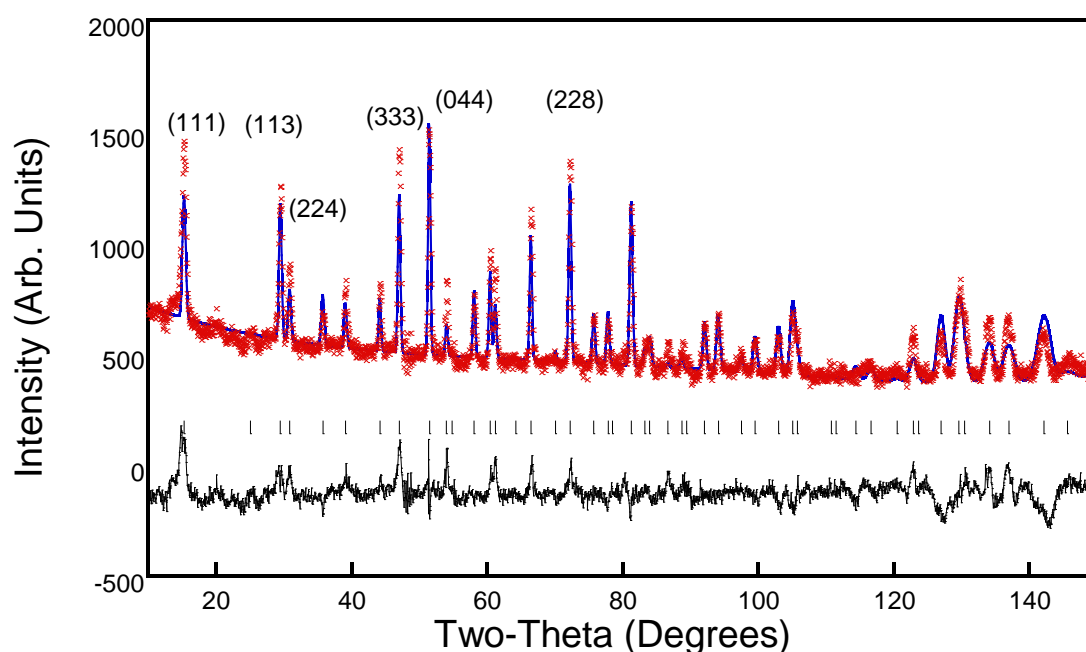
Figure 4.17 Rietveld refinement of neutron diffraction pattern of $CsFeCrF_6$ with ordered orthorhombic structure scanned at 1.5 K. observed pattern (blue), calculated pattern (red) and difference (black).
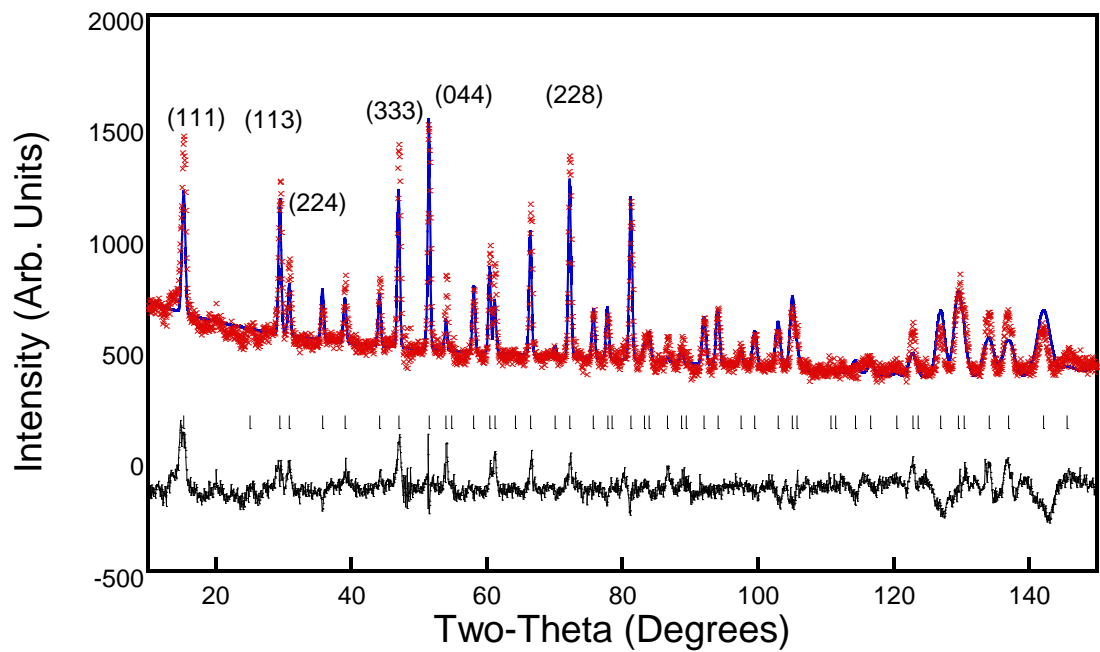
Figure 4.18 Rietveld refinement of neutron diffraction pattern of $CsFeCrF_6$ with ordered orthorhombic structure scanned at room temperature (298 K). observed pattern (blue), calculated pattern (red) and difference (black).

4.6.0 Overall conclusion

In this project, $RbFe_2F_6$, a charged ordered defect pyrochlore was synthesised successfully and characterised with XRD and neutron diffraction techniques. It was confirmed to have an orthorhombic structure with *Pnma* symmetry. Structural transition was observed below the temperature of 15 K in the neutron diffraction data, which is consistent with the literature [97] for the confirmation of magnetic ordering long ranged order arrangement. Cooling to temperatures below 10 K that has previously been unreported confirmed the average magnetic structure remains the same, despite significant magnetic dynamic changes recently observed from inelastic neutron scattering data.

A newly charged order phase $RbFe_{1.3}Cr_{0.7}F_6$ is synthesised and is crystallised in a different composition similar to the orthorhombic structure of $RbFe_2F_6$ with the space group *Pnma*. This structure is isolated since only one single crystal was characterised; it has also shown that specific compositions have the possibility to stabilise the orthorhombic phase. The $RbFeCrF_6$ samples scanned with powder neutron diffraction exhibits cubic symmetry common amongst the pyrochlores. The SQUID measurement shows this compound has a magnetic transition at ~10 K, with divergence between zero field cooled and field cooled magnetic susceptibility. Powder neutron diffraction showed this transition was spin-glass in nature and has no long ranged magnetic order.

The synthesis of $RbFeZnF_6$ was attempted and a SQUID measurement was taken, and this sample showed Curie-Weiss behaviour down to 2 K.

Reference and bibliography

[1]   Global energy demand grew by 2.1% in 2017, and carbon emissions rose for the firs, (n.d.). https://www.iea.org/newsroom/news/2018/march/global-energy-demand-grew-by-21-in-2017-and-carbon-emissions-rose-for-the-firs.html (accessed November 3, 2018).

[2]   P.R. Epstein, J.J. Buonocore, K. Eckerle, M. Hendryx, B.M. Stout III, R. Heinberg, R.W. Clapp, B. May, N.L. Reinhart, M.M. Ahern, S.K. Doshi, L. Glustrom, Full cost accounting for the life cycle of coal, Ann. N. Y. Acad. Sci. 1219 (2011) 73–98. https://doi.org/10.1111/j.1749-6632.2010.05890.x.

[3]   How do Photovoltaics Work? | Science Mission Directorate, (n.d.). https://science.nasa.gov/science-news/science-at-nasa/2002/solarcells (accessed November 3, 2018).

[4]   Solar Photovoltaic Technology Basics | NREL, (n.d.). https://www.nrel.gov/workingwithus/re-photovoltaics.html (accessed November 3, 2018).

[5]   D. Zhao, C. Wang, Z. Song, Y. Yu, C. Chen, X. Zhao, K. Zhu, Y. Yan, Four-Terminal All-Perovskite Tandem Solar Cells Achieving Power Conversion Efficiencies Exceeding 23%, ACS Energy Lett. 3 (2018) 305–306. https://doi.org/10.1021/acsenergylett.7b01287.

[6]   C.C. Stoumpos, D.H. Cao, D.J. Clark, J. Young, J.M. Rondinelli, J.I. Jang, J.T. Hupp, M.G. Kanatzidis, Ruddlesden-Popper Hybrid Lead Iodide Perovskite 2D Homologous Semiconductors, Chem. Mater. 28 (2016) 2852–2867. https://doi.org/10.1021/acs.chemmater.6b00847.

[7]   Supplementary Figure 1 . Crystal structure of MAPbI under ambient conditions. Estimated atomic coordinates were extracted from maxima in the nuclear scattering density reconstructed from powder neutron diffraction data. Atoms shown are lead (grey), iodine, 2 (n.d.).

[8]   F. Hao, C.C. Stoumpos, P. Guo, N. Zhou, T.J. Marks, R.P.H. Chang, M.G. Kanatzidis, Solvent-Mediated Crystallization of CH3NH3SnI3 Films for Heterojunction Depleted Perovskite Solar Cells, J. Am. Chem. Soc. 137 (2015) 11445–11452. https://doi.org/10.1021/jacs.5b06658.

[9]   L.-C. Chen, Z.-L. Tseng, ZnO-Based Electron Transporting Layer for Perovskite Solar Cells, Nanostructured Sol. Cells. (2017). https://doi.org/10.5772/65056.

[10]   S. Chatterjee, A.J. Pal, Influence of metal substitution on hybrid halide perovskites: Towards lead-free perovskite solar cells, J. Mater. Chem. A. 6 (2018) 3793–3823. https://doi.org/10.1039/c7ta09943f.

[11]   A. Fakharuddin, F. De Rossi, T.M. Watson, L. Schmidt-Mende, R. Jose, Research Update: Behind the high efficiency of hybrid perovskite solar cells, Cit. APL Mater. 4 (2016) 91505. https://doi.org/10.1063/1.4962143.

[12]   Band Theory for Solids, (n.d.). http://hyperphysics.phy-astr.gsu.edu/hbase/Solids/band.html#c2https://energyeducation.ca/encyclopedia/Va

lence_band (accessed September 4, 2018).

[13]   Fermi level and Fermi function, (n.d.). http://hyperphysics.phy-astr.gsu.edu/hbase/Solids/Fermi.html#c17 (accessed September 1, 2018).

[14]   Exciton | physics | Britannica.com, (n.d.). https://www.britannica.com/science/exciton (accessed August 6, 2018).

[15]   P Type Semiconductor | Doping | Extrinsic Semiconductor, (n.d.). http://www.science-campus.com/engineering/electronics/semiconductor_theory/semiconductor_8.html (accessed September 4, 2018).

[16]   N Type Semiconductor | Doping | Extrinsic Semiconductor, (n.d.). http://www.science-campus.com/engineering/electronics/semiconductor_theory/semiconductor_7.html (accessed September 2, 2018).

[17]   Electron Hole Pair (EHP) Generation | Semiconductor Theory, (n.d.). http://www.science-campus.com/engineering/electronics/semiconductor_theory/semiconductor_5.html (accessed September 5, 2018).

[18]   G.P. Andrew Burrows, John Holman, Andrew Parsons, Chemistry³, second, OUP Oxford University Press, Oxford, 2013.

[19]   Diffusion and drift of charge carriers, (n.d.). http://psi.phys.wits.ac.za/teaching/Connell/phys284/2005/lecture-07/lecture_07/node7.html (accessed September 5, 2018).

[20]   J.M. Azpiroz, E. Mosconi, J. Bisquert, F. De Angelis, Defect migration in methylammonium lead iodide and its role in perovskite solar cell operation, Energy Environ. Sci. 8 (2015) 2118–2127. https://doi.org/10.1039/C5EE01265A.

[21]   J.L. Minns, P. Zajdel, D. Chernyshov, W. Van Beek, M.A. Green, Structure and interstitial iodide migration in hybrid perovskite methylammonium lead iodide, Nat. Commun. 8 (2017) 1–5. https://doi.org/10.1038/ncomms15152.

[22]   J.W. Morris, Materials Science, n.d. http://www.mse.berkeley.edu/groups/morris/MSE205/Extras/defects.pdf (accessed September 30, 2018).

[23]   P.H. Svensson, L. Kloo, Synthesis, Structure, and Bonding in Polyiodide and Metal Iodide–Iodine Systems, (2003). https://doi.org/10.1021/cr0204101.

[24]   B.M. Preston Harris, E. Mack, F.C. Blake, THE ATOMIC ARRANGEMENT IN THE CRYSTAL OF ORTHORHOMBIC IODINE, UTC, 2018. https://pubs.acs.org/sharingguidelines (accessed November 11, 2018).

[25]   Interstitial Iodide Migration and Diatomic Iodine Formation in a Hybrid Perovskite, (2009).

[26]   Anthony R. West, Solid State Chemistry and its Applications, Wiley-Blackwell,

Chichester, 2014.

[27]   A.M.A. Leguy, J.M. Frost, A.P. McMahon, V.G. Sakai, W. Kochelmann, C. Law, X. Li, F. Foglia, A. Walsh, B.C. O'Regan, J. Nelson, J.T. Cabral, P.R.F. Barnes, The dynamics of methylammonium ions in hybrid organic-inorganic perovskite solar cells, Nat. Commun. 6 (2015) 1–11. https://doi.org/10.1038/ncomms8124.

[28]   M.T. Weller, O.J. Weber, P.F. Henry, A.M. Di Pumpo, T.C. Hansen, Complete structure and cation orientation in the perovskite photovoltaic methylammonium lead iodide between 100 and 352 K, Chem. Commun. 51 (2015) 4180–4183. https://doi.org/10.1039/c4cc09944c.

[29]   A.A. Bakulin, O. Selig, H.J. Bakker, Y.L.A. Rezus, C. Müller, T. Glaser, R. Lovrincic, Z. Sun, Z. Chen, A. Walsh, J.M. Frost, T.L.C. Jansen, Real-Time Observation of Organic Cation Reorientation in Methylammonium Lead Iodide Perovskites, J. Phys. Chem. Lett. 6 (2015) 3663–3669. https://doi.org/10.1021/acs.jpclett.5b01555.

[30]   L.C. Chen, C.C. Chen, J.C. Chen, C.G. Wu, Annealing effects on high-performance CH3NH3PbI3perovskite solar cells prepared by solution-process, Sol. Energy. 122 (2015) 1047–1051. https://doi.org/10.1016/j.solener.2015.10.019.

[31]   J. Ye, H. Zheng, L. Zhu, X. Zhang, L. Jiang, W. Chen, G. Liu, X. Pan, S. Dai, High-temperature shaping perovskite film crystallization for solar cell fast preparation, Sol. Energy Mater. Sol. Cells. 160 (2017) 60–66. https://doi.org/10.1016/j.solmat.2016.10.022.

[32]   Solar Cell Efficiency, PVEducation.Org. (2019). https://www.pveducation.org/pvcdrom/solar-cell-operation/solar-cell-efficiency (accessed March 2, 2020).

[33]   H. Choi, J. Jeong, H.-B. Kim, S. Kim, G.-H. Kim, J.Y. Kim, Cesium-doped methylammonium lead iodide perovskite light absorber for hybrid solar cells, Nano Energy. 7 (2014) 80–85. https://doi.org/10.1016/j.nanoen.2014.04.017.

[34]   Y. Zhao, K. Zhu, Charge transport and recombination in perovskite (CH3NH3)PbI3sensitized TiO2Solar Cells, J. Phys. Chem. Lett. 4 (2013) 2880–2884. https://doi.org/10.1021/jz401527q.

[35]   W. Zhao, Z. Yao, F. Yu, D. Yang, S.F. Liu, Alkali Metal Doping for Improved CH$_3$NH$_3$PbI$_3$ Perovskite Solar Cells, Adv. Sci. 1700131 (2017) 1700131. https://doi.org/10.1002/advs.201700131.

[36]   M.T. Klug, A. Osherov, A.A. Haghighirad, S.D. Stranks, P.R. Brown, S. Bai, J.T.W. Wang, X. Dang, V. Bulović, H.J. Snaith, A.M. Belcher, Tailoring metal halide perovskites through metal substitution: Influence on photovoltaic and material properties, Energy Environ. Sci. 10 (2017) 236–246. https://doi.org/10.1039/c6ee03201j.

[37]   A. Kooijman, L.A. Muscarella, R.M. Williams, Perovskite thin film materials stabilized and enhanced by zinc(II) doping, Appl. Sci. 9 (2019). https://doi.org/10.3390/app9081678.

[38]   Ivan Pelant, Jan Valenta, Non-radiative recombination - Oxford Scholarship, Oxford Univ. Press. (2012).

https://www.oxfordscholarship.com/view/10.1093/acprof:oso/9780199588336.001. 0001/acprof-9780199588336-chapter-6 (accessed March 5, 2020).

[39]   M.C. Chang, Ferromagnetism and antiferromagnetism • ferromagnetism (FM) • exchange interaction, Heisenberg model • spin wave, magnon • antiferromagnetism (AFM) • ferromagnetic domains • nanomagnetic particles Magnetic order, n.d. https://phy.ntnu.edu.tw/~changmc/Teach/SS/SS_note/chap12.pdf (accessed September 30, 2018).

[40]   Magnetism on the Atomic Level, (n.d.). http://physics.bu.edu/~duffy/semester2/c16_atomic.html (accessed September 17, 2018).

[41]   William Clegg, X-Ray Crystallography, Second, OUP Oxford University Press, Oxford, 2015.

[42]   Lenz's law | physics | Britannica.com, (n.d.). https://www.britannica.com/science/Lenzs-law (accessed September 20, 2018).

[43]   What is Magnetism? | Magnetic Fields & Magnetic Force, (n.d.). https://www.livescience.com/38059-magnetism.html (accessed September 23, 2018).

[44]   J. M. D. Coey, Magnetism and Magnetic Materials, Cambridge University Press, Cambridge, 2010.

[45]   Classes of Magnetic Materials, (n.d.). http://www.irm.umn.edu/hg2m/hg2m_b/hg2m_b.html (accessed September 23, 2018).

[46]   Anthony R. West, solid state chemistry, in: Solid State Chem. Its Appl., 2014: p. 382.

[47]   P.A. Joy, A. Kumar, S.K. Date, The relationship between field - cooled and zero - field - cooled susceptibilities of some ordered magnetic systems, J . Phys . Condens . Matter. 10 (1998) 11049–11054. https://doi.org/10.1088/0953-8984/10/48/024.

[48]   Ferroelectricity | physics | Britannica.com, (n.d.). https://www.britannica.com/science/ferroelectricity/ (accessed September 25, 2018).

[49]   Frustrated Magnetism :: User Sites :: USNA, (n.d.). https://www.usna.edu/Users/physics/helton/Research/Frustrated Magnetism.php (accessed November 14, 2018).

[50]   F. Fr´, F. Fréd´, F. Mila, 7 Frustrated Spin Systems, n.d. http://www.cond-mat.de/events/correl15 (accessed October 1, 2018).

[51]   J. M. D. Coey, Magnetism and Magnetic Materials, Cambridge University Press, Cambridge, 2010.

[52]   J. Carrasquilla, Z. Hao, R.G. Melko, A two-dimensional spin liquid in quantum kagome ice, Nat. Commun. 6 (2015) 7421. https://doi.org/10.1038/ncomms8421.

[53]   L. Lin, Y.L. Xie, J.-J. Wen, S. Dong, Z.B. Yan, J.-M. Liu, Experimental observation of

magnetoelectricity in spin ice Dy 2 Ti 2 O 7, New J. Phys. 17 (2015) 123018. https://doi.org/10.1088/1367-2630/17/12/123018.

[54]   Sun Woo Kim;a Sang-Hwan Kim;a P. Shiv Halasyamani;a;* Mark A. Green;b Kanwal Preet Bhatti;c C. Leighton;c;* Hena Das;d and Craig J. 1 Fennied, Y. Liu, M. Li, H. Huang, H.M. Xu, R.J. Hong, H. Shen, RbFe2+Fe3+F6: Synthesis, Structure, and Characterization of a New Charge-Ordered Magnetically Frustrated Pyrochlore-Related Mixed-Metal 5 Fluoride, Optoelectron. Adv. Mater. Rapid Commun. 4 (2010) 1166–1169. https://doi.org/10.1039/b000000x.

[55]   B. Harbick, L. Suh, J. Fong, Closest Packed Structures - Chemistry LibreTexts, Chem. Libr. (2017). https://chem.libretexts.org/Bookshelves/Physical_and_Theoretical_Chemistry_Textb ook_Maps/Supplemental_Modules_(Physical_and_Theoretical_Chemistry)/Physical_ Properties_of_Matter/States_of_Matter/Properties_of_Solids/Crystal_Lattice/Closest _Pack_Structures (accessed March 2, 2020).

[56]   B.A. Trump, S.M. Koohpayeh, K.J.T. Livi, J.-J. Wen, K.E. Arpino, Q.M. Ramasse, R. Brydson, M. Feygenson, H. Takeda, M. Takigawa, K. Kimura, S. Nakatsuji, C.L. Broholm, T.M. McQueen, Universal geometric frustration in pyrochlores, Nat. Commun. 9 (2018) 2619. https://doi.org/10.1038/s41467-018-05033-7.

[57]   B. P. Mandal and A. K. Tyagi, Pyrochlores: Potential multifunctional materials, 2010. http://www.barc.gov.in/publications/nl/2010/2010030402.pdf (accessed September 30, 2018).

[58]   F.X. Zhang, M. Lang, R.C. Ewing, Atomic disorder in Gd2Zr2O7 pyrochlore, Appl. Phys. Lett. 106 (2015). https://doi.org/10.1063/1.4921268.

[59]   P.S. Maram, S. V. Ushakov, R.J.K. Weber, C.J. Benmore, A. Navrotsky, Probing disorder in pyrochlore oxides using in situ synchrotron diffraction from levitated solids-A thermodynamic perspective, Sci. Rep. 8 (2018) 1–11. https://doi.org/10.1038/s41598-018-28877-x.

[60]   N.P. Raju, M. Dion, M.J.P. Gingras, T.E. Mason, J.E. Greedan, Transition to Long Range Magnetic Order in the Highly Frustrated Insulating Pyrochlore Antiferromagnet Gd 2 Ti 2 O 7, 1999. https://arxiv.org/pdf/cond-mat/9906043.pdf (accessed November 13, 2018).

[61]   Frustrated magnets, (n.d.). http://www-thphys.physics.ox.ac.uk/people/FionaBurnell/frusmag.html (accessed September 16, 2018).

[62]   beta-pyrochlore oxide, (n.d.). http://hiroi.issp.u-tokyo.ac.jp/yone/research/beta-pyrochlore.htm (accessed September 17, 2018).

[63]   P. Lunkenheimer, T. Götzfried, R. Fichtl, Apparent giant dielectric constants, dielectric relaxation, and ac-conductivity of hexagonal perovskites La 1.2 Sr 2.7 B O 7.33, J. Solid State Chem. 33 (2006) 1–8. https://doi.org/10.1016/j.jssc.2006.09.005.

[64]   Basics of radiation and production of x rays, (n.d.). https://www.slideshare.net/dbc9427/basics-of-radiation-and-production-of-x-rays

(accessed September 15, 2018).

[65] J. Vannimenus, G. Toulouse, Theory of the frustration effect. II. Ising spins on a square lattice, J. Phys. C Solid State Phys. 10 (1977) L537–L542. https://doi.org/10.1088/0022-3719/10/18/008.

[66] S.T. Banks, S.T. Bramwell, Magnetic frustration in the context of pseudo-dipolar ionic disorder, (2011). https://doi.org/10.1209/0295-5075/97/27005.

[67] How x-radiation is produced, (n.d.). https://www.ucd.ie/vetanat/radiology2001/the_x-ray_tube.html (accessed September 10, 2018).

[68] M. Uo, T. Wada, T. Sugiyama, Applications of X-ray fluorescence analysis (XRF) to dental and medical specimens, Jpn. Dent. Sci. Rev. 51 (2015) 2–9. https://doi.org/10.1016/j.jdsr.2014.07.001.

[69] BraggsLaw, (n.d.). https://serc.carleton.edu/research_education/geochemsheets/BraggsLaw.html (accessed November 11, 2018).

[70] X.-B. Theory, Introduction to X-ray Diffraction (XRD) Learning Activity, n.d. https://www.asdlib.org/onlineArticles/ecourseware/Bullen_XRD/LearningActivity_Diffraction_BraggsLaw.pdf (accessed March 15, 2020).

[71] William Clegg, X-Ray Crystallography, second, OUP Oxford University Press, Oxford, 2015.

[72] Anthony R. West, Solid State Chemistry and its Applications, Wiley-Blackwell, Chichester, 2014.

[73] ISIS What is a neutron?, (n.d.). https://www.isis.stfc.ac.uk/Pages/What-is-a-neutron-About.aspx# (accessed February 11, 2021).

[74] D.L. Price, K. Skold, Introduction to Neutron Scattering, Methods Exp. Phys. 23 (1986) 1–97. https://doi.org/10.1016/S0076-695X(08)60554-2.

[75] ILL Neutrons for Society - Instrument layout, (2001). https://www.ill.eu/users/instruments/instruments-list/d2b/characteristics/ (accessed February 19, 2019).

[76] R. Pynn, An Introduction to Neutron Scattering, Indiana Univ. Oak Ridge Natl. Lab. (n.d.). https://doi.org/10.1016/B978-0-12-398374-9.00001-2.

[77] G. L. Squires, Introduction to the Theory of Thermal Neutron Scattering, 3rd ed., Cambridge University Press, Cambridge, 2012.

[78] K.G. Stamplecoskie, J.S. Manser, P. V Kamat, Supporting Information Dual Nature of the Excited State in Organic-Inorganic Lead Halide Perovskites, 2014. http://www.rsc.org/suppdata/ee/c4/c4ee02988g/c4ee02988g1.pdf (accessed November 21, 2018).

[79] M. Toma, N. Ursulean, D. Marconi, A. Pop, Structural and optical characterization of Cu doped ZnO thin films deposited by RF magnetron sputtering, J. Electr. Eng. 70

(2019) 127–131. https://doi.org/10.2478/jee-2019-0054.

[80] S.R. Raga, M.C. Jung, M. V Lee, M.R. Leyden, Y. Kato, Y. Qi, Influence of air annealing on high efficiency planar structure perovskite solar cells, Chem. Mater. 27 (2015) 1597–1603. https://doi.org/10.1021/cm5041997.

[81] J. Zhao, Y. Deng, H. Wei, X. Zheng, Z. Yu, Y. Shao, J.E. Shield, J. Huang, Strained hybrid perovskite thin films and their impact on the intrinsic stability of perovskite solar cells, Sci. Adv. 3 (2017). https://doi.org/10.1126/sciadv.aao5616.

[82] L. Zhang, M.G. Ju, W. Liang, The effect of moisture on the structures and properties of lead halide perovskites: A first-principles theoretical investigation, Phys. Chem. Chem. Phys. 18 (2016) 23174–23183. https://doi.org/10.1039/c6cp01994c.

[83] J.M. Frost, K.T. Butler, F. Brivio, C.H. Hendon, M. Van Schilfgaarde, A. Walsh, Atomistic origins of high-performance in hybrid halide perovskite solar cells, Nano Lett. 14 (2014) 2584–2590. https://doi.org/10.1021/nl500390f.

[84] C. Sites, The Body-Centered Tetragonal Lattice (A a), (2012) 1–2. https://homepage.univie.ac.at/michael.leitner/lattice/struk/a_a.html (accessed June 27, 2020).

[85] Y. Calagé, F. Varret, The crystalline structure of pyrochlores AIFeIIBIIIF6: A Mössbauer investigation, Chem. Phys. Lett. 55 (1978) 380–382. https://doi.org/10.1016/0009-2614(78)87044-4.

[86] C. V Ramana, K.K. Bharathi, A. Garcia, A.L. Campbell, Growth behavior, lattice expansion, strain, and surface morphology of nanocrystalline, monoclinic HfO 2 thin films, J. Phys. Chem. C. 116 (2012) 9955–9960. https://doi.org/10.1021/jp211109h.

[87] F.X. Xie, D. Zhang, H. Su, X. Ren, K.S. Wong, M. Grätzel, W.C.H. Choy, Vacuum-assisted thermal annealing of CH3NH3PbI3 for highly stable and efficient perovskite solar cells, ACS Nano. 9 (2015) 639–646. https://doi.org/10.1021/nn505978r.

[88] L. Qin, L. Lv, C. Li, L. Zhu, Q. Cui, Y. Hu, Z. Lou, F. Teng, Y. Hou, Temperature dependent amplified spontaneous emission of vacuum annealed perovskite films, RSC Adv. 7 (2017) 15911–15916. https://doi.org/10.1039/C7RA01155E.

[89] S. Ming-Chung Wu, K.-M. Lee, W.-F. Su, M.-C. Wu, abc Shun-Hsiang Chan, abc Shih-Hsuan Chen, M.-H. Jao, Y.-F. Chen, Enhancing the efficiency of perovskite solar cells using mesoscopic zinc-doped TiO2 as the electron extraction layer through band alignment†, J. Mater. Chem. A. 6 (2018). https://doi.org/10.1039/c8ta05291c.

[90] Y. Kim, B. Park, Understanding charge trapping/detrapping at the zinc oxide (ZnO)/MAPbI 3 perovskite interface in the dark and under illumination using a ZnO/perovskite/ZnO test platform, Nanoscale. 10 (2018) 20377–20383. https://doi.org/10.1039/c8nr06820h.

[91] W. Zhao, D. Yang, Z. Yang, S. (Frank) Liu, Zn-doping for reduced hysteresis and improved performance of methylammonium lead iodide perovskite hybrid solar cells, Mater. Today Energy. 5 (2017) 205–213. https://doi.org/10.1016/j.mtener.2017.06.009.

[92] S.W. Kim, S.H. Kim, P.S. Halasyamani, M.A. Green, K.P. Bhatti, C. Leighton, H. Das, C.J. Fennie, RbFe2+Fe3+F6: Synthesis, structure, and characterization of a new charge-ordered magnetically frustrated pyrochlore-related mixed-metal fluoride, Chem. Sci. 3 (2012) 741–751. https://doi.org/10.1039/c2sc00765g.

[93] CrysAlis(Pro) | Rigaku, (n.d.). https://www.rigaku.com/en/products/smc/crysalis (accessed February 19, 2019).

[94] M. Songvilay, E.E. Rodriguez, R. Lindsay, M.A. Green, H.C. Walker, J.A. Rodriguez-Rivera, C. Stock, Anharmonic Magnon Excitations in Noncollinear and Charge-Ordered RbFe2+Fe3+ F6, Phys. Rev. Lett. 121 (2018) 87201. https://doi.org/10.1103/PhysRevLett.121.087201.

[95] M. Songvilay, E.E. Rodriguez, R. Lindsay, M.A. Green, H.C. Walker, J.A. Rodriguez-Rivera, C. Stock, Anharmonic Magnon Excitations in Noncollinear and Charge-Ordered RbFe2+Fe3+ F6, Phys. Rev. Lett. 121 (2018) 087201. https://doi.org/10.1103/PhysRevLett.121.087201.

[96] E.V. Bogdanov, A. Tressaud, A.S. Krylov, A.V. Kartashev, E.V. Eremin, M.V. Gorev, O.A. Bayukov, I.N. Flerov, Heat capacity and magnetic properties of fluoride CsFe 2+ Fe 3+ F 6 with defect pyrochlore structure, J. Solid State Chem. 237 (2016) 330–335. https://doi.org/10.1016/j.jssc.2016.02.045.

[97] S.W. Kim, S.H. Kim, P.S. Halasyamani, M.A. Green, K.P. Bhatti, C. Leighton, H. Das, C.J. Fennie, RbFe 2+Fe 3+F 6: Synthesis, structure, and characterization of a new charge-ordered magnetically frustrated pyrochlore-related mixed-metal fluoride, Chem. Sci. 3 (2012) 741–751. https://doi.org/10.1039/c2sc00765g.

[98] C.J. Kim, Sun Woo; Kim, Sang-Hwan; Halasyamani, P.Shiv; Green, Mark A.; Bhatti, Kanwal Preet; Leighton, C.; Das, Hena; Fennie, ICSD - RbFe2F6 Published Crystal Structure, (n.d.). https://doi.org/10.1039/c2sc00765g.

Appendix 1

Chapter 3. Methylammonium lead iodide MAPbI$_3$ (n= ∞)

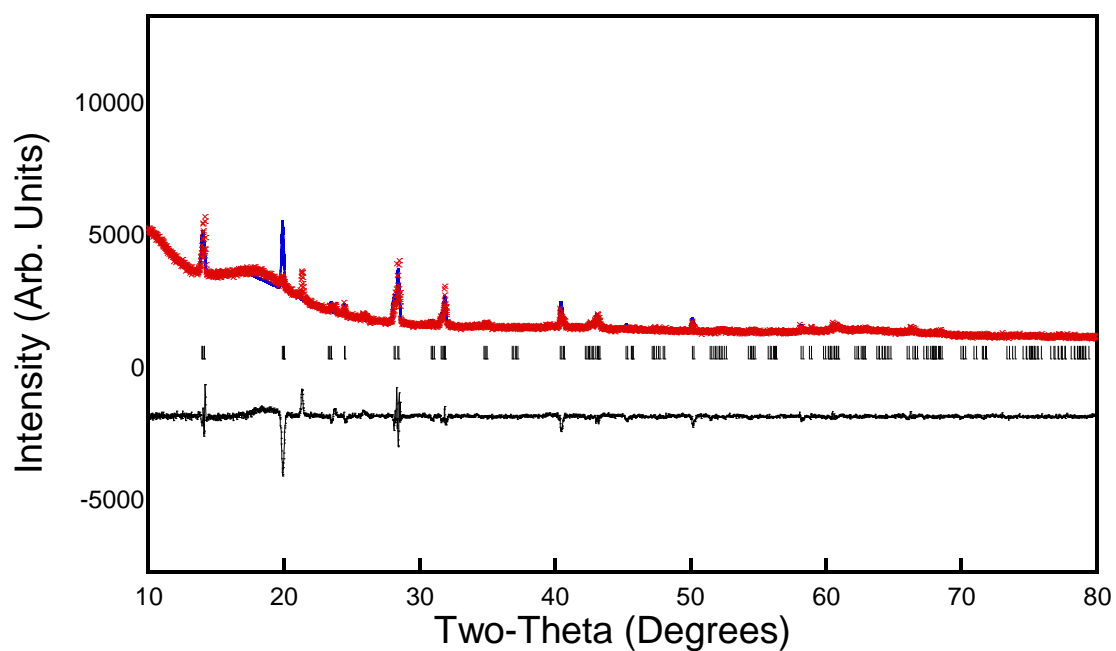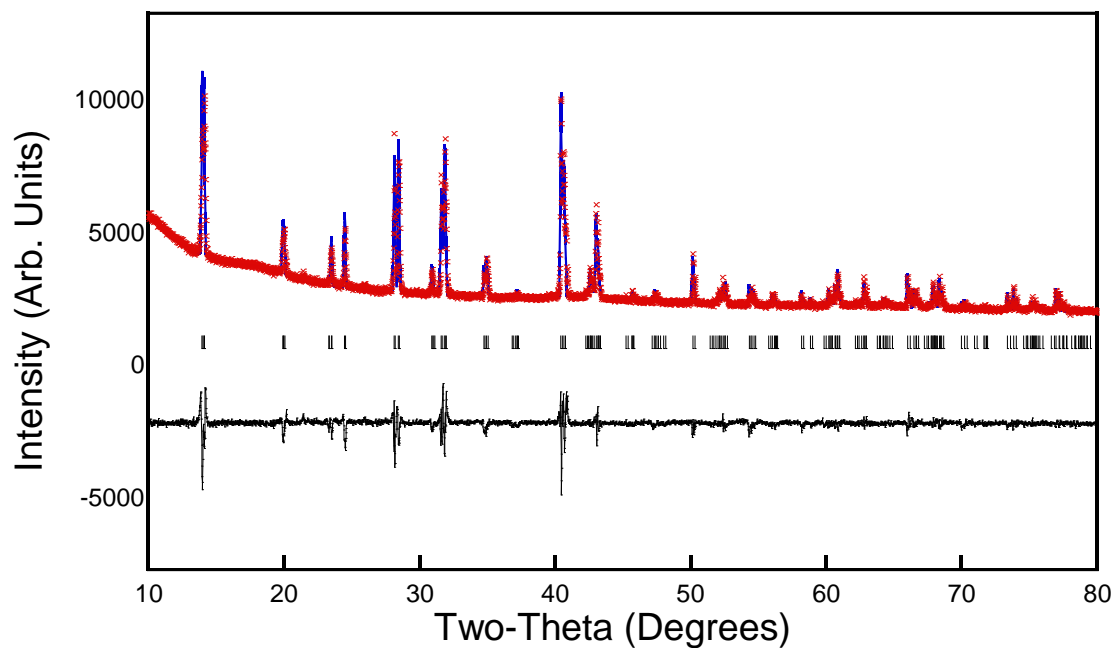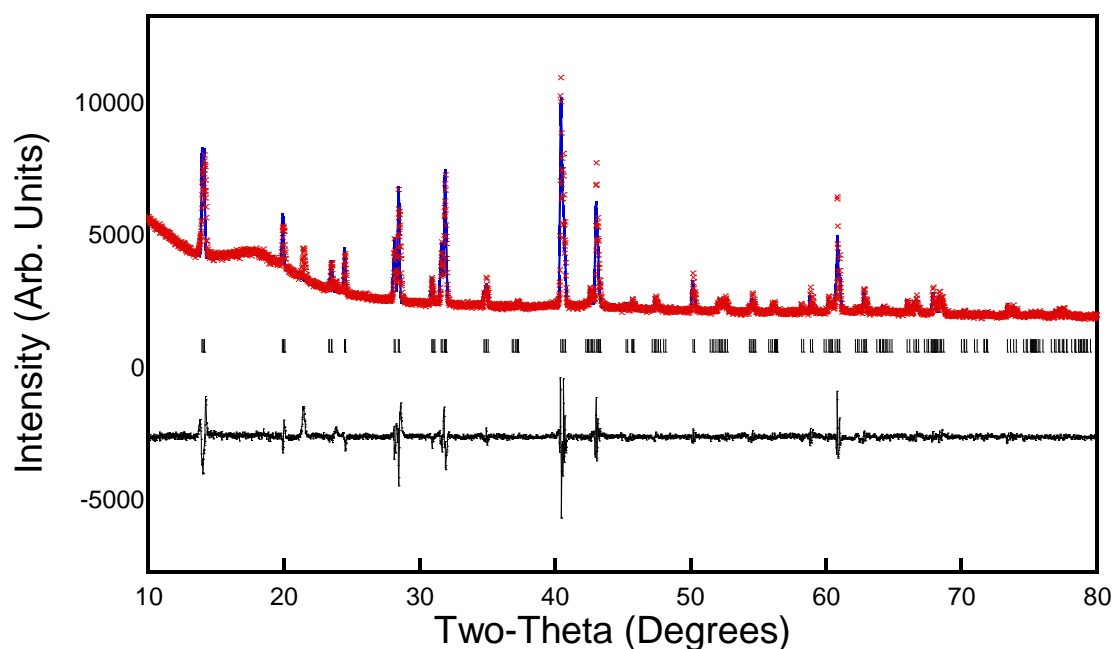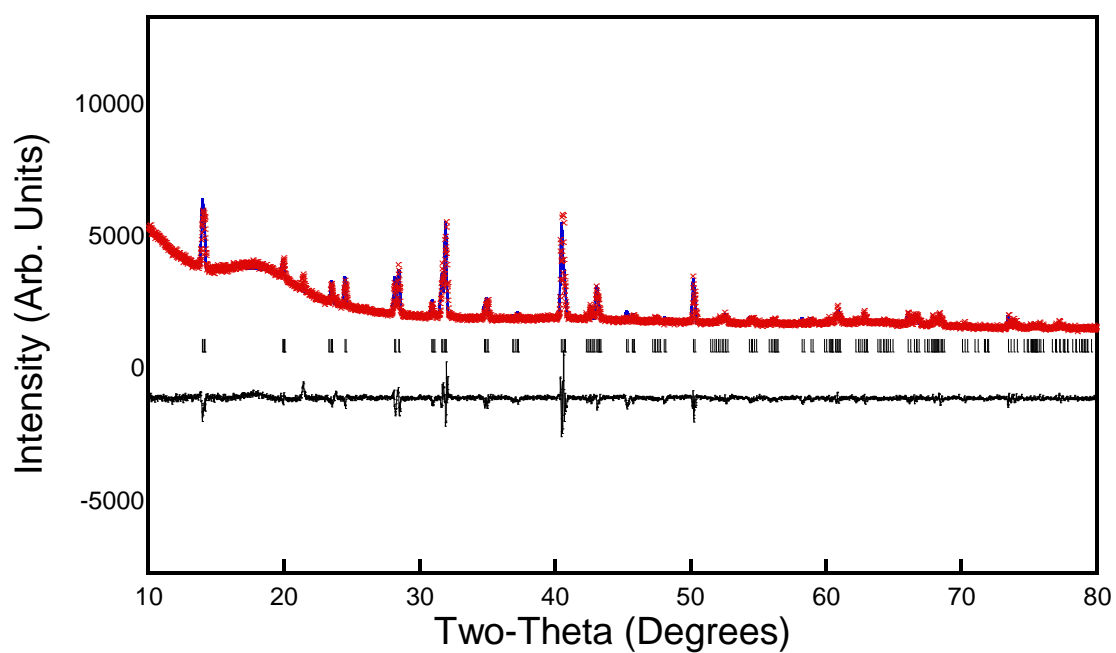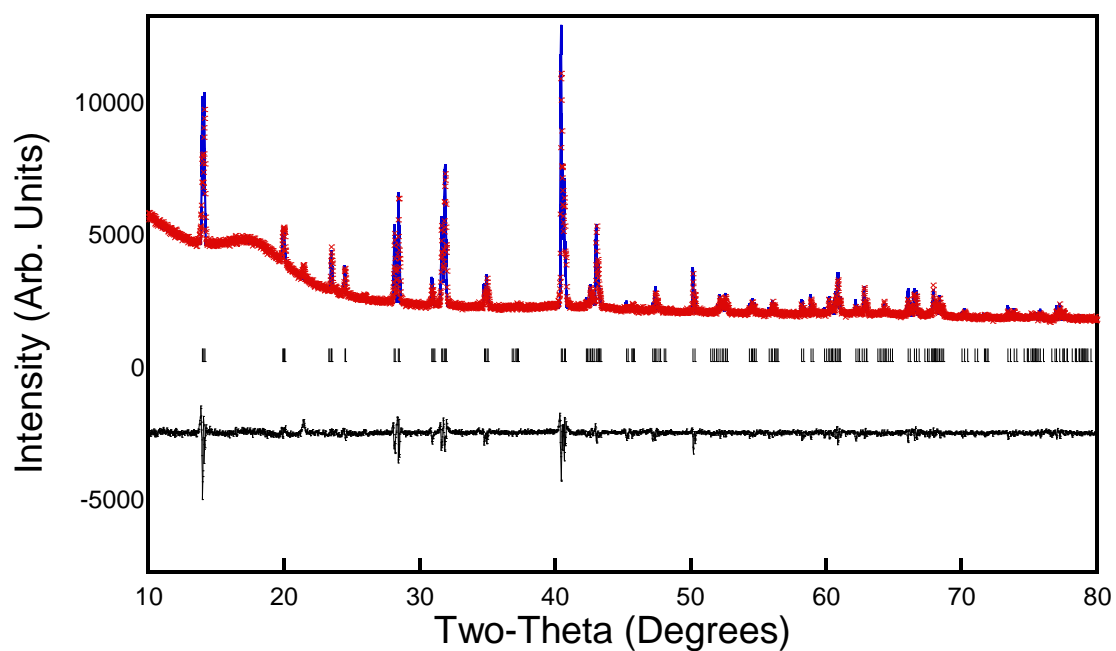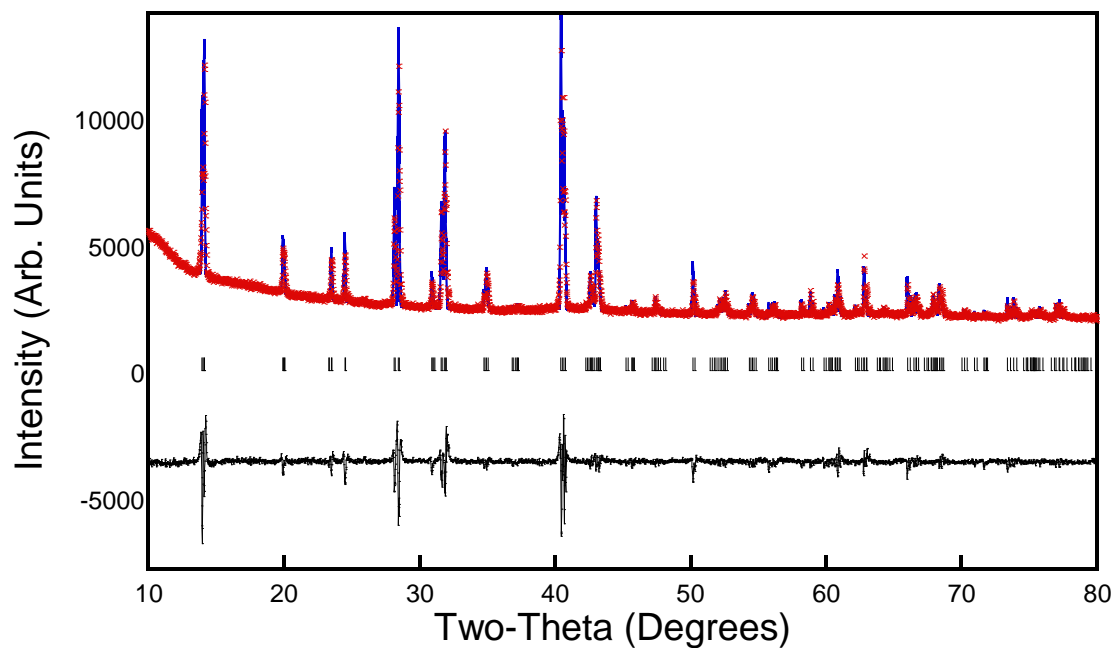Air-annealed of MAPbI$_3$ compound 1 at 50, 70, 90 and 110 $^{\circ}$C for 1 hour.
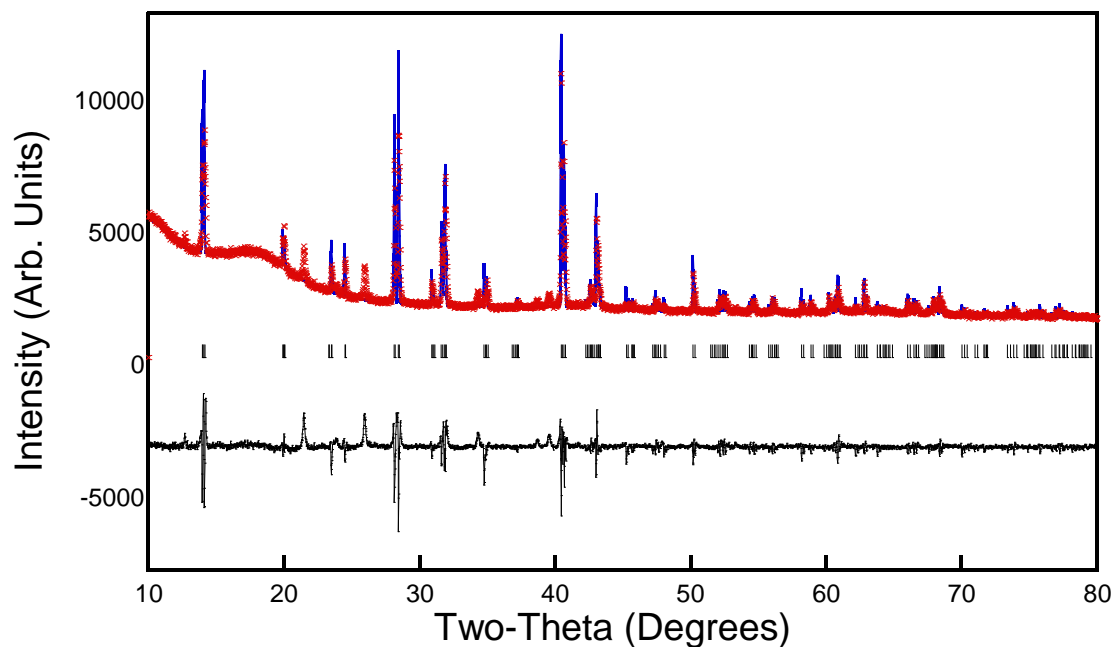
Figure 1A – 1 Observed (blue), calculated (red) and difference (black) data obtained from profile matching with constant scale factor of powder X-ray diffraction data of MAPbI$_3$ compound 1 annealed at 50 $^{\circ}$C for 1 hour.
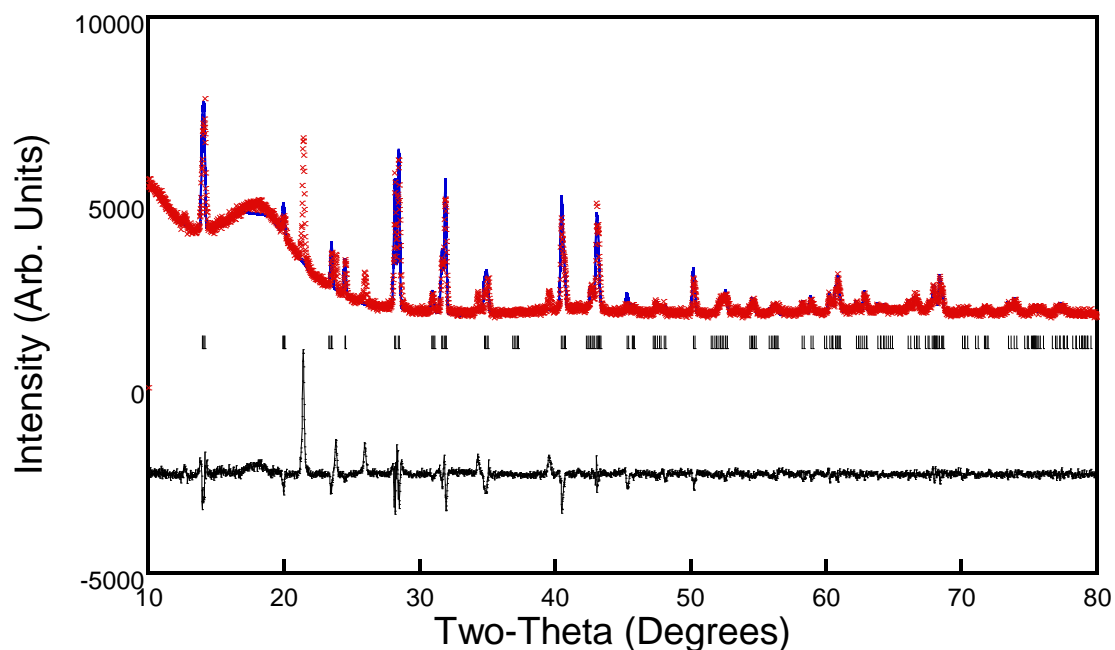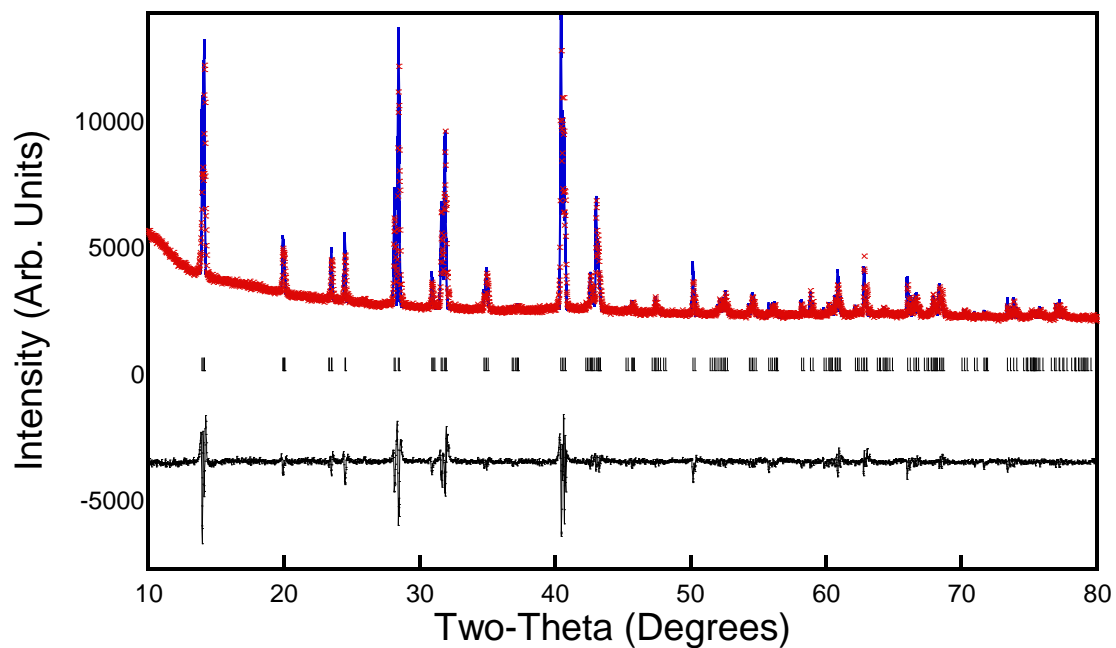

Figure 1A – 2 Observed (blue), calculated (red) and difference (black) data obtained from profile matching with constant scale factor of powder X-ray diffraction data of MAPbI$_3$ compound 1 annealed at 70 $^{\circ}$C for 1 hour.
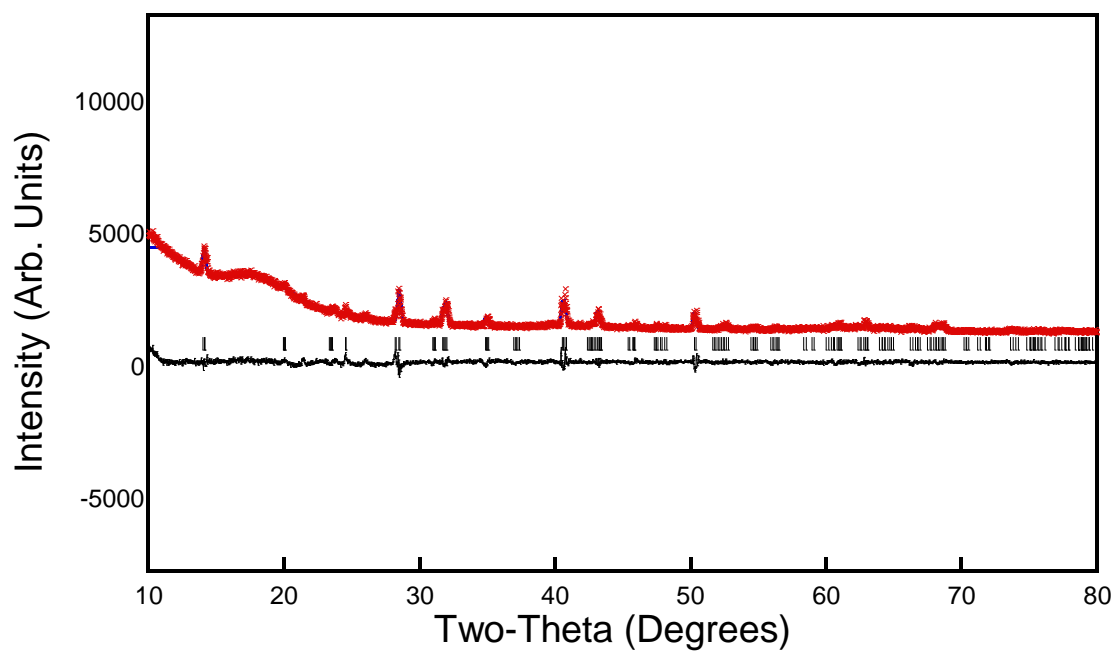
Figure 1A – 3 Observed (blue), calculated (red) and difference (black) data obtained from profile matching with constant scale factor of powder X-ray diffraction data of MAPbI$_3$ compound 1 annealed at 90 °C for 1 hour.
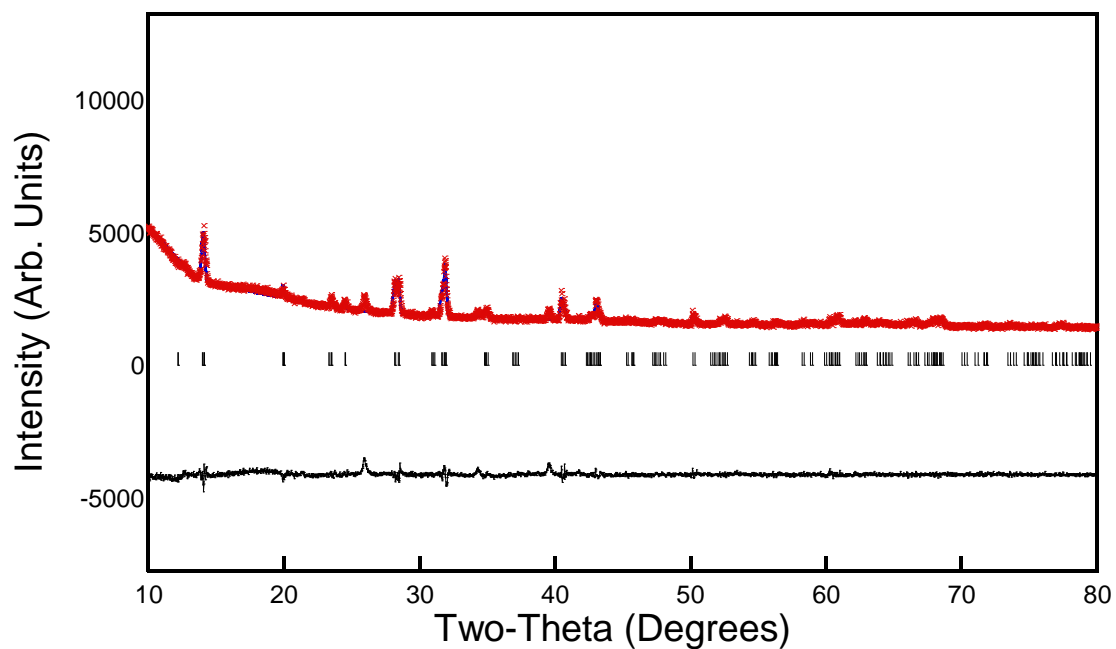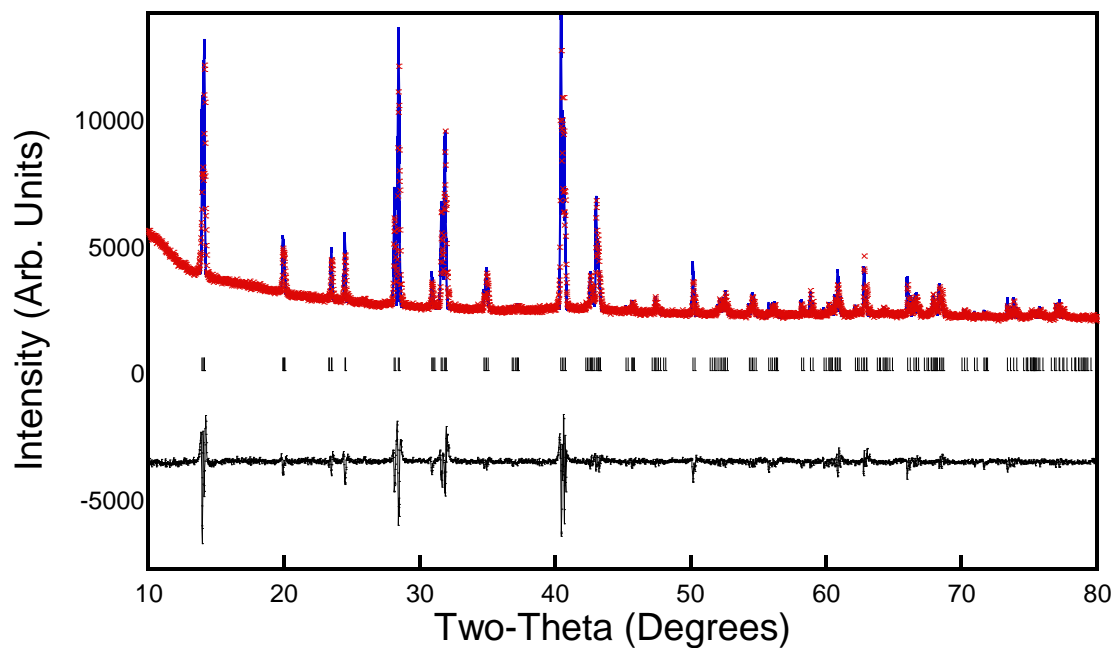

Figure 1A – 4 Observed (blue), calculated (red) and difference (black) data obtained from profile matching with constant scale factor of powder X-ray diffraction data of MAPbI$_3$ compound 1 annealed at 110 °C for 1 hour.

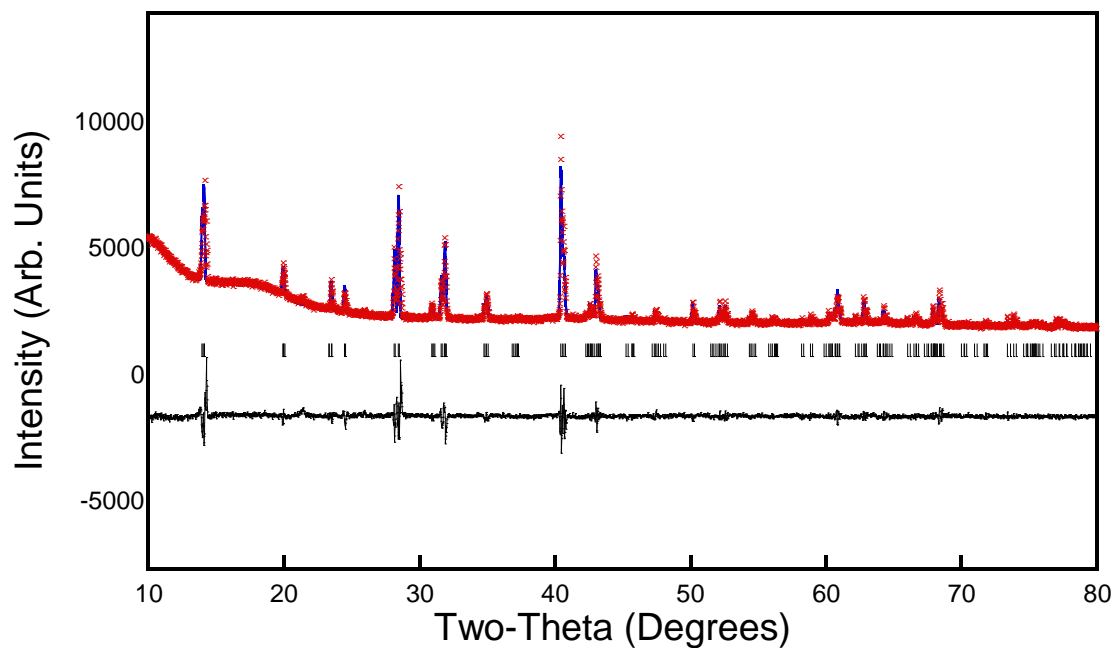**Air-annealed of MAPbI₃ compound 1 at 50, 70, 90 and 110ºC for 3 hours.**
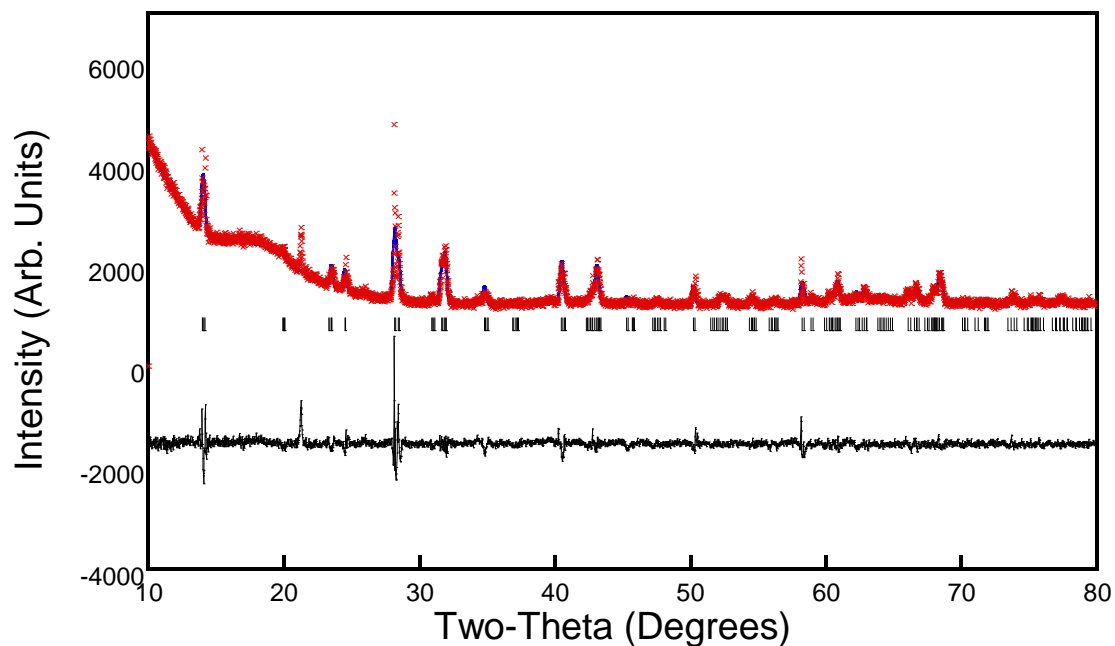
Figure 1A – 5 Observed (blue), calculated (red) and difference (black) data obtained from profile matching with constant scale factor of powder X-ray diffraction data of MAPbI₃ compound 1 annealed at 50 °C for 3 hours.
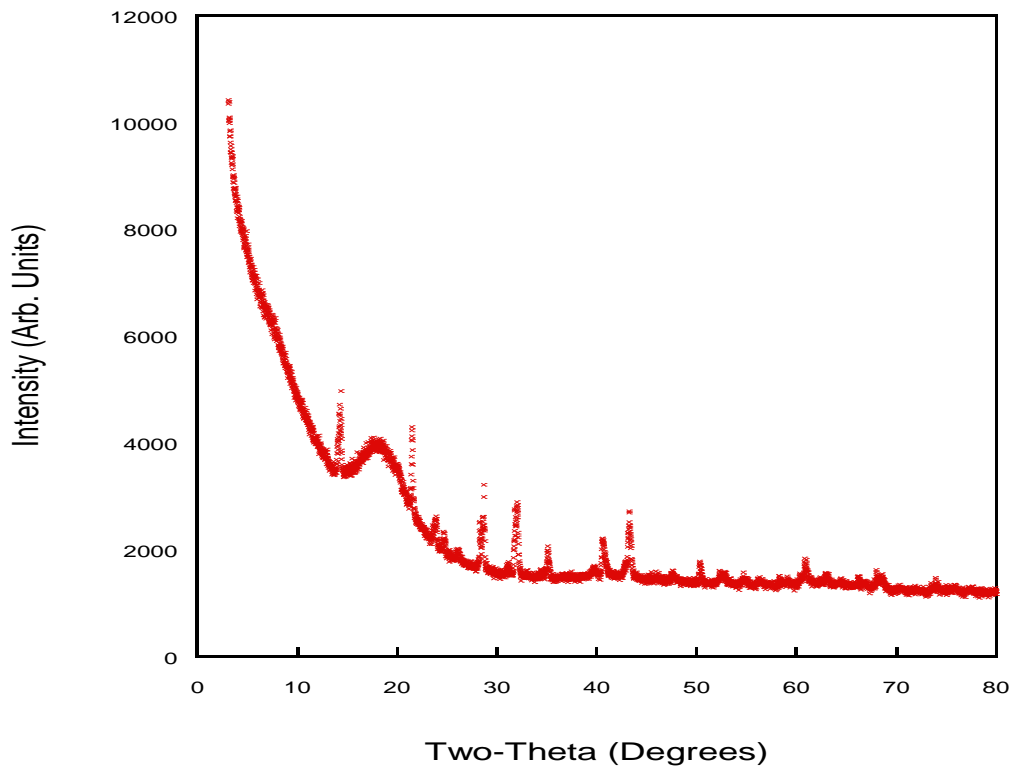
Figure 1A – 6 powder X-ray diffraction patterns of MAPbI₃ compound 1 annealed at 70 °C for 3 hours.
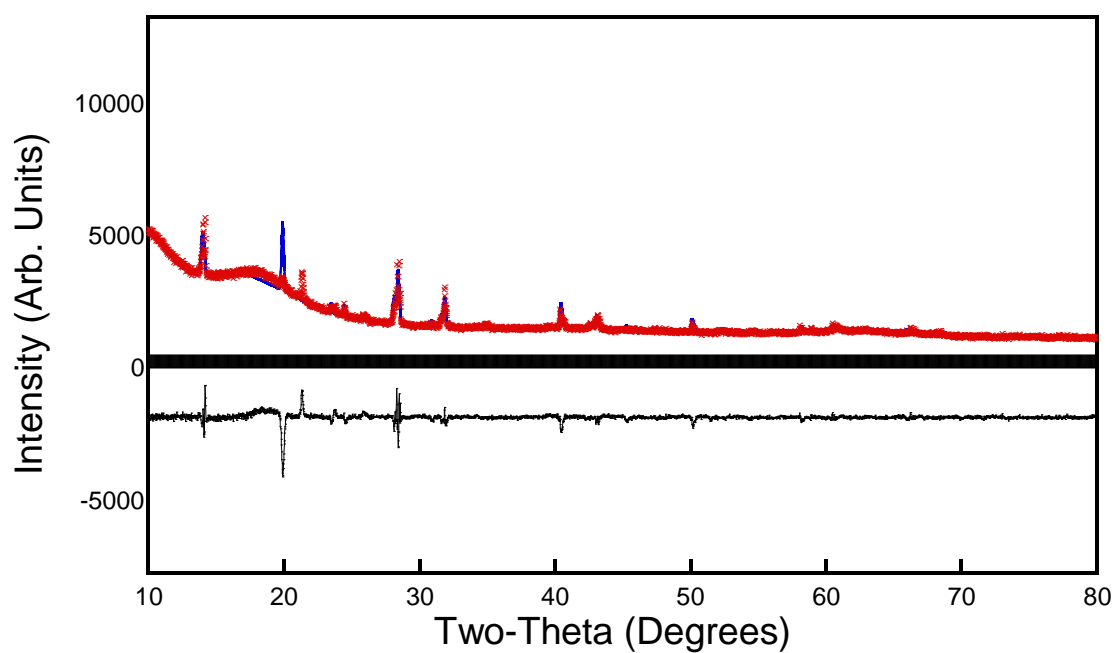
Figure 1A – 7 Observed (blue), calculated (red) and difference (black) data obtained from profile matching with constant scale factor of powder X-ray diffraction data of MAPbI$_3$ compound 1 annealed at 90 ^{o}C for 3 hours.

Figure 1A – 8 Observed (blue), calculated (red) and difference (black) data obtained from profile matching with constant scale factor of powder X-ray diffraction data of MAPbI$_3$ compound 1 annealed at 110 ^{o}C for 3 hours.

Figure 1A – 9 Observed (blue), calculated (red) and difference (black) data obtained from profile matching with constant scale factor of powder X-ray diffraction data of MAPbI$_3$ compound 2 annealed at 50 °C for 1 hours.

Figure 1A – 10 Observed (blue), calculated (red) and difference (black) data obtained from profile matching with constant scale factor of powder X-ray diffraction data of MAPbI$_3$ compound 2 annealed at 70 °C for 1 hours.

Figure 1A – 11 Observed (blue), calculated (red) and difference (black) data obtained Profile Matching with constant scale factor of powder X-ray diffraction data of MAPbI$_3$ compound 2 annealed at 90 ^{o}C for 1 hours.

Figure 1A – 12 Observed (blue), calculated (red) and difference (black) data obtained from profile matching with constant scale factor of powder X-ray diffraction data of MAPbI$_3$ compound 2 annealed at 110 ^{o}C for 1 hours.

Figure 1A – 13 Observed (blue), calculated (red) and difference (black) data obtained from profile matching with constant scale factor of powder X-ray diffraction data of MAPbI$_3$ compound 2 annealed at 50 ^{o}C for 3 hours.

Figure 1A – 14 Observed (blue), calculated (red) and difference (black) data obtained from profile matching with constant scale factor of powder X-ray diffraction data of MAPbI$_3$ compound 2 annealed at 70 ^{o}C for 3 hours.

Figure 1A – 15 Observed (blue), calculated (red) and difference (black) data obtained from profile matching with constant scale factor of powder X-ray diffraction data of MAPbI$_3$ compound 2 annealed at 90 ^{o}C for 3 hours.
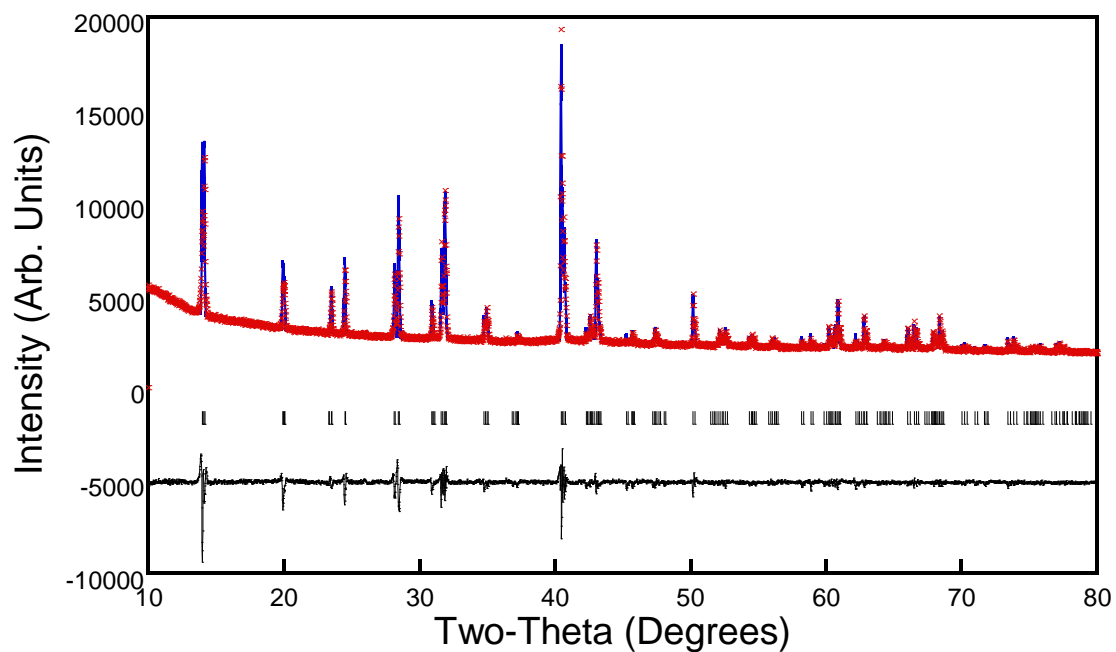

Figure 1A – 16 Observed (blue), calculated (red) and difference (black) data obtained from profile matching with constant scale factor of powder X-ray diffraction data of MAPbI$_3$ compound 2 annealed at 110 ^{o}C for 3 hours.

Tables of lattice parameter *a*, *c* and *c/a* ratio

Table 1. Compound 1 annealed for 1 hour

Temperature	Lattice *a*	Lattice *a* error	Lattice *c*	Lattice *c* error	*c/a* ratio
50.000	8.867860	1.000000e-04	12.67301	0.0001700000	1.429095
70.000	8.867900	0.0001900000	12.66556	0.0003200000	1.428248
90.000	8.855080	0.0005800000	12.64067	0.0008000000	1.427505
110.00	8.872890	0.0004000000	12.67035	0.0006900000	1.427984

Table 2. Compound 1 annealed for 3 hours

Temperature	Lattice *a*	Lattice *a* error	Lattice *c*	Lattice *c* error	*c/a* ratio
50.000	8.868440	0.0003400000	12.67663	0.0006000000	1.42941
70.000	8.870410	0.0001300000	12.68001	0.0002300000	1.42947
90.000	8.870110	0.0003300000	12.66697	0.0004700000	1.42805
110.00	8.866570	0.0002000000	12.67619	0.0003500000	1.42966

Table 3. Compound 2 annealed for 1 hour

Temperature	Lattice *a*	Lattice *a* error	Lattice *c*	Lattice *c* error	*c/a* ratio
50.000	8.869400	0.0001100000	12.67687	0.0001900000	1.429282
70.000	8.870350	0.0001300000	12.67780	0.0002500000	1.429233
90.000	8.866620	0.0002400000	12.66988	0.0003800000	1.428941
110.00	8.866180	8.000000e-05	12.67167	0.0001400000	1.429214

Table 4. Compound 2 annealed for 3 hours

Temperature	Lattice *a*	Lattice *a* error	Lattice *c*	Lattice *c* error	*c/a* ratio
50.000	8.868830	1.000000e-04	12.67704	0.0001700000	1.42939
70.000	8.870510	9.000000e-05	12.67935	0.0001700000	1.42938
90.000	8.868770	9.000000e-05	12.67249	0.0001500000	1.42889
110.00	8.869680	0.0001200000	12.67710	0.0002200000	1.42926

Table of atomic positions x,y,z and isotropic displacement parameter (B) for MAPbI$_3$ compound 1.

Atom	Atomic positions			
	x	*y*	*z*	Isotropic displacement parameter (B)
C1*	-0.03500(-)	0.43800(-)	0.22100(-)	23.55957(-)
I1	0.00000(-)	0.00000(-)	0.24972(13)	4.82246(-)
I2	-0.21272(17)	-0.28589(17)	0.50000(-)	4.82246(-)
Pb1	0.00000(-)	0.00000(-)	0.00000(-)	1.03126(-)
Pb2	0.00000(-)	0.00000(-)	0.50000(-)	1.03126(-)

3.2.6 Discussion of the vacuum annealing treatment at 90 °C
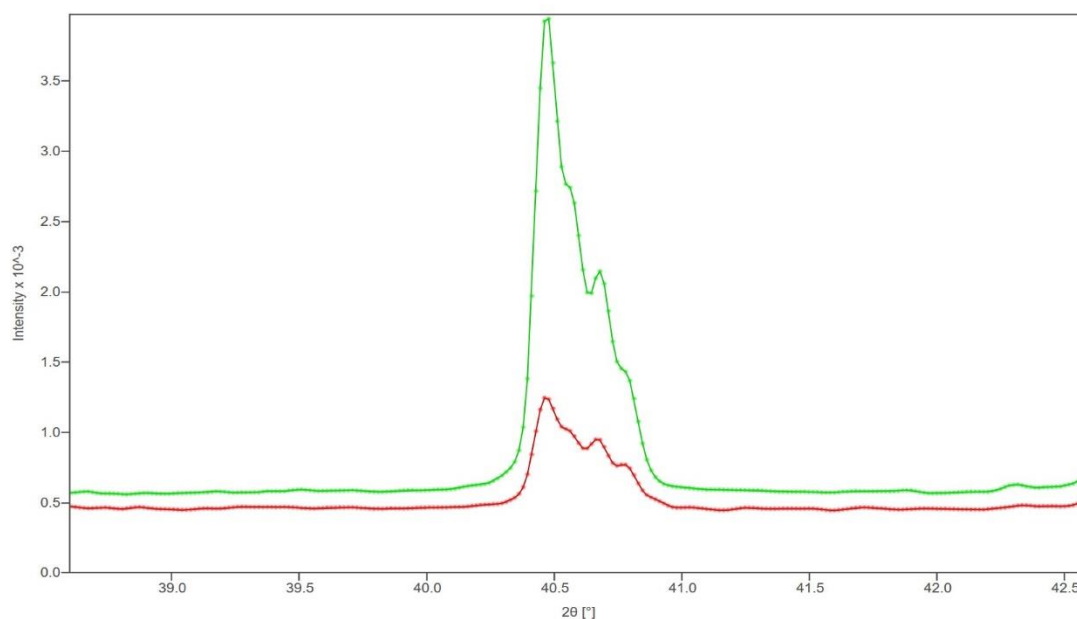
Figure 1A – 17. A comparison between MAPbI$_3$ compound 1 annealed at 90 °C for 1 hour and 72 hours, a significant increase in X-ray diffraction intensity is shown in 40.5 °C (224).

Time (hour)	Lattice a	Lattice a error	Lattice c	Lattice c error	c/a ratio
1.0000	8.868250	0.0001400000	12.67105	0.0002400000	1.4288
2.0000	8.866470	8.000000e-05	12.67128	0.0001400000	1.4291
3.0000	8.866940	8.000000e-05	12.67214	0.0001500000	1.4291
4.0000	8.869700	1.000000e-04	12.67838	0.0001700000	1.4294
5.0000	8.869500	9.000000e-05	12.67873	0.0001700000	1.4295
24.000	8.868160	9.000000e-05	12.67397	0.0001600000	1.4292
48.000	8.867960	8.000000e-05	12.67313	0.0001500000	1.4291
72.000	8.870570	9.000000e-05	12.67591	0.0001500000	1.4290

Table 5. Table of lattice parameter a,b and c/a ratio of MAPbI3 vacuum annealing treatment.

Results of structural characterisation of MAPbI₃ with vacuum annealing treatment at 90 °C
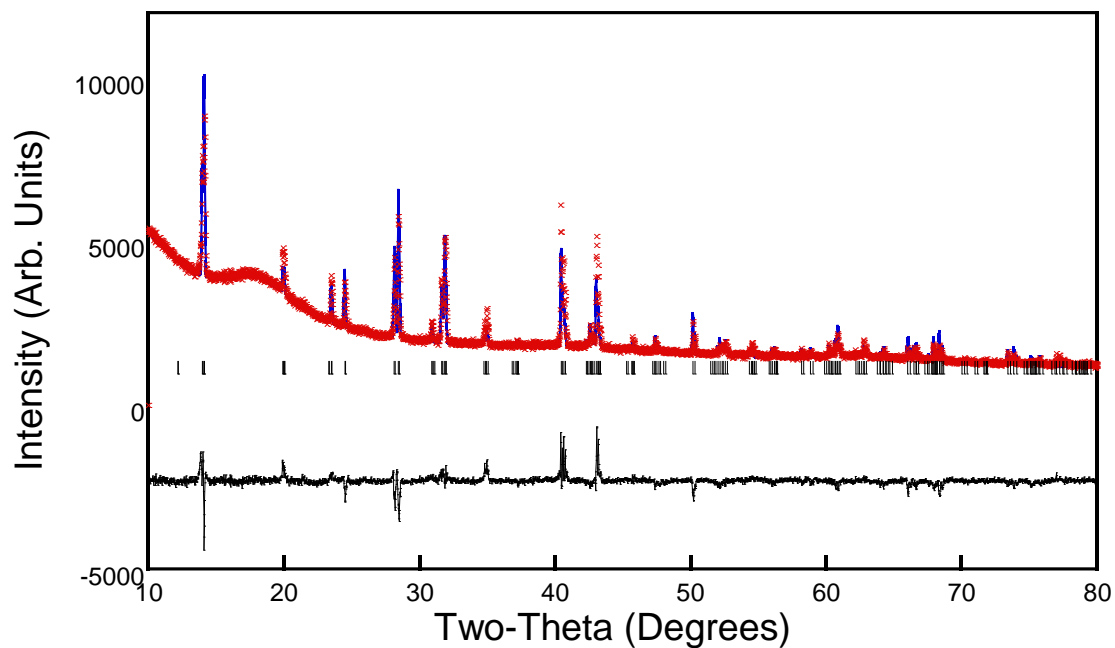
Figure 1A – 18 Observed (blue), calculated (red) and difference (black) data obtained from Rietveld refinement of powder X-ray diffraction data of MAPbI₃ compound 1 annealed at 90 °C for 1 hour.
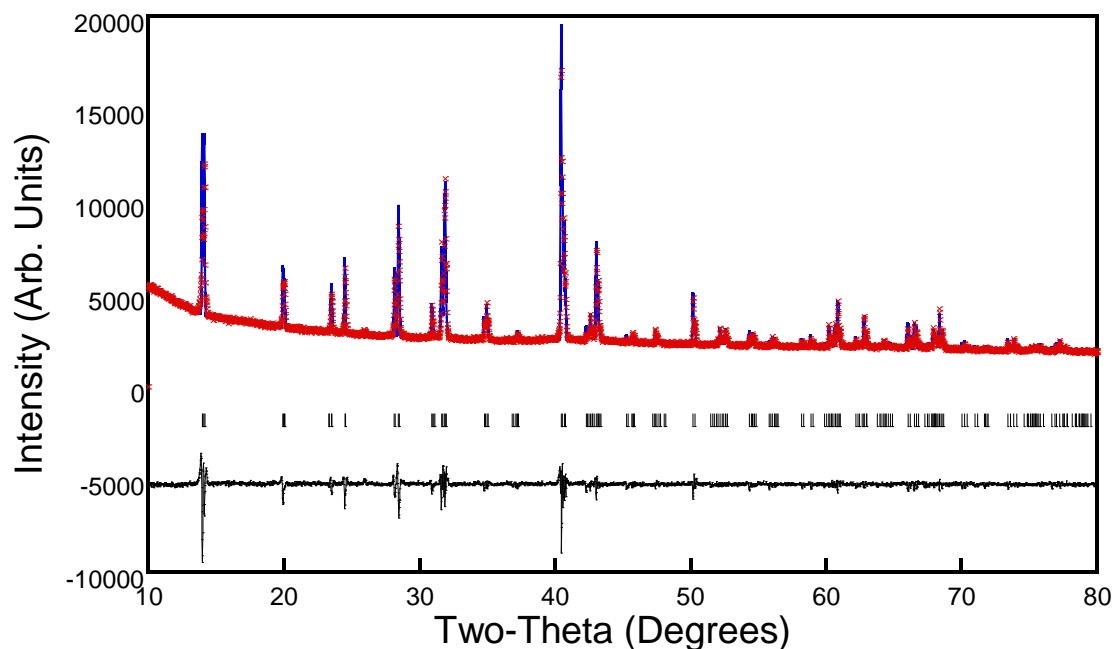
Figure 1A – 19 Observed (blue), calculated (red) and difference (black) data obtained from Rietveld refinement of powder X-ray diffraction data of MAPbI₃ compound 1 annealed at 90 °C for 2 hours.
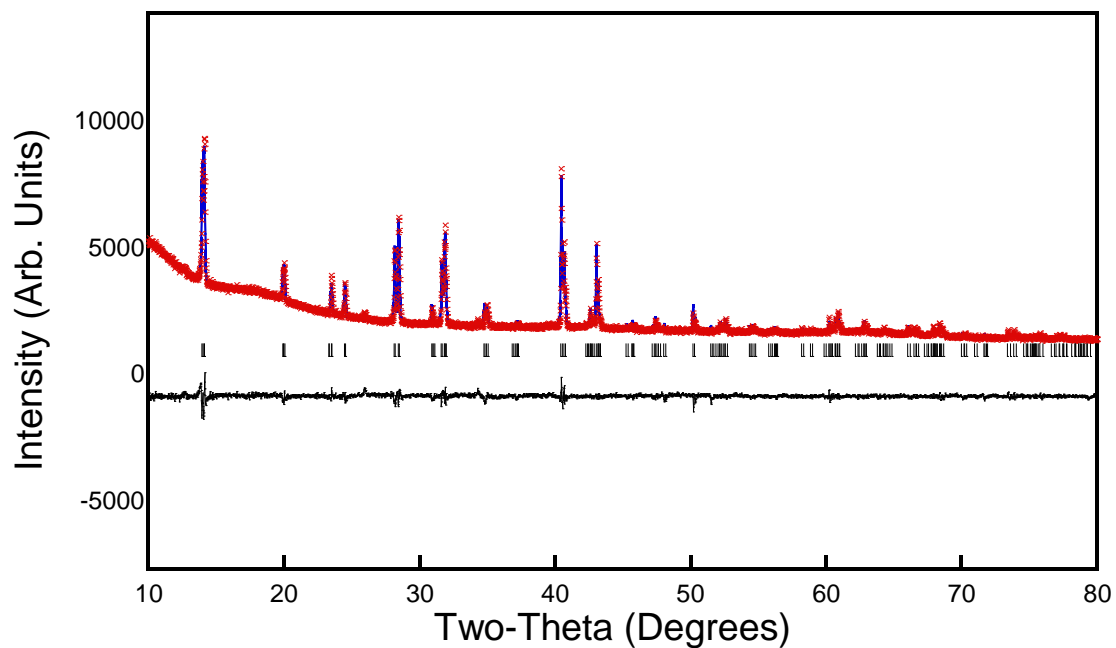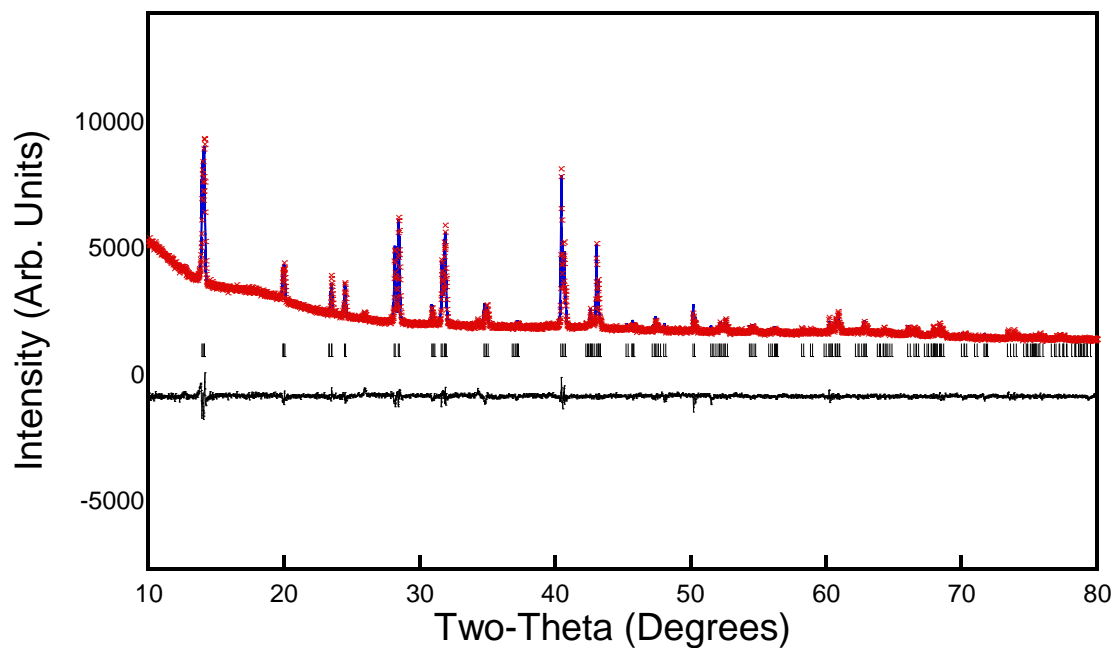
Figure 1A – 20 Observed (blue), calculated (red) and difference (black) data obtained profile matching with constant scale factor of powder X-ray diffraction data of MAPbI$_3$ compound 1 annealed at 90 ^{o}C for 3 hours.
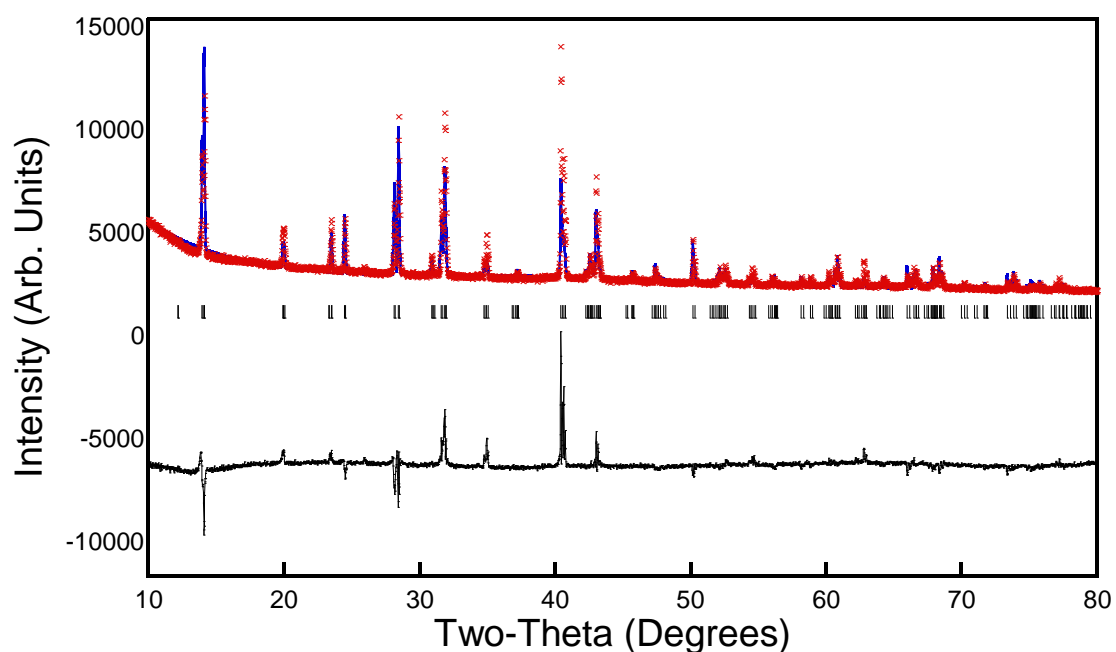
Figure 1A – 21 Observed (blue), calculated (red) and difference (black) data obtained from Rietveld refinement of powder X-ray diffraction data of MAPbI$_3$ compound 1 annealed at 90 ^{o}C for 4 hours.
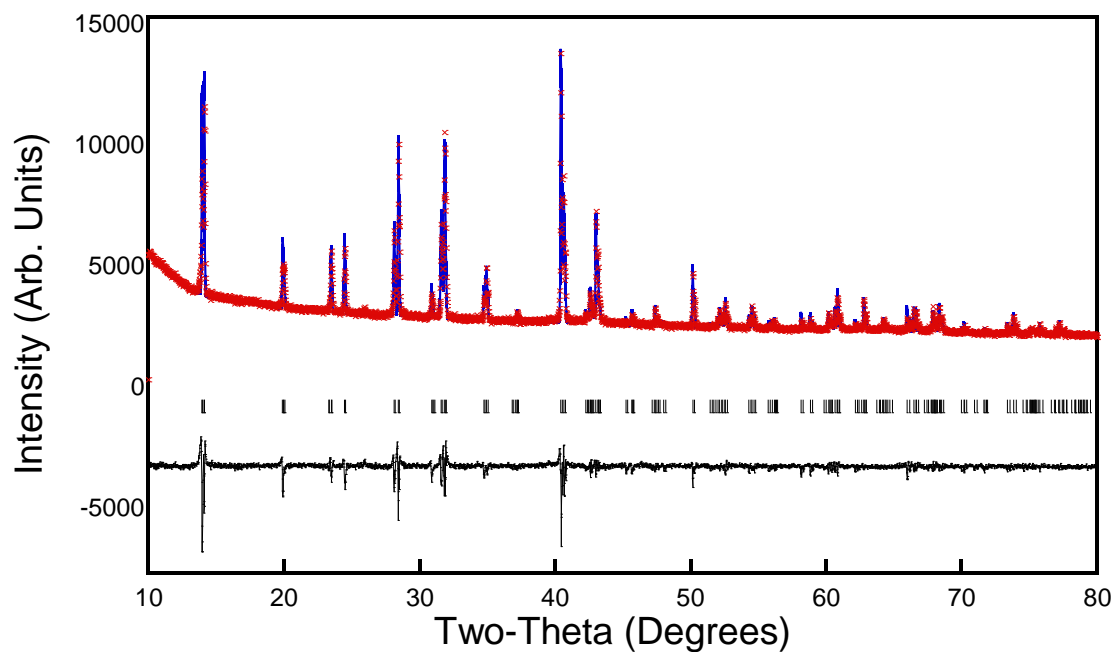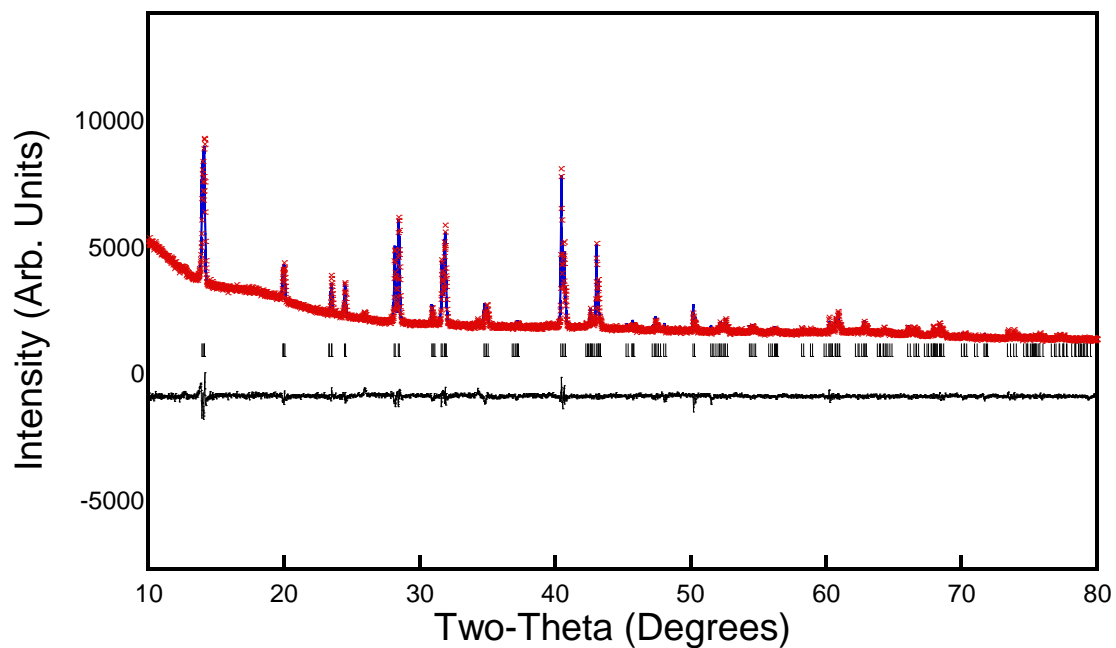
Figure 1A – 22 Observed (blue), calculated (red) and difference (black) data obtained profile matching with constant scale factor of powder X-ray diffraction data of MAPbI₃ compound 1 annealed at 90 °C for 5 hours.
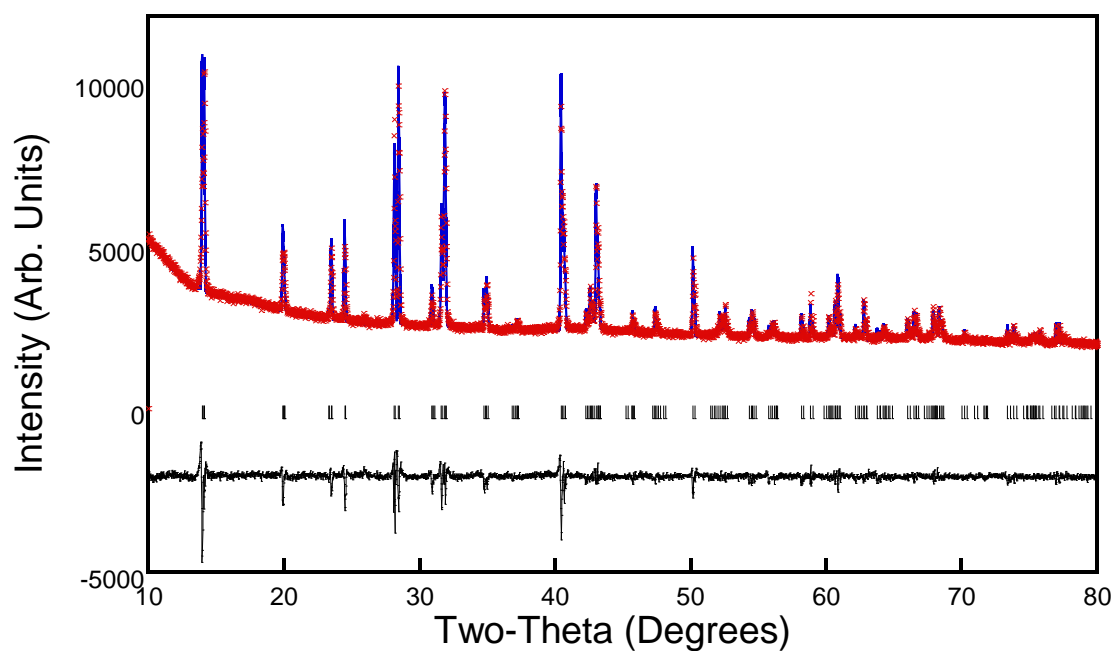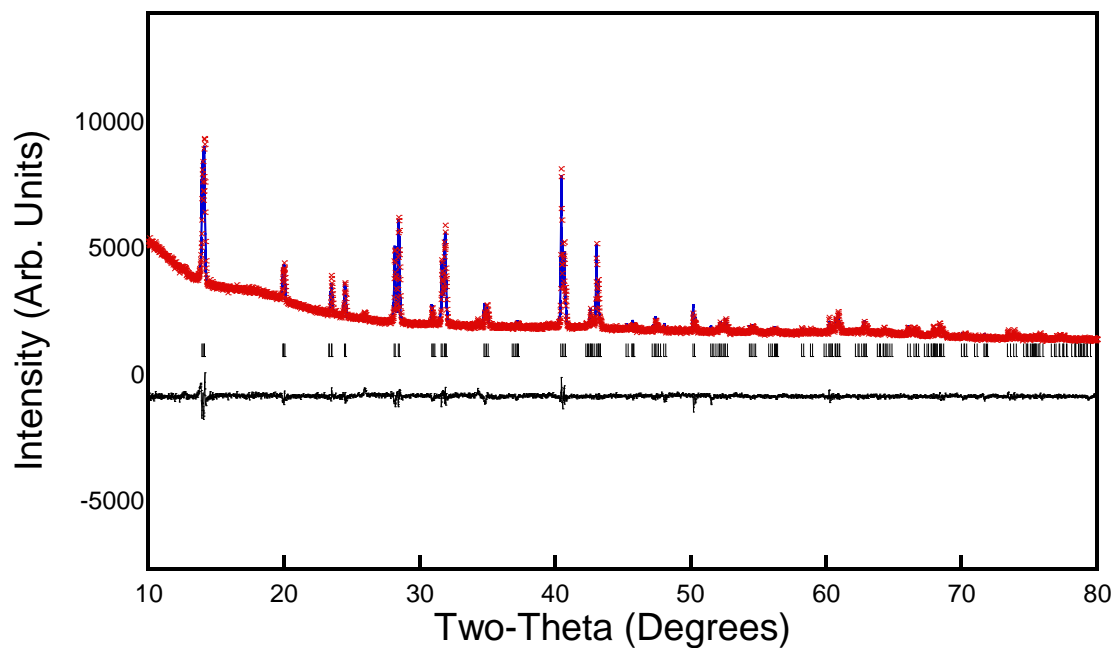

Figure 1A – 23 Observed (blue), calculated (red) and difference (black) data obtained profile matching with constant scale factor of powder X-ray diffraction data of MAPbI₃ compound 1 annealed at 90 °C for 24 hours.
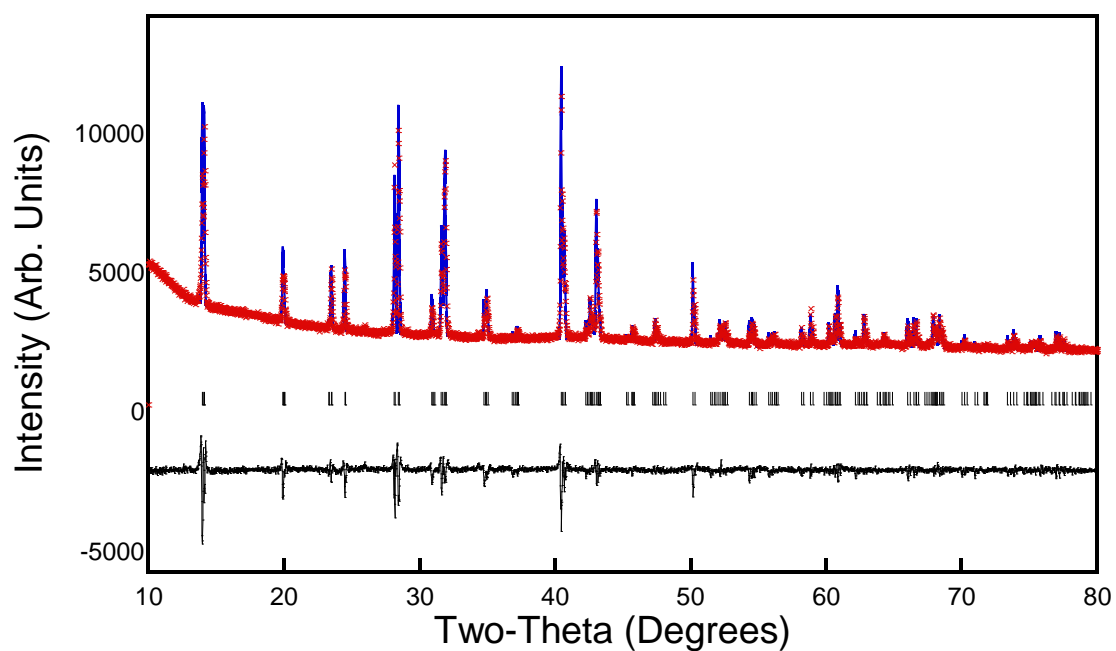
Figure 1A – 24 Observed (blue), calculated (red) and difference (black) data obtained profile matching with constant scale factor of powder X-ray diffraction data of MAPbI$_3$ compound 1 annealed at 90 $^{\circ}$C for 48 hours.
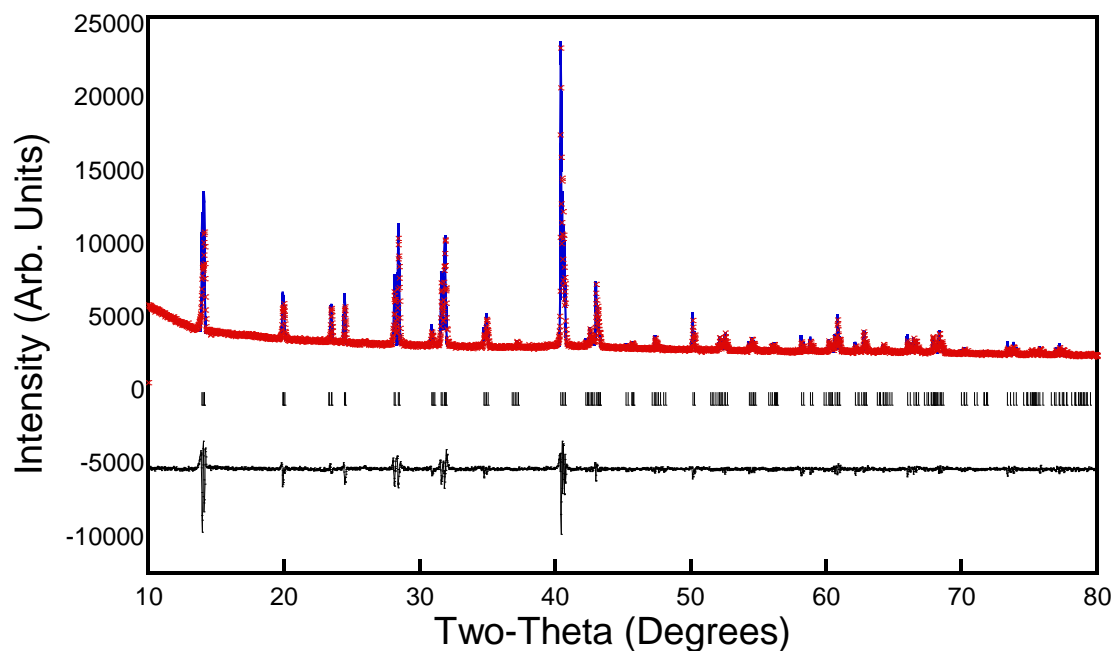
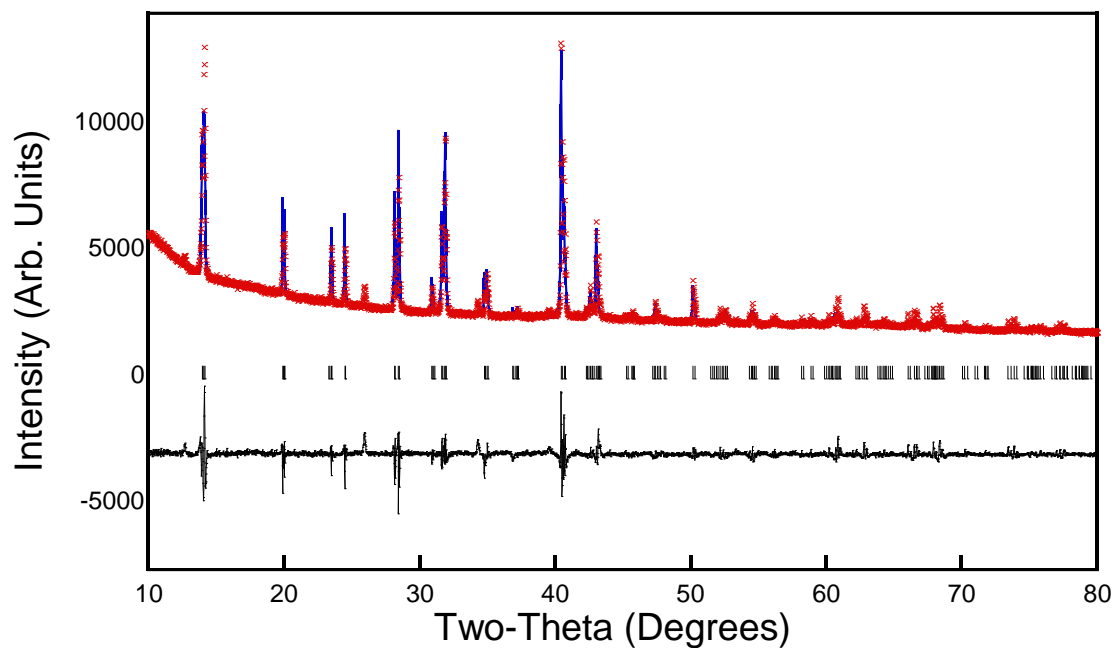Figure 1A – 25 Observed (blue), calculated (red) and difference (black) data obtained profile matching with constant scale factor of powder X-ray diffraction data of MAPbI$_3$ compound 1 annealed at 90 $^{\circ}$C for 78 hours.

3.2.8 Annealing with zinc metal at 100°C, 150 °C and 200 °C under vacuum condition
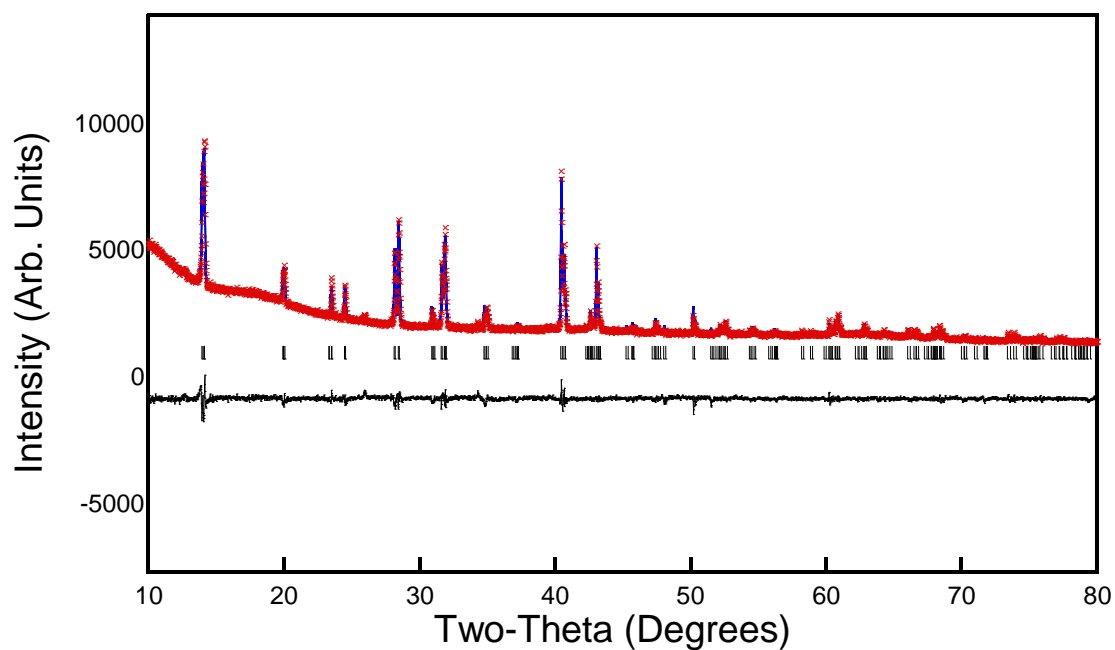
Figure 1A – 26 Observed (blue), calculated (red) and difference (black) data obtained from profile matching with constant scale factor of powder X-ray diffraction data of MAPbI₃ annealed without zinc metal under vacuum condition at 90 °C.
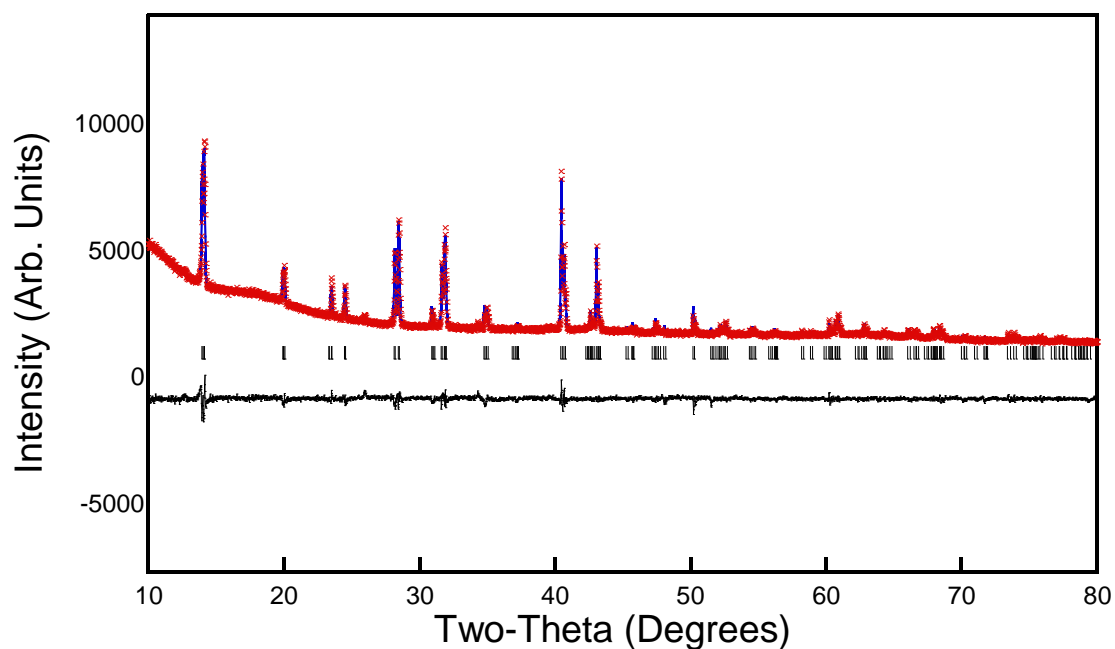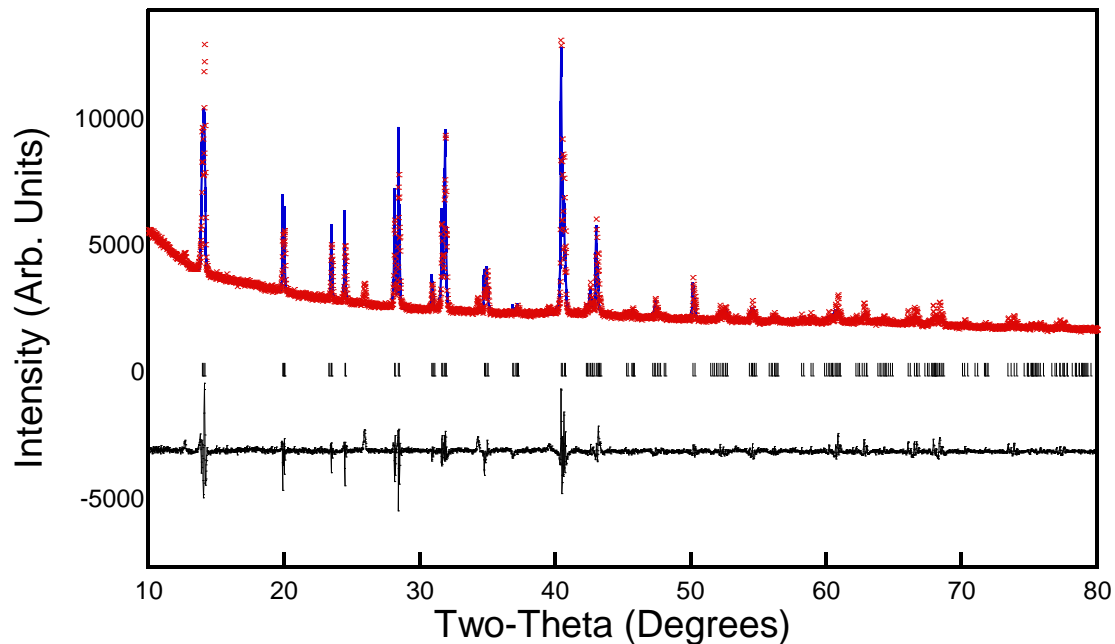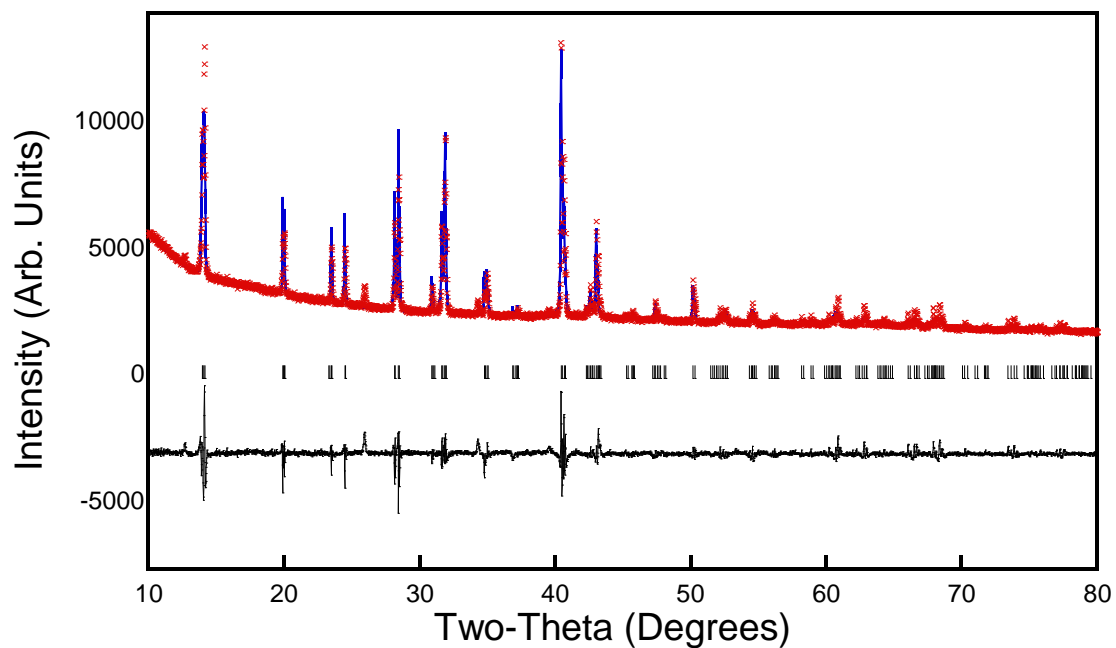

Figure 1A – 27 Observed (blue), calculated (red) and difference (black) data obtained from profile matching with constant scale factor of powder X-ray diffraction data of MAPbI₃ annealed without zinc metal under vacuum condition at 95 °C
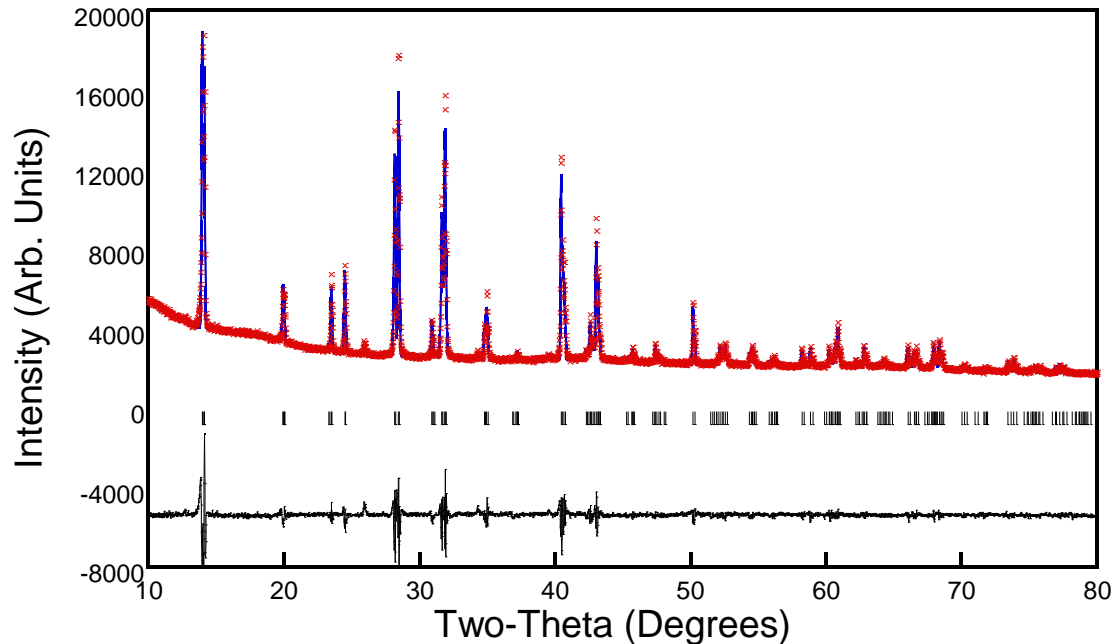
Figure 1A – 28 Observed (blue), calculated (red) and difference (black) data obtained from profile matching with constant scale factor of powder X-ray diffraction data of MAPbI₃ annealed with zinc metal under vacuum condition at 90 °C.

Figure 1A – 29 Observed (blue), calculated (red) and difference (black) data obtained from profile matching with constant scale factor of powder X-ray diffraction data of MAPbI₃ annealed with zinc metal under vacuum condition at 95 °C.
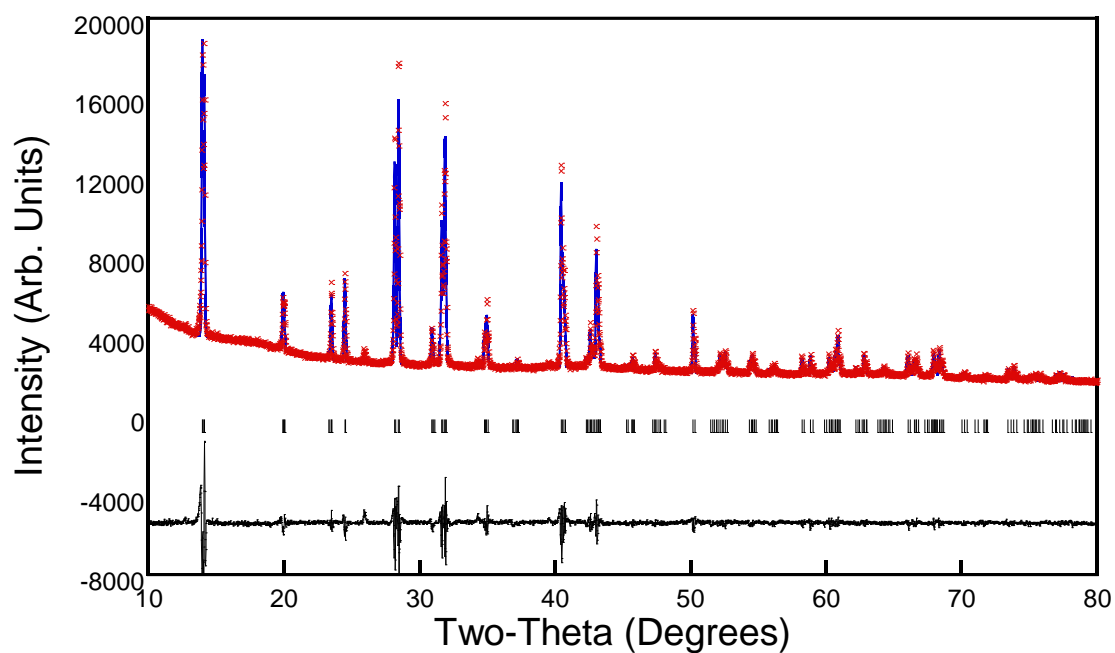
Figure 1A – 30 Observed (blue), calculated (red) and difference (black) data obtained from profile matching with constant scale factor of powder X-ray diffraction data of MAPbI$_3$ annealed with zinc metal under vacuum condition at 100 $^{\circ}$C.
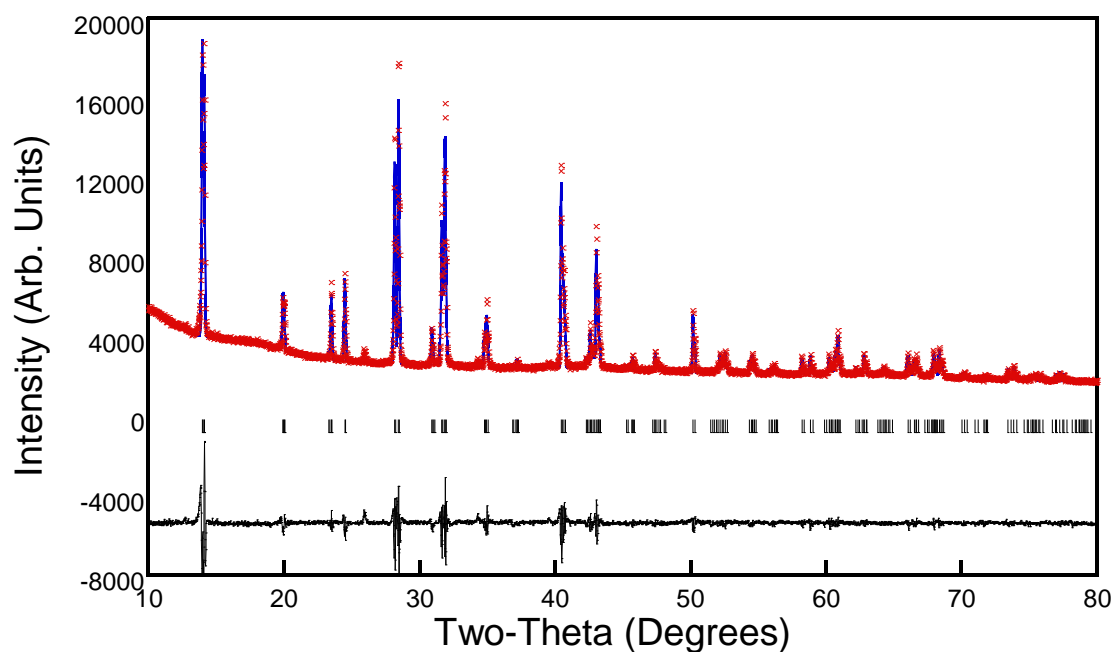

Figure 1A – 31 Observed (blue), calculated (red) and difference (black) data obtained from profile matching with constant scale factor of powder X-ray diffraction data of MAPbI$_3$ annealed with zinc metal under vacuum condition at 100 $^{\circ}$C.

Figure 1A – 32 Observed (blue), calculated (red) and difference (black) data obtained from profile matching with constant scale factor of powder X-ray diffraction data of MAPbI$_3$ annealed without zinc metal under vacuum condition at 140 °C.
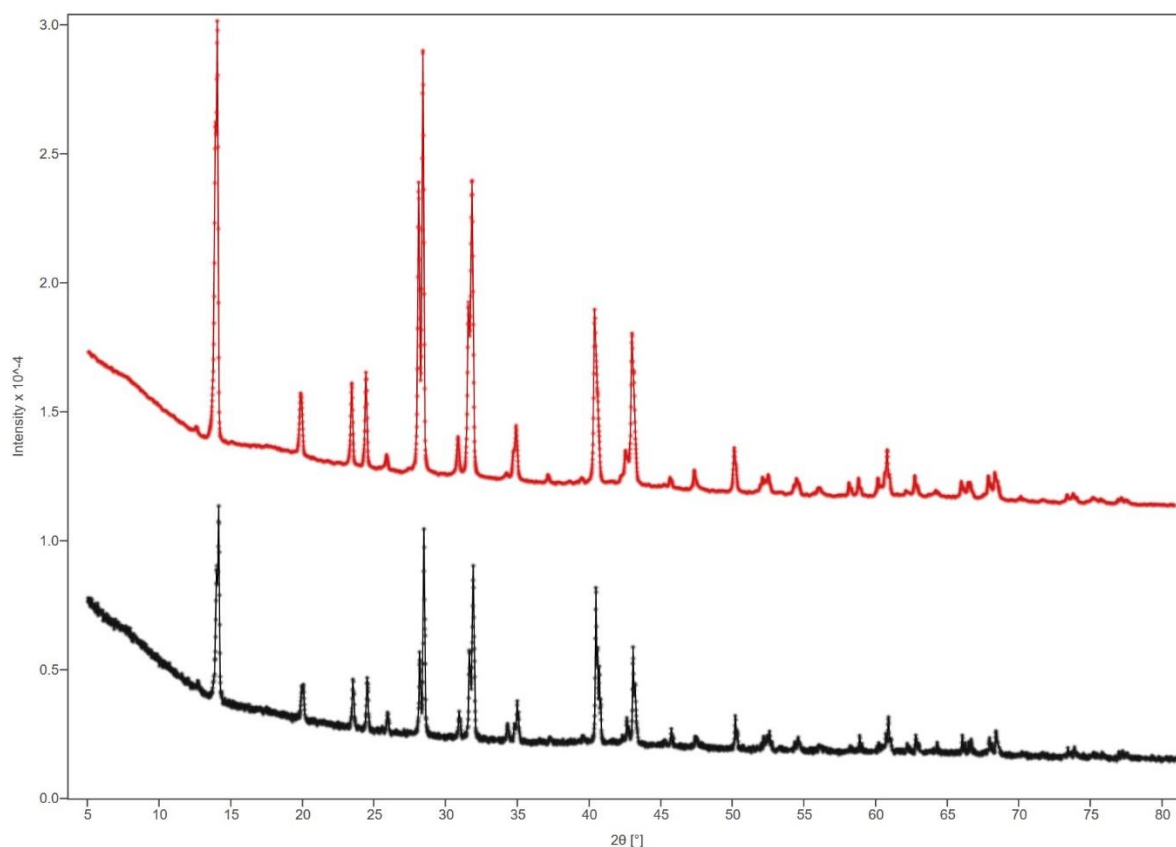

Figure 1A – 33 Observed (blue), calculated (red) and difference (black) data obtained from profile matching with constant scale factor of powder X-ray diffraction data of MAPbI$_3$ annealed without zinc metal under vacuum condition at 145 °C.

Figure 1A – 34 Observed (blue), calculated (red) and difference (black) data obtained from profile matching with constant scale factor of powder X-ray diffraction data of MAPbI₃ annealed without zinc metal under vacuum condition at 150 °C.

Figure 1A – 35 Observed (blue), calculated (red) and difference (black) data obtained from profile matching with constant scale factor of powder X-ray diffraction data of MAPbI₃ annealed with zinc metal under vacuum condition at 140 °C.

Figure 1A – 36 Observed (blue), calculated (red) and difference (black) data obtained from profile matching with constant scale factor of powder X-ray diffraction data of MAPbI₃ annealed with zinc metal under vacuum condition at 145 ℃.

Figure 1A – 37 Observed (blue), calculated (red) and difference (black) data obtained from profile matching with constant scale factor of powder X-ray diffraction data of MAPbI₃ annealed with zinc metal under vacuum condition at 150 ℃.

Figure 1A – 35 A comparison of the X-ray diffraction patterns of MAPbI$_3$ annealed with zinc (red) and without zinc (black).

Temperature (°C)	Lattice a	Lattice a error	Lattice c	Lattice c error	c/a ratio
90	8.875660	0.0002400000	12.68056	0.0003700000	1.42869
95	8.868030	0.0002200000	12.67046	0.0003200000	1.42878
100	8.867870	0.0001400000	12.67023	0.0002200000	1.42878
140	8.868150	0.0001100000	12.66757	0.0001800000	1.42843
145	8.864810	0.0001900000	12.66368	0.0003000000	1.42853
150	8.885910	0.0002500000	12.69102	0.0004200000	1.42822

Table 6. Lattice parameter *a, c* and *c/a* ratio of MAPbI$_3$ compound 2 annealed with zinc metal at 100, 150 and 200 °C.

Temperature (°C)	Lattice a	Lattice a error	Lattice c	Lattice c error	c/a ratio
90	8.864130	6.000000e-05	12.66370	0.0001200000	1.42865
95	8.866970	0.0001700000	12.66987	0.0002700000	1.42888
100	8.871120	0.0002300000	12.67380	0.0003500000	1.42866
140	8.865860	0.0001800000	12.67000	0.0002600000	1.429077
145	8.868440	0.0001800000	12.67209	0.0002900000	1.428897
150	8.867750	0.0001700000	12.67191	0.0002600000	1.428988

Table 7. Lattice parameter *a, c* and *c/a* ratio of MAPbI$_3$ compound 2 annealed without zinc metal at 100, 150 and 200 °C.

Appendix 2

Chapter 4. Synthesis, structural characterisation of a new mixed valence iron (Fe^{2+}/Fe^{3+}) metal fluoride pyrochlores

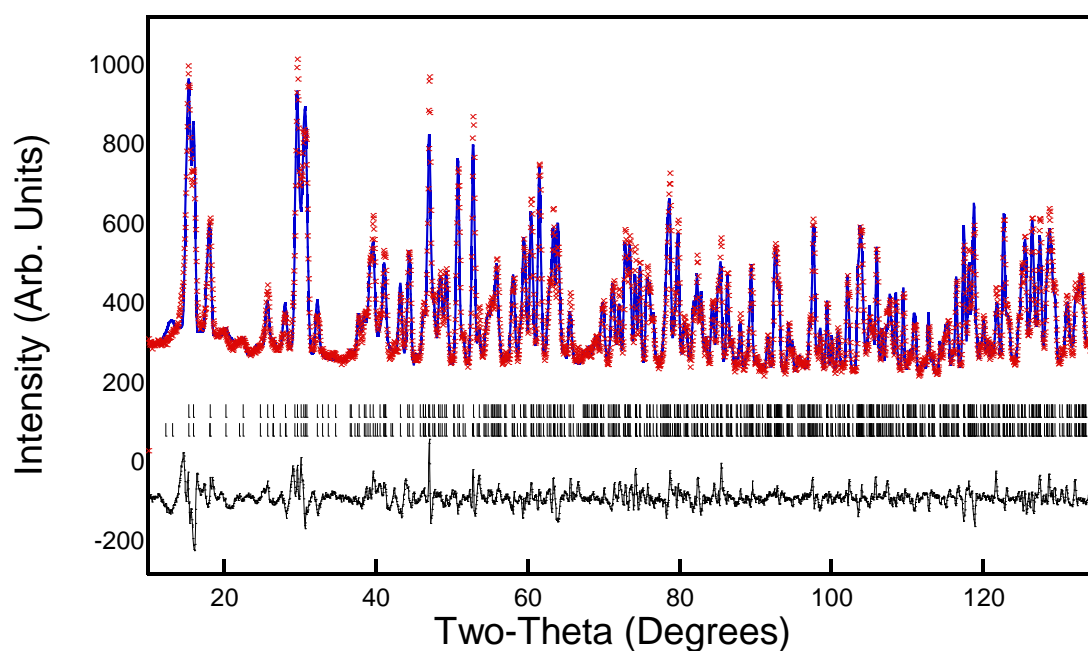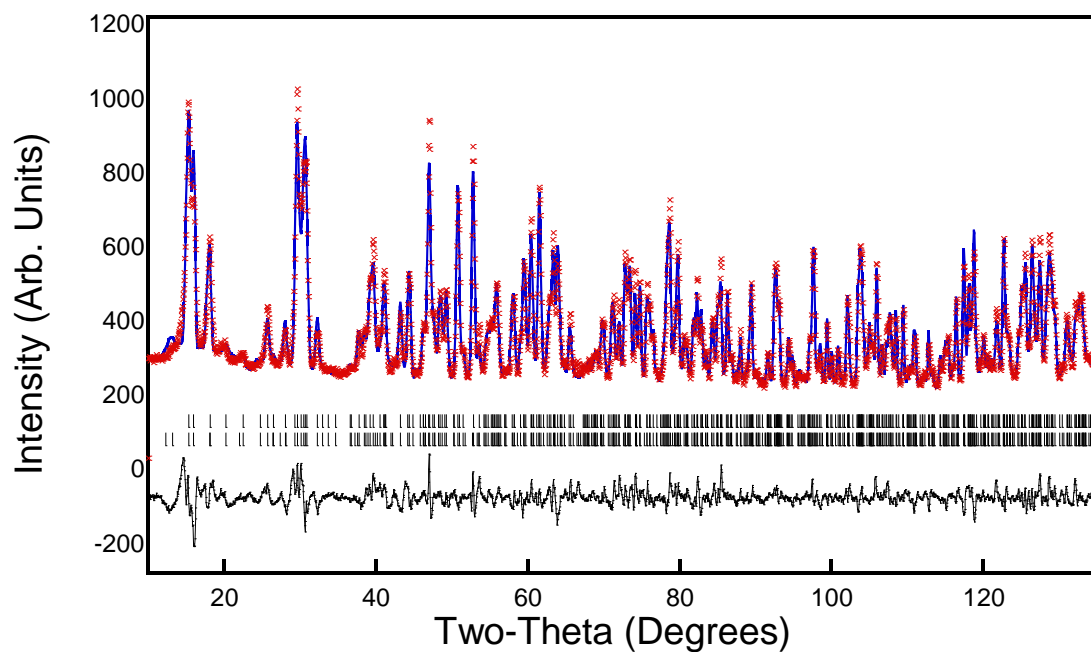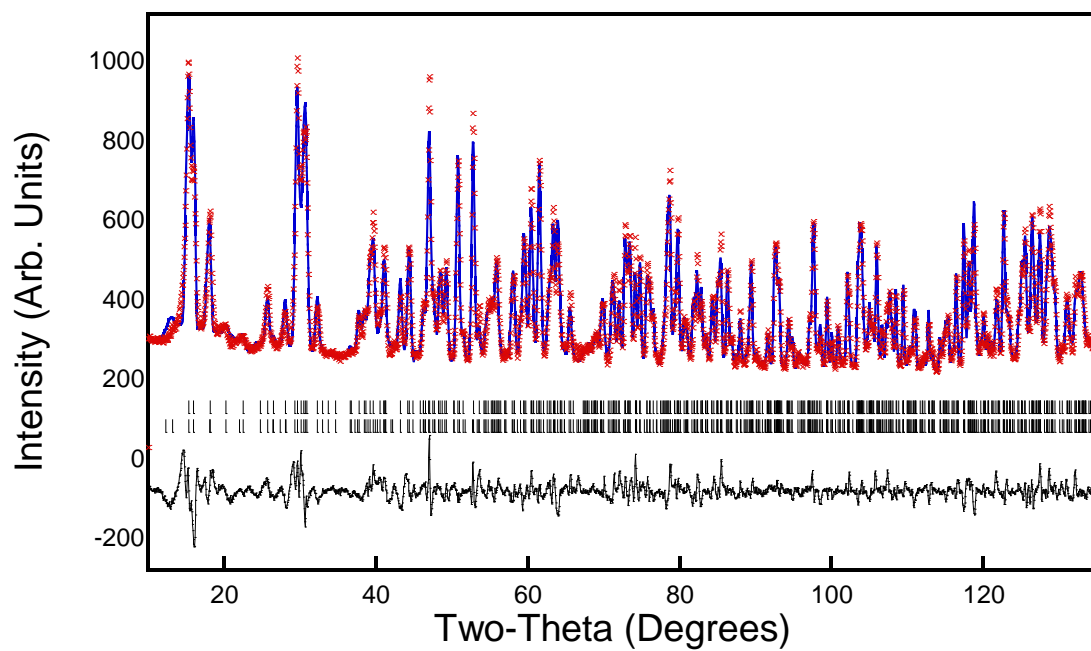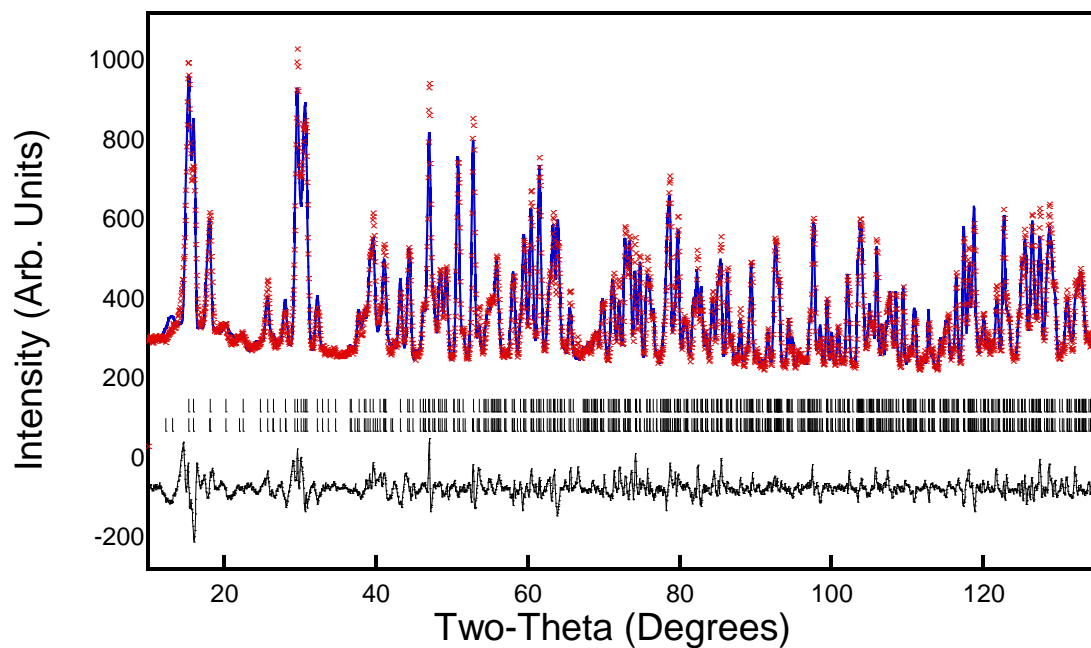Rietveld refinement of powder neutron diffraction data of $RbFe_2F_6$ between 1.5 K to 100 K.
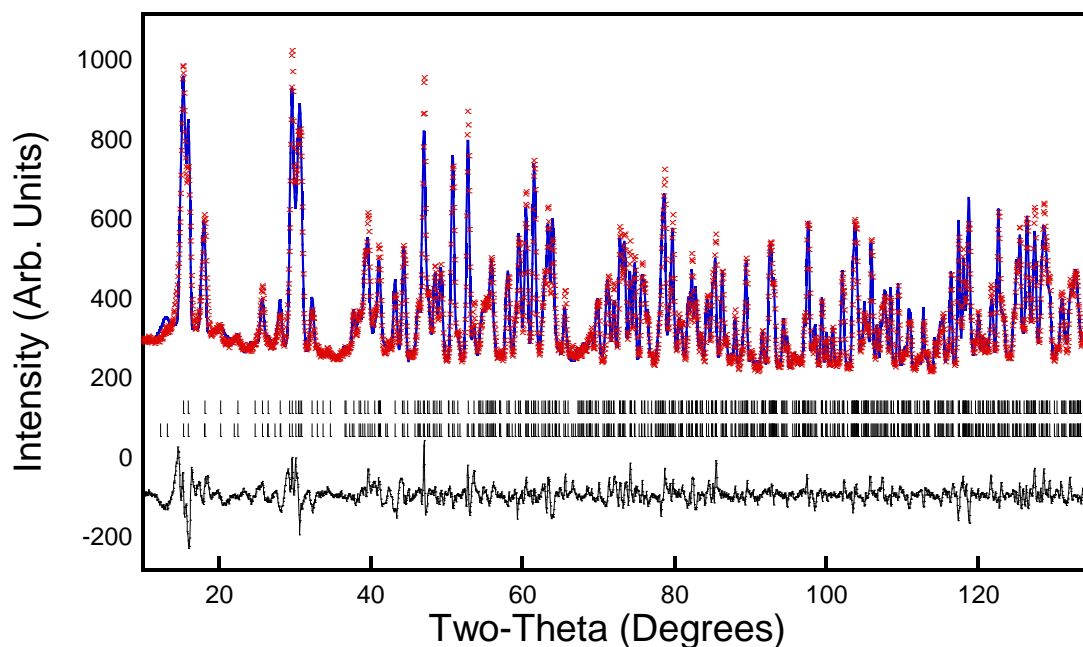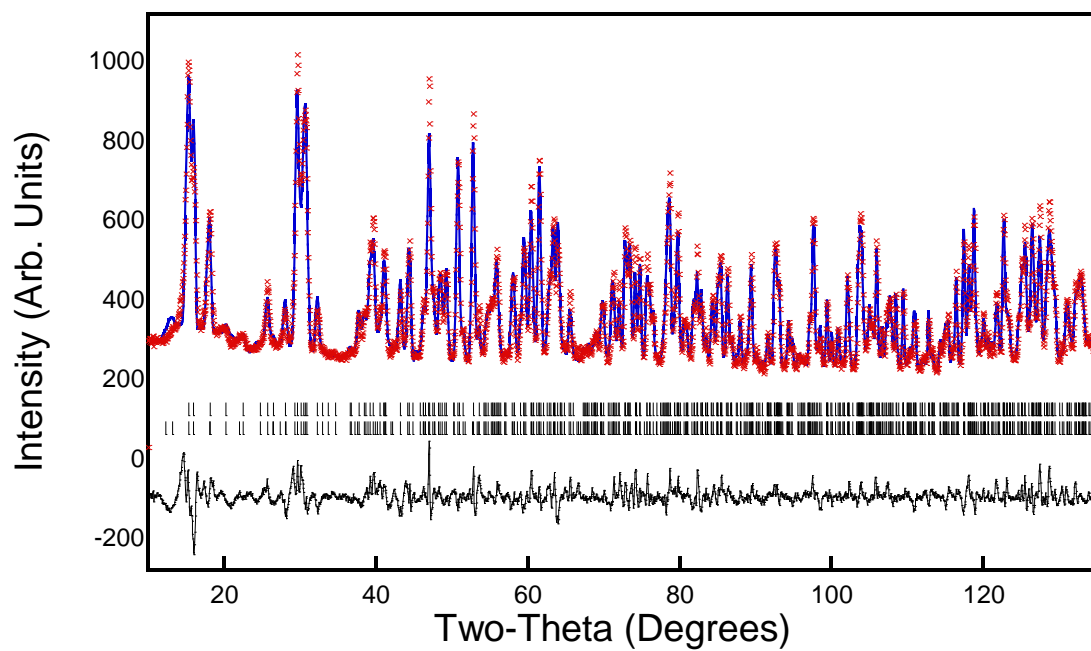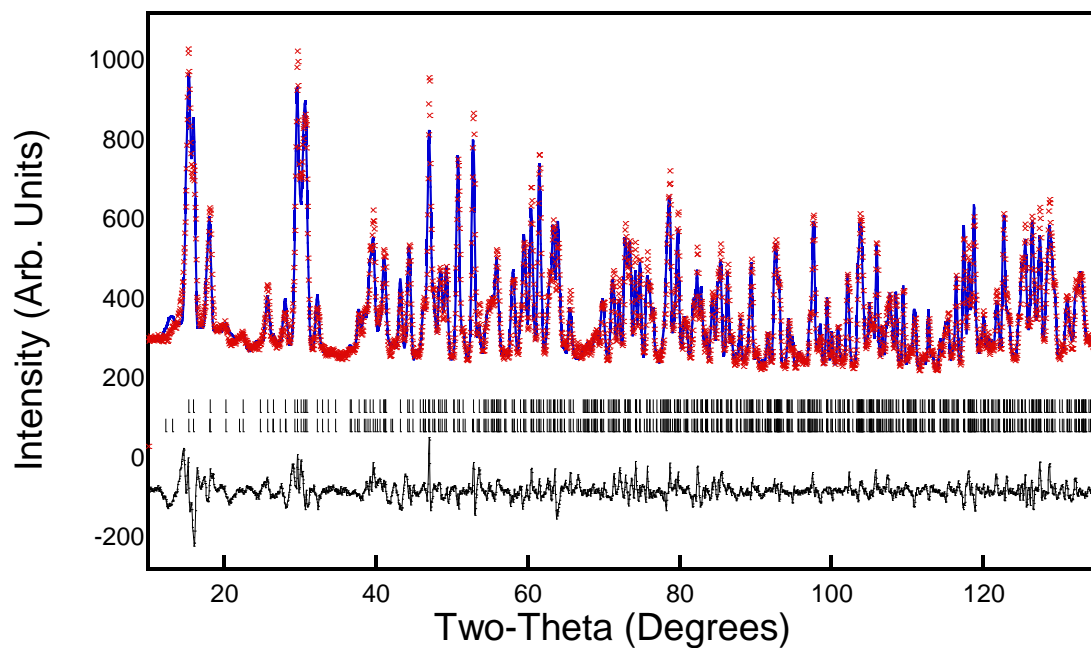

Figure 2A – 1. Observed (red markers), calculated (blue lines) and difference (black lines) obtained from Rietveld refinement of powder neutron diffraction data of $RbFe_2F_6$ at 1.5 K.

Figure 2A – 2. Observed (red markers), calculated (blue lines) and difference (black lines) obtained from Rietveld refinement of powder neutron diffraction data of $RbFe_2F_6$ at 2 K.

Figure 2A – 3. Observed (red markers), calculated (blue lines) and difference (black lines) obtained from Rietveld refinement of powder neutron diffraction data of $RbFe_2F_6$ at 2.5 K.
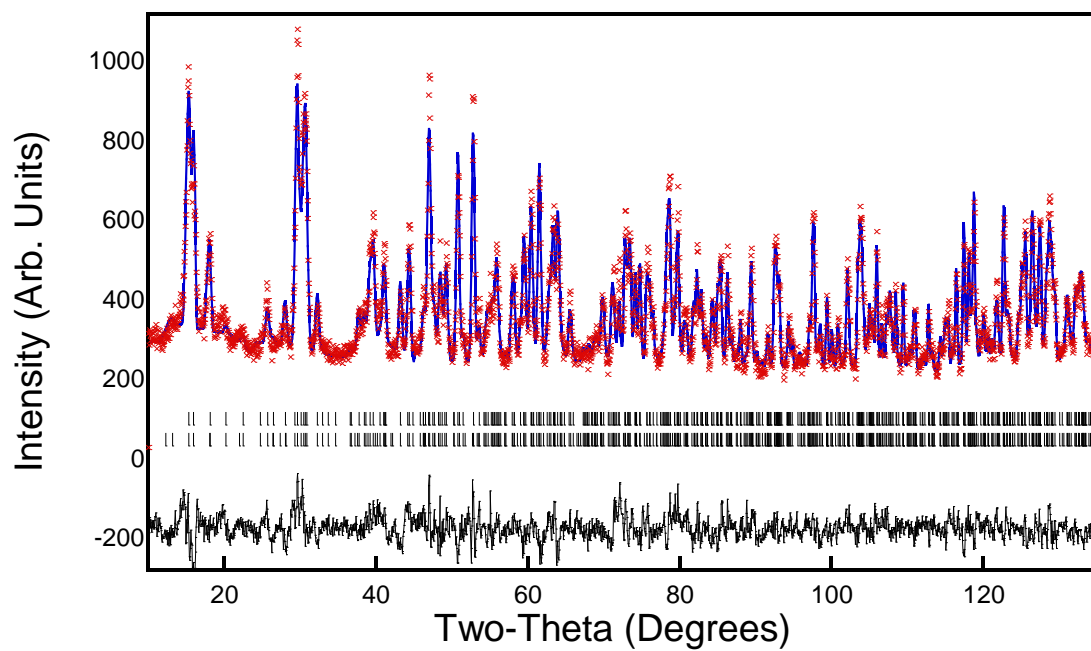

Figure 2A – 4. Observed (red markers), calculated (blue lines) and difference (black lines) obtained from Rietveld refinement of powder neutron diffraction data of $RbFe_2F_6$ at 3 K.
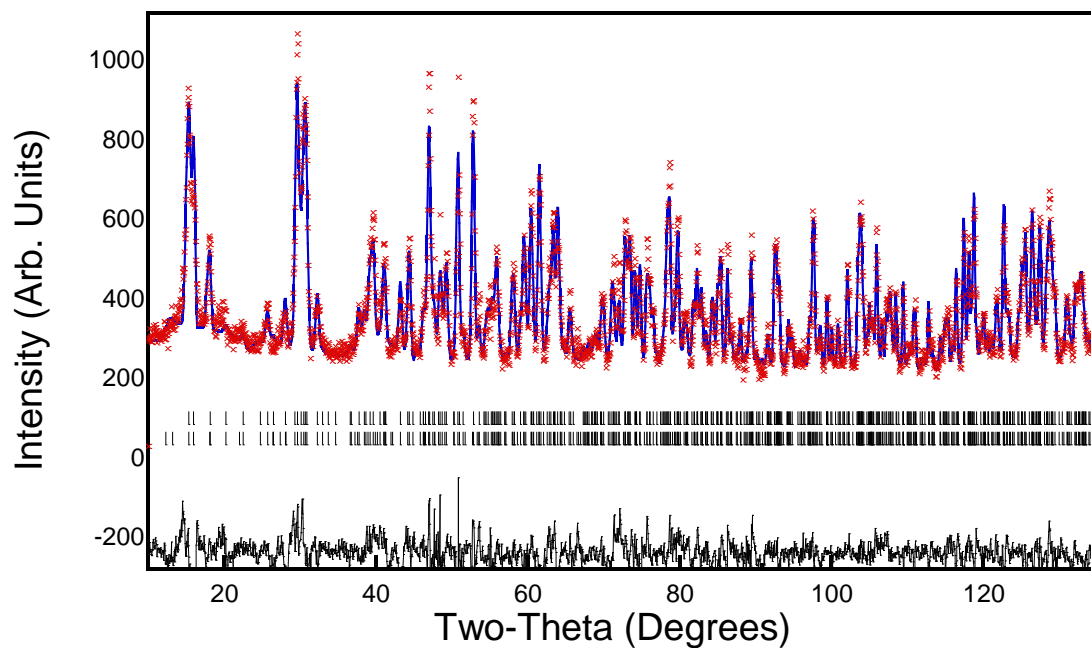
Figure 2A – 5. Observed (red markers), calculated (blue lines) and difference (black lines) obtained from Rietveld refinement of powder neutron diffraction data of RbFe$_2$F$_6$ at 4 K.
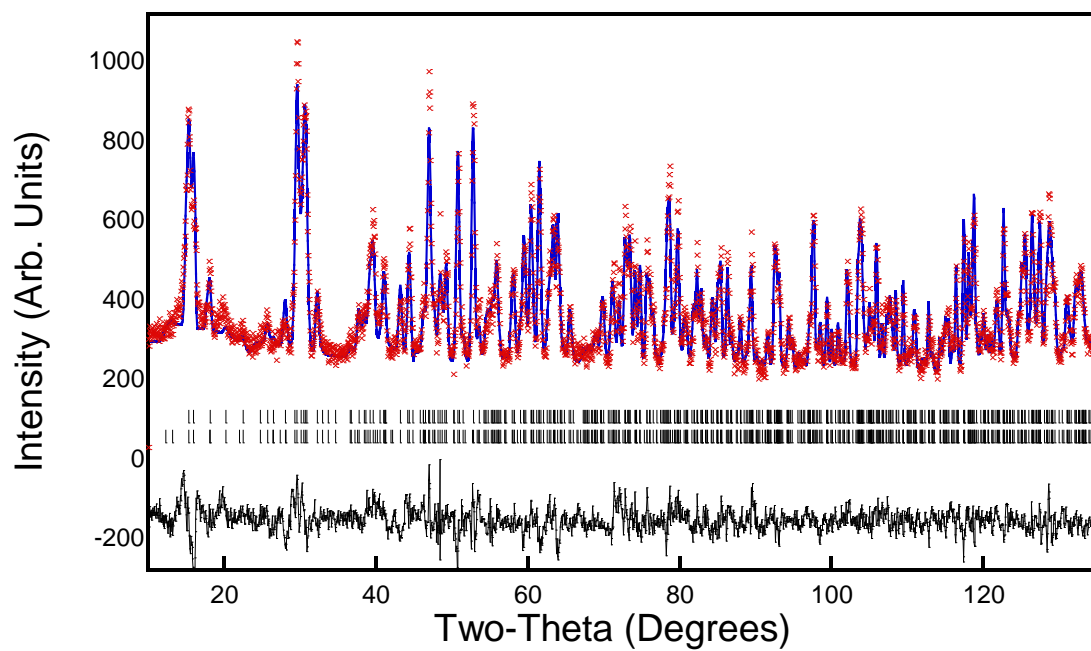

Figure 2A – 6. Observed (red markers), calculated (blue lines) and difference (black lines) obtained from Rietveld refinement of powder neutron diffraction data of RbFe$_2$F$_6$ at 4.5 K.

Figure 2A – 7. Observed (red markers), calculated (blue lines) and difference (black lines) obtained from Rietveld refinement of powder neutron diffraction data of RbFe$_2$F$_6$ at 5 K.
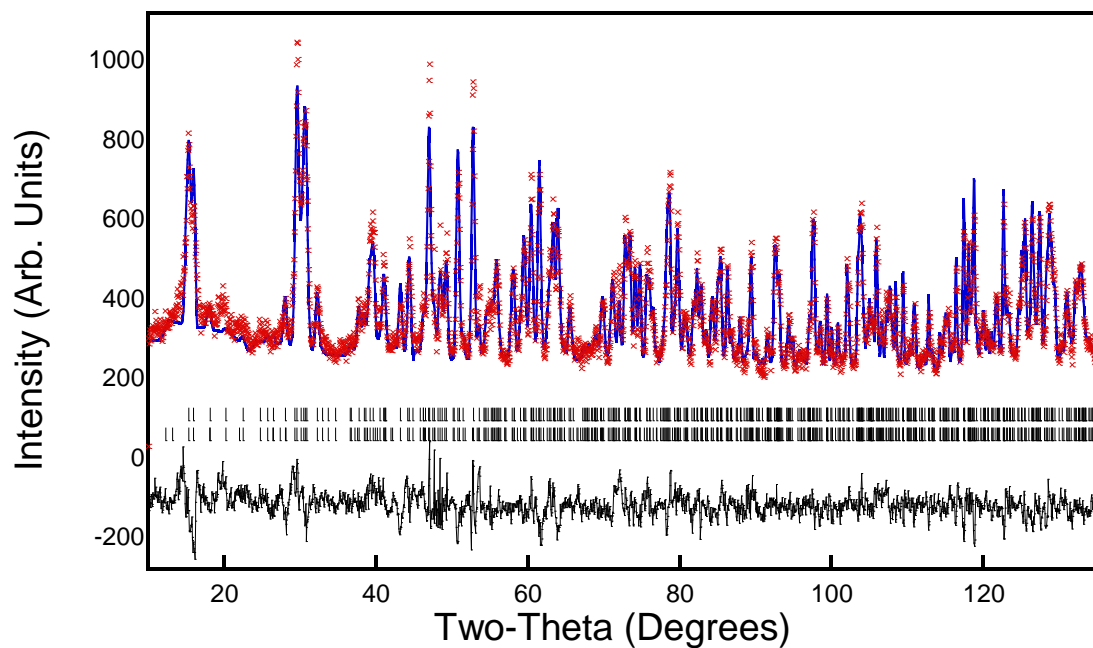

Figure 2A – 8. Observed (red markers), calculated (blue lines) and difference (black lines) obtained from Rietveld refinement of powder neutron diffraction data of RbFe$_2$F$_6$ at 10 K.

Figure 2A – 9. Observed (red markers), calculated (blue lines) and difference (black lines) obtained from Rietveld refinement of powder neutron diffraction data of RbFe$_2$F$_6$ at 12.5 K.
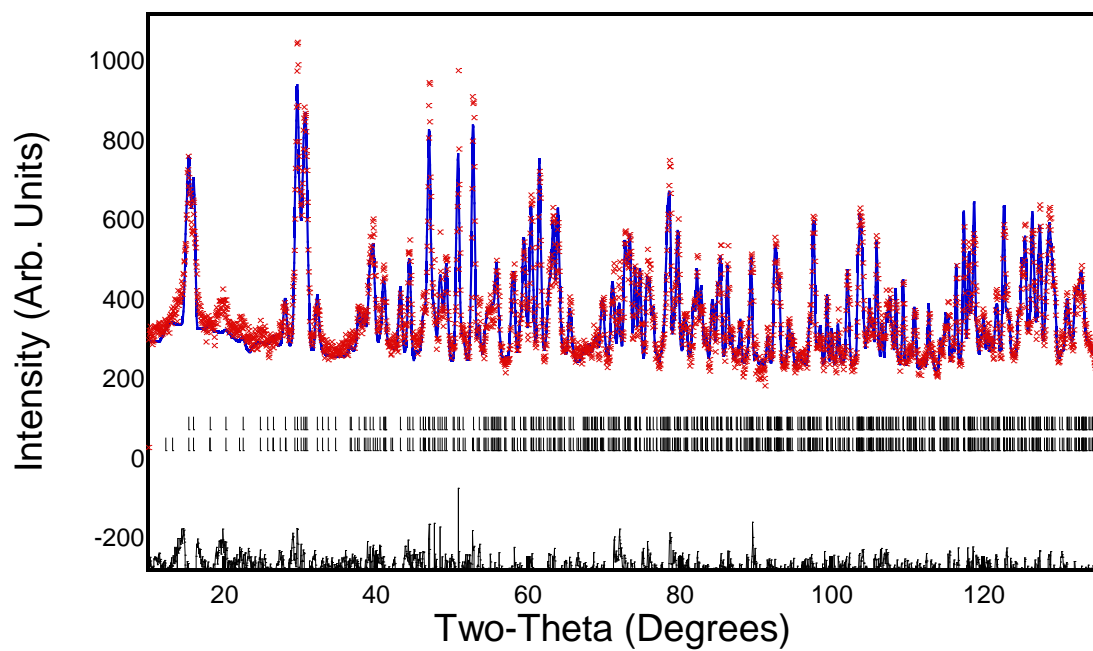

Figure 2A – 10. Observed (red markers), calculated (blue lines) and difference (black lines) obtained from Rietveld refinement of powder neutron diffraction data of RbFe$_2$F$_6$ at 15 K.
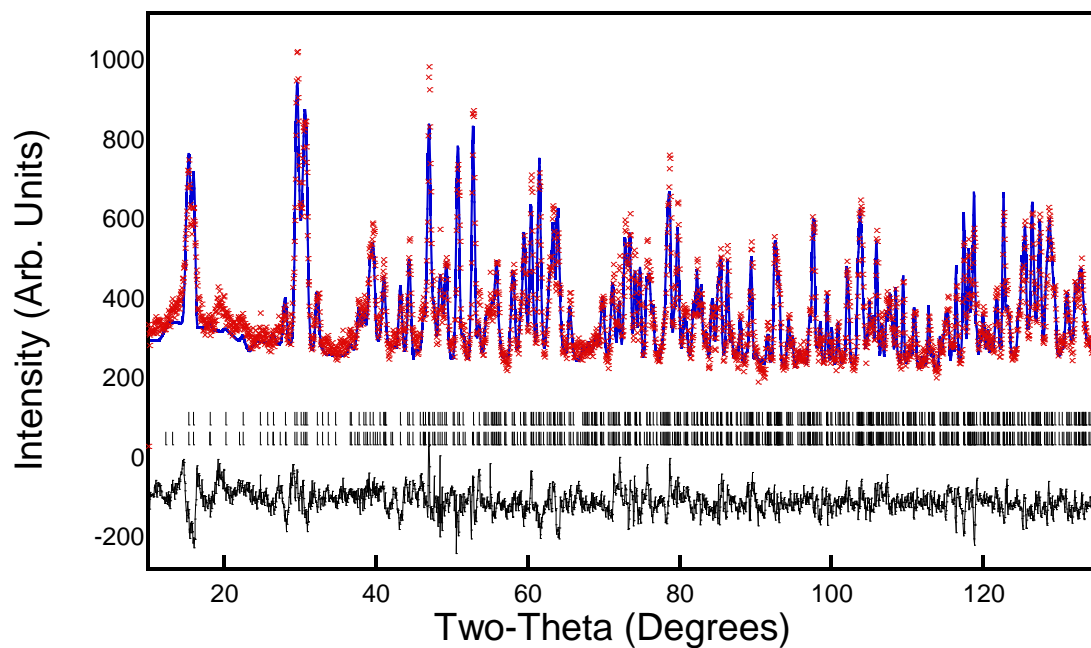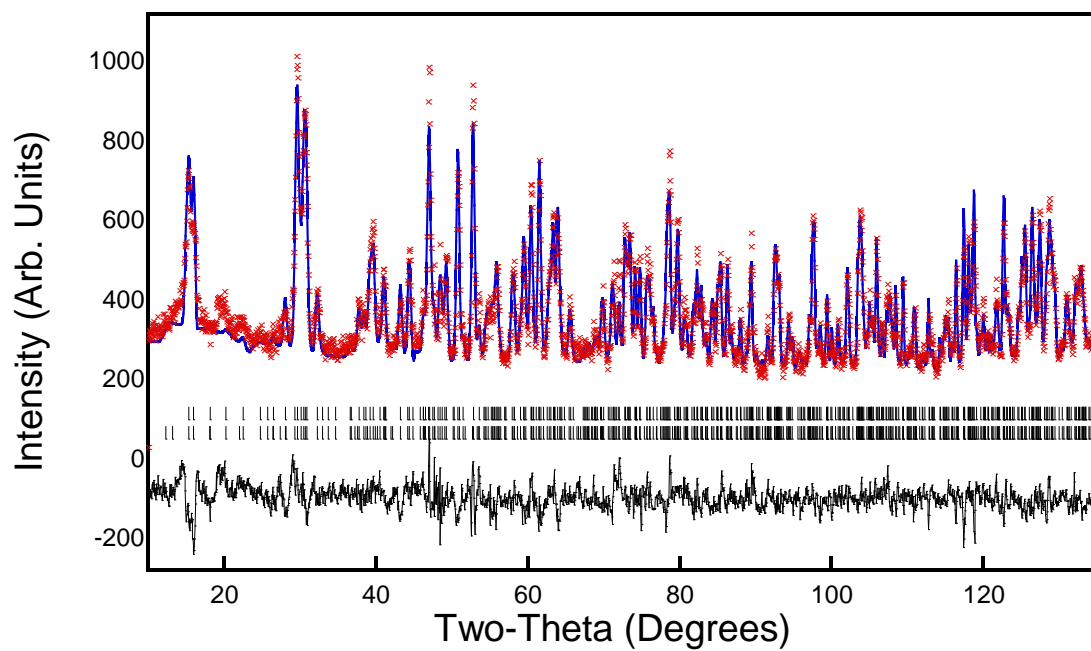
Figure 2A – 11. Observed (red markers), calculated (blue lines) and difference (black lines) obtained from Rietveld refinement of powder neutron diffraction data of RbFe$_2$F$_6$ at 17.5 K.

Figure 2A – 12. Observed (red markers), calculated (blue lines) and difference (black lines) obtained from Rietveld refinement of powder neutron diffraction data of RbFe$_2$F$_6$ at 20 K.

Figure 2A – 13. Observed (red markers), calculated (blue lines) and difference (black lines) obtained from Rietveld refinement of powder neutron diffraction data of $RbFe_2F_6$ at 22.5 K.

Figure 2A – 14. Observed (red markers), calculated (blue lines) and difference (black lines) obtained from Rietveld refinement of powder neutron diffraction data of $RbFe_2F_6$ at 25 K.
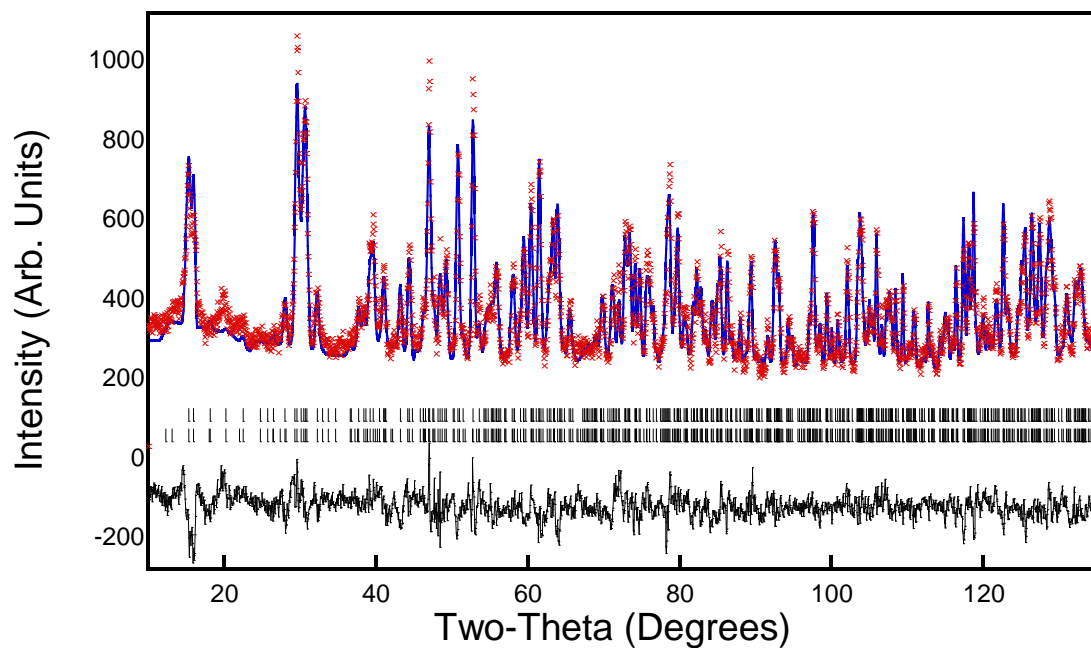
Figure 2A – 15. Observed (red markers), calculated (blue lines) and difference (black lines) obtained from Rietveld refinement of powder neutron diffraction data of $RbFe_2F_6$ at 50 K.
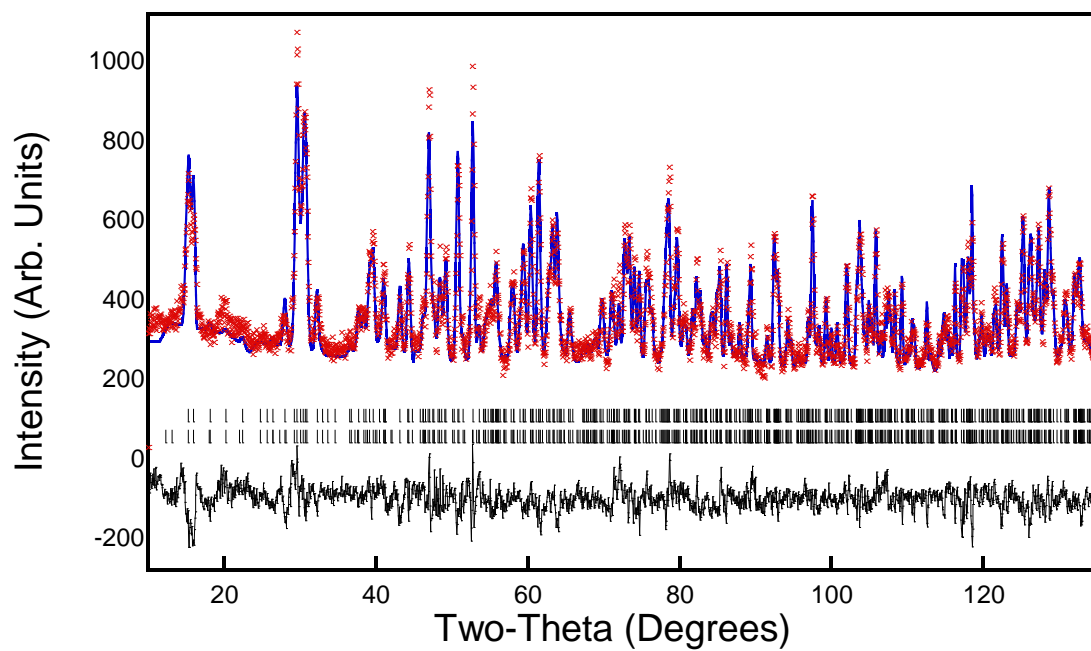

Figure 2A – 16. Observed (red markers), calculated (blue lines) and difference (black lines) obtained from Rietveld refinement of powder neutron diffraction data of $RbFe_2F_6$ at 100 K.

Rietveld refinement of powder neutron diffraction data of CsFeCrF$_6$ between 1.5 K to 35 K
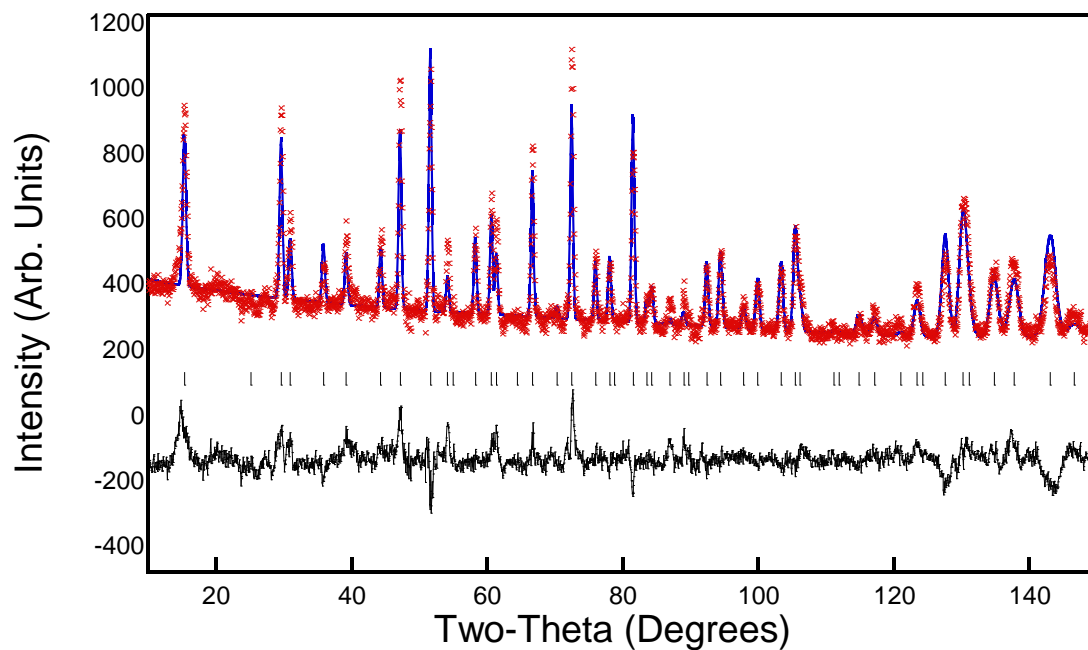

Figure 2A – 17. Observed (red markers), calculated (blue lines) and difference (black lines) obtained from Rietveld refinement of powder neutron diffraction data of RbFeCrF$_6$ at 1.5 K.

Figure 2A – 17. Observed (red markers), calculated (blue lines) and difference (black lines) obtained from Rietveld refinement of powder neutron diffraction data of RbFeCrF$_6$ at 5 K.
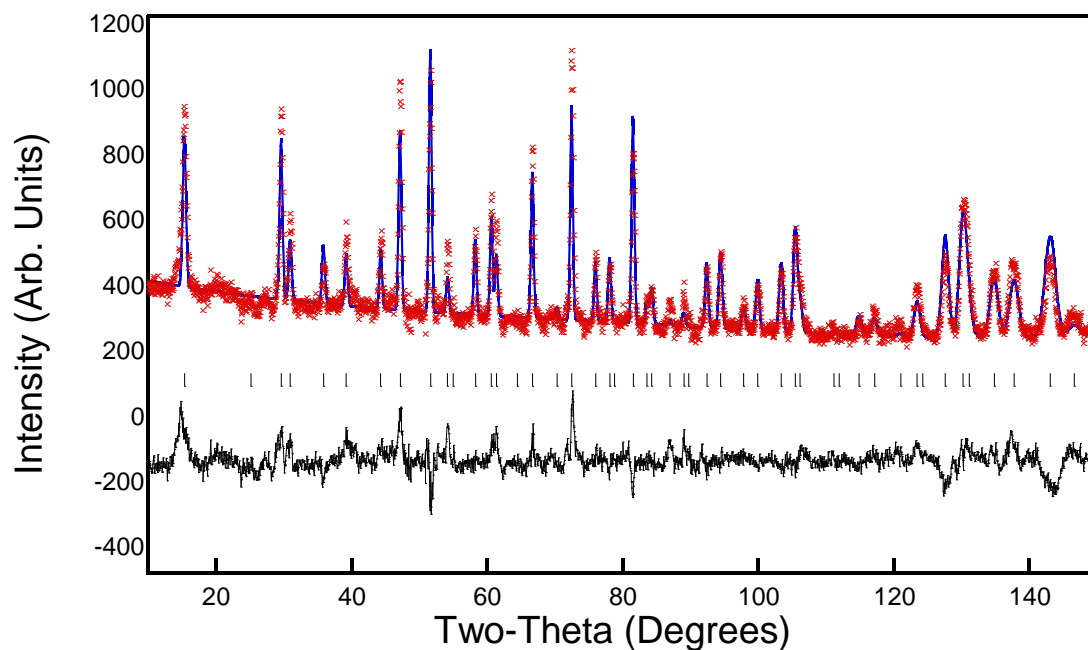
Figure 2A – 17. Observed (red markers), calculated (blue lines) and difference (black lines) obtained from Rietveld refinement of powder neutron diffraction data of $RbFeCrF_6$ at 10 K.
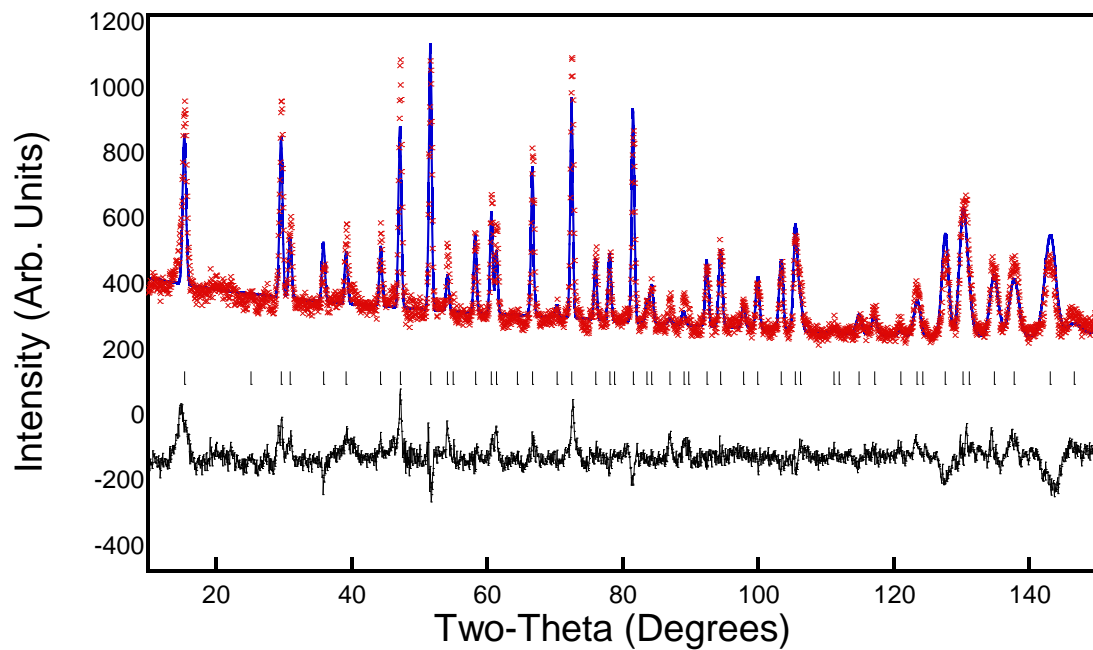

Figure 2A – 18. Observed (red markers), calculated (blue lines) and difference (black lines) obtained from Rietveld refinement of powder neutron diffraction data of $RbFeCrF_6$ at 15 K.
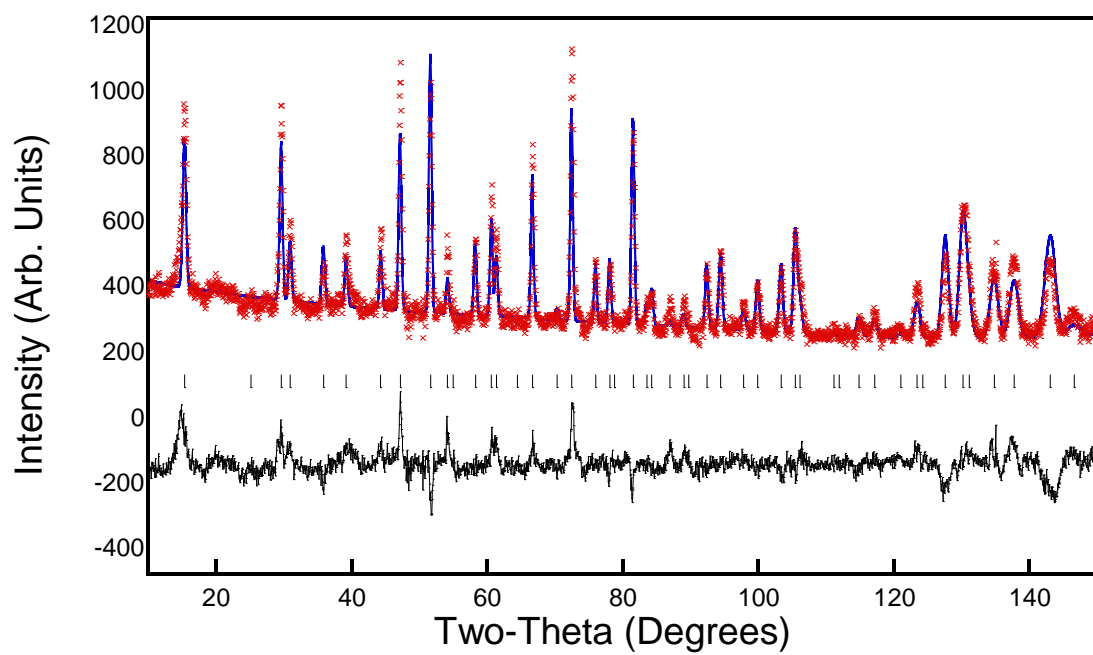
Figure 2A – 19. Observed (red markers), calculated (blue lines) and difference (black lines) obtained from Rietveld refinement of powder neutron diffraction data of RbFeCrF$_6$ at 20 K.

Figure 2A – 20. Observed (red markers), calculated (blue lines) and difference (black lines) obtained from Rietveld refinement of powder neutron diffraction data of RbFeCrF$_6$ at 25 K.
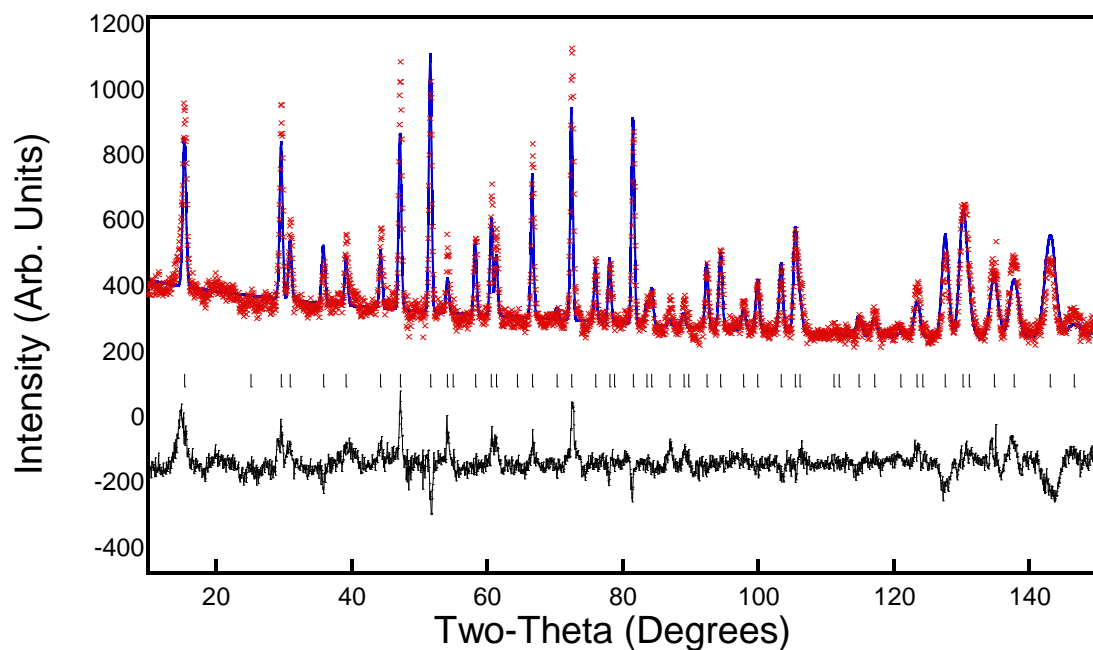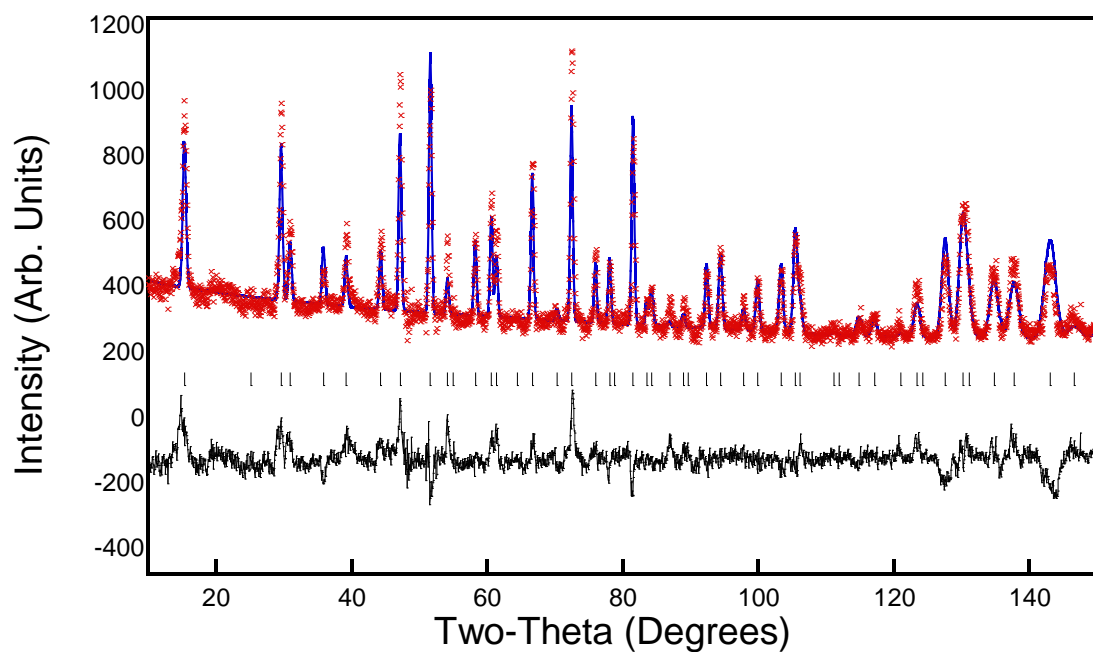
Figure 2A – 21. Observed (red markers), calculated (blue lines) and difference (black lines) obtained from Rietveld refinement of powder neutron diffraction data of RbFeCrF$_6$ at 30 K.

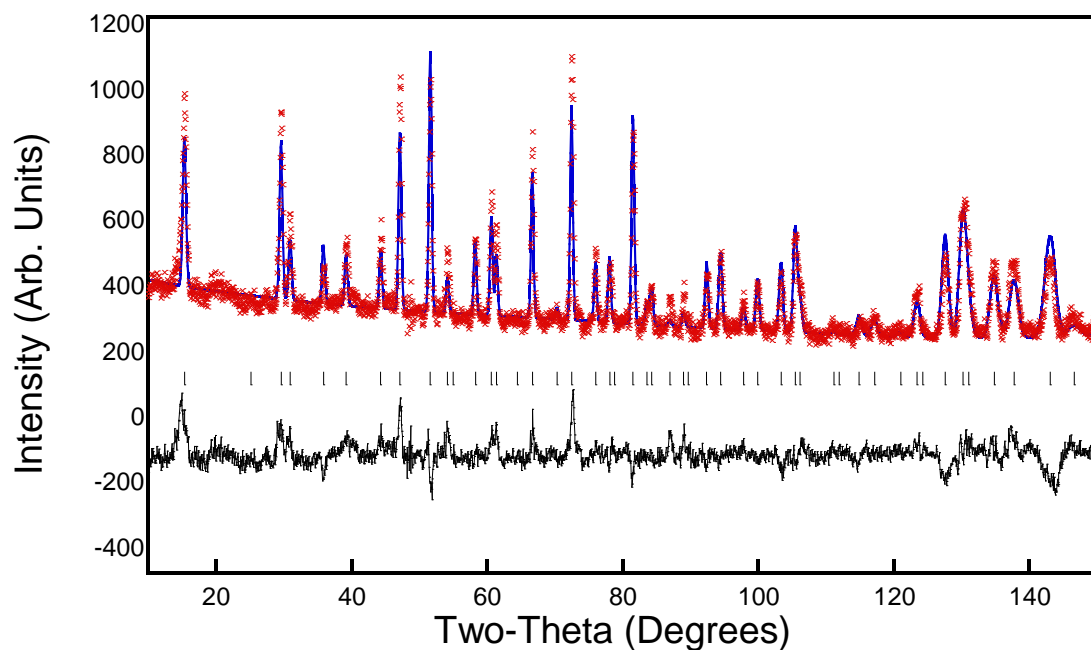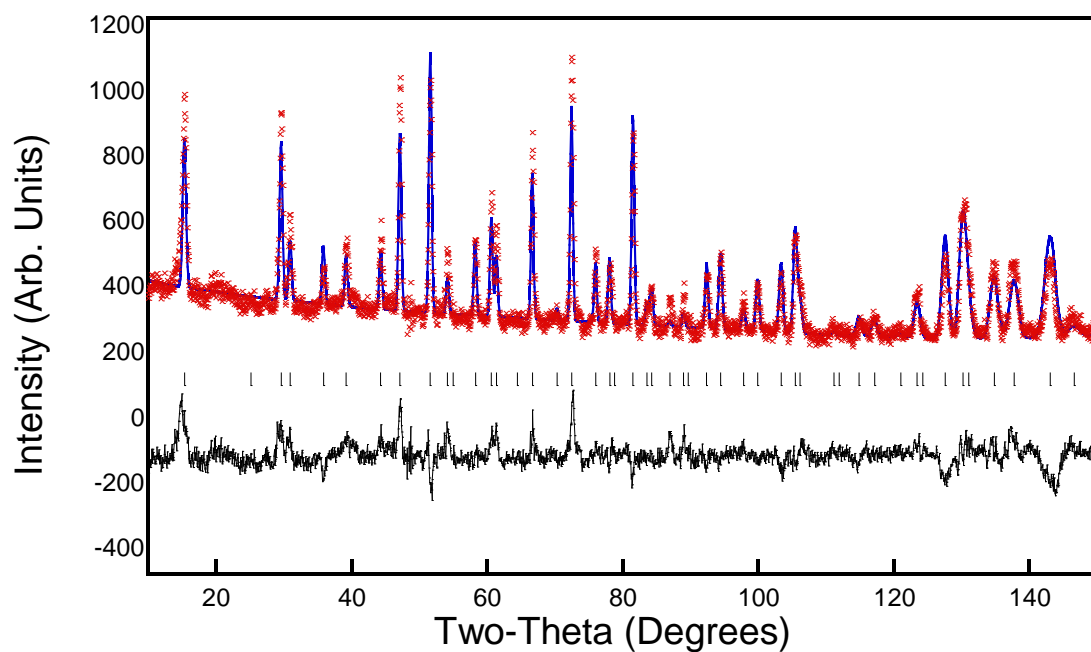

Figure 2A – 22. Observed (red markers), calculated (blue lines) and difference (black lines) obtained from Rietveld refinement of powder neutron diffraction data of RbFeCrF$_6$ at 35 K.

Squid magnetometry
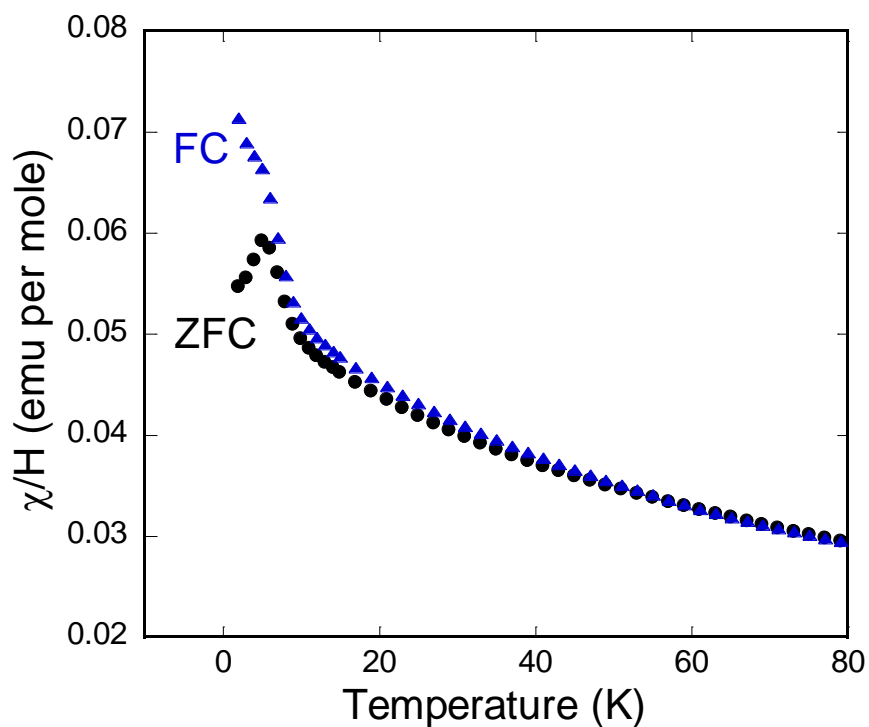
Figure 3A – 1 FC (blue), ZFC (black) of SQUID moment plots of RbFeCrF$_6$ measured at 1000 Oe from 2 to 80 K under ZFC/FC.

Figure 3A – 2 FC (blue), ZFC (black) of SQUID moment plots of RbFeCrF$_6$ measured at 100 Oe from 2 to 300 K under ZFC/FC.

Figure 3A – 3 FC (blue), ZFC (black) of SQUID moment plots of RbFeZnF$_6$ measured at 1000 Oe from 2 to 80 K under ZFC/FC.

Figure 3A – 4 Magnetic moment of Fe in $RbFe^{2+}/Fe^{3+}F_6$ as obtained from Rietveld refinement of powder neutron diffraction data

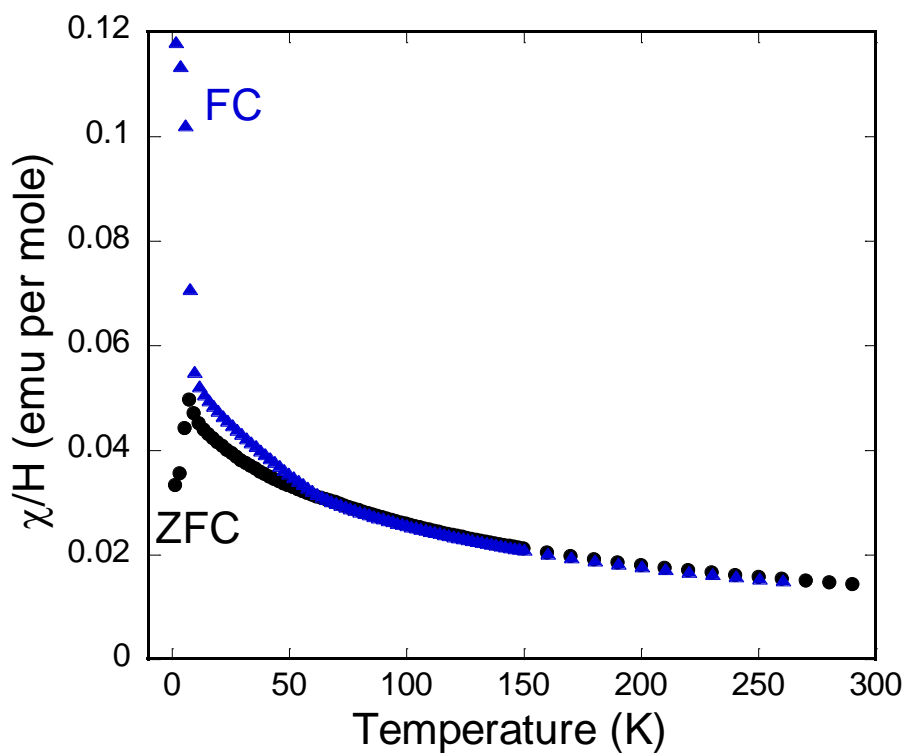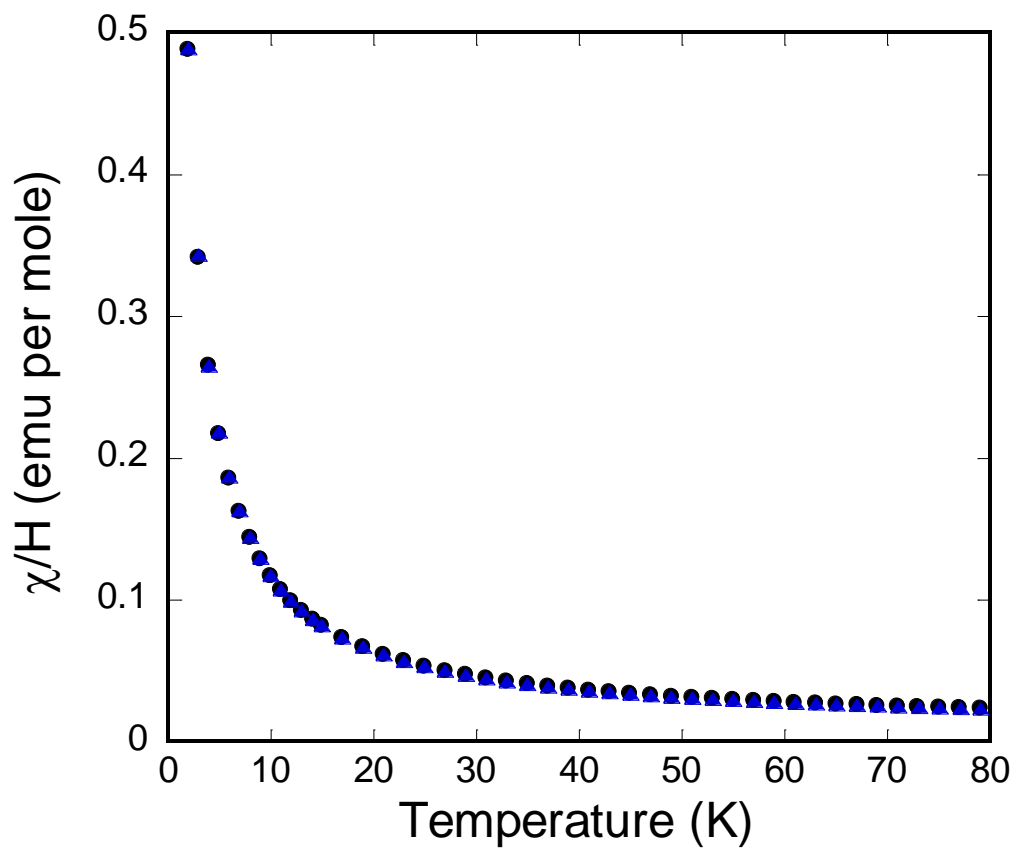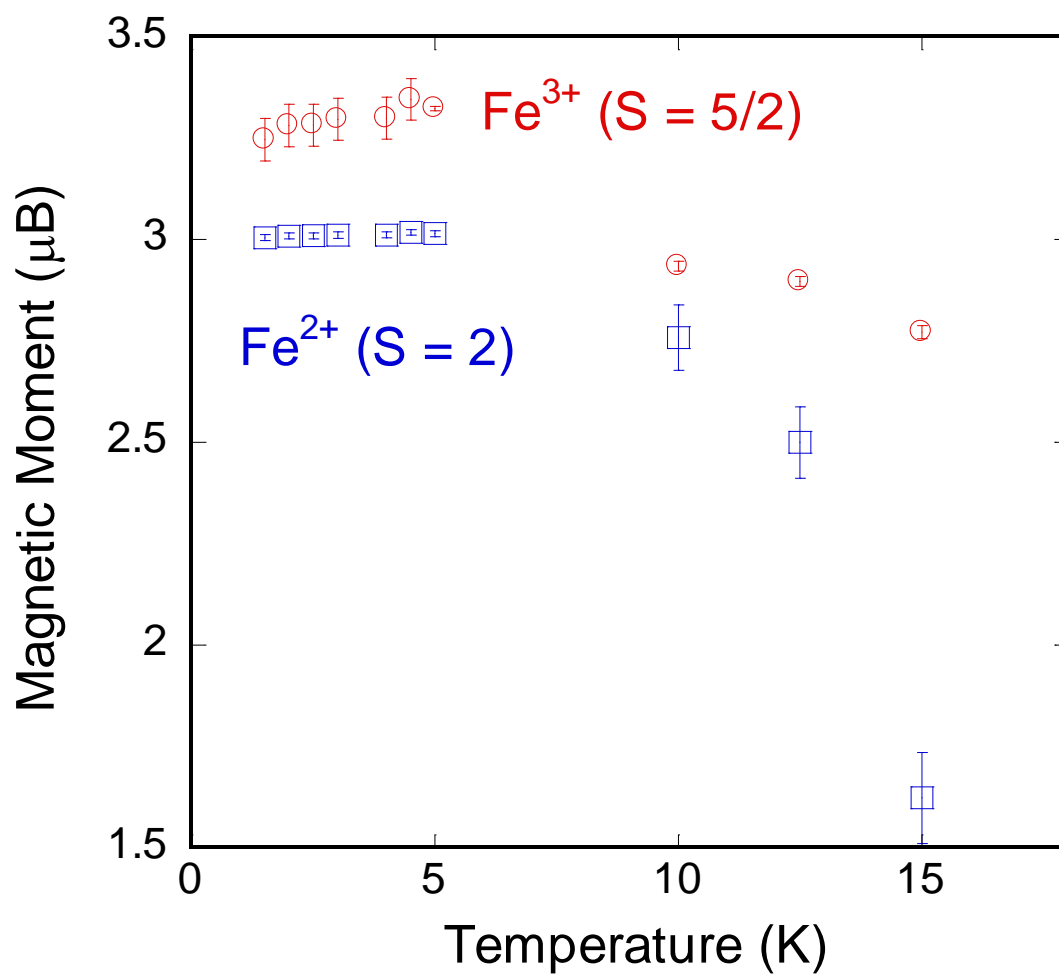rbcrfef6_vt_1_100_00 [Full Structure]

rbcrfef6_vt_1_100_00 [Full Structure] Model

Cr F6 Fe Rb
(Imported from a CIF file.)

Crystal Structure Data

Symmetry

Spacegroup Symbol:	P n m a	
Lattice Type:	P	
General Equivalent Positions:	+x +y +z 1/2-x -y 1/2+z -x 1/2+y -z 1/2+x 1/2-y 1/2-z	-x -y -z 1/2+x +y 1/2-z +x 1/2-y +z 1/2-x 1/2+y 1/2+z

Unit Cell Parameters

a [Å]	b [Å]	c [Å]	α [°]	β [°]	γ [°]
6.9970(4)	7.3397(5)	10.1081(7)	90.000(0)	90.000(0)	90.000(0)

Fractional Coordinates of Atoms in the Asymmetric Unit

	Site	Occupancy	x	y	z
1	F004	F 1.0	0.2632(3)	0.5626(3)	0.0815(2)
2	F005	F 1.0	0.6268(3)	0.5110(3)	0.1659(2)
3	F006	F 1.0	0.4369(4)	0.7500(0)	0.3397(3)
4	F007	F 1.0	0.4346(4)	0.2500(0)	0.0370(3)
5	Fe02	Fe 1.0	0.2049(1)	0.7500(0)	0.2318(1)
6	Fe03	Cr 0.7 Fe 0.3	0.5000(0)	0.5000(0)	0.0000(0)
7	Rb01	Rb 1.0	0.5094(1)	0.7500(0)	0.6230(1)

Atomic Displacement Parameters

Site	U11	U22	U33	U23	U13	U12	Uiso	Type

1	F004	0.0094	0.0074	0.0103	−0.0005	0.0032	0.0004	●	Uij
2	F005	0.0134	0.0142	0.0072	−0.0020	−0.0025	−0.0022	●	Uij
3	F006	0.0064	0.0119	0.0125	0.0000	−0.0007	0.0000	●	Uij
4	F007	0.0118	0.0038	0.0183	0.0000	0.0031	0.0000	●	Uij
5	Fe02	0.0065	0.0035	0.0040	0.0000	0.0007	0.0000	●	Uij
6	Fe03	0.0066	0.0012	0.0027	−0.0005	0.0010	−0.0005	●	Uij
7	Rb01	0.0140	0.0155	0.0095	0.0000	0.0019	0.0000	●	Uij

rbcrfef6_vt_2_300_00

rbcrfef6_vt_2_300_00 Model

Cr F6 Fe Rb
(Imported from a CIF file.)

Crystal Structure Data

Symmetry

Spacegroup Symbol:	P n m a	
Lattice Type:	P	
General Equivalent Positions:	+x +y +z 1/2-x -y 1/2+z -x 1/2+y -z 1/2+x 1/2-y 1/2-z	-x -y -z 1/2+x +y 1/2-z +x 1/2-y +z 1/2-x 1/2+y 1/2+z

Unit Cell Parameters

a [Å]	b [Å]	c [Å]	α [°]	β [°]	γ [°]
7.0474(6)	7.3482(7)	10.1591(9)	90.000(0)	90.000(0)	90.000(0)

Fractional Coordinates of Atoms in the Asymmetric Unit

	Site	Occupancy	x	y	z
1	Cr03	Cr 1.0	0.5000(0)	0.5000(0)	0.5000(0)
2	F004	F 1.0	0.2676(4)	0.5617(3)	0.5849(3)
3	F005	F 1.0	0.5595(6)	0.7500(0)	0.4622(4)
4	F006	F 1.0	0.4402(6)	0.7500(0)	0.8379(4)
5	F007	F 1.0	0.3691(4)	0.4871(4)	0.3366(3)
6	Fe02	Fe 1.0	0.2078(1)	0.7500(0)	0.7330(1)
7	Rb01	Rb 1.0	0.5105(1)	0.7500(0)	1.1234(1)

Atomic Displacement Parameters

	Site	U11	U22	U33	U23	U13	U12	Uiso	Type

1	Cr03	0.0102	0.0040	0.0056	−0.0016	0.0013	−0.0004	•	Uij
2	F004	0.0179	0.0161	0.0193	−0.0048	0.0056	0.0026	•	Uij
3	F005	0.0279	0.0048	0.0290	0.0000	0.0063	0.0000	•	Uij
4	F006	0.0115	0.0330	0.0208	0.0000	−0.0029	0.0000	•	Uij
5	F007	0.0279	0.0270	0.0124	−0.0043	−0.0058	−0.0001	•	Uij
6	Fe02	0.0122	0.0094	0.0087	0.0000	0.0016	0.0000	•	Uij
7	Rb01	0.0328	0.0379	0.0261	0.0000	0.0046	0.0000	•	Uij